PROGRAMA DOUTORAL EM ENGENHARIA ELECTROTÉCNICA E DE COMPUTADORES

POWER GENERATION SYSTEM FOR SERIES HYBRID ELECTRIC VEHICLES

RUI MIGUEL MONTEIRO DE BRITO

PhD Thesis

Supervisor: ADRIANO DA SILVA CARVALHO

Co-supervisor: MANUEL GRADIM DE OLIVEIRA GERICOTA

May 2015

this page was intentionally left blank

Agradecimentos

Agradeço ao professor Adriano Carvalho, meu orientador, os conhecimentos teóricos, práticos e "de vida" que me transmitiu. A sua experiência foi decisiva em momentos cruciais. Talvez o momento mais marcante tenha sido aquele em que, perante uma dificuldade "enorme" e sem aparente solução, me disse assim: "divides esse teu problema em vários problemazinhos, resolves cada um deles em separado e no final terás essa tua dificuldade ultrapassada". Funcionou!

Manuel Gericota, agradeço do fundo do coração toda a dedicação e esforço colocado nesta coorientação, em particular na revisão e formatação da tese e ainda com "o inglês", o que terá ajudado certamente a que ficasses com mais alguns cabelos brancos.

Carlos Paiva, agradeço a tua preciosa ajuda no desenho e montagem das placas de circuito impresso, sem a qual não teria sido possível efetuar os ensaios laboratoriais em tempo útil. Quero realçar aqui o profissionalismo colocado em tudo o que fazes. Aquela placa controladora é admirada por todos. Aprendi o teu lema: "demora tanto a fazer (as coisas) bem como (a fazê-las) mal".

Ricardo Soares, agradeço a tua ajuda e a disponibilidade que sempre tiveste para comigo, nomeadamente para a discussão dos assuntos técnicos. O meu obrigado também pela revisão crítica da tese. Tocaste em pontos fulcrais. És das poucas pessoas que conhece o meu trabalho a fundo e que pela tua formação e experiencia consegues discuti-lo "de fio a pavio".

Ao Bruno Azevedo agradeço o "pontapé" inicial com o XMC4500 e ainda a boa disposição que impunhas ao laboratório. Ainda me lembro quando no inverno chegavas, abrias as janelas todas, saias novamente porta fora e, quem ficasse que aguentasse…

Ao Alexandre Silveira, amigo e companheiro nesta luta, quero agradecer a amizade, honestidade, afeto, respeito, confiança e tudo mais que se pode dizer de um amigo. Obrigado meu amigo.

Ao Ataollah Mokhberdoran agradeço a simpatia, disponibilidade e sabedoria, assim como a ajuda específica com as figuras e revisão do artigo para o IET.

Ao Agostinho Rocha, companheiro nestes últimos meses, agradeço a simpatia e amizade.

Ao ISEP/IPP agradeço a aposta que está a fazer na formação dos docentes e no meu caso particular a dispensa de serviço concedida nestes últimos meses, que se revelou crucial para que pudesse estar focado na organização de ideias e na escrita da tese.

Agradeço ainda a todos aqueles que de uma ou outra forma me ajudaram nesta longa caminhada. Bem hajam.

this page was intentionally left blank

Abstract

The focus of this thesis is the electric vehicle with an internal combustion engine (ICE) as range extender (RE) and in particular the efficient control of the power delivered by the ICE to the vehicle lithium-ion battery-based DC bus.

In this vehicle, classified in specialized literature as a series hybrid electric vehicle (HEV), there is an ICE working only at an efficient regime, i.e. almost constant power and speed, that feeds an electric generator, which, after appropriate AC/DC conversion feeds the vehicle DC bus.

The DC bus is based on Li-ion batteries, capacitors and electric drives (inverters) that feed traction electric motors and other vehicle auxiliary systems.

To perform the energy conversion from mechanical to electrical, a permanent magnet synchronous machine, working as generator, i.e. a PMSG, is direct coupled to the ICE shaft.

Currently, PMSMs are the electrical machines with higher power density (less volume and weight for the same power), and therefore suitable for electric mobility and for the avionics industry.

For the AC to DC conversion it is adopted a voltage source converter (VSC), which is based on IGBTs hard switched at high frequencies, e.g. 20kHz.

To extract the maximum power from the ICE/PMSG with minimal losses, an in-depth knowledge of the PMSG and VSC subsystems is required. Furthermore, the rotor position and speed have to be known to efficiently control the PMSG. The rotor position can be acquired using a shaft sensor (encoder or resolver), or a sensorless position estimator.

This thesis goes through the different subsystem areas, namely: PMSG modeling; VSC modeling; pulse-width modulation (PWM) techniques; PMSG control techniques; PMSG control strategies; PMSG sensorless synchronization techniques.

Original contributions are given for: VSC modeling; controller design; PWM techniques (in particular to space vector modulation (SVM)); PLL-based sensorless rotor and speed estimator, based on phase current measurements.

A new sensorless controller is designed and analyzed using the power simulator PSIM. Results show that its dynamic response is excellent, comparable to sensor based controllers. These simulation results were validated experimentally, also confirming the robustness of the system.

Keywords: hybrid electric vehicle, range extender, permanent magnet synchronous generator, voltage source converter, space vector modulation, sensorless rotor position estimation, phase locked loop, field oriented control.

this page was intentionally left blank

Resumo

Esta tese tem como objeto de estudo os veículos elétricos que têm um motor de combustão interna (MCI) a funcionar como extensor de autonomia (EA), centrando-se em particular sobre o controlo eficiente da potência transferida do MCI para o barramento de CC do veículo que é suportado por baterias de iões de lítio.

Neste veículo, denominado na literatura por veículo elétrico híbrido (VEH) com topologia série, existe um MCI a trabalhar num regime eficiente, isto é, velocidade e potência praticamente constantes, que aciona um gerador que, após uma conversão CA/CC, alimenta o barramento CC do referido veículo.

O barramento CC contém baterias de iões de lítio, condensadores e acionadores elétricos (inversores de potência), que alimentam os motores elétricos de tração, assim como outros sistemas auxiliares do veículo.

Para fazer a conversão de energia mecânica para elétrica é utilizada uma máquina síncrona de ímanes permanentes (MSIP) a funcionar como gerador, ou seja, um GSIP, acoplado diretamente ao veio do MCI. Os MSIP são atualmente as máquinas elétricas que possuem a maior densidade de potência (menor volume e peso, para a mesma potência), sendo, por isso, adequadas à mobilidade elétrica e à indústria da aviação.

Para a conversão CA/CC é utilizado um retificador com modulação de largura de impulso (MLI), baseado em IGBTs a operar a alta frequência, por exemplo, a 20kHz.

Por forma a extrair a máxima potência do MCI/MSIP, com perdas mínimas, é necessário conhecer em profundidade a MSIP e o retificador com MLI. Além disso, a posição do rotor e a velocidade da MSIP têm que ser conhecidas para a poder controlar de forma eficiente. A posição do rotor pode ser conhecida através de um sensor de posição colocado no veio da máquina (um *encoder* ou *resolver*) ou obtida com base num estimador.

Esta tese integra os contributos de várias áreas de conhecimento, nomeadamente: modelização da MSIP; modelização de retificadores/inversores com MLI; técnicas de MLI; técnicas de controlo do GSIP; estratégias de controlo do GSIP; e técnicas de estimação/sincronização para GSIP.

Por outro lado, contribui para o avanço do saber em áreas como a modelização de retificadores/inversores com MLI; controladores para GSIP; técnicas de MLI; estimadores de posição do rotor baseados em PLL e em medição de correntes.

O resultado final do trabalho desenvolvido é a conceção de um novo controlador que não necessita de um sensor no veio. As suas prestações foram avaliadas com o simulador PSIM, tendo os resultados, que foram validados experimentalmente, mostrado uma dinâmica excelente, comparável à dos controladores que utilizam sensor, o que confirma a robustez do sistema.

Palavras-chave: veículos elétricos híbridos, extensor de autonomia, gerador síncrono de ímanes permanentes, retificador MLI, modulação espacial vetorial, estimação da posição do rotor, controlo baseado em orientação do campo.

this page was intentionally left blank

Acronyms

$\alpha\beta$	*alpha-beta* reference frame
abc	*abc* reference frame
ADC	Analog-to-digital converter
App	Software application
dq	Direct-quadrature reference frame
DSC	Direct self-control
DSP	Digital signal processor
DTC	Direct torque control
EKF	Extended Kalman filter
ELO	Extended Luenberger observer
ESR	Equivalent series resistor
EV	Electric vehicle
FILO	First-in-last-out memory
FOC	Field oriented control
FPGA	Field-programmable gate array
HCCI	Homogeneous charge compression ignition
HEV	Hybrid electric vehicle
ICE	Internal combustion engine
IM	Induction motor
ISU	International system of units
LEM	Manufacturer's brand of solutions for measuring electrical parameters
LPF	Low-pass filter
M	Modulation index M
m	Modulation index m
MAV	Moving average filter
MCU	Microcontroller unit
MTPA	Maximum torque-per-ampere
MTPV	Maximum torque-per-voltage
PCB	Printed circuit board
PF	Power factor

PI	Proportional integral controller
PLL	Phase locked loop
PM	Permanent magnet
PMSG	Permanent magnet synchronous generator
PMSM	Permanent magnet synchronous machine
PWM	Pulse-width modulation
RE	Range extender
SMO	Sliding mode observer
SO	Symmetrical optimum PI tuning method
SPWM	Sinusoidal pulse-width modulation
SRF-PLL	Synchronous reference frame PLL
SVM	Space vector modulation
UPF	Unity power factor
VCO	Voltage controlled oscillator
VSC	Voltage source Converter

Index

1
Introduction

Two main factors are contributing to an important change in the transportation sector:

- First of all, the oil price. Its peak price was achieved in 2008 and no one believes that it will return to previous levels. The demand is continuously growing [1], in particular due to emergent markets like China and India [2], and reserves tend to decrease, despite some recent oil reserve discoveries (e.g. in Brazil) [3].
- Second one, the global awareness that carbon emissions are effectively leading to catastrophic climate changes. That awareness is in part due to the extra taxes and prohibitions imposed to polluters, particularly in Europe. In some cases, the city center traffic is taxed (e.g. in London) [4] or interdict to older vehicles (e.g. in Lisbon) [5].

These two facts lead to a new transportation paradigm: car makers are applying their efforts to reduce fuel consumption and emissions. This has been achieved with new and more efficient types of fuel, lighter Internal Combustion Engine (ICE), and new powertrain/drivetrain concepts [6].

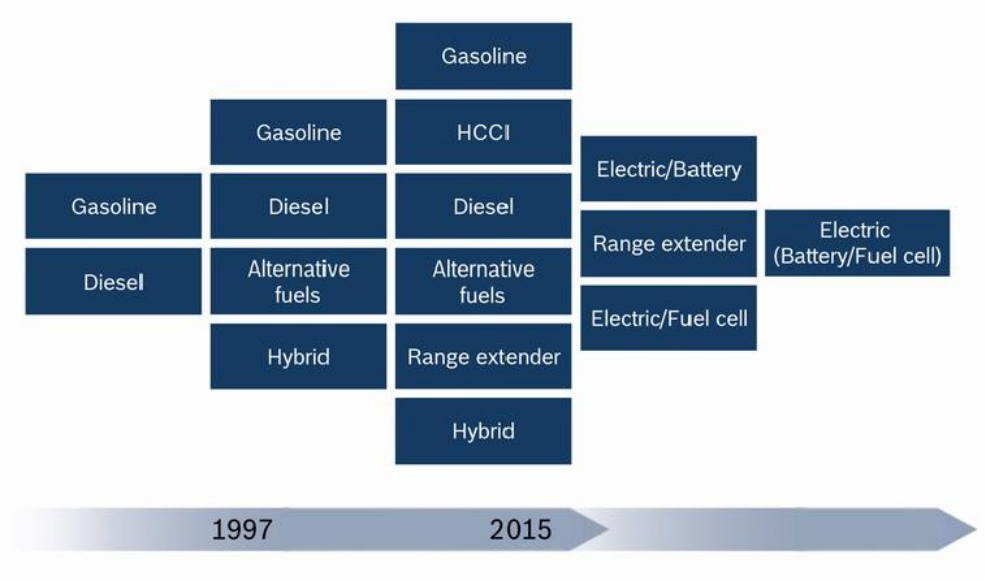

Figure 1.1 - Powertrain technologies for passengers vehicles – timetable [6]

In the future it is expected that vehicles will be purely electric or, at least, will have exclusively electric propulsion (see Figure 1.1). In the meanwhile, that is, while batteries do not have suitable energy densities, recharge cycles, weight and price, hybridization, i.e. powertrain electrification, will be the solution to cope with mid and long journeys.

In the beginning of the Millennium, the Toyota Prius started a new era of hybridization. The concept was simple – adding an electric motor to the ICE Block to help it to work almost entirely at efficient regimes, but the implementation proved complicated. This topology was appropriately called Complex Hybrid Powertrain by some authors [7].

According to some players in the automotive industry, e.g., Bosch in International Automotive Press Briefing 2009 [6], the present and near future is reserved for two, not new, powertrain concepts: the electrical vehicle with an ICE as Range Extender (RE); and the electrical vehicle with a fuel cell (Figure 1.2). Both are commonly called as series powertrain topologies as the extenders are used to generate electricity that will feed batteries and electric traction motors. Although both powertrains have RE, the designation RE is usually reserved for electric vehicles with an ICE as RE. The Opel Ampera (aka. Chevrolet Volt in the U.S.), or the BMW i3 with RE, are nowadays series production examples of RE vehicles. The introduction of electric fuel cell vehicles in the market has been delayed mainly due to the lack of a proper hydrogen production and distribution network.

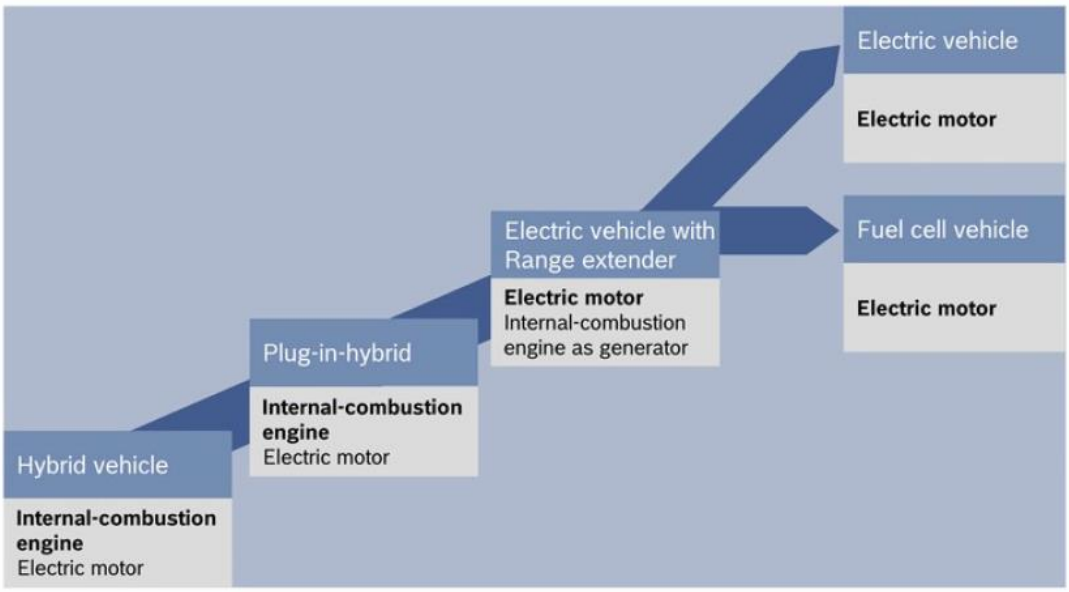

Figure 1.2 - Powertrain electrification – scenario [6]

The focus of this thesis is the electric vehicle with an ICE as Range Extender, in particular the efficient control of the power delivered by the ICE to the vehicle lithium-ion battery-based DC-bus (Figure 1.3).

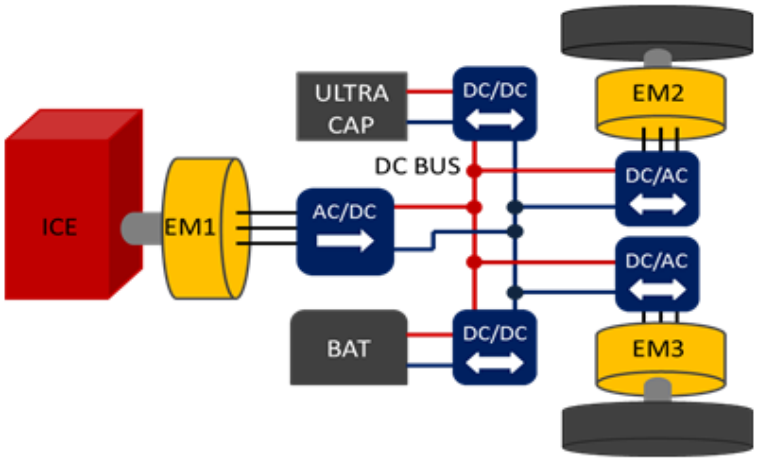

Figure 1.3 – Series hybrid powertrain with an ICE as range extender

Considering that the ICE only works at efficient regimes, i.e., at almost constant velocity and constant power, this thesis targets two subsystems:

- the electric generator, a Permanent Magnet Synchronous Machine (PMSM);
- the AC/DC power converter, a bi-directional three-phase Voltage Source Converter (VSC) and its control.

In order to efficiently control the PMSG, a vector control technique is adopted. Vector control techniques require that rotor position and speed are known. They can be acquired via shaft sensor, an encoder or resolver, or can be estimated by means of a sensorless synchronization technique.

This thesis goes through the different subsystem areas, namely:

- PMSG modeling;
- VSC modeling;
- PWM techniques;
- PMSG control techniques (Direct torque control (DTC) vs Field Oriented Control (FOC));
- PMSG control strategies;
- PMSG sensorless synchronization techniques with emphasis on the synchronous reference frame PLL (SRF-PLL).

At the end a new sensorless PMSG controller using FOC and a SRF-PLL, based on current measurements, is designed. Experimental results validate the solution and show its robustness.

1.1 Original Contributions

The main original contributions of this thesis are:

- Development of a new VSC Laplace model in dq frame which excludes the carrier frequency from the model while highlighting the cross-coupling

between d and q quantities, enabling the design of a suitable current-controller. PSIM simulator analysis shows that (1) both Laplace model and its electrical equivalent have the same dynamic behavior and (2) the benefits on the circuit's dynamics from having a decoupled controller.

- Two new PSIM implementations of Space Vector Modulation (SVM) are designed.

- Development of a Synchronous Reference Frame Phase Locked-Loop (SRF-PLL) based exclusively on current measurements that prove to be a robust solution to estimate the electrical angle θ_e and speed ω_e variables, needed to perform sensorless Field Oriented Control (FOC) in generator operation.

- Development of a new estimation technique for electrical angle θ_e and speed ω_e, based on line currents and on two dq frames which is particularly suited when the i_d current reference is not zero.

1.2 Thesis Outline

The thesis is organized in 8 chapters and two annexes.

Chapter 1 is this introduction.

Chapter 2 addresses the PMSM which is the machine adopted in this work. PMSMs are classified according to its rotor topology. Its relationship with the rotor anisotropy is analyzed since it directly influences the way the PMSM should be controlled. The electromagnetic torque of the PMSM is modeled in dq frame and three different but equivalent torque equations are derived as functions of three different definitions of the torque angle.

Chapter 3 discusses the VSC modeling in Laplace and dq frame, with the converter's carrier frequency excluded from the modeling process. Based on the developed models an integrated current controller is designed. The dynamic behavior of the Laplace model is compared with its equivalent electric model, as well as the dynamic behavior of the designed decoupled current controller is compared with a non-decoupled one.

In Chapter 4 two of the most widely used PWM techniques applied to VSCs, the Sinusoidal PWM (SPWM) and the Space Vector Modulation (SVM) are analyzed and compared. Two new PSIM SVM implementations are derived using exclusively PSIM blocks. Application examples are provided to show VSC's dynamic behavior as function of the PWM technique adopted.

In Chapter 5 a survey of sensorless techniques is presented. PLL sensorless techniques are discussed with more detail, in particular the Synchronous Reference Frame PLL (SRF-PLL). The application of the SRF-PLL technique to highly harmonic polluted currents and step dynamic amplitude variation (from 1.5% to 100%) is evaluated.

Chapter 6 is dedicated to PMSM control. Field Oriented Control (FOC) and Direct Torque Control (DTC) are briefly discussed. A comprehensive set of control strategies addressed to FOC is presented and discussed. According to the characteristics of the PMSM used on the experimental setup, which has an isotropic rotor, the Constant-angle Control strategy is adopted ($\delta_i = 90^o \Rightarrow i_d^* = 0$). A set of analysis performed with the help of PSIM, firstly based on sensor FOC and later on sensorless FOC with SRF-PLL are evaluated and compared. The final PSIM version is running "microcontroller-ready" C code, the same code later used in the experimental setup.

The sensorless FOC theory based on SRF-PLL is extended to cope with any i_d current reference different from zero, and for motor and generator operation. This theory is based on two dq reference frames, one for flux and voltages, and the other for currents.

Chapter 7 is dedicated to the experimental setup design and to the practical experiments done to validate the theoretical concepts explored in previous chapters.

Finally chapter 8 is reserved for the conclusions.

Annex 1 deals with reference frame transformations and its compatibility with PSIM's reference frame transformation blocks while the schematics of the developed hardware are included in Annex 2.

1.3 References

[1] The-Wall-Street-Journal. (2014). *Global Energy Demand May Outpace Supply in Future [Online]*. Available: http://www.wsj.com/articles/global-energy-demand-may-outpace-supply-in-future-iea-says-1415750651

[2] BP. (2014). *BP Energy Outlook 2035 [Online]*. Available: http://www.bp.com/content/dam/bp/pdf/Energy-economics/Energy-Outlook/Energy_Outlook_2035_booklet.pdf

[3] Reuters. (2013). *Petrobras, IBV wells show major new oil find in Brazil [Online]*. Available: http://www.reuters.com/article/2013/09/26/us-brazil-oil-discovery-idUSBRE98P0T020130926

[4] Transport-for-London. (2015). *London congestion charge [Online]*. Available: http://www.tfl.gov.uk/modes/driving/congestion-charge

[5] CM-Lisboa. (2015). *Zonas de Emissões Reduzidas em Lisboa [Online]*. Available: http://www.cm-lisboa.pt/viver/mobilidade/zonas-emissoes-reduzidas

[6] BOSCH-AUTOMOTIVE, "International Automotive Press Briefing 2009 [Online]," http://www.bosch-presse.de/2009.

[7] A. Emadi, *Handbook of Automotive Power Electronics and Motor Drives*: Taylor & Francis Group, LLC, 2005.

2
Permanent Magnet Synchronous Machines

2.1 Introduction

Permanent Magnet Synchronous Machines (PMSM) are a particular set of synchronous machines in which the rotor field is created by permanent magnets instead of coils fed by direct currents.

The use of Permanent Magnets (PM) allows four key advantages: First, the space required by the PMs is small when compared to machines having electromagnetic excitation, so that the machine design exhibits some degree of freedom, e.g. in the flux orientation or the shape [1, 2]; Second, since there are no magnetization losses the PM machines features high torque and power density with a fast dynamic response, leading to a higher efficiency over wide speed ranges [3, 4]; Third, as they have no brushes their reliability is higher even at very high speeds. Fourth, it is possible to achieve a smooth rotation with very low torque ripple using suitable control techniques.

The emergence of modern PM, e.g. the Neodymiun Iron Boron (NdFeB), with high energy density [2], makes the PMSM suitable for electric mobility.

PMSM are currently widely used in electric and hybrid vehicles. Recent areas of application include electric planes and energy recovery in heavy Internal Combustion Vehicles, e.g. trucks, where they are used to feed vehicle auxiliary systems and to produce cold and heat.

2.2 Synchronous Machines

Synchronous machines are rotary electrical machines in which the angular velocity of the shaft ω_m is directly proportional to the electrical line frequency f as follows:

$$\omega_m = \frac{\omega_e}{pp} = \frac{2\pi f}{pp}, rad/s \tag{2.1}$$

or

$$n = \frac{60 f}{pp}, rev/\min \tag{2.2}$$

where pp is the number of pole pairs of the machine, ω_e is the electrical angular velocity or *synchronous speed*, and n is the number of revolutions of the shaft per minute.

Synchronous machines are reversible machines: they can be operated either as motors or generators. If they are multi-phase generators they are called alternators [5].

When operating as a generator is the shaft velocity that imposes the line frequency while when running as a motor is the electrical line frequency that imposes the shaft velocity. In a normal operation both shaft and line frequency, are always in synchronism.

The synchronous machine has two groups of windings: the *stator* and the field windings. The *stator* winding is the AC electrical output power when the machine is operated as a generator and the AC input power when operated as a motor. A three-phase *stator* winding has a set of coils interconnected to form three independent phase windings. They are physically separated 120° apart.

The DC field windings are normally located in the rotor. Rotor flux varies with the DC field windings current. When the rotor magnetic field poles of a generator moves along the *stator* surface, the rotor flux induce alternating currents in the three-phase *stator* windings according to the Lenz's law. Those currents produce their own poles that are electrically rotating following the rotor poles movement. The interaction between the rotor flux and the electrically rotating stator flux produces a torque (in this case contrary to the shaft rotational movement), which is a function of its angular displacement. The resulting flux is called in literature air gap magnetic flux.

A similar analysis can be done if the synchronous machine is operated as a motor.

2.3 Permanent Magnet Synchronous Machine Classification Based on Rotor Technology

In a PMSM the stator has the same role as in a regular Synchronous Machine as its purpose do not change. Yet, the rotor can have different configurations according to the way Permanent Magnets are placed in.

PMSMs are usually classified in two different topologies, according to the flux field direction: radial-field (the flux direction is along the radius of the machine); and axial-field (the flux direction is parallel to the rotor shaft). While the radial-field machines are common, the axial-field ones are expanding now due to their higher power density and acceleration[2].

An example of cutting-edge technology is the pancake axial flux synchronous PMSM machine shown in Figure 2.1 that positions the rotor on the outside of the machine and the stator inside. The rotor has several surface-mounted magnets, and the stator has many coils.

In radial-field machines the rotor PMs can be placed in several different ways [1, 2]. The most common are classified as: Surface-mounted PM Machines (SPM), inset PM Machines (inset PM) and Interior PM Machines (IPM). The principle of operation of a PMSM remains unchanged regardless of the manner the PMs are mounted on the rotor. However, the applications and the way PMSMs are controlled can differ as discussed later.

Figure 2.1- Pancake axial flux PMSM [6]

The SPMs are generally intended for low speed applications while the IPMs, more robust, are intended for high speed applications i.e., generally greater than 3000 rpm[2].

2.3.1 Rotor Anisotropy

The method adopted to mount the PMs on the rotor has a direct influence on the *direct* and *quadrature* inductance values [2]. The rotor magnetic axis is called direct axis and is the main flux path through the magnets. By definition, when the direct axis or magnets are aligned with the stator winding, the stator inductance is the direct axis inductance or L_d. By rotating the magnets 90° from the aligned position, the stator flux sees interpolar area of the rotor containing only the iron path. By definition, in this position the stator inductance is the quadrature axis inductance or L_q. d and q axis are represented in Figure 2.2.

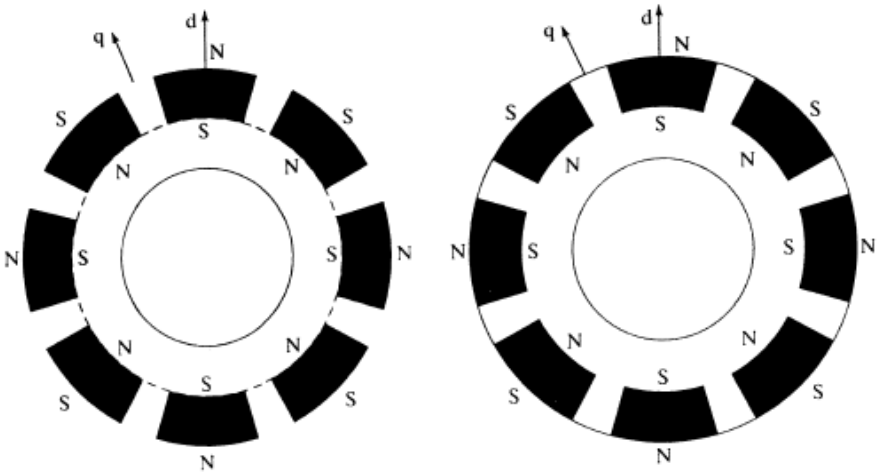

Figure 2.2 - a) Surface PM synchronous machine rotor; b) inset PM synchronous machine rotor [2]

Figure 2.2a) represents a cross-section of a Surface PM rotor machine. The PMs are placed in the rotor surface. Since the PMs permeability is close to the air permeability these machines have an isotropic [1] rotor which means that the radial-flux is almost uniform (similar Reluctance for d and q axes), resulting in $L_d \approx L_q$.

Figure 2.2b) shows an inset PM rotor. The magnet thickness results in an extension of the air gap by the same amount (PM and *air* have similar permeability). So because of the iron teeth, the direct-axis reluctance is greater than the quadrature-

axis reluctance. That unequal reluctance results in $L_d < L_q$ which is called inverse anisotropy[7] as it is contrary to common wound rotor synchronous machines anisotropy where $L_d > L_q$. The anisotropy or saliency-ratio ξ is defined as:

$$\xi = L_d / L_q \tag{2.3}$$

When the rotor is anisotropic, i.e. $L_d \neq L_q$, the PMSM have two torque components: the PM excitation torque and the reluctance torque. Different degrees of anisotropy require different control settings in order to obtain maximum PMSM efficiency, normally referred as Maximum Torque per Ampere (MTPA). This subject is discussed later in this chapter.

Figure 2.3 show the placement of the PM in the interior of the rotor with a) radial and b) tangential or circumferential orientation. These configurations are referred in literature as Interior PM synchronous machines. The construction is more complex but robust and suitable for high-speed applications. The level of anisotropy is higher compared to inset PM configuration enabling the development of a reluctance torque component.

In PMSM with tangential flux orientation rotors the direct axis is the sum of the flux of two PMs. Machines of this type are normally build with higher number of poles in order to produce higher concentration of flux in the air gap, resulting in higher power density.

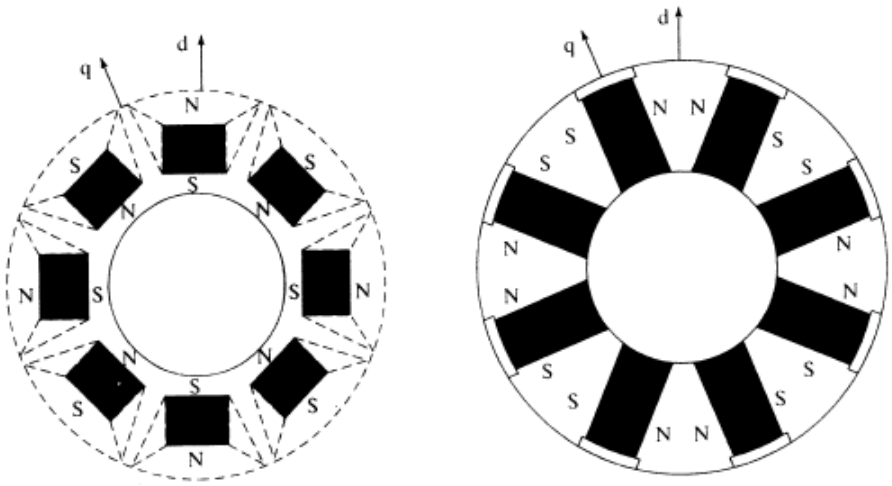

Figure 2.3 - Interior PM synchronous machine rotor with a) radial; b) circumferential orientation [2]

2.4 Dynamic Modeling of a Permanent Magnet Synchronous Machine

A suitable dynamic model of the PMSM is needed to design efficient vector-control algorithms. The developed model aims to decouple the air gap flux and *torque* components. This dynamic model is derived from the conversion of a multi-phase machine into a two-phase fictitious equivalent machine. This simplifies the model by making it possible to represent all PMSM parameters and variables in a two axis referential system.

The basic PMSM stator equations (2.4) for a three-phase PMSM are derived from the stator electrical diagram represented in Figure 2.4 [8].

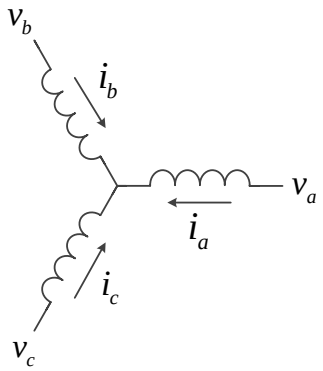

Figure 2.4 - PMSM stator electrical diagram

$$\begin{aligned} v_a &= R_a i_a + \frac{d\psi_a}{dt} \\ v_b &= R_b i_b + \frac{d\psi_b}{dt} \\ v_c &= R_c i_c + \frac{d\psi_c}{dt} \end{aligned} \tag{2.4}$$

where the fluxes are given by

$$\begin{bmatrix} \psi_a \\ \psi_b \\ \psi_c \end{bmatrix} = \begin{bmatrix} L_a M_{ab} M_{ac} \\ M_{ba} L_b M_{bc} \\ M_{ca} M_{cb} L_c \end{bmatrix} \begin{bmatrix} i_a \\ i_b \\ i_c \end{bmatrix} + \psi_f \begin{bmatrix} \cos(\theta_e) \\ \cos(\theta_e - 2\pi/3) \\ \cos(\theta_e + 2\pi/3) \end{bmatrix} \tag{2.5}$$

L_a, L_b, L_c are the stator phase self-inductances and $M_{ab} = M_{ba}$, $M_{bc} = M_{cb}$, $M_{ca} = M_{ac}$ are the mutual inductances between the respective stator phases. The term ψ_f represents the magnetic flux generated by the permanent magnets. θ_e is the angle measured between the rotor direct axis d and the stator phase a axis, being mentioned in literature as *rotor angle*.

The inductances are also expressed as function of θ_e as follows

$$\begin{aligned} L_a &= L_0 + L_m \cos(2\theta_e) \\ L_b &= L_0 + L_m \cos(2\theta_e - \frac{2\pi}{3}) \\ L_c &= L_0 + L_m \cos(2\theta_e + \frac{2\pi}{3}) \end{aligned} \tag{2.6}$$

And

$$
\begin{aligned}
M_{ab} &= -\frac{1}{2}L_0 + L_m \cos(2\theta_e) \\
M_{bc} &= -\frac{1}{2}L_0 + L_m \cos(2\theta_e - \frac{2\pi}{3}) \\
M_{ac} &= -\frac{1}{2}L_0 + L_m \cos(2\theta_e + \frac{2\pi}{3})
\end{aligned}
\tag{2.7}
$$

where L_0 and L_m are physical parameters [8, 9] of the PMSM

The magnetic coupled fluxes can be represented as

$$
\begin{bmatrix} \psi_{fa} \\ \psi_{fb} \\ \psi_{fc} \end{bmatrix} = \psi_f \begin{bmatrix} \cos(\theta_e) \\ \cos(\theta_e - 2\pi/3) \\ \cos(\theta_e + 2\pi/3) \end{bmatrix}
\tag{2.8}
$$

In the compact form the PMSM equations (2.4) and (2.5) are [8].

$$
\begin{aligned}
[v_{abc}] &= [R_s][i_{abc}] + \left[\frac{d\psi_{abc}}{dt}\right] \\
[\psi_{abc}] &= [L_{abc}][i_{abc}] + [\psi_{fabc}]
\end{aligned}
\tag{2.9}
$$

Where

$$
\begin{aligned}
[v_{abc}] &= [v_a \quad v_b \quad v_c]^T \\
[i_{abc}] &= [i_a \quad i_b \quad i_c]^T \\
[\psi_{abc}] &= [\psi_a \quad \psi_b \quad \psi_c]^T \\
[\psi_{fabc}] &= [\psi_{fa} \quad \psi_{fb} \quad \psi_{fc}]^T
\end{aligned}
\tag{2.10}
$$

and

$$
[R_s] = \begin{bmatrix} R_s & 0 & 0 \\ 0 & R_s & 0 \\ 0 & 0 & R_s \end{bmatrix}
\tag{2.11}
$$

where $R_a = R_b = R_c = R_s$, and

$$
[L_{abc}] = \begin{bmatrix} L_a & M_{ab} & M_{ac} \\ M_{ba} & L_b & M_{bc} \\ M_{ca} & M_{cb} & L_c \end{bmatrix}
\tag{2.12}
$$

Notice that inductances, mutual inductances and the fluxes ψ_{abc} vary sinusoidally as function of the rotor angle θ_e. This coupling or dependency is eliminated performing a reference frame transformation, from three-phase stationary reference frame abc to a rotational dq reference frame.

The dq reference frame is called *rotational* as it rotates synchronously with the rotor. In dq reference frame PMSM parameters become invariant with respect to the rotor angle θ_e.

The reference frame transformation can be done in two steps: applying the Clarke's transform followed by the Park's transform as shown in Figure 2.5.

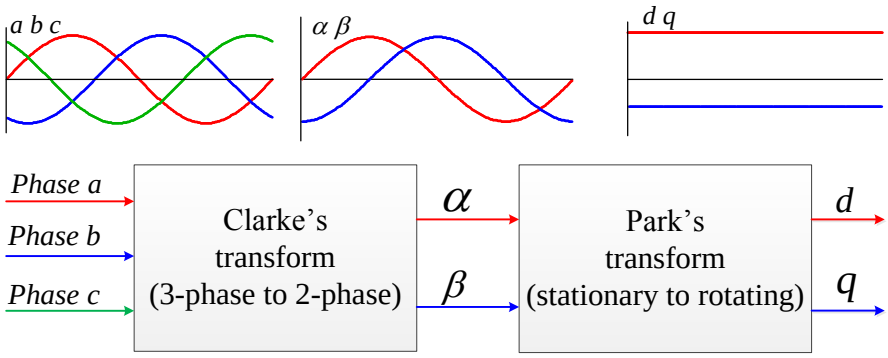

Figure 2.5 – Clarke's and Park's reference frame transformations

2.4.1 Clarke's Transform

The Clarke's transform converts a three-phase stationary reference frame abc in a two-phase fictitious stationary orthogonal reference frame designated alpha-beta or $\alpha\beta$ reference frame. The $\alpha\beta$ components are obtained by projecting the three-phase abc vectors in the two α and β axis as represented in Figure 2.6, which results in the Clarke's transform equation (2.13). This transformation is applied to voltages but may also be applied in the same way to currents and fluxes.

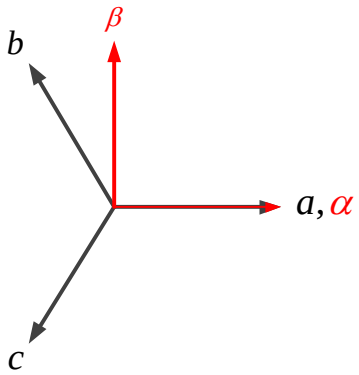

Figure 2.6 - abc and $\alpha\beta$ reference frames relationship

$$\begin{bmatrix} v_\alpha \\ v_\beta \end{bmatrix} = \frac{2}{3}\begin{bmatrix} 1 & -\frac{1}{2} & -\frac{1}{2} \\ 0 & \frac{\sqrt{3}}{2} & -\frac{\sqrt{3}}{2} \end{bmatrix}\begin{bmatrix} v_a \\ v_b \\ v_c \end{bmatrix} \tag{2.13}$$

In the stationary $\alpha\beta$ referential the (2.4) equations become:

$$\begin{aligned} v_\alpha &= R_s i_\alpha + \frac{d\psi_\alpha}{dt} \\ v_\beta &= R_s i_\beta + \frac{d\psi_\beta}{dt} \end{aligned} \tag{2.14}$$

2.4.2 Park's Transform

The Park's transform converts the stationary fictitious two phase $\alpha\beta$ quantities into a new fictitious reference frame dq that rotates synchronously with the PMSM rotor at the electric velocity ω_e. In this way dq quantities become constant in steady state. To perform this transformation is necessary to know the rotor angular position θ_e. The direct axis d is kept in phase with rotor magnetic flux north pole while the q axis is 90 electrical degrees ahead. The Figure 2.7 represents the relationship among the three reference frames from which the Park's transform equation (2.15) is derived.

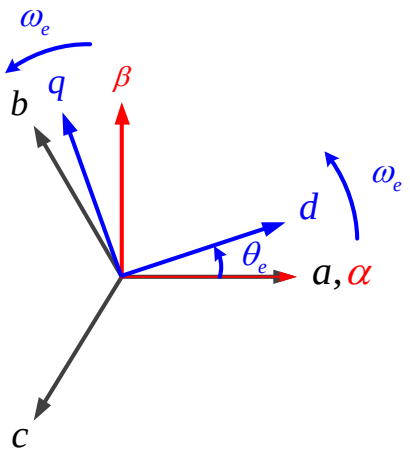

Figure 2.7 - abc, $\alpha\beta$ **and** dq **reference frames relationship**

$$\begin{bmatrix} v_d \\ v_q \end{bmatrix} = \begin{bmatrix} \cos\theta_e & \sin\theta_e \\ -\sin\theta_e & \cos\theta_e \end{bmatrix}\begin{bmatrix} v_\alpha \\ v_\beta \end{bmatrix} \tag{2.15}$$

It is also possible to do a one-step transformation from abc to $dq0$ according to (2.16). This transformation is also known[9] as the Park's transform. The v_0 variable has no meaning (is always null) as the PMSM is in fact a balanced system.

$$\begin{bmatrix} v_d \\ v_q \\ v_0 \end{bmatrix} = \frac{2}{3} \begin{bmatrix} \cos(\theta_e) & \cos(\theta_e - \frac{2\pi}{3}) & \cos(\theta_e + \frac{2\pi}{3}) \\ -\sin(\theta_e) & -\sin(\theta_e - \frac{2\pi}{3}) & -\sin(\theta_e + \frac{2\pi}{3}) \\ \frac{1}{2} & \frac{1}{2} & \frac{1}{2} \end{bmatrix} \begin{bmatrix} v_a \\ v_b \\ v_c \end{bmatrix} \tag{2.16}$$

2.4.3 Developing PMSM Equations in *dq*

In Figure 2.8 ψ_f is the rotor field flux produced by the permanent magnets, ψ_s is the stator flux produced by stator currents and ψ_{AG} is the air gap flux that results from their interaction. In the complex form ψ_{AG} can be represented as:

$$\overrightarrow{\psi_{AG}} = \psi_d + j\psi_q \tag{2.17}$$

By definition the rotor flux is aligned with the direct-axis so $\psi_{fq} = 0$ and $\psi_{fd} = \psi_f$. On the other hand the stator flux ψ_s depends on the current vector i_d and i_q components.

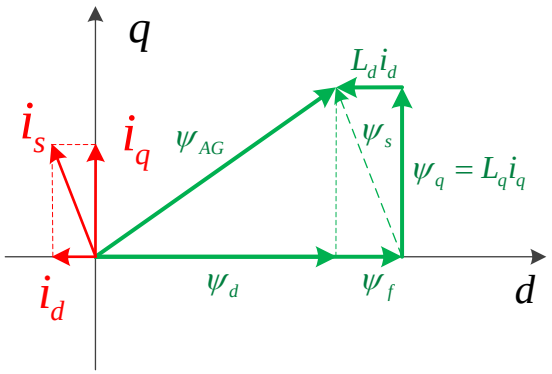

Figure 2.8 - Flux vectors in the PMSM

The fluxes in the direct and quadrature axes are:

$$\begin{aligned} \psi_d &= L_d i_d + \psi_f \\ \psi_q &= L_q i_q \end{aligned} \tag{2.18}$$

Or, in a matrix form:

$$\left[\psi_{dq}\right] = \begin{bmatrix} \psi_d \\ \psi_q \end{bmatrix} = \begin{bmatrix} L_d i_d \\ L_q i_q \end{bmatrix} + \begin{bmatrix} \psi_f \\ 0 \end{bmatrix} \tag{2.19}$$

where according to [8, 9]

$$L_d = \frac{3}{2}\left(L_0 - L_m\right)$$
$$L_q = \frac{3}{2}\left(L_0 + L_m\right) \tag{2.20}$$

Merging eq. (2.14) and (2.15) gives:

$$\begin{bmatrix} v_d \\ v_q \end{bmatrix} = \begin{bmatrix} \cos\theta_e & \sin\theta_e \\ -\sin\theta_e & \cos\theta_e \end{bmatrix} \begin{bmatrix} v_\alpha = Ri_\alpha + \dfrac{d\psi_\alpha}{dt} \\ v_\beta = Ri_\beta + \dfrac{d\psi_\beta}{dt} \end{bmatrix} \tag{2.21}$$

Resulting on:

$$\begin{bmatrix} v_d \\ v_q \end{bmatrix} = R_s \begin{bmatrix} \cos\theta_e & \sin\theta_e \\ -\sin\theta_e & \cos\theta_e \end{bmatrix} \begin{bmatrix} i_\alpha \\ i_\beta \end{bmatrix} + \begin{bmatrix} \cos\theta_e & \sin\theta_e \\ -\sin\theta_e & \cos\theta_e \end{bmatrix} \frac{d}{dt} \left(\begin{bmatrix} \cos\theta_e & \sin\theta_e \\ -\sin\theta_e & \cos\theta_e \end{bmatrix}^{-1} \begin{bmatrix} \psi_d \\ \psi_q \end{bmatrix} \right) \tag{2.22}$$

and since:

$$\begin{bmatrix} \cos\theta_e & \sin\theta_e \\ -\sin\theta_e & \cos\theta_e \end{bmatrix}^{-1} = \begin{bmatrix} \cos\theta_e & -\sin\theta_e \\ \sin\theta_e & \cos\theta_e \end{bmatrix} \tag{2.23}$$

then:

$$\begin{bmatrix} v_d \\ v_q \end{bmatrix} = R_s \begin{bmatrix} \cos\theta_e & \sin\theta_e \\ -\sin\theta_e & \cos\theta_e \end{bmatrix} \begin{bmatrix} i_\alpha \\ i_\beta \end{bmatrix} + \begin{bmatrix} \cos\theta_e & \sin\theta_e \\ -\sin\theta_e & \cos\theta_e \end{bmatrix} \frac{d}{dt} \left(\begin{bmatrix} \cos\theta_e & -\sin\theta_e \\ \sin\theta_e & \cos\theta_e \end{bmatrix} \begin{bmatrix} \psi_d \\ \psi_q \end{bmatrix} \right) \tag{2.24}$$

Taking into account that $\theta_e = \omega_e t$ then $\dfrac{d\theta_e}{dt} = \omega_e$, leading to

$$\begin{bmatrix} v_d \\ v_q \end{bmatrix} = R_s \begin{bmatrix} i_d \\ i_q \end{bmatrix} + \begin{bmatrix} \cos\theta_e & \sin\theta_e \\ -\sin\theta_e & \cos\theta_e \end{bmatrix} \left(\begin{bmatrix} -\omega_e \sin\theta_e & -\omega_e \cos\theta_e \\ \omega_e \cos\theta_e & -\omega_e \sin\theta_e \end{bmatrix} \begin{bmatrix} \psi_d \\ \psi_q \end{bmatrix} + \begin{bmatrix} \cos\theta_e & -\sin\theta_e \\ \sin\theta_e & \cos\theta_e \end{bmatrix} \frac{d}{dt} \begin{bmatrix} \psi_d \\ \psi_q \end{bmatrix} \right) \tag{2.25}$$

and then

$$\begin{bmatrix} v_d \\ v_q \end{bmatrix} = R_s \begin{bmatrix} i_d \\ i_q \end{bmatrix} + \begin{bmatrix} 0 & -\omega \\ \omega & 0 \end{bmatrix} \begin{bmatrix} \psi_d \\ \psi_q \end{bmatrix} + \frac{d}{dt} \begin{bmatrix} \psi_d \\ \psi_q \end{bmatrix} \tag{2.26}$$

Substituting using (2.19) leads to:

$$\begin{bmatrix} v_d \\ v_q \end{bmatrix} = R_s \begin{bmatrix} i_d \\ i_q \end{bmatrix} + \begin{bmatrix} 0 & -\omega \\ \omega & 0 \end{bmatrix} \left(\begin{bmatrix} L_d i_d \\ L_q i_q \end{bmatrix} + \begin{bmatrix} \psi_f \\ 0 \end{bmatrix} \right) + \frac{d}{dt} \left(\begin{bmatrix} L_d i_d \\ L_q i_q \end{bmatrix} + \begin{bmatrix} \psi_f \\ 0 \end{bmatrix} \right) \tag{2.27}$$

This is in fact a two system equation:

$$\begin{aligned} v_d &= R_s i_d - \omega_e L_q i_q + \frac{d}{dt}\left(L_d i_d + \psi_f\right) \\ v_q &= R_s i_q + \omega_e \left(L_d i_d + \psi_f\right) + \frac{d}{dt} L_q i_q \end{aligned} \tag{2.28}$$

or

$$\begin{aligned} v_d &= R_s i_d + \frac{d\psi_d}{dt} - \underbrace{\omega_e \psi_q}_{e_q} \\ v_q &= R_s i_q + \frac{d\psi_q}{dt} + \underbrace{\omega_e \psi_d}_{e_d} \end{aligned} \tag{2.29}$$

In the equation (2.29) the $\frac{d\psi_{dq}}{dt}$ components are the *transformer voltages* that link rotor and stator. The $\omega_e \psi_{dq}$ components are the *speed voltages* e_{dq} and their value is proportional to: (a) the machine electrical speed ω_e and (b) the direct and quadrature components of the air gap flux linkage ψ_{AG}.

$$\begin{aligned} v_d &= R_s i_d + \frac{d\psi_d}{dt} - e_q \\ v_q &= R_s i_q + \frac{d\psi_q}{dt} + e_d \end{aligned} \tag{2.30}$$

From a generator's point of view the *speed voltages* are responsible for the Electromotive Force (EMF) generation and the *transformer voltages* are responsible for the Back-EMF. In other words, the e_{dq} voltages are the internal voltages of the generator and the v_{dq} voltages are the terminal voltages in the synchronous reference frame. At no-load $v_d = 0$ and $v_q = e_d = \omega_e \psi_f = E_f$ which is, in this particular case, the phase-to-neutral peak voltage of v_a, v_b or v_c. E_f is also referred as the internal voltage or the EMF produced by PMs.

From a motor's point of view the EMF and Back-EMF roles are reversed.

In steady state the *transformer voltages* $\frac{d\psi_{dq}}{dt}$ are null. In this case, the equations of the PMSM in the synchronous reference frame are (2.31) and the matching electrical circuit is presented in Figure 2.9. Notice the cross-coupling between d and q quantities.

$$\begin{aligned} v_d &= R_s i_d - \omega_e L_q i_q \\ v_q &= R_s i_q + \omega_e \left(L_d i_d + \psi_f\right) \end{aligned} \tag{2.31}$$

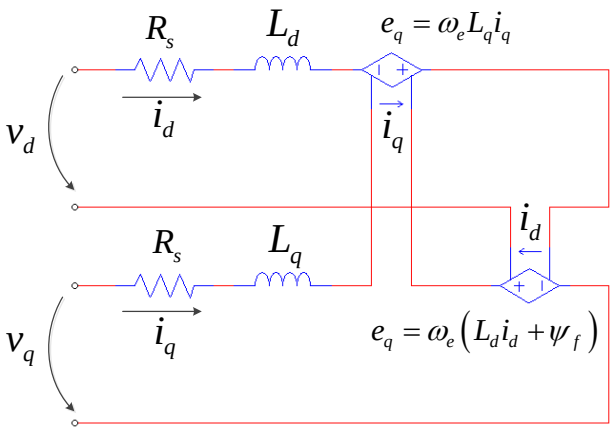

Figure 2.9 - Steady-state equivalent circuit of the PMSM in dq

The Figure 2.10 represents a vector diagram of a PMSM for a given working point in the dq reference frame. All relevant quantities are represented as fluxes, currents and voltages, except the voltage drops across the stator coil resistors R_s as they usually have very small values when compared with the other voltage components.

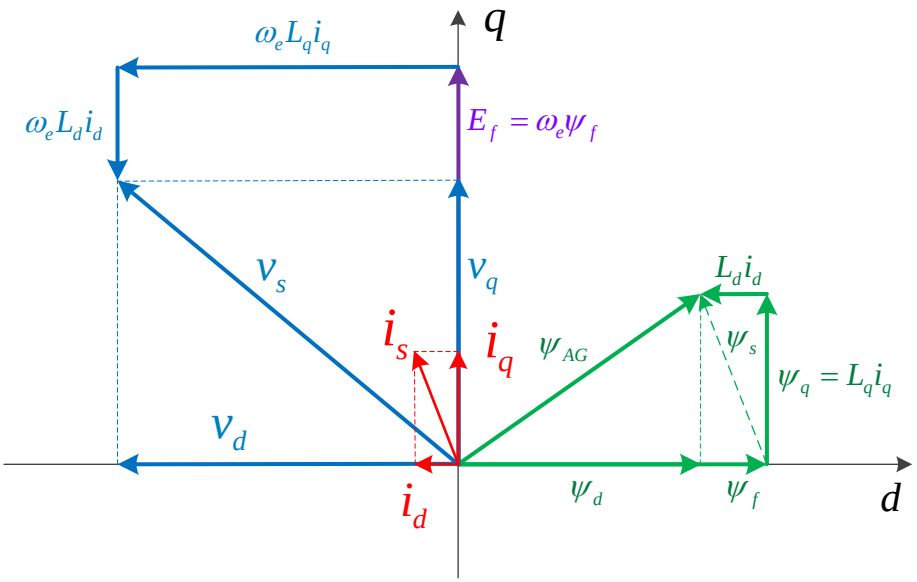

Figure 2.10 - Steady-state dq diagram of the PMSM working as a motor

In Figure 2.10 the PMSM is working as a motor since the i_q component of the phase current i_s is positive and in phase with E_f. There is a (rotor) field weakening as the $L_d i_d$ component of the stator flux opposes the rotor flux ψ_f, because i_d is negative.

In the vector diagram of Figure 2.11 the i_q component of the phase current i_s is 180° out of phase with respect to E_f, meaning that the PMSM is working as a

generator. As a result, the rotor field is reinforced as the $L_d i_d$ component of the stator flux adds to the rotor flux ψ_f, because i_d is positive.

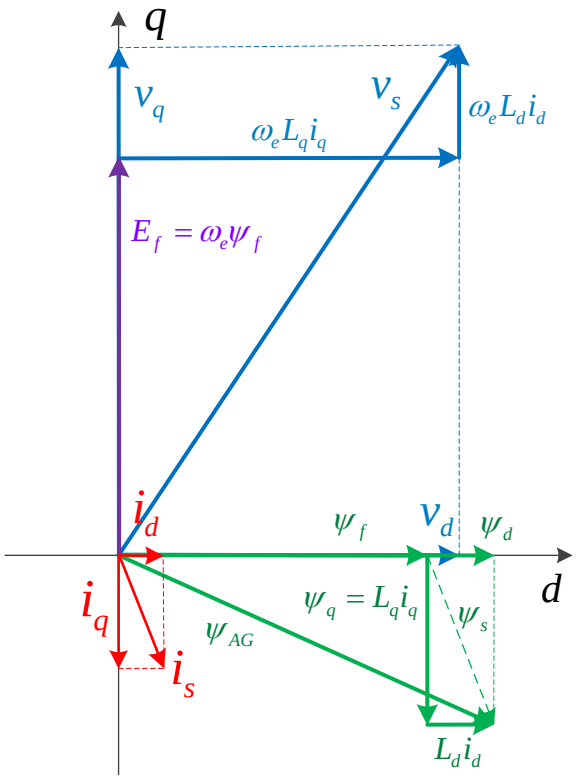

Figure 2.11 - Steady-state dq diagram of the PMSM working as a generator

2.5 Electric Power

The instantaneous electrical power p_e of the three-phase PMSM is given by the sum of instantaneous voltage-current products in each phase as

$$p_e = v_a i_a + v_b i_b + v_c i_c = \left[v_{abc}\right]^T \left[i_{abc}\right] \tag{2.32}$$

where according to the Park's transform equations (2.16)

$$\begin{aligned} \left[v_{abc}\right] &= \left[T_{dq0}\right]^{-1} \left[v_{dq0}\right] \\ \left[i_{abc}\right] &= \left[T_{dq0}\right]^{-1} \left[i_{dq0}\right] \end{aligned} \tag{2.33}$$

leads to the electrical power equation in dq for a balanced three-phase machine

$$P_e = \frac{3}{2}\left(v_d i_d + v_q i_q\right) \tag{2.34}$$

Replacing now v_d and v_q in equation (2.34) by the respective (2.29) equation leads to the electric power equation:

$$P_e = \underbrace{\frac{3}{2} R_s \left(i_d^2 + i_q^2 \right)}_{p_{cu}} + \underbrace{\frac{3}{2} \left(i_d \frac{d\psi_d}{dt} + i_q \frac{d\psi_q}{dt} \right)}_{P_L} + \underbrace{\frac{3}{2} \omega_e \left(\psi_d i_q - \psi_q i_d \right)}_{P_{em}} \tag{2.35}$$

The equation (2.35) can be separated in three different terms [10]: The term P_{cu} refers to power lost in conductors; P_L refers to the change time rate of stored energy in the machine inductances [10]; Finally the last term refers to the energy conversion from electrical to mechanical (generator) or vice-versa (motor). This is the so called electromechanical power P_{em} or simply P

$$P = \frac{3}{2} \omega_e \left(\psi_d i_q - \psi_q i_d \right) \tag{2.36}$$

2.6 Electromagnetic Torque in the PMSM

For the sake of simplicity the electromagnetic torque analysis will not take into account the stator windings copper losses given by $\frac{3}{2} R_s \left(i_d^2 + i_q^2 \right)$.

By definition the rotational mechanical power P_m is given by the product between the electromagnetic torque T_m and the mechanical angular velocity ω_m.

$$P_m = T_m \omega_m \tag{2.37}$$

As seen in (2.1) the mechanical velocity is related to the electrical velocity by means of the number of pole pairs pp of the machine. If losses are excluded, it is possible to write $P_m = P$ where P is the electrical power of the PMSM. Considering now equations (2.1), (2.31), (2.36) and (2.37) the electromagnetic torque $T_e = T_m$ is given by:

$$T_e = \frac{3}{2} pp \left(\psi_f i_q + (L_d - L_q) i_d i_q \right) \tag{2.38}$$

Equation (2.39), derived from (2.38), shows that the electromagnetic torque T_e is the sum of two components: the first component is the excitation torque T_{ex} which is the main component of the torque in a PMSM and results from the interaction between the PM field flux and the i_q component of the stator current; and the second is the reluctance torque T_r with a magnitude that depends on the rotor anisotropy defined by (2.3) and on the stator current orientation. If $L_d \approx L_q$, as it occurs in Surface PM rotor machines, the reluctance torque is residual.

$$T_e = \underbrace{\frac{3}{2} pp \psi_f i_q}_{T_{ex}} + \underbrace{\frac{3}{2} pp (L_d - L_q) i_d i_q}_{T_r} \tag{2.39}$$

In the next chapters it will be seen that this particular expression is very useful for vector control purposes. Different expressions for the electromagnetic torque can be derived[10, 11] , e.g. considering (a) the interaction between the internal voltage E_f and the terminal voltage v_s , (b) the interaction between rotor flux ψ_f and the air gap flux ψ_{AG} , and (c) the interaction between the air gap flux ψ_{AG} and stator current i_s .

2.6.1 The cogging torque

In reality there is a third torque component which is referred in literature[1, 8, 12] as the cogging torque. The *cogging* torque is a ripple torque due to the interaction between the field flux ψ_f due to the PMs and the stator teeth.

Including the *cogging torque* T_p in the equation (2.39) gives

$$T_e = \frac{3}{2} pp.\psi_f i_q + \frac{3}{2} pp.(L_d - L_q) i_d i_q + \frac{\partial W_m^{'}}{\partial \theta_m}_{T_p} \qquad (2.40)$$

Where $W_m^{'}$ is the magnetic coenergy [1, 12] which is a function of i_d , i_q and θ_m .

Many of the commercial available PMSM have a cogging torque that is 5% to 10% of the nominal torque [12]. For high-performance applications it does not exceed 1% to 2% of the rated torque. The cogging torque is reduced by improving the PMSM design. Figure 2.12 shows an example of the cogging torque varying with the rotor position.

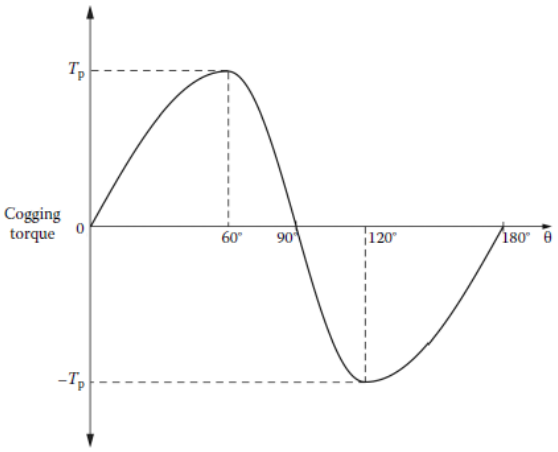

Figure 2.12 - Example of cogging torque T_p versus rotor position [12]

The cogging torque is not considered in the PMSM analysis done in this work.

2.7 Effect of Iron Saturation in PMSM

The iron saturation introduces a non-linear behavior in the PMSMs due to a reduction of the air gap flux density. In fact the inductances L_d and L_q vary with the currents i_d and i_q, decreasing when currents increase [1, 13]. Additionally there is a cross-coupling between d and q axis quantities, expressed in the equations (2.31) and shown in the electric circuit of Figure 2.9, which complicates the saturation effect analysis. To overcome this issue, an accurate magnetic model of the PMSM is needed. On such model the flux linkages ψ_d and ψ_q are more complex and given by:

$$\begin{aligned} \psi_d &= \psi_d\left(i_d, i_q\right) \\ \psi_q &= \psi_q\left(i_d, i_q\right) \end{aligned} \tag{2.41}$$

This model is necessary to accurately describe the PMSM performance, which is out of the scope of this work. Here, the iron saturation effect is not taken into account so the L_d and L_q inductances are considered as constants.

2.8 The Torque Angle

The authors are not consensual about the definition of torque angle. In fact, several definitions [11] can be found in literature. In [1, 2, 14] the torque angle δ_i is defined as the angle between the rotor flux ψ_f and the stator current vector. In [15] the torque angle δ_v is defined as the angle between the terminal voltage v_s and the internal voltage E_f. Again in [1] the torque angle δ_ψ is also defined as the angle between the rotor flux ψ_f and the air gap flux ψ_{AG}.

Actually these different torque angle definitions are used with different machine control strategies. As an example, the torque angle δ_i is commonly associated to Field Oriented Control (FOC) while δ_ψ is used in Direct Torque Control (DTC) as it will be seen later.

2.8.1 The torque angle δ_v

According to[15] the torque angle δ_v, also known in this particular case as the *power angle*, is expressed as a function of v_s and E_f vectors. δ_v is defined as positive when v_s leads E_f and negative when v_s lags E_f.

Figure 2.13 shows a comprehensive diagram where all relevant quantities are represented. According to the diagram, it is possible to derive the expressions (2.42) to (2.45).

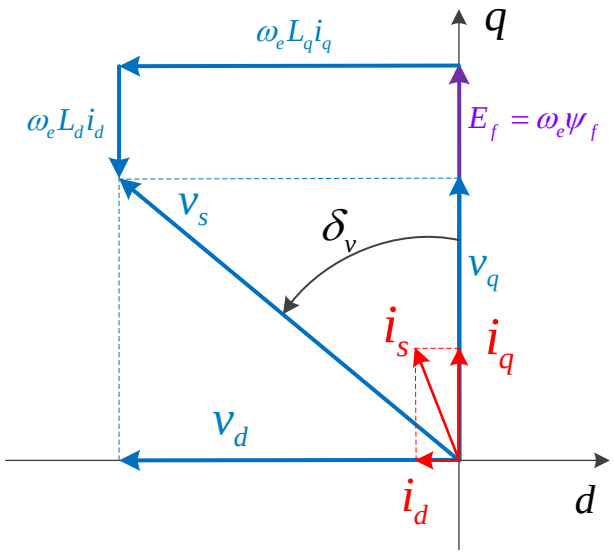

Figure 2.13 - Torque angle δ_v defined as the angle between E_f and v_s

$$v_s = \sqrt{v_d^2 + v_q^2} = \sqrt{\left(\omega_e L_q i_q\right)^2 + \left(\omega_e L_d i_d + E_f\right)^2} \tag{2.42}$$

$$\begin{aligned} v_d &= v_s \sin\delta_v \\ v_q &= v_s \cos\delta_v \end{aligned} \tag{2.43}$$

$$\delta_v = \tan^{-1}\left(\frac{L_q i_q}{L_d i_d + \dfrac{E_f}{\omega_e}}\right) \tag{2.44}$$

$$\begin{aligned} i_d &= \frac{v_s \cos\delta_v - E_f}{\omega_e L_d} \\ i_q &= \frac{v_s \sin\delta_v}{\omega_e L_q} \end{aligned} \tag{2.45}$$

Substituting the (2.45) currents in the electromagnetic torque equation (2.39) gives:

$$T_e = \frac{3}{2} pp \frac{E_f}{\omega_e} \underbrace{\frac{v_s \sin\left(\delta_v\right)}{\omega_e L_q}}_{i_q} + \frac{3}{2} pp (L_d - L_q) \underbrace{\frac{v_s \cos\delta_v - E_f}{\omega_e L_d}}_{i_d} \underbrace{\frac{v_s \sin\left(\delta_v\right)}{\omega_e L_q}}_{i_q} \tag{2.46}$$

Leading, after some mathematical manipulation, to:

$$T_e = \frac{3}{2} \frac{pp}{\omega_e^2} \frac{E_f v_s}{L_d} \sin\left(\delta_v\right) + \frac{3}{2} \frac{pp}{\omega_e^2} (L_d - L_q) \frac{v_s^2}{2 L_d L_q} \sin\left(2\delta_v\right) \tag{2.47}$$

This (2.47) torque equation has two components:

- The first one is the excitation torque that represents the main torque in a PMSM. It depends on the E_f and v_s product and on the sine of the angle δ_v between them;
- The second term represents the reluctance torque and depends on the v_s^2 and on the sine of $2\delta_v$. Note that if $L_d \approx L_q$ the reluctance torque has a residual value.

Looking at (2.47) equation, apparently the torque also depends on the electric or synchronous velocity ω_e which in fact is not true. Notice that the voltages themselves depend on ω_e as, e.g. $E_f = \omega_e \psi_f$, so the synchronous velocity is inside the torque equation (2.47) just to cancel its own effect. This is clearer in the torque equations (2.53) and (2.57).

2.8.2 The torque angle δ_ψ

Based on Figure 2.14, where the torque angle δ_ψ is defined as the angle between the rotor flux vector ψ_f and the air gap flux vector ψ_{AG} that results from the interaction between rotor and stator ψ_s fluxes, the expressions (2.48), (2.49) and (2.50) are derived.

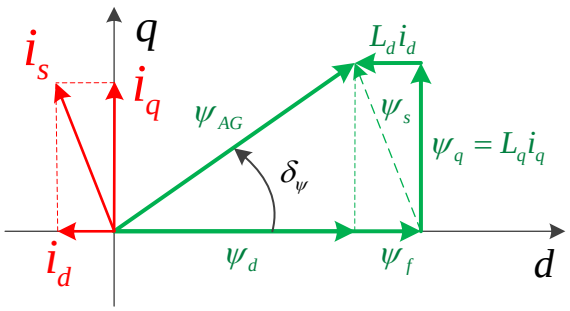

Figure 2.14 - Torque angle δ_ψ defined as the angle between the rotor flux ψ_f and the air gap flux ψ_{AG}

$$\psi_{AG} = \sqrt{\psi_d^2 + \psi_q^2} = \sqrt{\left(L_d i_d + \psi_f\right)^2 + \left(L_d i_d\right)^2} \tag{2.48}$$

$$\begin{aligned} \psi_d &= \psi_{AG} \cos\delta_\psi \\ \psi_q &= \psi_{AG} \sin\delta_\psi \end{aligned} \tag{2.49}$$

$$\delta_\psi = \tan^{-1}\left(\frac{L_q i_q}{L_d i_d + \psi_f}\right) \tag{2.50}$$

The currents i_d and i_q can be expressed as

$$\begin{aligned} i_d &= \frac{\psi_{AG}\cos\delta_\psi - \psi_f}{L_d} \\ i_q &= \frac{\psi_{AG}\sin\delta_\psi}{L_q} \end{aligned} \tag{2.51}$$

Substituting the (2.51) currents in the electromagnetic torque equation (2.39) gives:

$$T_e = \frac{3}{2}pp.\psi_f\frac{\psi_{AG}\sin\left(\delta_\psi\right)}{L_q} + \frac{3}{2}pp(L_d - L_q)\frac{\psi_{AG}\cos\delta_\psi - \psi_f}{L_d}\frac{\psi_{AG}\sin\left(\delta_\psi\right)}{L_q} \tag{2.52}$$

It is now possible to write the electromagnetic torque equation in the form:

$$T_e = \frac{3}{2}pp\frac{\psi_f\psi_{AG}}{L_d}\sin\left(\delta_\psi\right) + \frac{3}{2}pp(L_d - L_q)\frac{\psi_{AG}^2}{2L_dL_q}\sin\left(2\delta_\psi\right) \tag{2.53}$$

The torque equation has again two components:

- The excitation torque component is proportional to the product of the rotor flux ψ_f, the air gap flux ψ_{AG} and the sine angle δ_ψ between them;
- The reluctance torque component is a function of ψ_{AG}^2 and of the sine of $2\delta_\psi$.

This torque equation is very similar to the previous one (2.47). It is now clear that the electromagnetic torque does not depend on the synchronous velocity ω_e.

2.8.3 The Torque Angle δ_i

In the diagram of Figure 2.15, the torque angle δ_i is now defined as the angle between the rotor flux vector ψ_f and the stator current vector i_s. Equations (2.54), (2.55) and (2.56) can be deduced from Figure 2.15.

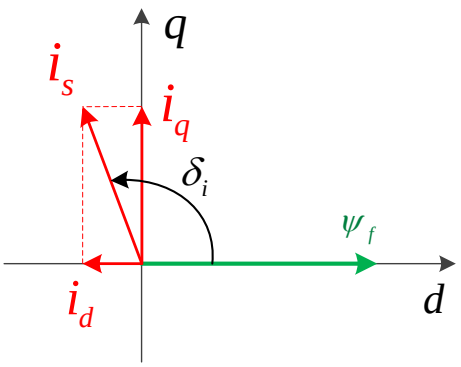

Figure 2.15 - Torque angle defined as the angle between the rotor flux ψ_f and the stator current i_s

$$i_s = \sqrt{i_d^2 + i_q^2} \tag{2.54}$$

$$\begin{aligned} i_d &= i_s \cos\delta_i \\ i_q &= i_s \sin\delta_i \end{aligned} \tag{2.55}$$

$$\delta_i = \tan^{-1}\left(\frac{i_q}{i_d}\right) \tag{2.56}$$

With the previous expressions it is possible now to express the torque equation (2.39) as a function of the stator current i_s and the torque angle δ_i as:

$$T_e = \frac{3}{2} pp.\psi_f i_s \sin(\delta_i) + \frac{3}{4} pp.(L_d - L_q) i_s^2 \sin(2\delta_i) \tag{2.57}$$

By analyzing the expression (2.57) notice the excitation torque is a function of the phase current amplitude i_s and of the sine of the torque angle δ_i. The reluctance torque depends on i_s^2 and on the sine of $2\delta_i$. Again, if $L_d \approx L_q$, the reluctance torque is not noteworthy.

In particular, this (2.57) equation form of the electromagnetic torque has a special meaning as all quantities are constant except the phase current i_s and its angle δ_i referenced to the d-axis, i.e. to the rotor position. This torque definition is particularly interesting when using a Vector Control method.

Vector control methods aims to reorient the current vector i_s, i.e. its amplitude and phase to some desired working point. The goal of reorienting the current i_s can be, e.g. to maximize the electromagnetic torque with the minimal current amplitude. This is known in the literature as the Maximum Torque Per Ampere control or MTPA. In mathematical formulation the question is: which torque angle δ_i is the one that maximizes the electromagnetic torque T_e for a given current i_s. To use Vector Control the rotor position has to be accurately known. Vector control methods are discussed later in Chapter 6.

2.9 Maximizing the Electromagnetic Torque

In the previous paragraphs three different electromagnetic torque expressions were derived associated to as many other different torque angle definitions. They all have two components: the first one related to the excitation torque; and the second one related to the reluctance torque. Those torque equations are all in fact equivalent.

The Figure 2.16 shows the machine electromagnetic torque curves as function of the torque angle δ when $L_d / L_q < 1$. Note that the torque angle δ may be δ_i or δ_v or δ_ψ that the curves remain unchanged. These are typical torque curves of an Interior PM synchronous machine with inverse anisotropy (2.3). Here the excitation torque is reinforced by the reluctance torque component. The maximum electromagnetic

torque T_e occurs for a torque angle $\delta_{\max}$ that is $90^o < |\delta_{\max}| < 180^o$ while, in a stable operation regime[15], $0^o < \delta < \delta_{\max}$ at motoring state and $-\delta_{\max} < \delta < 0^o$ at generating state.

Considering now a Surface PM synchronous machine whose rotor is typically isotropic, i.e. $L_d \approx L_q$, the electromagnetic torque is $T_e = T_{ex}$ as the reluctance torque is $T_r \approx 0$. In this case the maximum torque occurs when $|\delta_{\max}| \approx 90^o$ while, in a stable operation regime, $0^o < \delta < 90^o$ at motoring state and $-90^o < \delta < 0^o$ at generating state.

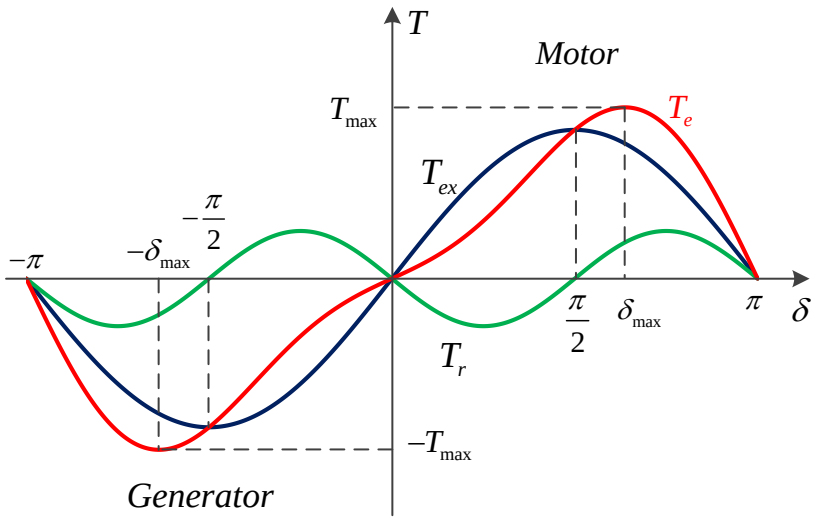

Figure 2.16 - Electromagnetic torque as a function of the torque angle δ when $L_d / L_q < 1$

Figure 2.17 shows typical electromagnetic curves for a common wound rotor synchronous machine where $L_d > L_q$. Notice that in this case the electromagnetic torque occurs for a torque angle $\delta_{\max}$ that is $0^o < |\delta_{\max}| < 90^o$ while, in a stable operation regime, $0^o < \delta < \delta_{\max}$ at motoring state and $-\delta_{\max} < \delta < 0^o$ at generating state.

When compared to wound rotor synchronous machines, the PMSMs, and in particular the Interior PMSM, present a wider torque angle range on stable operation regime.

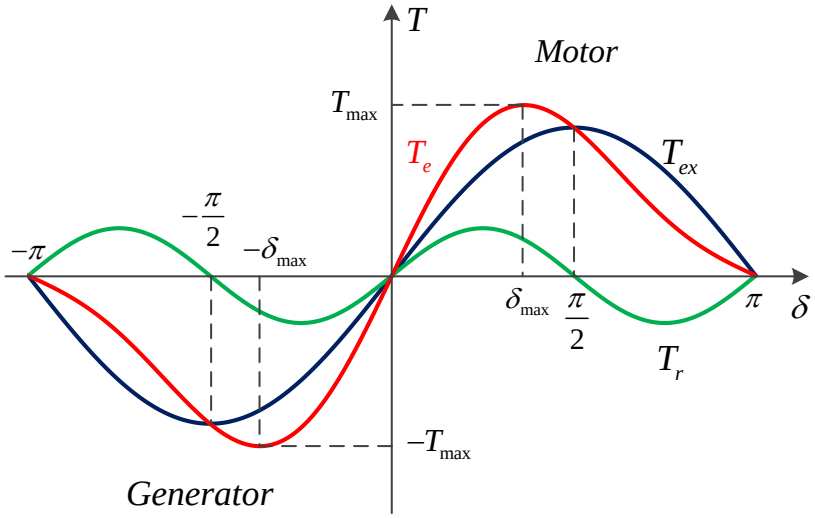

Figure 2.17 - Electromagnetic torque as a function of the torque angle δ when $L_d / L_q > 1$

To find the torque angle $\delta_{\max}$ that maximizes the electromagnetic torque T_e for a given current i_s it is necessary to derive the electromagnetic torque equation (2.57) in order to δ_i and equal it to zero [13]:

$$\begin{aligned}
&\frac{d}{d\delta}\left(\frac{3}{2}pp.\psi_f i_s \sin(\delta_i)+\frac{3}{4}pp.(L_d-L_q)i_s^2\sin(2\delta_i)\right)=0 \Leftrightarrow \\
&\frac{3}{2}pp.\psi_f i_s \cos(\delta_i)+\frac{3}{2}pp.(L_d-L_q)i_s^2\cos(2\delta_i)=0 \Leftrightarrow \\
&\frac{3}{2}pp\left(2(L_d-L_q)i_s^2\cos^2(\delta_i)+\psi_f i_s\cos(\delta_i)-(L_d-L_q)i_s^2\right)=0
\end{aligned} \tag{2.58}$$

And the solution is (2.59) where $\delta_{i\max}$ must be within $0^o < |\delta_{i\max}| < 180^o$

$$\delta_{i\max}=\cos^{-1}\frac{-\psi_f \pm\sqrt{\psi_f^2+8\left(L_d-L_q\right)^2 i_s^2}}{4\left(L_d-L_q\right)i_s} \tag{2.59}$$

The i_d and i_q components of the current i_s are obtained using the equations (2.55).

2.10 Conclusions

In this chapter, after reviewing the PMSM rotor topologies, its dynamic model in dq frame is derived and comprehensive PMSM Steinmetz diagrams are presented for motor and generator operation.

Different rotor topologies lead to different degrees of anisotropy, which directly influences the way the PMSM should be controlled. In fact, the PMSM electromagnetic torque is the sum of excitation and reluctance torques whose maximum depends on each particular rotor anisotropy.

The vector-control of the PMSM aims to maximize the electromagnetic torque supplied to or extracted from the PMSM. The vector control strategies rely on vector relationship between particular parameters that form a torque angle δ. Three different, but equivalent, torque equations are derived as function of torque angles: δ_v, δ_ψ and δ_i. Furthermore, comprehensive torque-angle graphics are provided for classical synchronous machines and for PMSMs which reflect, respectively, direct and inverse anisotropy.

2.11 References

[1] B. Wilamowski and J. Irvin, *The Industrial Electronics Hanbook - Power Electronics Handbook*, Bogdan M. Wilamowski; J. David Irvin ed. vol. 2: CRC Press, 2011.

[2] R. Krishnan, *Electric Motor Drives - Modeling, Analysis and Control*, 2001.

[3] S. Morimoto, M. Sanada, and Y. Takeda, "Wide-speed operation of interior permanent magnet synchronous motors with high-performance current regulator," *Industry Applications, IEEE Transactions on,* vol. 30, pp. 920-926, 1994.

[4] M. N. Uddin and M. Azizur Rahman, "High-Speed Control of IPMSM Drives Using Improved Fuzzy Logic Algorithms," *Industrial Electronics, IEEE Transactions on,* vol. 54, pp. 190-199, 2007.

[5] G. McPherson, *An Introduction to Electrical Machines and Transformers*. United States of America and Canada: John Wiley & Sons, 1981.

[6] G. Devices, "Direct drive pancake motor [Online]," ed, 2015.

[7] Â. P. Ferreira, "Problemática e Perspectivas da Utilização do Gerador de ìmanes Permanentes na Produção de Energia Eólica," Master, DEE, FEUP, Porto, Portugal, 2000.

[8] I. Boldea, *Variable Speed Generators: The Electric Generators Handbook* CRC Press, 2006.

[9] I. Boldea, *Synchronous Generators*, 2006.

[10] D. Novotny and T. Lipo, *Vector Control and Dynamics of AC Drives*: Clarendon Press - Oxford, 1996.

[11] R. Soares, "Traction Control for Hybrid Electric Vehicles," Master Thesis, FEUP DEE, FEUP - University of Porto, Porto, 2012.

[12] R. Krishnan, *Permanent Magnet Synchronous and Brushless DC Motor Drives*: CRC Press, 2010.

[13] T. M. Jahns, G. B. Kliman, and T. W. Neumann, "Interior Permanent-Magnet Synchronous Motors for Adjustable-Speed Drives," *Industry Applications, IEEE Transactions on,* vol. IA-22, pp. 738-747, 1986.

[14] M. Ehsani, Y. Gao, S. Gay, and A. Emadi, *Modern Electric, Hybrid Electric, and Fuel Cell Vehicles*: CRC PRESS, 2005.

[15] A. Emadi, *Handbook of Automotive Power Electronics and Motor Drives*: Taylor & Francis Group, LLC, 2005.

3
Three-phase Voltage Source Converters Modeling

3.1 Introduction

This chapter discusses the Voltage Source Converters (VSC) modeling. The notation adopted is the one established when interfacing VSCs with the grid. In this notation the grid voltage vector E is collinear with the *d*-axis in the *dq* frame. Chapter 4 also adopts this notation. In all the other chapters, the notation is the commonly used with motors/generators, where the field flux ψ_f is collinear with the *d*-axis, while the Back-EMF (or EMF) E_f is collinear with the *q*-axis in the *dq* frame.

VSCs, also known as a PWM Boost Rectifiers/Inverters, are widely used bidirectional power electronics converters. In these converters active and reactive power may be independently defined, i.e. the Power Factor may be controlled, and thus they may behave as a balanced resistive load to the grid – Unity Power Factor (UPF). They have a very good dynamic response showing a good robustness to disturbances from load parameters. They guarantee almost sinusoidal line currents as well as a high quality voltage in the DC-side [1].

VSCs are popular in high-power, high-performance applications, particularly in the automotive industry, where pure electric and hybrid vehicles require high performance drives to respond to frequent accelerations, decelerations and braking. Other application examples are renewable energy sources, like wind and solar, and more recently high-voltage direct current (HVDC) electric power transmission system solutions [2, 3].

The benefits of using a VSC instead of a diode or thyristor bridge rectifier can quickly be summarized as:

- Currents are almost harmonic free;
- Power Factor (PF) is completely controllable. In fact it can be set to 1, lead or lagging, independently of the load characteristics;
- It is a bidirectional converter;
- The DC voltage is almost ripple free.

As an example, when the grid feeds any load through a VSC, the load can be seen as a resistance by the grid if VSC's PF control is set to be 1.

This sub-chapter addresses the VSC modeling. The added value of modeling a VSC comes from the observability enabled by those models. VSC Laplace models are like a window through which it is possible to observe what is going on inside the "VSC black-box". Those models facilitate the comprehension of VSCs, VSCs' dynamics, and allow to develop adequate current controllers.

Some of the questions that Laplace models can answer are summarized as:

- what is the mathematical relationship between AC and DC voltages and currents;
- what defines the power flow direction;
- what kind of power flows are present in the VSC;
- which mathematical expressions traduce the dynamic behavior of the VSC and associated AC and DC Sources/Loads;
- how to control a VSC.

Precise VSC models can be found on specialized literature [4-8] but they are rather complex. Most of the complexity comes from including in the VSC modeling process the high-frequency carrier related to the power electronics commutators' operation. As an example Blasko and Kaura [9] derived a set of VSC Laplace models adopting three-phase (*abc*), alpha-beta ($\alpha\beta$) and direct-quadrature (*dq*) as reference frames.

Although these models are complete in the sense they accurately describe the VSCs, their complexity does not facilitate their analysis and the controller's design. Part of the complexity derives from including the converter's high-frequency carrier signal in the model.

In this chapter a new VSC Laplace model that excludes the converter's frequency carrier signal is described. The Laplace model is important as it highlights VSC cross-couplings, helping to develop more efficient VSC controllers. Based on the VSC Laplace model, a suitable current controller is proposed. Results show that the VSC Laplace model has a good dynamic behavior when compared to time-domain electrical model (Figure 3.1).

3.2 Three-phase VSC Operation

The Figure 3.1 shows a three-phase VSC with the associated AC and DC sources/loads. This generic representation highlights the converter's reversibility. It can work as PWM Inverter or as PWM Boost Rectifier, i.e. the (active) power can flow in both directions.

The AC source/load is considered ideal in the sense it is able to supply or absorb an infinite power. It can be viewed as the grid where the internal equivalent inductances can be considered null when compared to the circuit's inductances that typically have values in the order of hundreds of μH to some mH .

The generic DC source/load can be a battery, a DC motor, a resistor, a capacitor bank or even another power converter, among others.

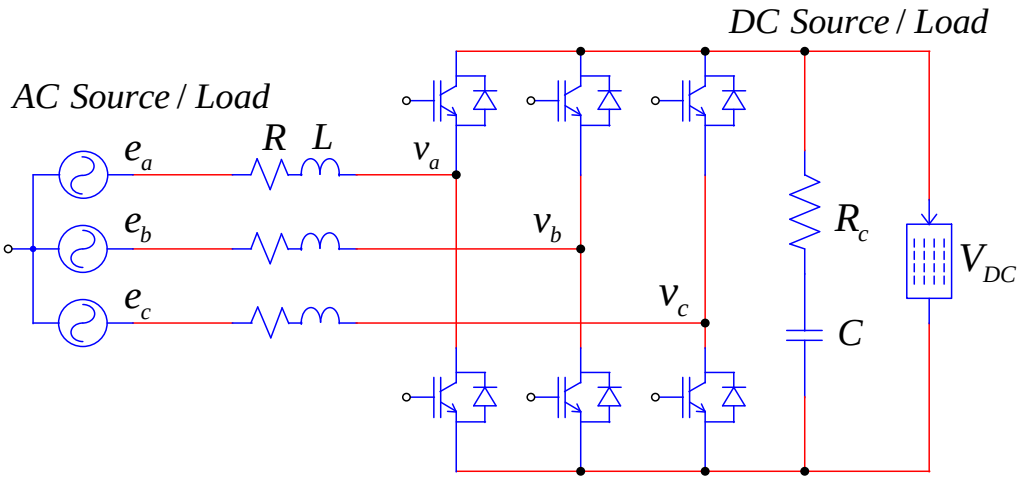

Figure 3.1 - Three-phase VSC with AC and DC sources/loads

The inductors and the capacitor are crucial components influencing the converter's dynamic operation. Inductors have two functions: to limit the line current ripple magnitude, reducing harmonics; and to act as energy-storage devices needed for PWM boost rectifier operation [7]. Frequently the internal inductance characteristic of the AC source/load meets the requested values so there is no need for an external inductor.

The DC side capacitor filter is necessary as it helps to stabilize the DC voltage, particularly after a DC source/load steep change. It must be designed to be a compromise between the dynamics of the converter (time response), and the need to limit overshoots/undershoots. The capacitor ESR-Equivalent Series Resistor, represented by R_c in Figure 3.1 must be included in this analysis since a low capacitor ESR reduces the high frequencies generated by the converter around and above the carrier frequency signal, improving the DC voltage quality.

In the VSC the power flow direction is determined by the system controller since it is considered that energy is available in both AC and DC-sides. The active/reactive power exchange between the AC source/load and the converter's AC-side depends on the power angle ε which is the phase between voltages e_a, e_b, e_c and v_a, v_b, v_c and on their relative amplitudes.

The goal of the converter's control is to generate v_a, v_b and v_c voltages that define the active power flow that crosses the converter from AC to DC-side, or vice-versa, and the reactive power that flows (only) between the AC source/load and the converter's AC-side.

The VSC analysis is divided in three parts: in the first, it is analyzed the VSC's AC side; in the second, the VSC's DC side; and the third is focused on linking both AC and DC VSC sides.

3.3 Three-phase VSC Modeling Coupled to an Ideal AC Source

For modeling purposes the following assumptions are made: (a) the converter AC side voltages v_a, v_b and v_c represent only the fundamental frequency; (b) the converter switches are ideal. The unique losses assumed are the inductor losses and the capacitor losses (see R and R_c in Figure 3.1).

3.3.1 The VSC AC Side Model

The VSC AC side can be analyzed as a two three-phase voltage source interconnected via inductors as represented in Figure 3.2 [9, 10]

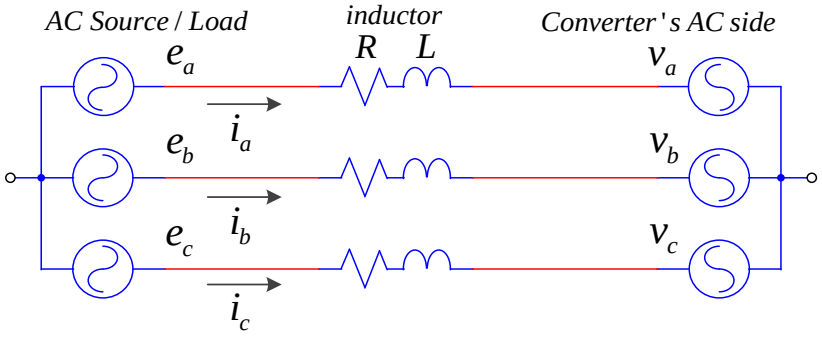

Figure 3.2 – Three-phase VSC AC side model

Considering the AC source/load voltages are expressed as

$$\begin{cases} e_a = E\cos\left(\theta_e\right) \\ e_b = E\cos\left(\theta_e - \dfrac{2\pi}{3}\right) \\ e_c = E\cos\left(\theta_e - \dfrac{4\pi}{3}\right) \end{cases} \tag{3.1}$$

the circuit equations are

$$\begin{cases} e_a = Ri_a + L\dfrac{di_a}{dt} + v_a \\ e_b = Ri_b + L\dfrac{di_b}{dt} + v_b \\ e_c = Ri_c + L\dfrac{di_c}{dt} + v_c \end{cases} \tag{3.2}$$

In order to simplify the mathematical analysis and the converter design, a two-step coordinate transformation is applied to the original three-phase system [7, 11]:

- Step 1 - *abc* to $\alpha\beta$ or Clarke's transform;
- Step 2 - $\alpha\beta$ to *dq* or Park's transform.

The transformations are done considering the relations between vectors presented in Figure 3.3. The three-phase *abc* reference frame is a *stationary* referential as well as the $\alpha\beta$ reference frame. The *dq* reference frame is a *synchronous* one as it rotates synchronously with the angular frequency or electric speed ω_e. In this reference frame there are in fact only DC quantities.

DC quantities facilitate the analysis and are suitable to project a controller if PI or PID controllers are used, because of the absence of frequency.

To learn more about Clarke's and Park's reference frame transformations consult Annex 1.

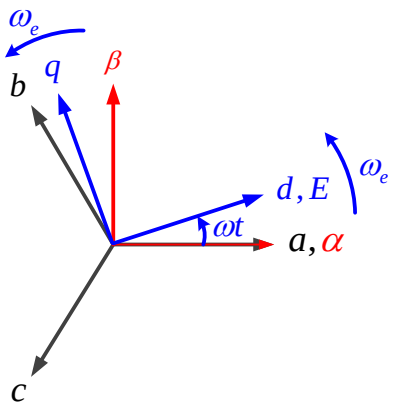

Figure 3.3 - abc, $\alpha\beta$ and *dq* reference frames

Considering the three-phase system represented by (3.1) and applying the Clarke's transform leads to

$$\begin{cases} e_\alpha = E\cos\theta_e \\ e_\beta = E\sin\theta_e \end{cases} \tag{3.3}$$

Applying now the Park's transform to the previous $\alpha\beta$ equations gives

$$\begin{bmatrix} e_d \\ e_q \end{bmatrix} = \begin{bmatrix} \cos\theta_e & \sin\theta_e \\ -\sin\theta_e & \cos\theta_e \end{bmatrix} \begin{bmatrix} e_\alpha \\ e_\beta \end{bmatrix} \tag{3.4}$$

leading to

$$\begin{cases} e_d = E \\ e_q = 0 \end{cases} \tag{3.5}$$

System equation (3.5) represents the e source/load in *dq*, which has constant values. Notice that $e_d = E$ = single-phase peak voltage.

Circuit equations (3.2) in $\alpha\beta$ are

$$\begin{cases} e_\alpha = Ri_\alpha + L\dfrac{di_\alpha}{dt} + v_\alpha \\ e_\beta = Ri_\beta + L\dfrac{di_\beta}{dt} + v_\beta \end{cases} \tag{3.6}$$

Considering now this $\alpha\beta$ to *dq* reference frame transformations

$$\begin{bmatrix} e_d \\ e_q \end{bmatrix} = \begin{bmatrix} \cos\theta_e & \sin\theta_e \\ -\sin\theta_e & \cos\theta_e \end{bmatrix} \begin{bmatrix} e_\alpha \\ e_\beta \end{bmatrix} \tag{3.7}$$

$$\begin{bmatrix} i_d \\ i_q \end{bmatrix} = \begin{bmatrix} \cos\theta_e & \sin\theta_e \\ -\sin\theta_e & \cos\theta_e \end{bmatrix} \begin{bmatrix} i_\alpha \\ i_\beta \end{bmatrix} \tag{3.8}$$

and the current's inverse *dq* to $\alpha\beta$ transformation

$$\begin{bmatrix} i_\alpha \\ i_\beta \end{bmatrix} = \begin{bmatrix} \cos\theta_e & \sin\theta_e \\ -\sin\theta_e & \cos\theta_e \end{bmatrix}^{-1} \begin{bmatrix} i_d \\ i_q \end{bmatrix} \tag{3.9}$$

the original (3.6) equations can be represented as

$$\begin{bmatrix} e_d \\ e_q \end{bmatrix} = \begin{bmatrix} \cos\theta_e & \sin\theta_e \\ -\sin\theta_e & \cos\theta_e \end{bmatrix} \begin{bmatrix} Ri_\alpha + L\dfrac{di_\alpha}{dt} + v_\alpha \\ Ri_\beta + L\dfrac{di_\beta}{dt} + v_\beta \end{bmatrix} \tag{3.10}$$

and the following mathematical developments can be done

$$\begin{bmatrix} e_d \\ e_q \end{bmatrix} = \begin{bmatrix} \cos\theta_e & \sin\theta_e \\ -\sin\theta_e & \cos\theta_e \end{bmatrix} L\frac{d}{dt}\begin{bmatrix} i_\alpha \\ i_\beta \end{bmatrix} + R\begin{bmatrix} \cos\theta_e & \sin\theta_e \\ -\sin\theta_e & \cos\theta_e \end{bmatrix}\begin{bmatrix} i_\alpha \\ i_\beta \end{bmatrix} + \begin{bmatrix} \cos\theta_e & \sin\theta_e \\ -\sin\theta_e & \cos\theta_e \end{bmatrix}\begin{bmatrix} v_\alpha \\ v_\beta \end{bmatrix} \Leftrightarrow$$
$$<=> \begin{bmatrix} e_d \\ e_q \end{bmatrix} = \begin{bmatrix} \cos\theta_e & \sin\theta_e \\ -\sin\theta_e & \cos\theta_e \end{bmatrix} L\frac{d}{dt}\begin{bmatrix} i_\alpha \\ i_\beta \end{bmatrix} + R\begin{bmatrix} i_d \\ i_q \end{bmatrix} + \begin{bmatrix} v_d \\ v_q \end{bmatrix} <=> \tag{3.11}$$

and since

$$\begin{bmatrix} \cos\theta_e & \sin\theta_e \\ -\sin\theta_e & \cos\theta_e \end{bmatrix}^{-1} = \begin{bmatrix} \cos\theta_e & -\sin\theta_e \\ \sin\theta_e & \cos\theta_e \end{bmatrix} \tag{3.12}$$

then

$$\begin{bmatrix} e_d \\ e_q \end{bmatrix} = \begin{bmatrix} \cos\theta_e & \sin\theta_e \\ -\sin\theta_e & \cos\theta_e \end{bmatrix} L\frac{d}{dt}\left(\begin{bmatrix} \cos\theta_e & -\sin\theta_e \\ \sin\theta_e & \cos\theta_e \end{bmatrix}\begin{bmatrix} i_d \\ i_q \end{bmatrix}\right) + R\begin{bmatrix} i_d \\ i_q \end{bmatrix} + \begin{bmatrix} v_d \\ v_q \end{bmatrix} \tag{3.13}$$

and taking into account that

$$\theta_e = \omega_e t \ and \ \omega_e = \frac{d\theta_e}{dt} \tag{3.14}$$

then

$$\begin{bmatrix} e_d \\ e_q \end{bmatrix} = \begin{bmatrix} \cos\theta_e & \sin\omega_e t \\ -\sin\theta_e & \cos\omega_e t \end{bmatrix} L \left(\begin{bmatrix} -\omega_e \sin\theta_e & -\omega_e \cos\theta_e \\ \omega_e \cos\theta_e & -\omega_e \sin\theta_e \end{bmatrix} \begin{bmatrix} i_d \\ i_q \end{bmatrix} + \begin{bmatrix} \cos\theta_e & -\sin\theta_e \\ \sin\theta_e & \cos\theta_e \end{bmatrix} \begin{bmatrix} \frac{di_d}{dt} \\ \frac{di_q}{dt} \end{bmatrix} \right) + R \begin{bmatrix} i_d \\ i_q \end{bmatrix} + \begin{bmatrix} v_d \\ v_q \end{bmatrix} \Leftrightarrow \tag{3.15}$$

$$\begin{bmatrix} e_d \\ e_q \end{bmatrix} = \begin{bmatrix} \cos\theta_e & \sin\omega t \\ -\sin\theta_e & \cos\omega t \end{bmatrix} L \left(\begin{bmatrix} -\omega_e \sin\theta_e & -\omega_e \cos\theta_e \\ \omega_e \cos\theta_e & -\omega_e \sin\theta_e \end{bmatrix} \begin{bmatrix} i_d \\ i_q \end{bmatrix} + \begin{bmatrix} \cos\theta_e & -\sin\theta_e \\ \sin\theta_e & \cos\theta_e \end{bmatrix} \begin{bmatrix} \frac{di_d}{dt} \\ \frac{di_q}{dt} \end{bmatrix} \right) + R \begin{bmatrix} i_d \\ i_q \end{bmatrix} + \begin{bmatrix} v_d \\ v_q \end{bmatrix} \tag{3.16}$$

$$<=> \begin{bmatrix} e_d \\ e_q \end{bmatrix} = L \begin{bmatrix} 0 & -\omega_e \\ \omega_e & 0 \end{bmatrix} \begin{bmatrix} i_d \\ i_q \end{bmatrix} + L \begin{bmatrix} 1 & 0 \\ 0 & 1 \end{bmatrix} \begin{bmatrix} \frac{di_d}{dt} \\ \frac{di_q}{dt} \end{bmatrix} + R \begin{bmatrix} i_d \\ i_q \end{bmatrix} + \begin{bmatrix} v_d \\ v_q \end{bmatrix} \tag{3.17}$$

The original (3.2) circuit equations are in the *dq* referential given by (3.18)

$$\begin{cases} e_d = Ri_d + L\frac{di_d}{dt} - \omega_e L i_q + v_d \\ e_q = Ri_q + L\frac{di_q}{dt} + \omega_e L i_d + v_q \end{cases} \tag{3.18}$$

Figure 3.4a) represents the converter single-phase AC side circuit. Figure 3.4b) shows the correspondent vector diagram. Considering that e is collinear with the $d-axis$, the amplitude of v and its relative phase to e, that is ε, defines the line current i_L.

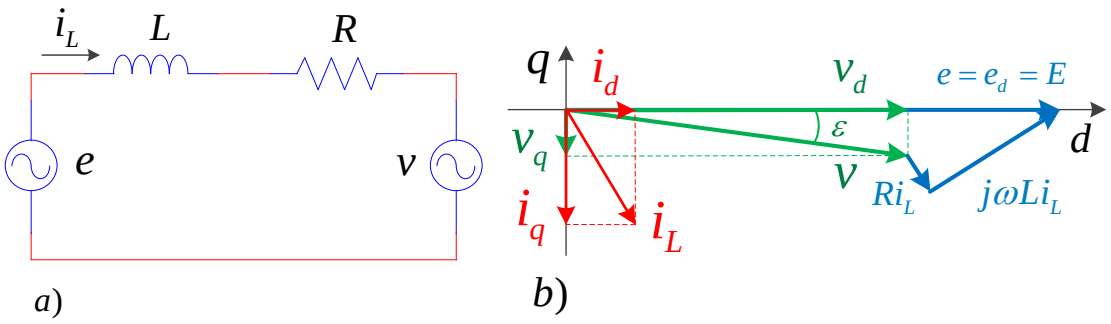

Figure 3.4 - VSC single-phase and *dq* vector diagram

From the VSC's AC terminals point of view equations (3.2) are in *dq*

$$\begin{cases} v_d = e_d - Ri_d - L\dfrac{di_d}{dt} + \omega L i_q \\ v_q = e_q - Ri_q - L\dfrac{di_q}{dt} - \omega L i_d \end{cases} \tag{3.19}$$

Figure 3.5 shows the diagram for: a) VSC working as a UPF Rectifier and b) VSC working as a UPF Inverter.

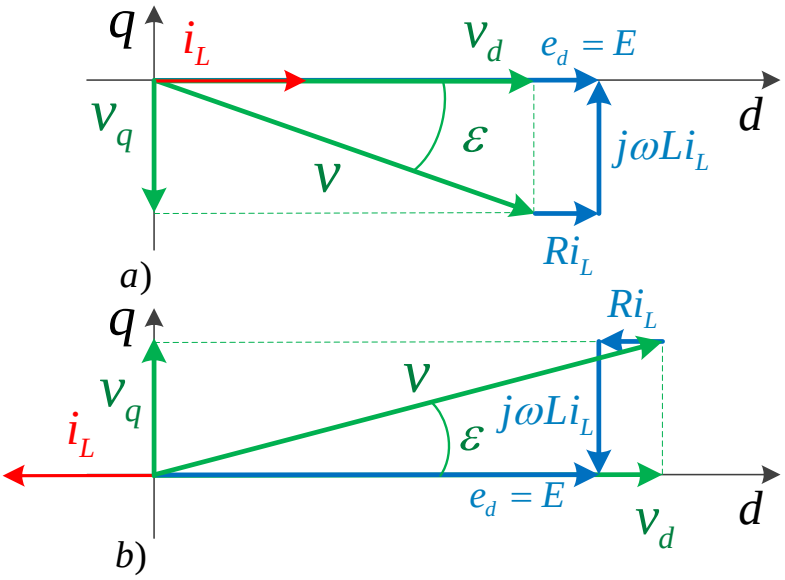

Figure 3.5 - VSC's AC side - a) rectification at UPF; b) inversion at UPF

In both cases, i_L is aligned with E that is collinear with $d-axis$. Note that in UPF, rectification v is smaller than e while in UPF inversion v is higher than e.

The Figure 3.6 shows the VSC's AC side circuit in *dq* according to equations (3.18). Notice that there is an inherent cross-coupling between d and q quantities.

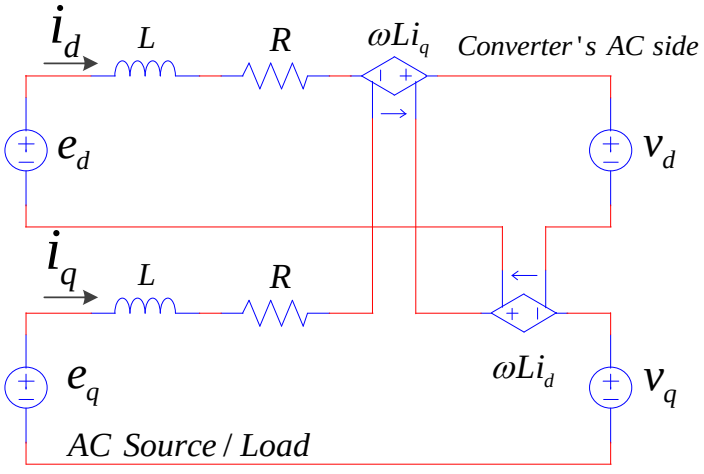

Figure 3.6 - Three-phase VSC AC side model in *dq*

$\omega_e L i_d$ and $\omega_e L i_q$ terms represent the cross-coupling or the interdependence between d and q quantities.

3.3.1.1 AC Side Active and Reactive Power

The instantaneous power at the e voltage source/load can be decomposed [12] in the Cartesian plane as

$$S_e = \left(e_a i_a + e_b i_b + e_c i_c\right) + j\frac{1}{\sqrt{3}}(e_{bc} i_a + e_{ca} i_b + e_{ab} i_c) \tag{3.20}$$

or

$$S_e = P_e + j_e Q \tag{3.21}$$

and according to Akagi [13] the related equation in $\alpha\beta$ and in *dq* reference frames are respectively

$$S_e = \left(e_\alpha i_\alpha + e_\beta i_\beta\right) + j(e_\beta i_\alpha - e_\alpha i_\beta) \tag{3.22}$$

$$S_e = \frac{3}{2}(e_d i_d + e_q i_q + j(e_q i_d - e_d i_q)) \tag{3.23}$$

In *dq* and taking into account the values of (3.5), the power equation (3.23) can be simplified to (3.24) and (3.25). A positive P_e represents the active power supplied by the e source/load, while a negative one represents the power absorbed by the e source/load. The reactive power Q_e exists if $i_q \neq 0$. If Q_e is positive it means that the *e* source/load is supplying reactive power while if negative it is absorbing reactive power.

As viewed before the source voltage e constitutes the referential for this study, so

$$S_e = \frac{3}{2}\left(e_d i_d - j e_d i_q\right) \text{ or } S_e = \frac{3}{2}\left(E i_d - j E i_q\right) \tag{3.24}$$

Active and reactive powers supplied or received by the source e are

$$\begin{cases} P_e = \frac{3}{2} E i_d \\ Q_e = -\frac{3}{2} E i_q \end{cases} \tag{3.25}$$

Notice that for $FP=1$ then e_d is in phase with i_d and in this case $i_d = I_L$ (single-phase peak current) and $i_q = 0$. The *rms* values of e_d and i_d are respectively

$$e_{rms} = \frac{e_d}{\sqrt{2}} = \frac{E}{\sqrt{2}} \;\; and \;\; i_{rms} = \frac{i_d}{\sqrt{2}} = \frac{I}{\sqrt{2}} \tag{3.26}$$

leading to

$$\begin{cases} P_e = \frac{3}{2} E i_d = \frac{3}{2}(\sqrt{2} e_{rms} \sqrt{2} i_{rms}) = 3 e_{rms} i_{rms} \\ Q_e = 0 \end{cases} \tag{3.27}$$

A similar analysis can be done for the VSC's AC side v voltage. Related equations in *dq* are

$$S_v = \frac{3}{2}(v_d i_d + v_q i_q + j(v_q i_d - v_d i_q)) \tag{3.28}$$

$$\begin{cases} P_v = \frac{3}{2}(v_d i_d + v_q i_q) \\ Q_v = \frac{3}{2}(v_q i_d - v_d i_q) \end{cases} \tag{3.29}$$

3.3.2 The VSC DC Side Model

The power that crosses the converter from the AC side to the DC side or vice-versa is only the active power P_v. As there are no switching or conduction losses in the converter itself, the power relations are stated by (3.30), where P_{DC} is the power at the DC side of the converter.

$$P_v = P_{VSC\ AC\ side} = P_{VSC\ DC\ side} = P_{DC} \tag{3.30}$$

The V_{DC} voltage depends on the associated DC circuit and on the power transferred from/to the AC side. Thus, an appropriate way to represent the converter DC side is by means of a current source I_o [10] being the power transferred according to

$$P_{DC} = V_{DC} I_o \tag{3.31}$$

The DC side circuit model of Figure 3.7 includes a small filter capacitor as well as a generic DC source/load. The capacitor can be analyzed as a current-to-voltage converter needed to define and stabilize the DC voltage as well as to filter the high-frequency switching harmonics generated by the converter. R_c is the capacitor

ESR. A low capacitor ESR reduces the high frequency switching related ripple, improving the DC voltage quality.

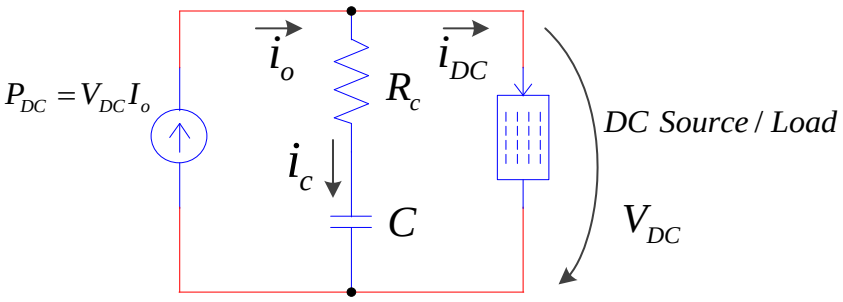

Figure 3.7 - Three-phase VSC DC side model

The energy stored in the capacitor C is

$$E_c = \frac{1}{2} C V_{DC}^2 \tag{3.32}$$

The derivative of the energy with respect to time represents the instantaneous power in the capacitor.

$$P_c = \frac{d}{dt}\left(\frac{1}{2} C V_{DC}^2\right) = V_{DC} C \frac{dV_{DC}}{dt} \tag{3.33}$$

This (3.33) power is the difference between instantaneous powers in the VSC and in the DC source/load

$$P_{DC} = V_{DC} C \frac{dV_{DC}}{dt} + P_{LOAD} \tag{3.34}$$

where P_{LOAD} is generically given by

$$P_{LOAD} = V_{DC} I_{DC} \tag{3.35}$$

3.3.3 The Complete VSC Model in *dq*

Taking P_v from equations (3.29), (3.30) and (3.31) it is possible to establish the power flow equation (3.36)

$$\frac{3}{2}\left(v_d i_d + v_q i_q\right) = V_{DC} I_o \tag{3.36}$$

Joining both Figure 3.6 AC side and Figure 3.7 DC side circuits according to equation (3.36) leads to the VSC circuit presented in Figure 3.8. This circuit models the VSC using the power flow requested to the converter as a model parameter.

In this circuit the VSC can be analyzed as a power transfer device that converts AC active power into DC power and vice-versa. This circuit is equivalent to the one presented in Figure 3.1 but it has some important advantages for control purposes as only DC quantities are used.

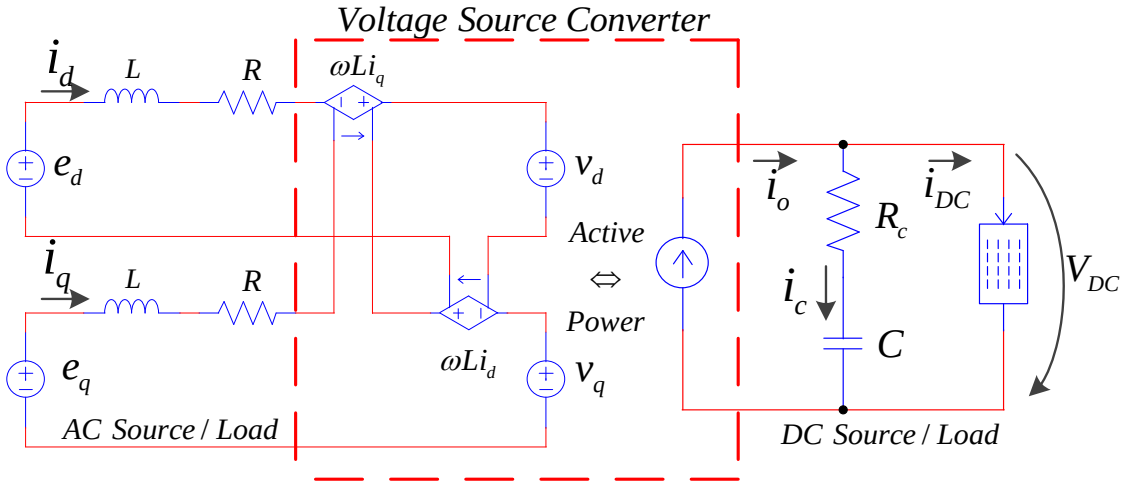

Figure 3.8 - Three-phase VSC model in dq

3.3.4 Laplace-domain VSC Analysis

Laplace-domain or frequency-domain analysis is an appropriate method to represent, simulate, design and test the VSC. In this sub-chapter the previous time-domain VSC equations are converted in their Laplace-domain equivalent.

3.3.4.1 Laplace-domain VSC AC Side Equations

Equation (3.37) is the Laplace-domain form of the time domain equation (3.18)

$$\begin{cases} e_d = (R + sL) i_d - \omega_e L i_q + v_d \\ e_q = (R + sL) i_q + \omega_e L i_d + v_q \end{cases} \tag{3.37}$$

This equation (3.37) can be manipulated in order to determine the currents i_d and i_q

$$\begin{cases} i_d = \left(e_d - v_d + \omega_e L i_q\right) \dfrac{1}{R + sL} \\ i_q = \left(e_q - v_q - \omega_e L i_d\right) \dfrac{1}{R + sL} \end{cases} \tag{3.38}$$

3.3.4.2 Laplace-domain VSC DC Side Circuits

3.3.4.2.1 VSC's DC Side With a Battery

Let's assume that the generic DC source/load represented in Figure 3.7 is now a battery. The battery is modeled as a large pre-charged capacitor C_1 in series with its ESR R_1. The new VSC DC side configuration is represented in Figure 3.9.

The filter capacitor represented by C and R_c is typically in the order of hundreds to thousands of micro-Farad, which is an insignificant capacity when compared to the battery modeled as a large C_1 capacity with, e.g. thousands of Farad. However, its ESR, represented by R_c, is typically in the order of a few $m\Omega$, while the battery internal resistance R_1 is typically in the order of hundreds of $m\Omega$. Thus the capacitor C with low ESR is highly efficient to short-circuit the high frequency harmonics caused by power electronic switching.

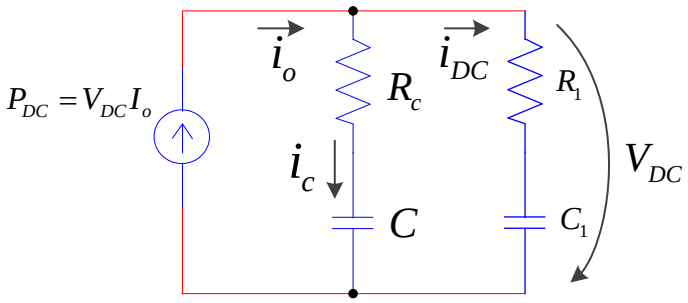

Figure 3.9 - VSC DC side with a battery modeled as a large capacitor C_1

Figure 3.10 shows the result of converting the circuit of Figure 3.9 to the Laplace domain.

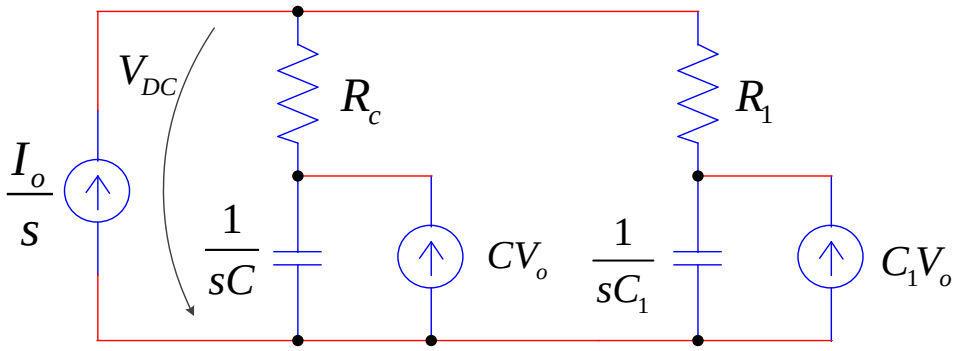

Figure 3.10 - VSC DC side representation of a battery modeled as a large capacitor

In Figure 3.10 V_0 is the initial capacitor's voltage.

The circuit's equation is

$$\frac{I_o}{s} = \underbrace{\left(\frac{R_c + R_1}{R_c R_1} - \frac{1}{R_1 \left(sR_1C_1 + 1 \right)} - \frac{1}{R_c \left(sR_cC + 1 \right)} \right)}_{A} V_{DC} - \left(\frac{C_1}{sR_1C_1 + 1} + \frac{C}{sR_cC + 1} \right) V_o \qquad (3.39)$$

where the expression A is

$$A = \frac{s^2 CC_1(R_c + R_1) + s(C + C_1)}{s^2 R_c R_1 CC_1 + s(R_c C + R_1 C_1) + 1} \tag{3.40}$$

and since the DC side power in Laplace domain is given by

$$P_{DC} = V_{DC} \frac{I_0}{s} \tag{3.41}$$

joining equations (3.39) and (3.41) gives

$$\frac{P_{DC}}{V_{DC}} = AV_{DC} - \left(\frac{C}{sR_c C + 1} + \frac{C_1}{sR_1 C_1 + 1} \right) V_0 \tag{3.42}$$

which can assume the form

$$V_{DC} = \frac{1}{A} \left(\frac{P_{DC}}{V_{DC}} + \left(\frac{C}{sR_c C + 1} + \frac{C_1}{sR_1 C_1 + 1} \right) V_0 \right) \tag{3.43}$$

Taking into account equations (3.29) and (3.30), the equation (3.43) becomes

$$V_{DC} = \frac{1}{A} \left(\frac{\frac{3}{2}\left(v_d i_d + v_q i_q \right)}{V_{DC}} + \left(\frac{C}{sR_c C + 1} + \frac{C_1}{sR_1 C_1 + 1} \right) V_0 \right) \tag{3.44}$$

Considering now AC and DC side Laplace domain equations (3.37) and (3.44), the model of Figure 3.11 is derived.

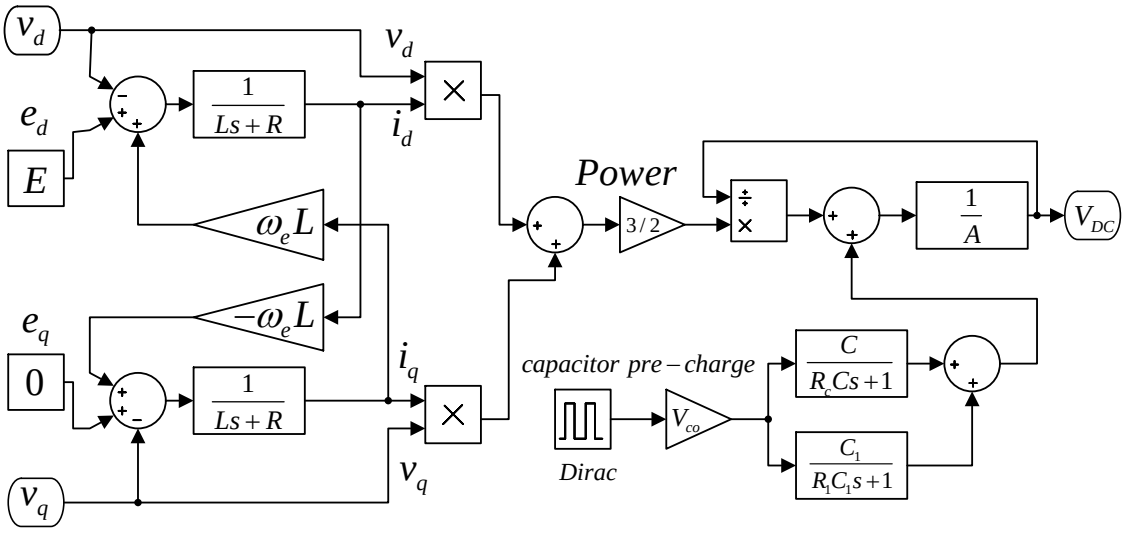

Figure 3.11 – VSC Laplace-model including a battery modeled as a large capacitor in the DC side

As an example, let's analyze the dynamic behavior of the open-loop system represented by Figure 3.11, assuming the following parameters: $e_d = E = 100V$; $e_q = 0$; $R = 100m\Omega$; $L = 1mH$; $C = 500\mu F$; $R_c = 20m\Omega$; $C_1 = 2000F$, $R_1 = 500m\Omega$, $V_{C0} = 300V$ (stand-by battery voltage), and $f = 50Hz$.

Then, equation (3.44) is defined as (3.45)

$$\frac{1}{A} = \frac{s^2 10m + s1000 + 1}{s^2 520m + s2000}$$
$$\frac{C}{sR_cC + 1} = \frac{500\mu}{s10\mu + 1} \quad and \quad \frac{C_1}{sR_1C_1 + 1} = \frac{2000}{s1000 + 1} \tag{3.45}$$

The PSIM circuit that describes this VSC open-loop system is presented in Figure 3.12.

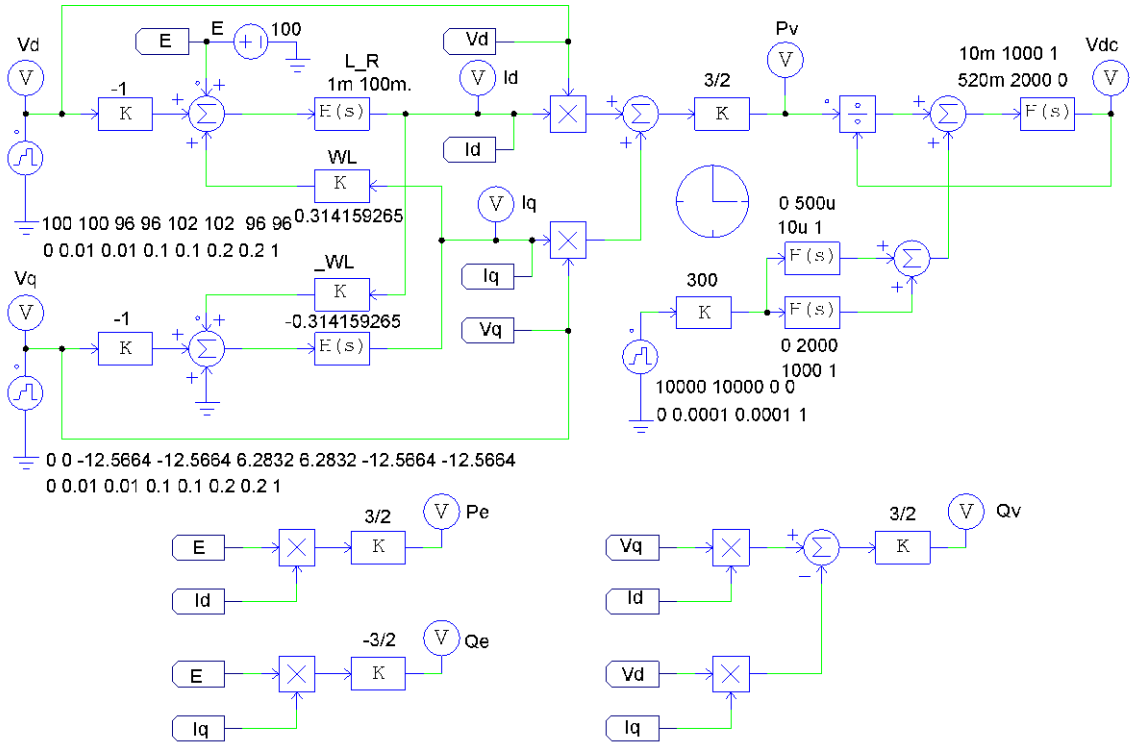

Figure 3.12 – PSIM VSC Laplace modeled with a battery (C_1+R_1) in the DC side

Suppose that, from the e source/load (e.g. the grid) point of view, it is intended to transfer to the DC side 6kW of power at UPF during a given interval and in another interval receive 3kW, again at UPF.

Starting from VSC equations (3.19), in steady state $\frac{di_d}{dt} = \frac{di_q}{dt} = 0$, so the equations are now

$$\begin{cases} v_d = E - Ri_d + \omega_e L i_q \\ v_q = 0 - Ri_q - \omega_e L i_d \end{cases} \quad (3.46)$$

Since at UPF the line current i_L is collinear to the correspondent single-phase e voltage (see Figure 3.5), and thus $i_q = 0$, equation (3.46) becomes

$$\begin{cases} v_d = E - Ri_d \\ v_q = -\omega_e L i_d \end{cases} \quad (3.47)$$

Table 3.1 is build taking into account power equations (3.25) and the UPF working point equations (3.47). The circuit input parameters v_d and v_q are calculated for the requested P_e active power. All units are in International System of Units (ISU)

P_e	Q_e	i_d	i_q	v_d	v_q	$P_v = P_{DC}$	Q_v
0	0	0	0	100	0	0	0
6k	0	40	0	96	-12.6	5760	-754
-3k	0	-20	0	102	6.3	-3060	-188

Table 3.1 – VSC steady state quantities for the requested power P_e

The resulting simulation waveforms are shown in Figure 3.13. The power flow is initially set up to be 0 ($v_d = 100$ and $v_q = 0$). At this time the battery voltage is $V_{DC} = 300V$.

At time 10ms the v_d and v_q voltages are modified to allow the VSC to act as a rectifier transferring 6kW to the DC side. As observed in Figure 3.14, at the time instant 90ms the power reaching the DC side battery is 5.76kW and V_{DC} increases to $309V$ (battery is charging). The power difference is due to losses in the AC side inductors.

At time instant 100ms the v_d and v_q voltages are modified again to allow the VSC to act as an inverter transferring 3kW to the AC side (the grid). To reach 3kW at the AC side, the battery has to supply 3.06kW to compensate its internal losses and the line inductor losses. In this case, the battery V_{DC} voltage drops to $295V$ (battery is discharging), as observed in Figure 3.13 and in Figure 3.14 at time instant 190ms.

Analyzing Figure 3.13 PSIM simulation waveforms the following considerations may be derived:

- after a v_d and v_q step change, i.e. a power flow working point change, the system reacts to achieve a new steady state point;

- due to the inherent cross-coupling given by the VSC $\omega_e L$ paths and to the presence of inductors and capacitors that store energy, the power flow change occurs with transient oscillations with particular evidence in the i_d and i_q currents, the V_{DC} voltage and P_e and Q_e powers. Notice the presence of reactive power Q_e only during transients.

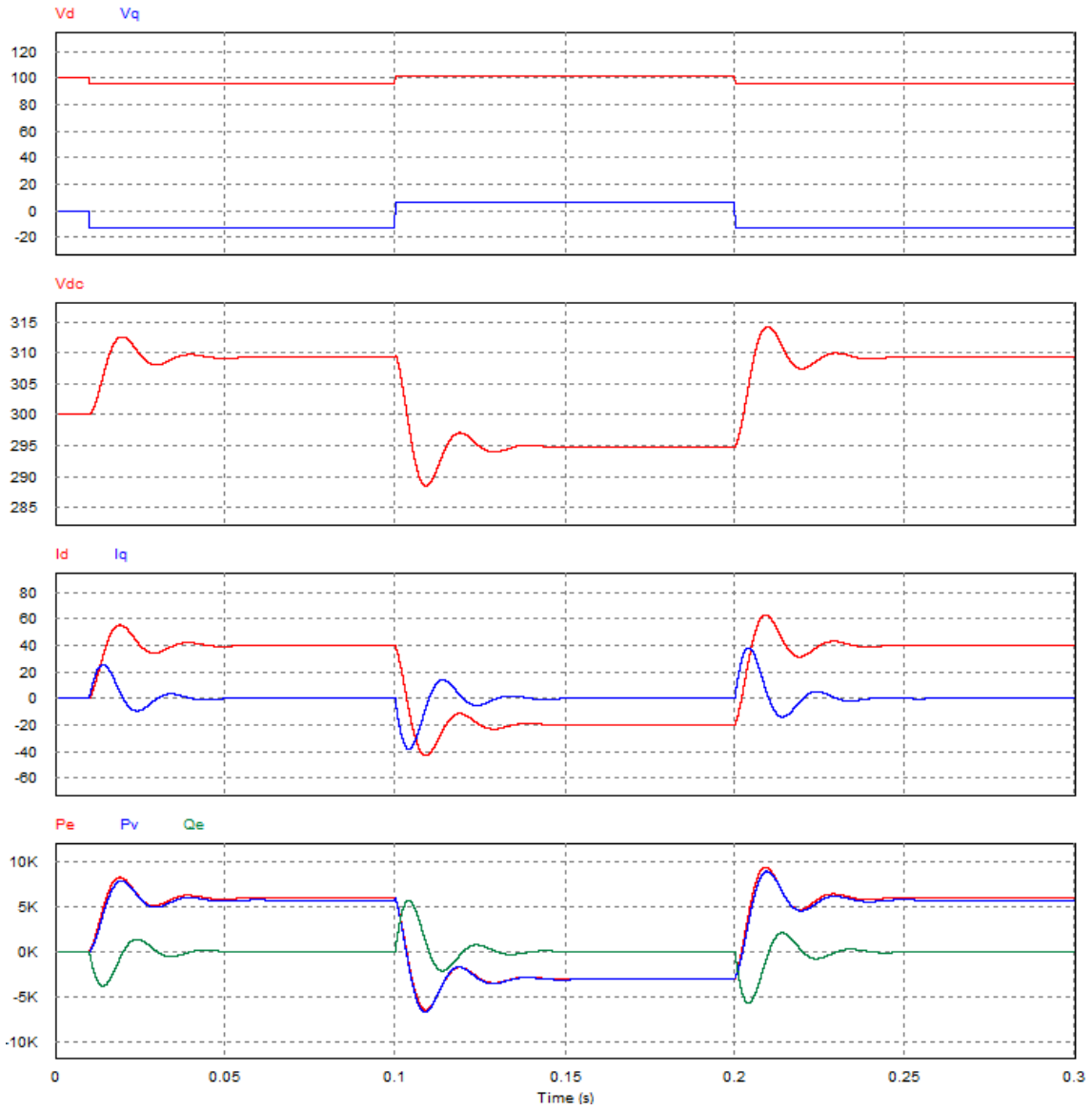

Figure 3.13 - PSIM VSC resulting waveforms for VSC with a battery in the DC side

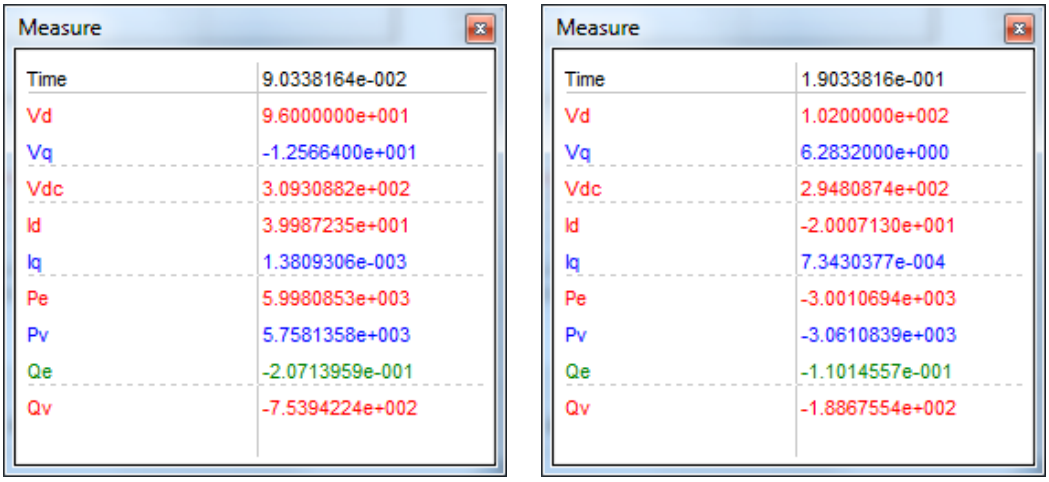

Figure 3.14 – PSIM VSC with a battery in the DC side - measurements at 90ms and 190ms

Figure 3.15 shows a PSIM Park's transform that is an add-in to the Figure 3.12 circuit. It allows to observe the phase voltages and currents. Figure 3.16 show the simulation waveform results. Notice that when the VSC is acting as a rectifier, voltage and current are in phase, and when acting as inverter they are 180^o out of phase.

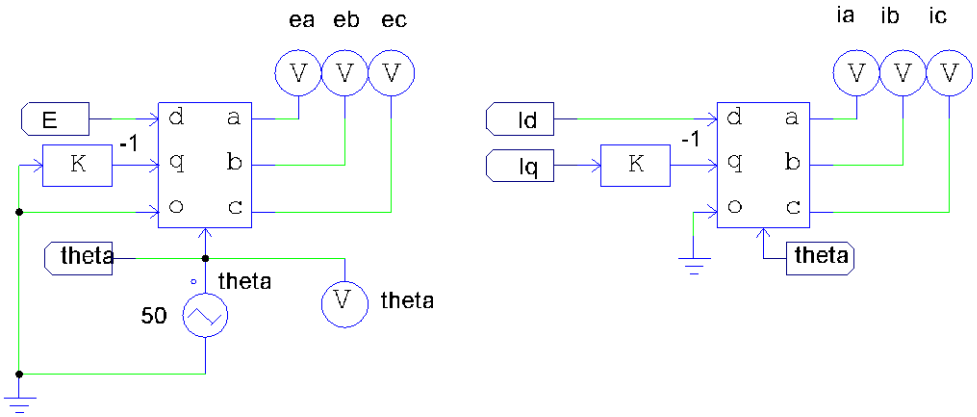

Figure 3.15 – PSIM Park's transform applied to give AC e voltages and line currents

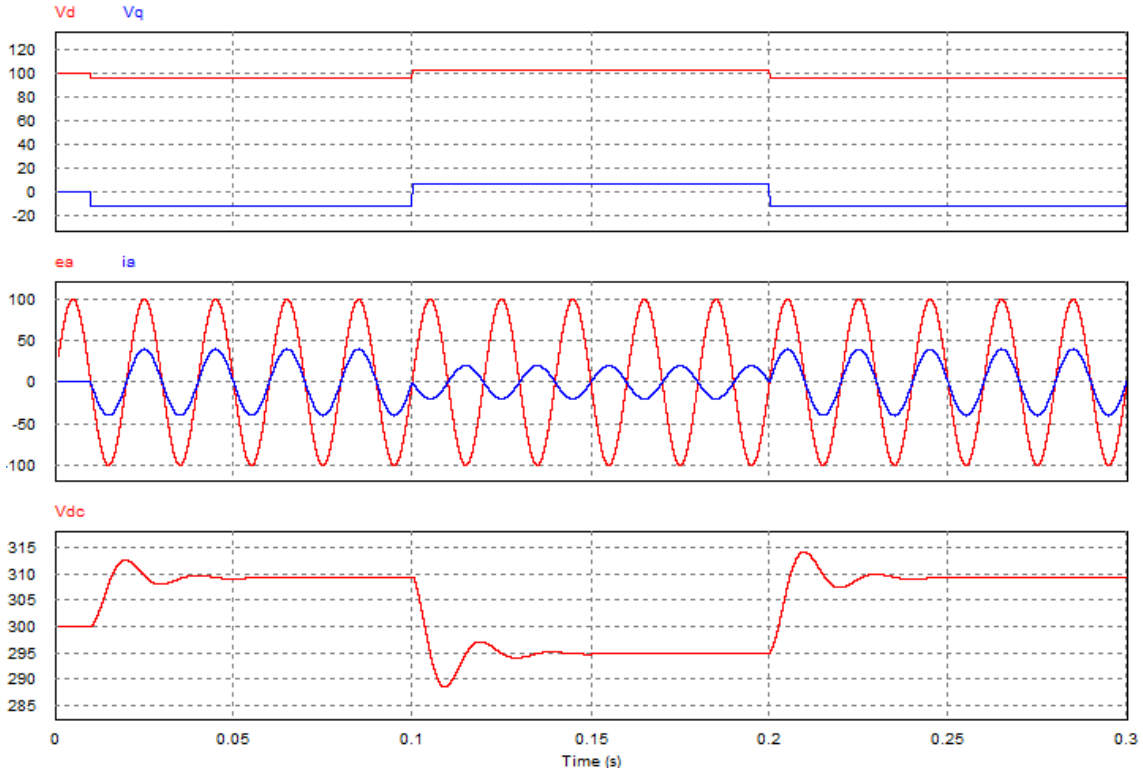

Figure 3.16 – PSIM Park's transform results

To accurately control the VSC dynamic behavior, i.e. to avoid or limit transients, it is necessary to design a suitable controller. Controller's analysis and design are addressed later in this chapter.

3.3.4.2.2 VSC's DC Side With a Load Resistance R_L

The VSC's DC side is now a load resistance R_L as represented in Figure 3.17.

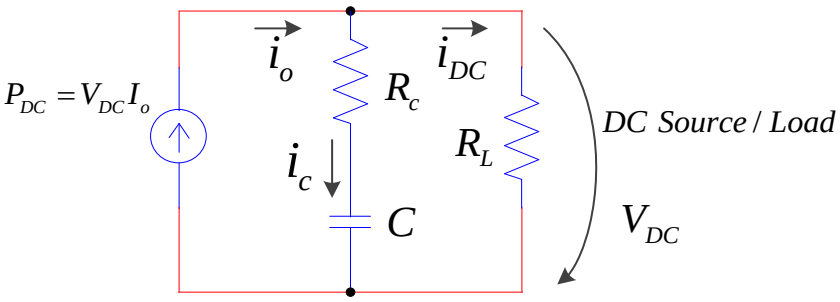

Figure 3.17 – VSC's DC side with R_L as a load resistance

Figure 3.18 shows the result of converting the circuit of Figure 3.17 to the Laplace domain.

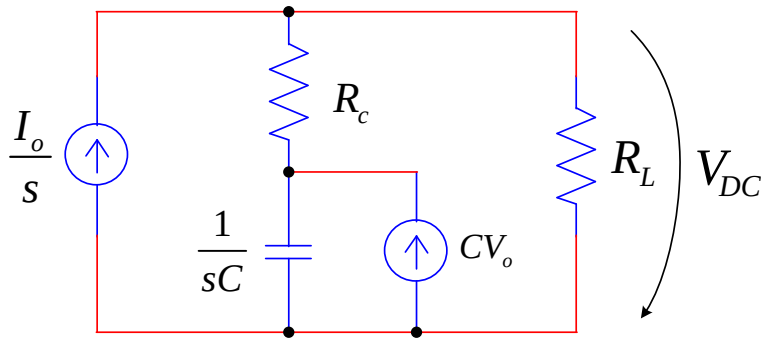

Figure 3.18 – VSC's DC side with R_L in Laplace-domain representation

Considering that the capacitor is initially discharged, then $V_{co} = 0$.

The circuit's equation is then

$$\frac{I_o}{s} = \frac{V_{DC}}{sR_cC} + \frac{V_{DC}}{R_L} \tag{3.48}$$

After some mathematical manipulation, the equation (3.48) can assume the form

$$V_{DC} = \frac{sR_cC+1}{sC}\left(\frac{I_o}{s} - \frac{V_{DC}}{R_L}\right) \tag{3.49}$$

Since in the Laplace domain, $P_{DC} = V_{DC}\frac{I_0}{s}$, then

$$V_{DC} = \frac{sR_cC+1}{sC}\left(\frac{P_{DC}}{V_{DC}} - \frac{V_{DC}}{R_L}\right) \tag{3.50}$$

The model of Figure 3.19 is derived considering AC and DC side Laplace domain equations (3.37) and (3.50).

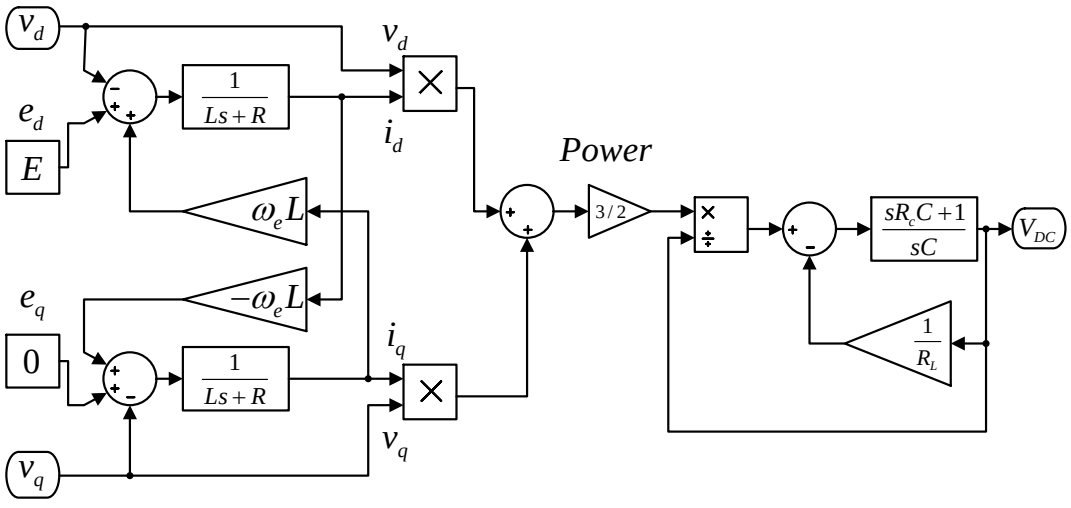

Figure 3.19 - VSC Laplace-model including a load resistance R_L in the DC side

As an example, let's analyze the dynamic behavior of an open-loop system represented by Figure 3.19, assuming the following parameters: $e_d = E = 100V$; $e_q = 0$; $R = 100m\Omega$; $L = 1mH$; $C = 500\mu F$; $R_c = 20m\Omega$; $R_L = 10\Omega$, and $f = 50Hz$.

Then, equation (3.50) assumes the form

$$V_{DC} = \frac{s10\mu + 1}{s500\mu}\left(\frac{P_{DC}}{V_{DC}} - \frac{V_{DC}}{R_L}\right) \tag{3.51}$$

Suppose that the aim is to have $V_{DC} = 300V$ with UPF (in the AC side), at one interval and to have $V_{DC} = 400V$ in a different interval, again with UPF. In steady state the power that flows to the DC side is given by $P_{DC} = \frac{V_{DC}^2}{R_L}$, which is 9kW for $V_{DC} = 300V$ and 16kW for $V_{DC} = 400V$.

The power that flows into the VSC AC side, P_v, is the same that flows in the DC side (see equation (3.30)), and is given by equation (3.29). Since $i_q = 0$ at UPF, then

$$\begin{cases} P_v = \frac{3}{2} v_d i_d \\ Q_v = \frac{3}{2} v_q i_d \end{cases} \tag{3.52}$$

The power supplied by the AC source/load e, that is P_e, is given by P_v plus the power losses in the line inductors.

$$P_e = P_v + P_{losses} \tag{3.53}$$

Since $i_q = 0$, the power losses in the line inductors are given in steady state by (3.54)

$$P_{losses} = \frac{3}{2} R i_d^2 \tag{3.54}$$

Taking into account equations (3.25), (3.30) and (3.54)

$$\frac{3}{2} R i_d^2 - \frac{3}{2} E i_d + P_{DC} = 0 \tag{3.55}$$

The solution to equation (3.55) is

$$i_d = \frac{\frac{3}{2}E \pm \sqrt{\left(\frac{3}{2}E\right)^2 - 6RP_{DC}}}{3R} \tag{3.56}$$

Table 3.2 is build taking into account equation (3.56), the power equations (3.25) and (3.29), and the UPF working point equations (3.47). The circuit input parameters v_d and v_q are calculated for the requested V_{DC} voltage. All units are in ISU.

V_{DC}	$P_{DC} = P_v$	Q_v	i_d	i_q	v_d	v_q	P_e	Q_e
0	0	0	0	0	100	0	0	0
300	9000	-1937	64.11	0	93.59	-20.14	9617	0
400	16000	-6946	121.41	0	87.86	-38.14	18211	0

Table 3.2 - VSC Steady state quantities for the wanted V_{DC} voltage

Figure 3.20 represents the PSIM VSC circuit with a resistance in the DC side. It is build based on AC Laplace equation (3.38) and on DC Laplace equation (3.51).

The resulting PSIM simulation waves are shown in Figure 3.21. The power flow is initially set up to be 0 ($v_d = 100$ and $v_q = 0$). At this instant the load resistance voltage is $V_{DC} = 0V$.

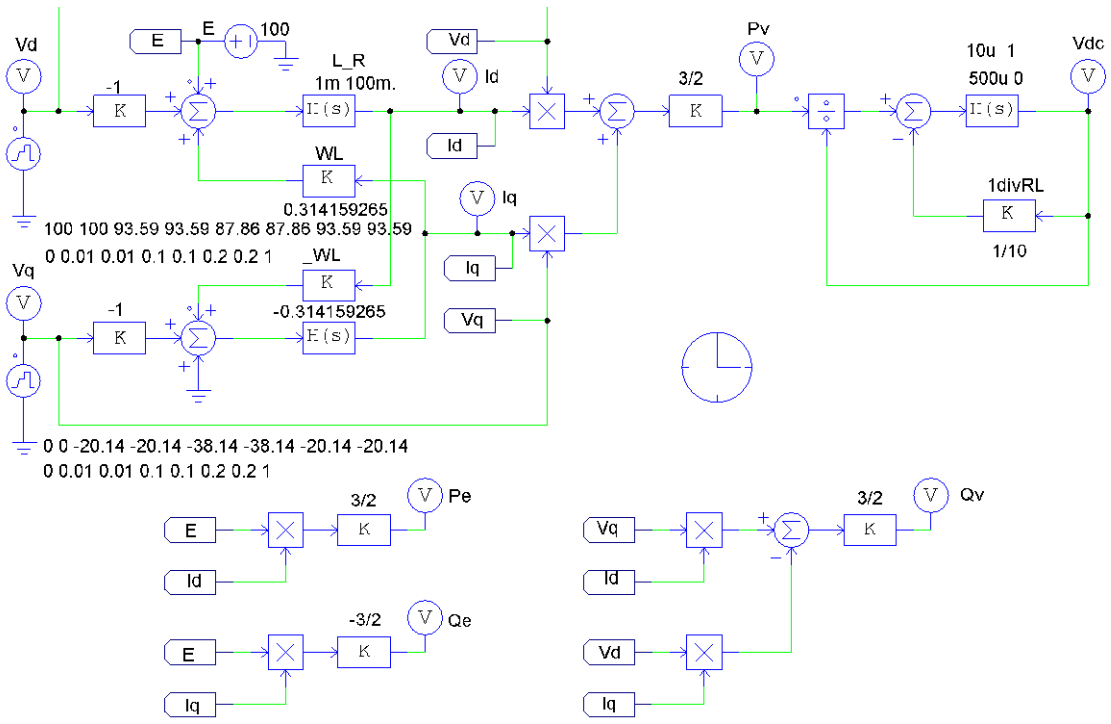

Figure 3.20 - PSIM VSC Laplace model with a resistance R_L in the DC side

At time instant 10ms, the v_d and v_q voltages are modified to allow the VSC to act as a rectifier transferring 9.0kW to the load resistance and with $V_{DC} = 300V$. As observed in Figure 3.21 and Figure 3.22, at time instant 90ms the power dissipated by the load resistance is effectively 9.0kW and to compensate the line inductor losses, the active power supplied by the AC source e is 9.6kW.

At time instant 100ms the v_d and v_q voltages are modified again to allow the VSC to transfer 16.0kW to the DC side with $V_{DC} = 400V$. In this case, the active power supplied by the AC source is 18.2kW (see Figure 3.22 at 190ms), which confirms the values of Table 3.2.

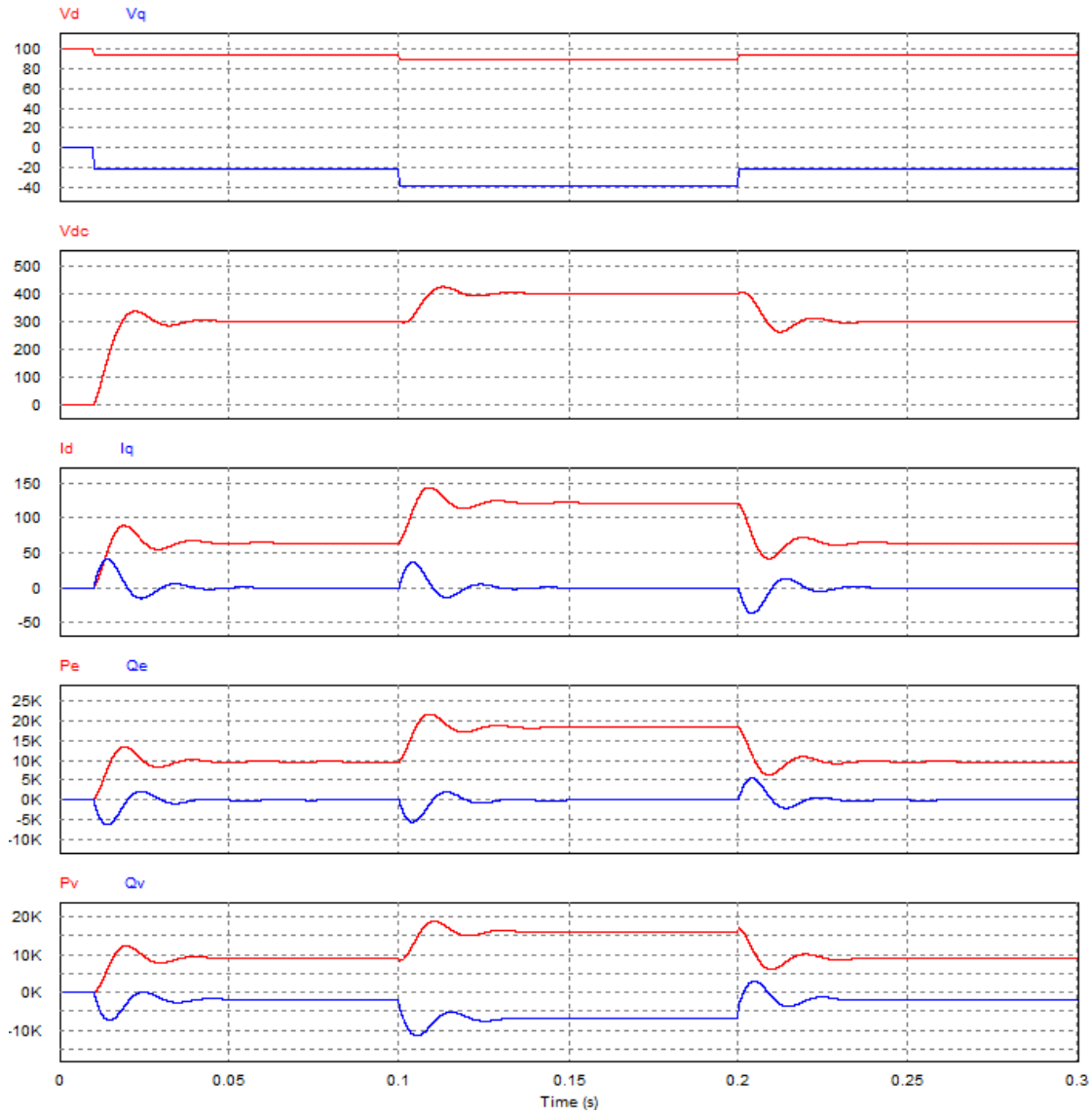

Figure 3.21 - PSIM VSC resulting waveforms for VSC with R_L in the DC side

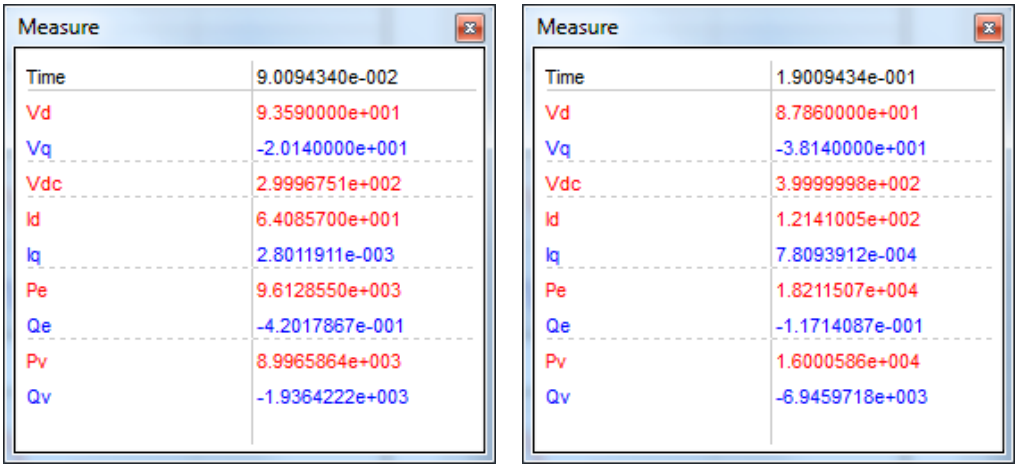

Figure 3.22 - PSIM VSC with R_L in the DC side - measurements at 90ms and 190ms

3.3.5 The VSC Control Principle

Considering the generic VSC representation of Figure 3.1, where energy is stored in both AC and DC sides, the goal of the VSC controller is to define:

- the active power that flows through the VSC and its direction;
- the reactive power exchange between the AC source/load and the VSC which can be inductive, capacitive or null (UPF);

According to equations (3.25), the active and reactive power supplied or absorbed by the e source are proportional to i_d and i_q currents respectively. Controlling the power flow is the process of making i_d and i_q currents to track the current references i_d^* and i_q^*. Thus, according to (3.19), to achieve i_d and i_q requested values, appropriate v_d and v_q voltages have to be built by the converter.

The generation of v_d and v_q results from VSC operation, based on a switching frequency higher than the fundamental one, using Nyquist theorem and Fourier analysis to design appropriate waveforms. This design is performed by adopting an appropriate PWM method [6]. Among others, the Sinusoidal PWM (SPWM) and Space Vector Modulation (SVM) are often chosen: the SPWM is popular due to its simple implementation method; the SVM, a computation intensive technique, can deliver better results because of its extra linear operating zone.

Converter dynamics depends on:

- the VSC circuit itself and associated AC and DC sources/loads, generically represented in Figure 3.8;
- the VSC controller;
- the modulation technique adopted since the related linear gain varies according to it.

3.3.5.1 Voltage Source Converter Modulation Index

The equation (3.57) defines the modulation index M [8]. M is important as it determines the limits of the allowed v and V_{DC} relative amplitudes. Theoretically, it can take any value between 0 and 1. Values of M near 0 mean that v and V_{DC} have big relative voltage amplitudes. On the other hand, higher M values are limited by the modulation technique adopted.

$$M = \frac{\pi}{2}\frac{v}{V_{DC}} = \frac{\pi}{2}\frac{\sqrt{v_d^2 + v_q^2}}{V_{DC}} \tag{3.57}$$

The equation (3.58) shows the maximum M index value for Sinusoidal PWM (SPWM) in linear operation, while (3.59) shows the same limit for Space Vector PWM (SVM) [10]. Above $M_{\max}$ the converter operates in overmodulation (or saturation). In general, the overmodulation operation is not desirable mainly because of two factors:

- changes in v almost do not produce changes in V_{DC} and vice-versa;
- it generates undesirable low frequency current harmonics in the AC line.

$$M_{\max} = \frac{\pi}{4} = 0.7854 \tag{3.58}$$

$$M_{\max} = \frac{\pi}{2\sqrt{3}} = 0.9069 \tag{3.59}$$

From equation (3.57) it is clear that V_{DC} is always higher than the voltage phase peak v. As an example, for SVM within linear operation ($M \le 0.9069$), $V_{DC} \ge \sqrt{3}v$ or $V_{DC} \ge \sqrt{\frac{3}{2}}v_{rms}$, where v_{rms} is the single-phase RMS voltage at the VSC terminal. That means the VSC only works as a Boost rectifier or as a Buck inverter.

3.3.5.2 The VSC Current Controller

The objective of the current controller is to make line currents i_d and i_q to track reference currents i_d^* and i_q^*.

Working in the dq reference frame puts in evidence (see Figure 3.8) the VSC's cross-couplings between d and q quantities. Thus, if the application entails/requires to modify one of the components (component i_d usually), the system will have to counteract it in order to guarantee a high dynamic performance.

According to [7, 8, 14], for high performance applications where an accurate current tracking is necessary, the decoupled PI-type controller should be used.

The controller equations derived from (3.19) are

$$\begin{cases} v_d = e_d - Ri_d - \Delta v_d + \omega L i_q \\ v_q = e_q - Ri_q - \Delta v_q - \omega L i_d \end{cases} \tag{3.60}$$

where Δv_d and Δv_q are the control actions of the PI controllers

$$\begin{cases} \Delta v_d = k_p\left(i_d^* - i_d\right) + k_i \int \left(i_d^* - i_d\right) dt \\ \Delta v_q = k_p\left(i_q^* - i_q\right) + k_i \int \left(i_q^* - i_q\right) dt \end{cases} \tag{3.61}$$

The current controller receives current measurements i_d and i_q from the converter (see Figure 3.11 or Figure 3.19), and generates v_d and v_q command output voltages that are the inputs of the converter.

Taking into account equations (3.60) and (3.61), a suitable decoupled current controller is presented in Figure 3.23. The current controller decoupling paths are $-\omega L$ and ωL. Notice that these controller decoupling paths cancel the same coupling paths observed in the VSC model, as detailed in Figure 3.24. The R paths compensate the losses across the inductors.

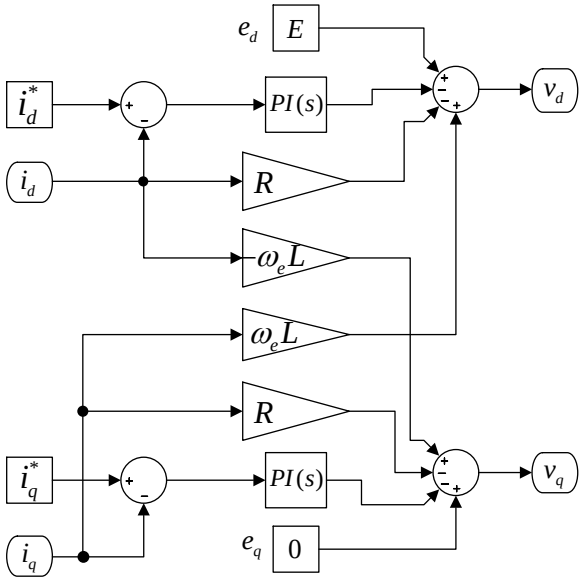

Figure 3.23 - Decoupled current controller for the three-phase VSC

With the decoupled current controller, the converter, which is originally a coupled system, becomes a first linear system [7].

In the next sub-chapter, it is evaluated the performance of the two VSCs modeled in Laplace and the decoupled current controller specifically designed based on those Laplace models.

3.3.5.2.1 Decoupled and Non-decoupled Current Controllers Performance Comparison

To evaluate the performance of the decoupled current controller, a simple non-decoupled current controller is also considered for a comparative analysis. In this current controller, derived from (3.60), only the PIs are considered as represented in (3.62).

$$\begin{cases} v_d = -\Delta v_d \\ v_q = -\Delta v_q \end{cases} \tag{3.62}$$

Both controllers are evaluated using the electrical circuit model from Figure 3.25, with the following parameters: $e_d = E = 100V$; $e_q = 0$; $R = 100m\Omega$; $L = 1mH$; $C = 500\mu F$; $R_c = 20m\Omega$; $C_1 = 2000F$, $R_1 = 500m\Omega$, $V_{C0} = 300V$ (standby battery voltage), and $f = 50Hz$. The modulation technique adopted is the SPWM with a carrier frequency of 10kHz.

The PSIM version of the decoupled current controller (equivalent to the one in Figure 3.23) is represented in Figure 3.26 and the PSIM non-decoupled current controller that results from equation (3.62) is represented in Figure 3.27.

Notice that the first big difference between the decoupled and non-decoupled controller is that the former needs to collect accurate values from the circuit in analysis such as:

- the e source/load phase amplitude and frequency;
- the line inductance and resistance.

The controller references are: $I_d = +50A; -80A; +150A$ applied at different interval (see Figure 3.26 or Figure 3.27), and $I_q = 0$. When I_d is positive the power flows from the AC side to the DC side and when negative the power flow is reversed. Since $I_q = 0$, the reactive power should be null, i.e. UPF.

From the waveform analysis (see Figure 3.28) it is noted that:

- in the non-decoupled controller waveforms, there is an initial peak because the controller do not have information about the single-phase e source/load amplitude;
- there is a slight overshot in the i_d, P_e and V_{DC} in the non-decoupled controller waveforms when compared to the decoupled ones;
- during the transient that occurs after an i_d reference change (i_d^*), the reactive power Q_e is not null; in fact, the voltage e_a and the current i_a are out of phase at that time; the reactive power Q_e is almost null for the decoupled controller waveforms (see Figure 3.28b));
- the transient is shorter for the decoupled controller;

- for both $M\ index$ waveforms notice that during transients an extra linear zone proportioned by a better modulation technique is desirable as it is during transients that the modulation index reaches its limits; in fact the PI proportional and integral values have to be tuned taking into account, in particular, the maximum value admissible for the $M\ index$ in the linear zone.

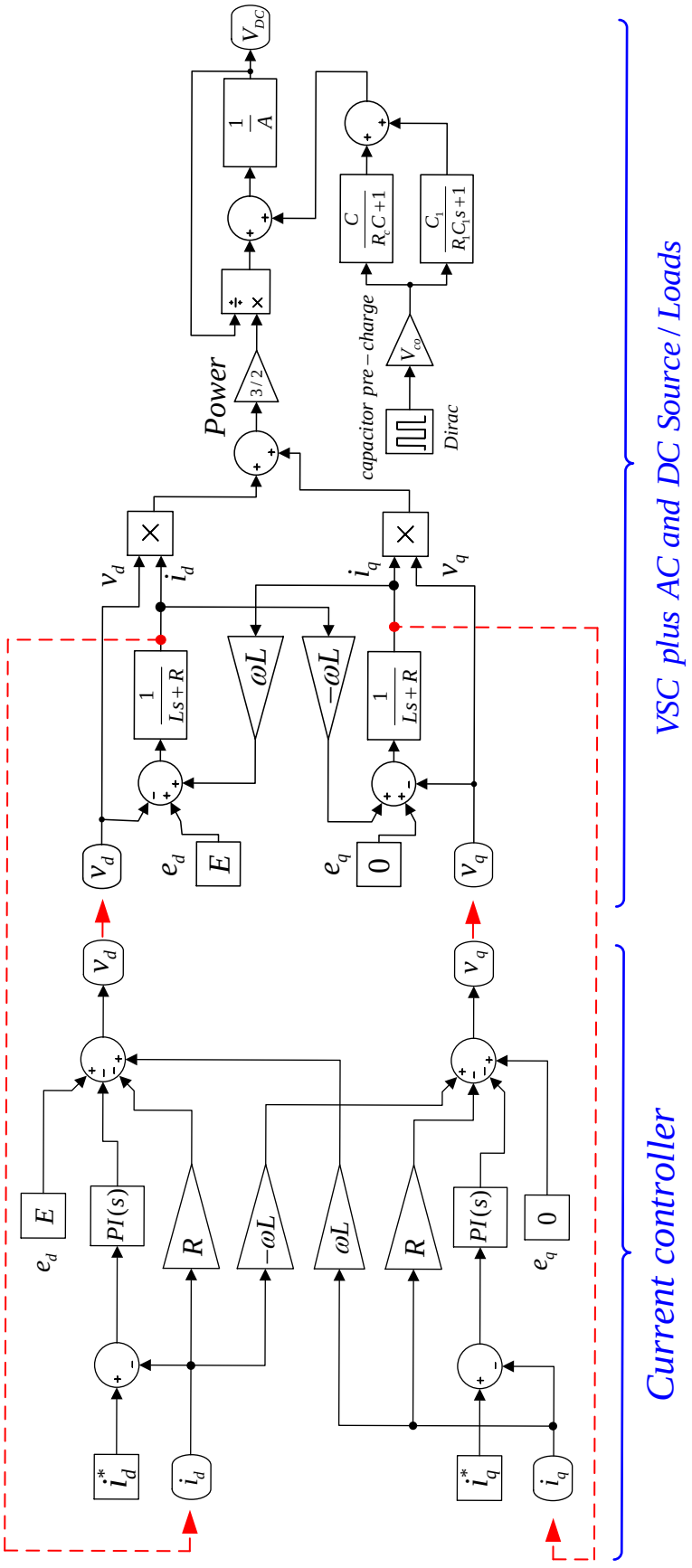

Figure 3.24 - Current controller and VSC Laplace model with a battery modeled as a capacitor in the DC side

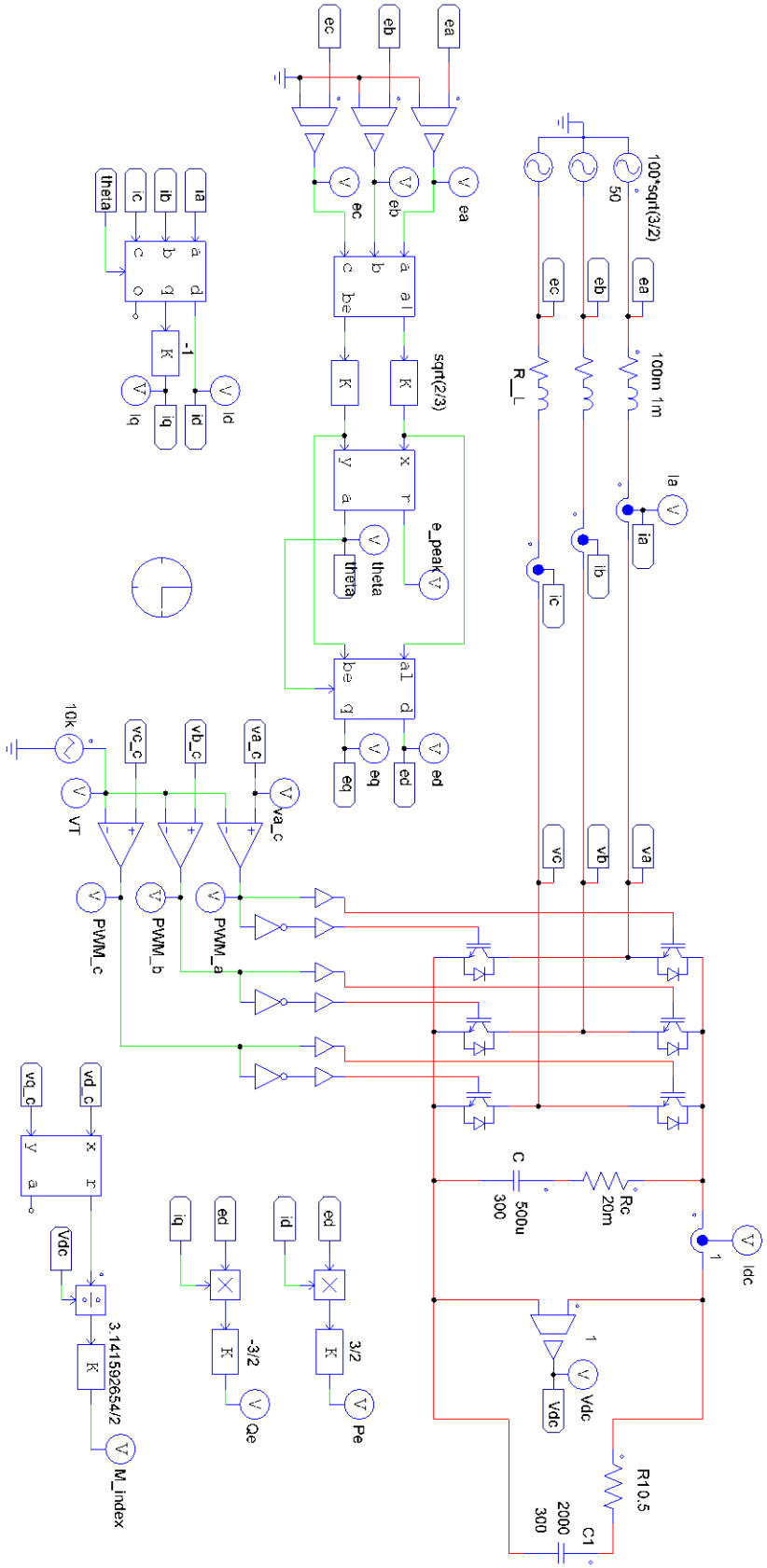

Figure 3.25 – PSIM VSC electrical model with a battery modeled as a capacitor in the DC side

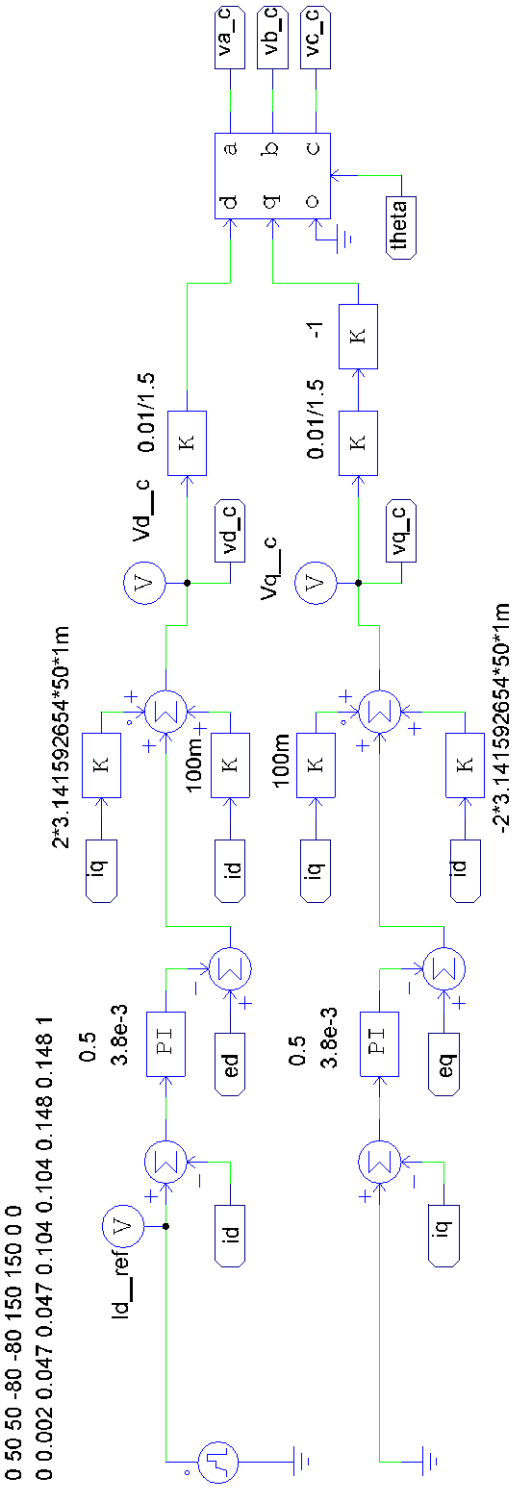

Figure 3.26 - VSC decoupled current controller for the electric model in PSIM

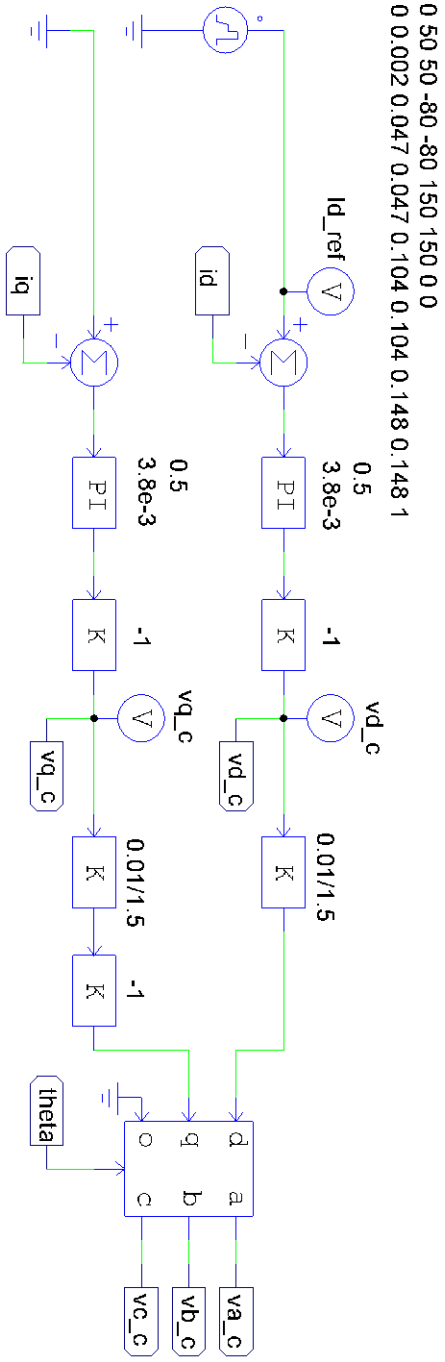

Figure 3.27 - VSC non-decoupled current controller for the electric model in PSIM

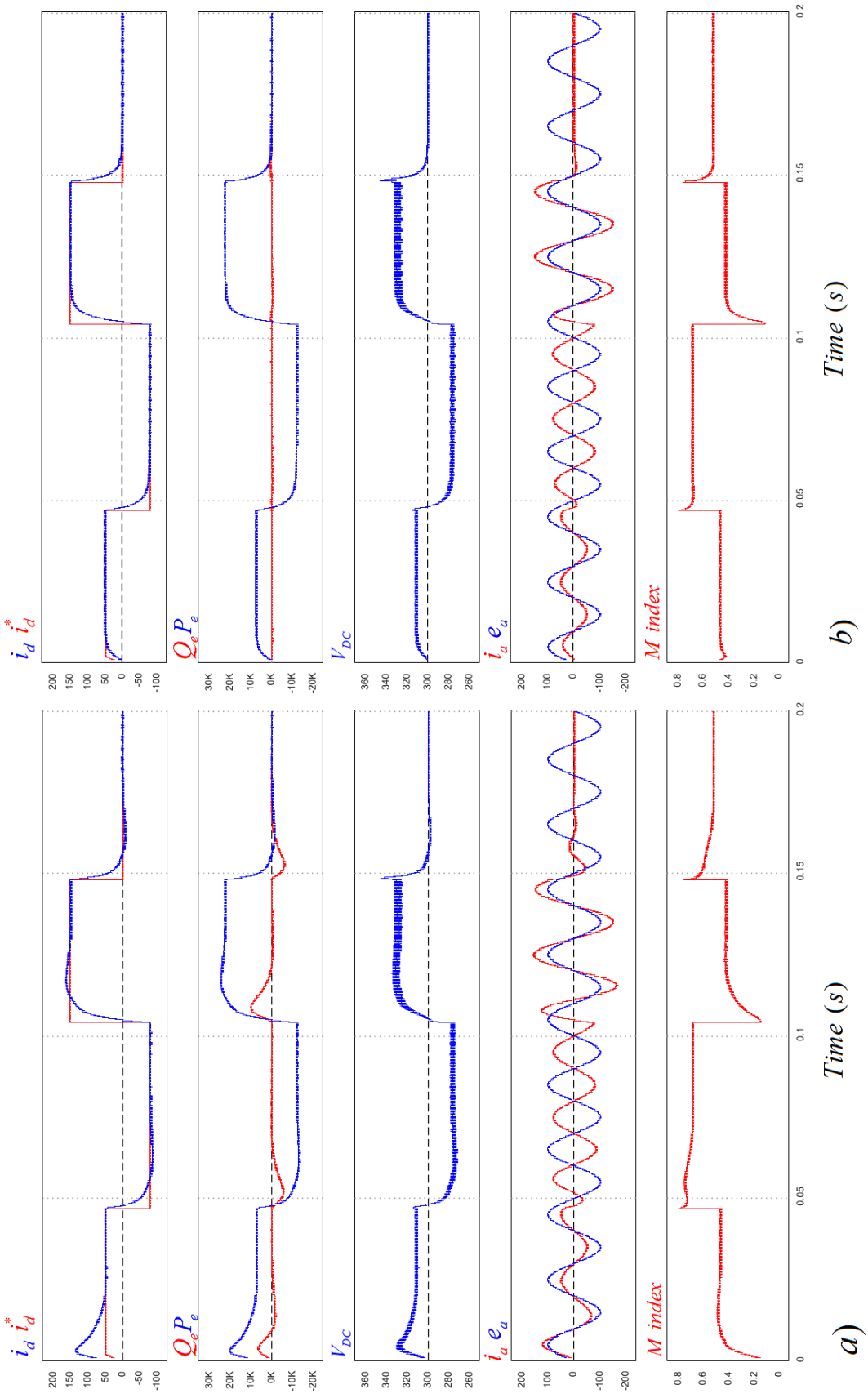

Figure 3.28 - VSC electrical model simulation waveforms a) with the non-decoupled controller and b) with the decoupled controller

As a final conclusion, the benefits of having a suitable decoupled current controller can be summarized as:

- any step change in the reference current i_d^* (or active power), results in smooth controlled changes in all the controlled variables; in other words, the overshoots present in the current, voltage an power waveforms can be almost completely eliminated;
- the transient time after a reference change is shortened;
- the reactive power does not change when the active power is changed; they become decoupled quantities.

On the other hand, to build a suitable decoupled current controller the parameters of the AC side, namely the line parameters L and R, and the e source/load amplitude and frequency have to be known.

3.3.5.2.2 Electric and Laplace Models Performance Comparison

In this sub-chapter the performance of the Laplace model of Figure 3.11 is compared with its correspondent electrical model of Figure 3.25. Both circuits have the following parameters: $e_d = E = 100V$; $e_q = 0$; $R = 100m\Omega$; $L = 1mH$; $C = 500\mu F$; $R_c = 20m\Omega$; $C_1 = 2000F$, $R_1 = 500m\Omega$, $V_{C0} = 300V$ (standby battery voltage), and $f = 50Hz$. The modulation technique adopted or the electrical model is the SPWM with the carrier frequency of 10kHz.

The PSIM Laplace circuit used in this evaluation is represented in the right-hand side of Figure 3.30.

To better evaluate the performance of the VSC Laplace model two different simulations are compared. The first one uses the non-decoupled current controllers from Figure 3.27 and Figure 3.29, respectively for the electrical and Laplace model. The non-decoupled current controllers differ from each other because the electrical version includes the voltage adaption and the reference frame transformation (from dq-to-abc), needed to generate the PWM signals.

The resulting waveforms are presented in Figure 3.31.

The second simulation uses the decoupled current controller (see Figure 3.26 and Figure 3.29), and the resulting waveforms are presented in Figure 3.32.

In both simulations and to allow the comparison between the e source/load single-phase voltages and currents from the electrical and Laplace models, a variation of VSC Laplace model was built using PSIM blocks for reference frame transformation from abc-to-dq and its inverse. The PSIM circuit is shown in Figure 3.33.

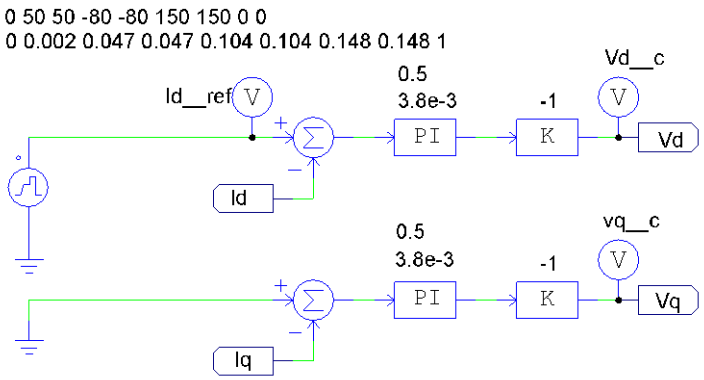

Figure 3.29 - PSIM non-decoupled current controller used with Laplace models

From the waveform analysis (see Figure 3.31 and Figure 3.32) it is noted that:

- the resulting waveforms from both electrical and Laplace models are nearly equal; the unique difference is the high-frequency present in the electrical model simulations;
- the VSC dynamics for i_d reference step changes are equal in both models.

As a final conclusion:

- the VSC Laplace models are accurate and respond dynamically as well as their equivalent (time-domain) electrical models;
- the added value of the VSC Laplace models come from the observability enabled by those models; in fact, VSC Laplace models are like a window through which it is possible to observe what is going on inside the "VSC black-box", allowing the design of the most suitable current controllers.

Note that in Laplace models there is no limit for the modulation index, while for the electric models the maximum value for the modulation index depends on the modulation technique adopted.

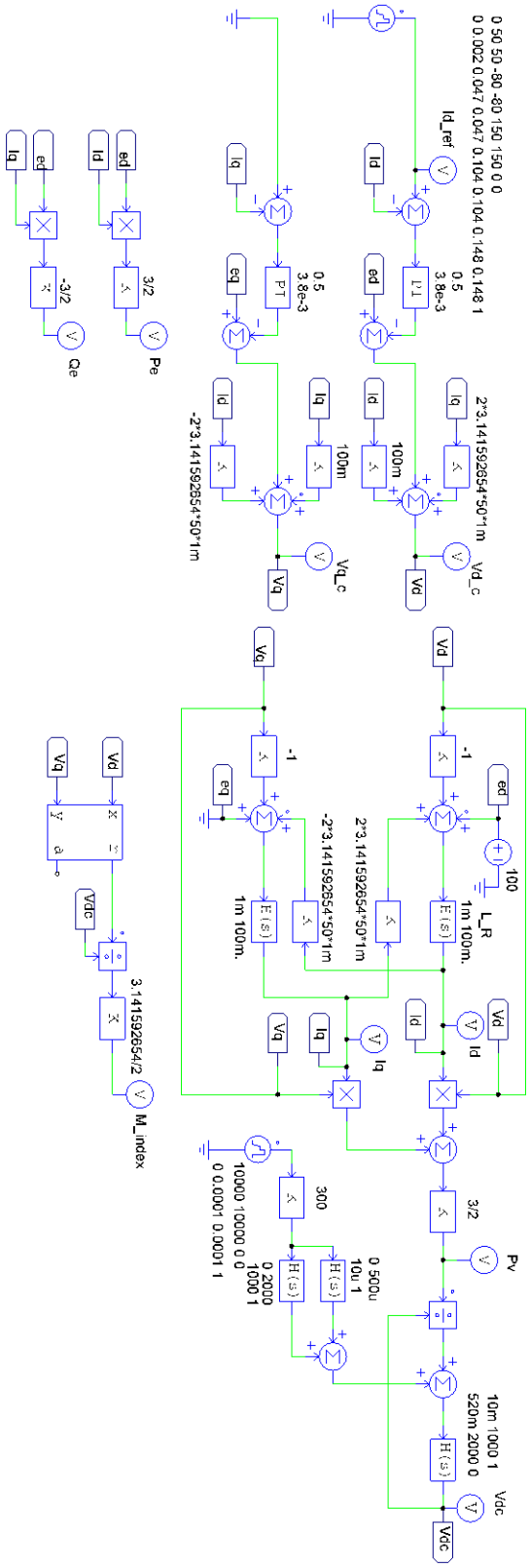

Figure 3.30 - PSIM VSC Laplace model with a battery modeled as a capacitor in the DC side (on de right), with the decoupled current controller (on the left) and the P_e , Q_e and $M\ index$ measurement blocks (below)

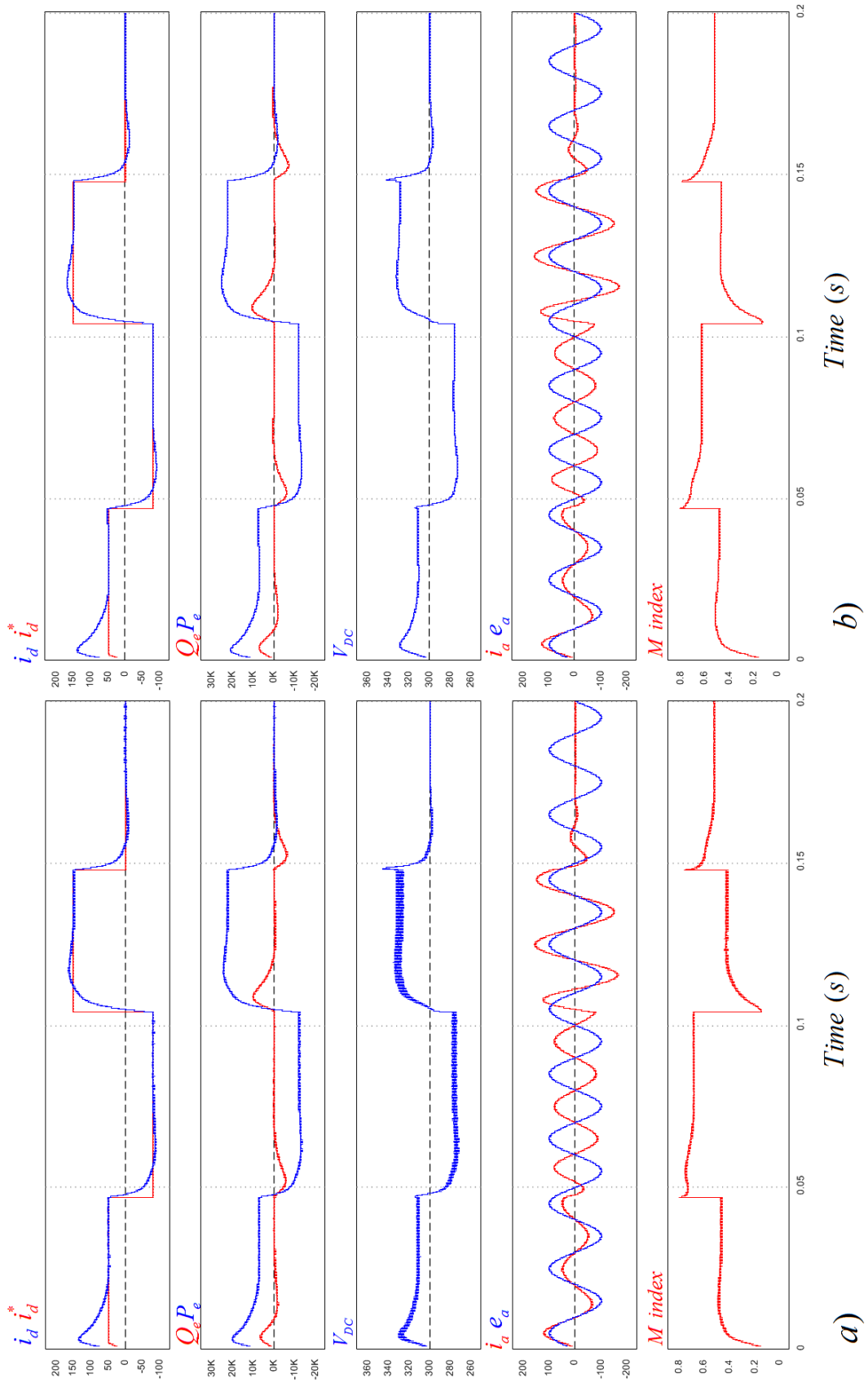

Figure 3.31 - VSC a) electrical model and b) Laplace model simulation waveforms with the non-decoupled current controller

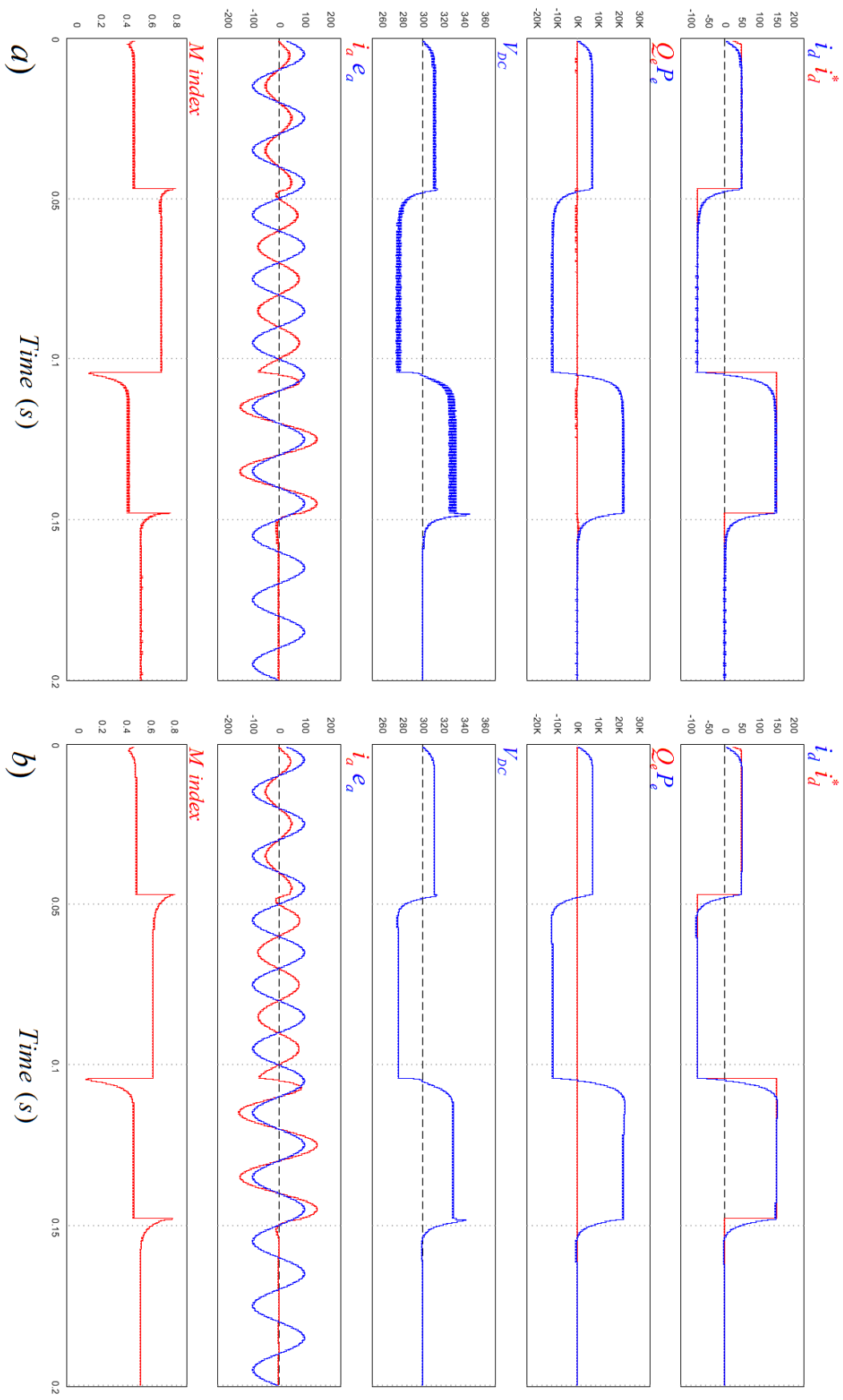

Figure 3.32 - VSC a) electrical model and b) Laplace model simulation waveforms with the decoupled current controller

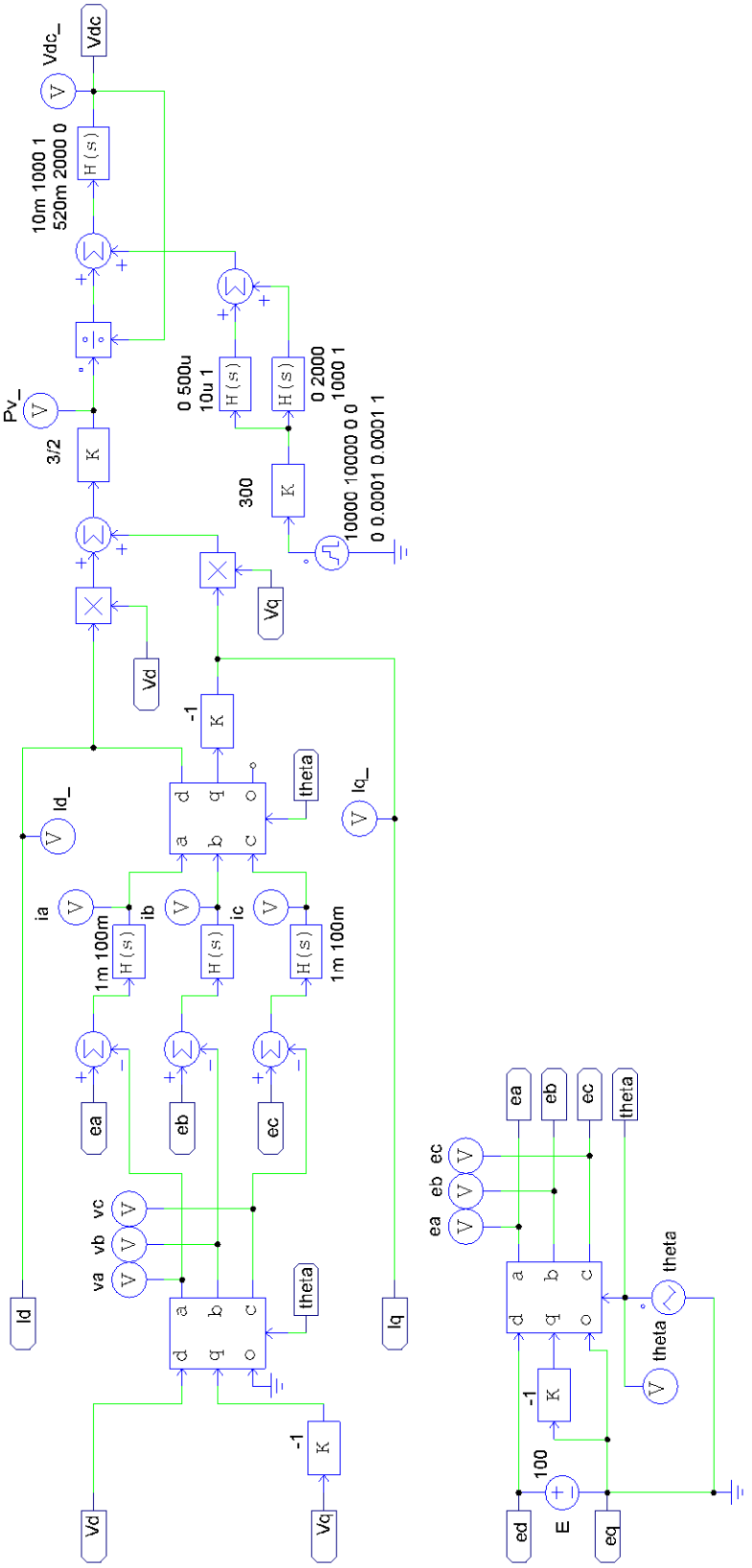

Figure 3.33 - Modified PSIM Laplace model to observe single-phase voltage e_a and current i_a

3.3.5.3 The VSC Voltage Controller

The goal of the VSC voltage controller is to set the DC voltage at the desired level. One of the best known techniques to implement the voltage controller is acting directly on the current controller reference i_d^* as this is responsible to set the (active) power that flows through the VSC. This voltage control methodology is known in literature as a two loop voltage controller [4, 6-9], comprising an inner, fast response, PI current controller, and an outer, slower response, PI voltage controller.

The VSC voltage controller compares the command voltage V_{DC}^* with the actual V_{DC} with the error signal applied to a PI to generate the command current i_d^*, as represented in Figure 3.34.

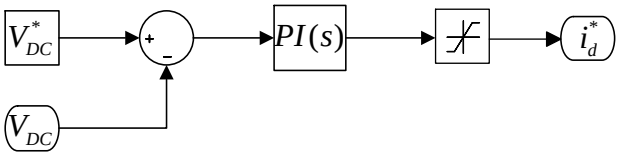

Figure 3.34 - VSC voltage controller

To evaluate the voltage controller performance, it is used the VSC electrical circuit represented in Figure 3.35. Note that in the DC side there is a $10\,\Omega$ load resistance. Figure 3.36 shows the voltage controller plus the decoupled current controller used to control it.

The Laplace equivalent model was previously designed and it is shown in Figure 3.19. Combining the VSC Laplace model with the voltage and decoupled current controllers results in the scheme of Figure 3.37. The PSIM equivalent VSC is in Figure 3.38.

Both electrical and Laplace VSC circuits are compared. The V_{DC} reference voltage is changed from 300V to 400V and back to 300V at specific instants. Simulation waveforms are presented in Figure 3.39.

A second simulation scenario is built to analyze a steep change in the power delivered to a variable load. In this scenario, the load resistance is changed from $10\,\Omega$ to $20\,\Omega$ and back to $10\,\Omega$, maintaining the reference voltage set to 300V.

The corresponding electrical and Laplace models can be seen in Figure 3.40 and Figure 3.41 respectively and the resulting waveforms in Figure 3.42.

Final remarks on the waveforms observed:

- the voltage controller behaves as expected maintaining the Vdc voltage at the desired level after a transient period;
- the VSC transients observed are determined by the circuit itself, by the modulation technique adopted and by the overall control process; different dynamic behaviors are achieved with different controller tuning parameters.
- the electrical and Laplace models have a similar dynamic response apart from the high-frequency related to the switching process.

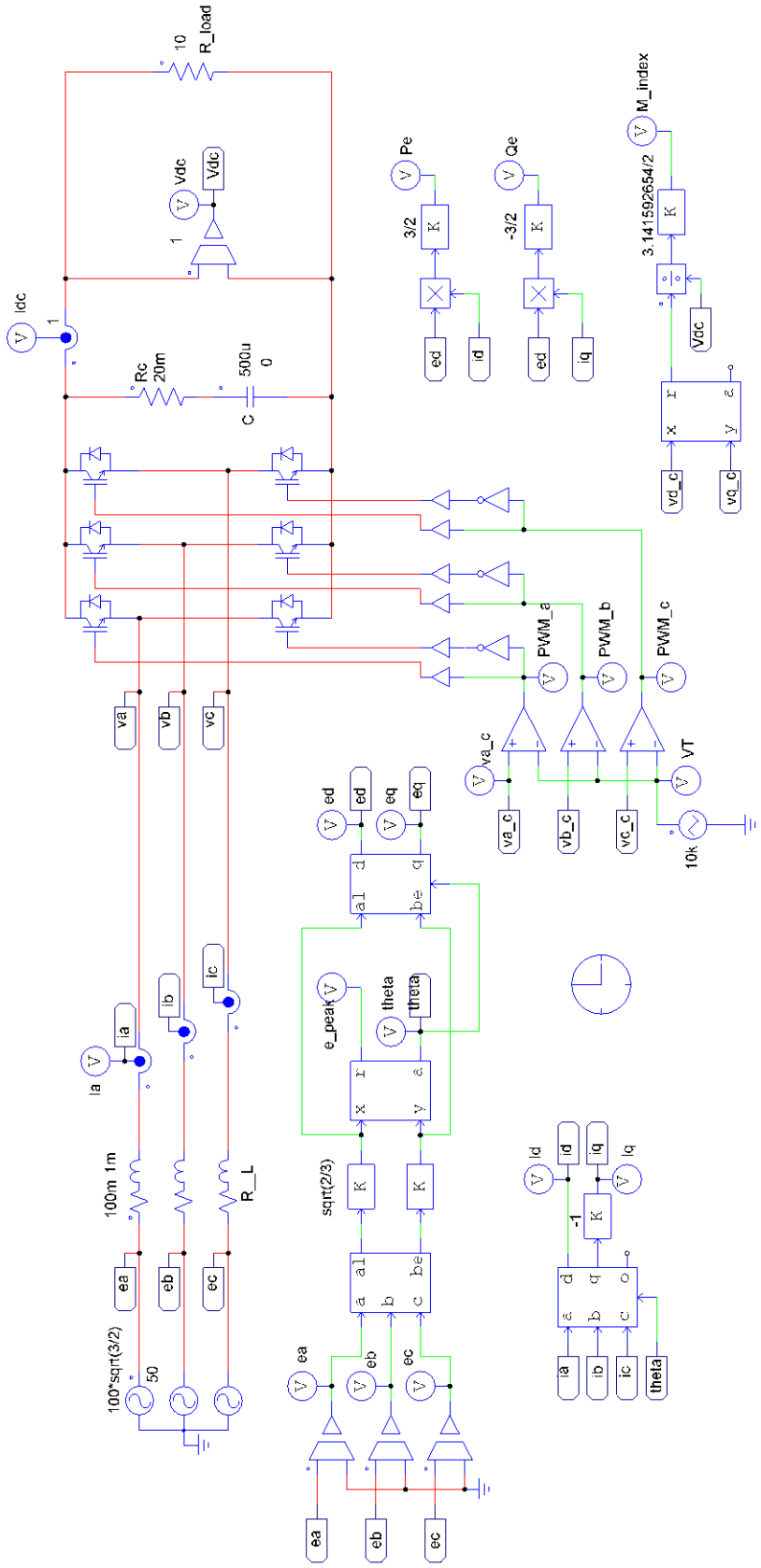

Figure 3.35 - VSC electrical model with a load resistance of 10 Ω in the DC side, in PSIM

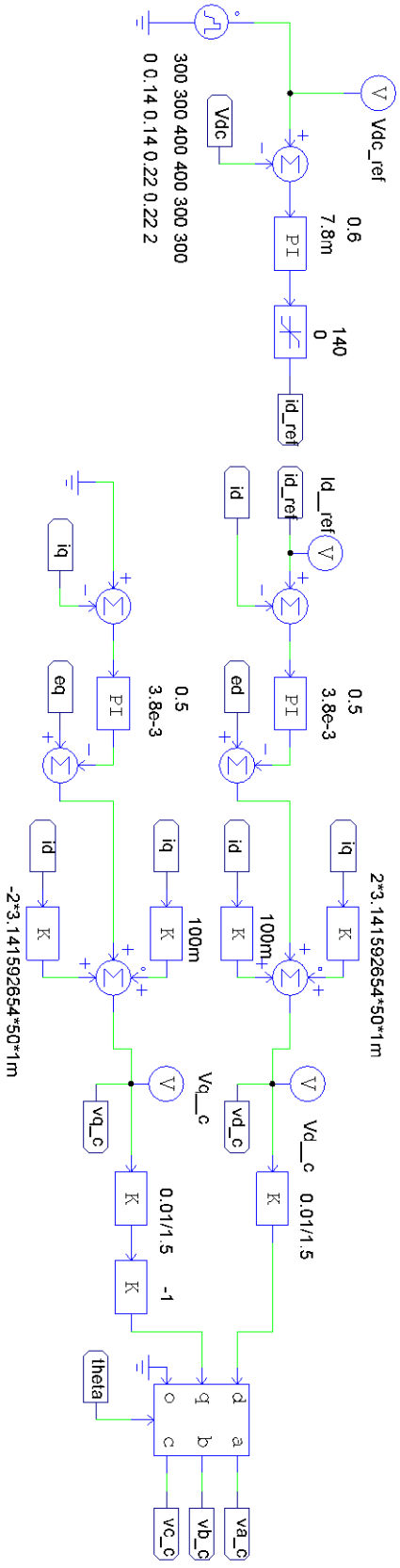

Figure 3.36 - VSC voltage controller + decoupled current controller arrangement for the electric model in PSIM

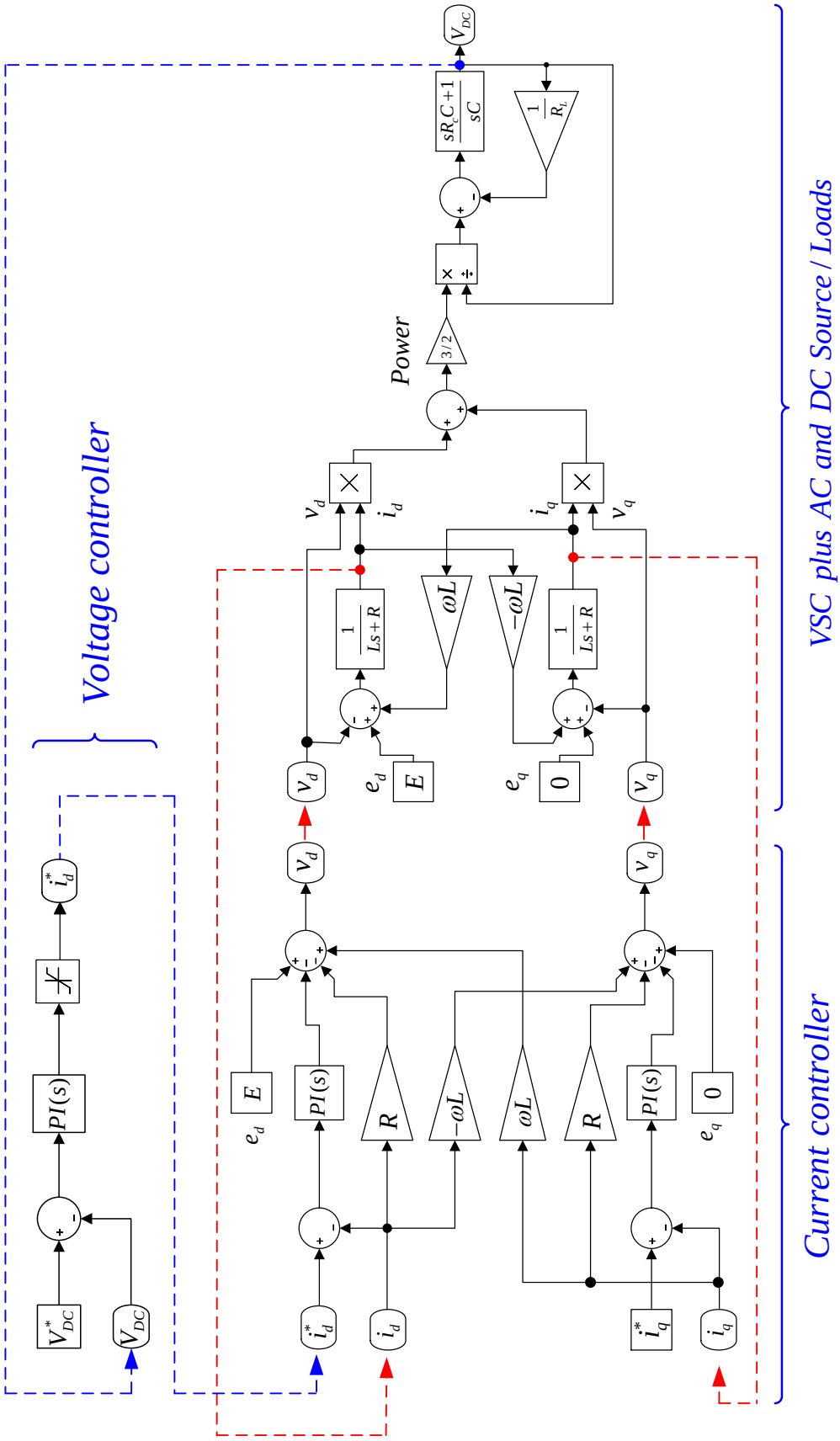

Figure 3.37 - Laplace VSC electrical model with a load resistance R_L in the DC side plus voltage and current controllers

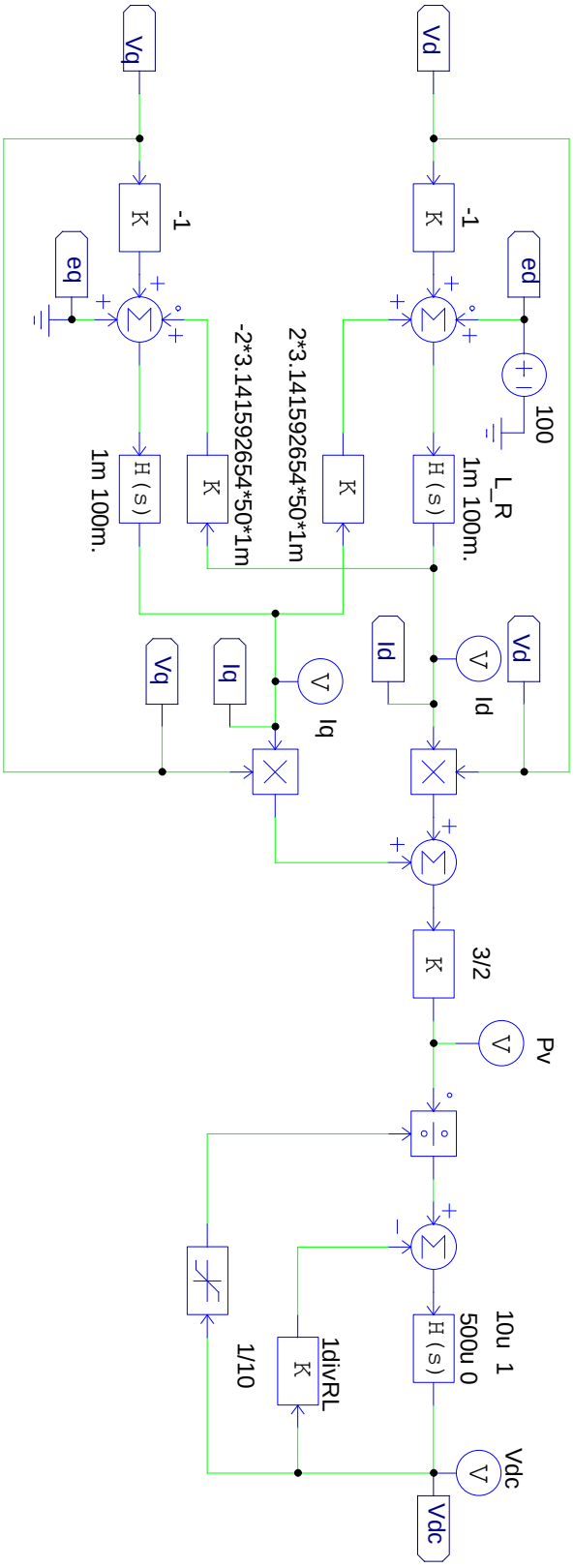

Figure 3.38 - Laplace VSC electrical model with a load resistance of 10 Ω in the DC side, in PSIM

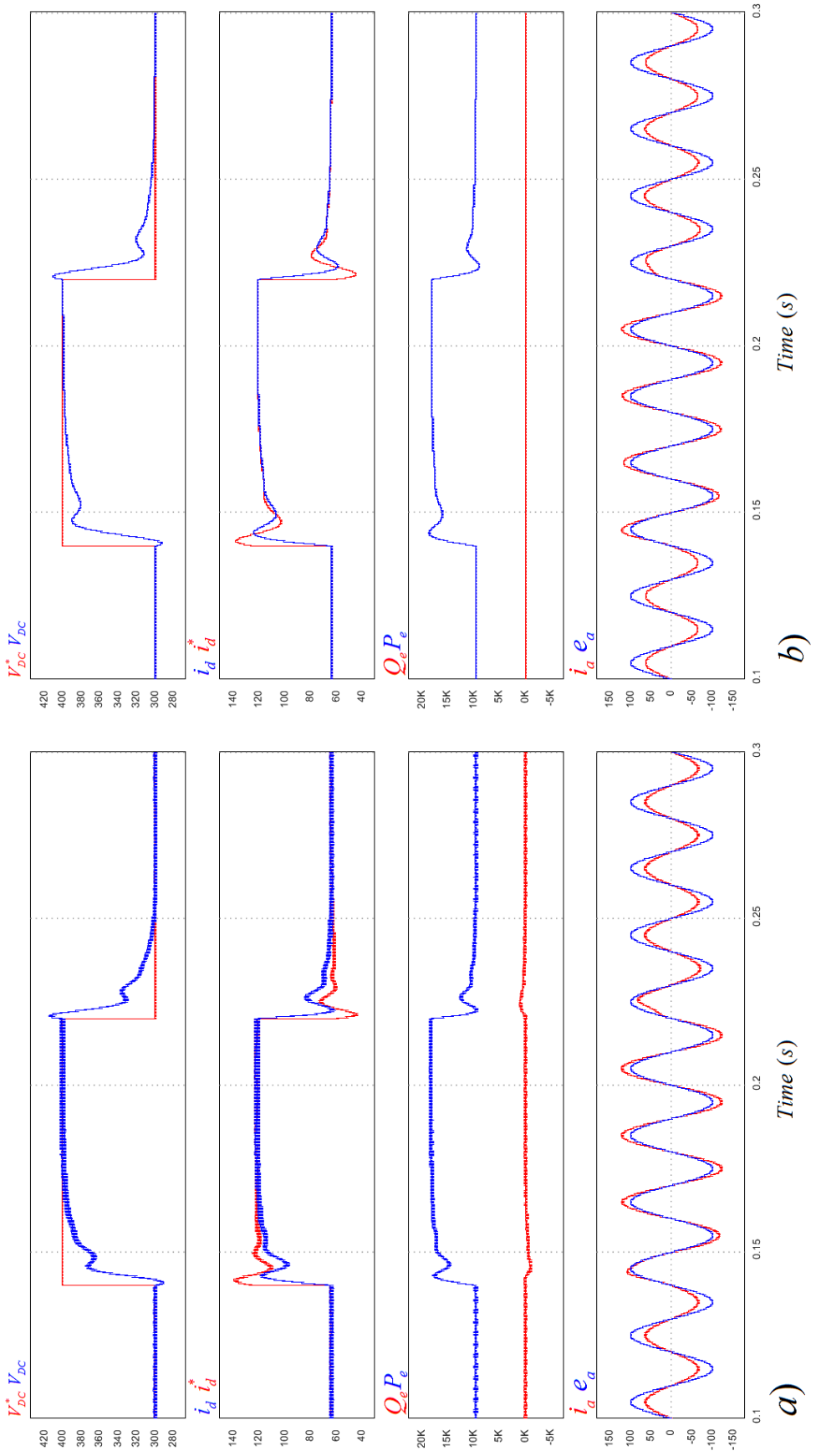

Figure 3.39 - Voltage controller simulation waveforms when changing the reference voltage V_{DC}^{*}

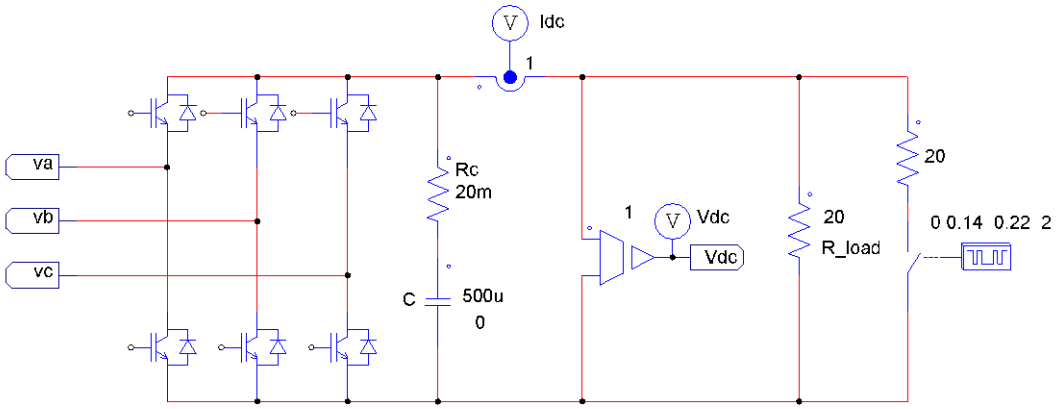

Figure 3.40 - VSC electrical model with a load resistance steep change, in PSIM

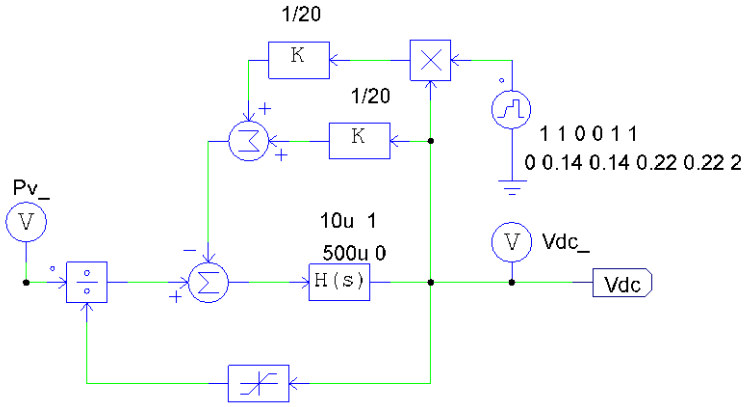

Figure 3.41 - VSC Laplace model with a load resistance steep change, in PSIM

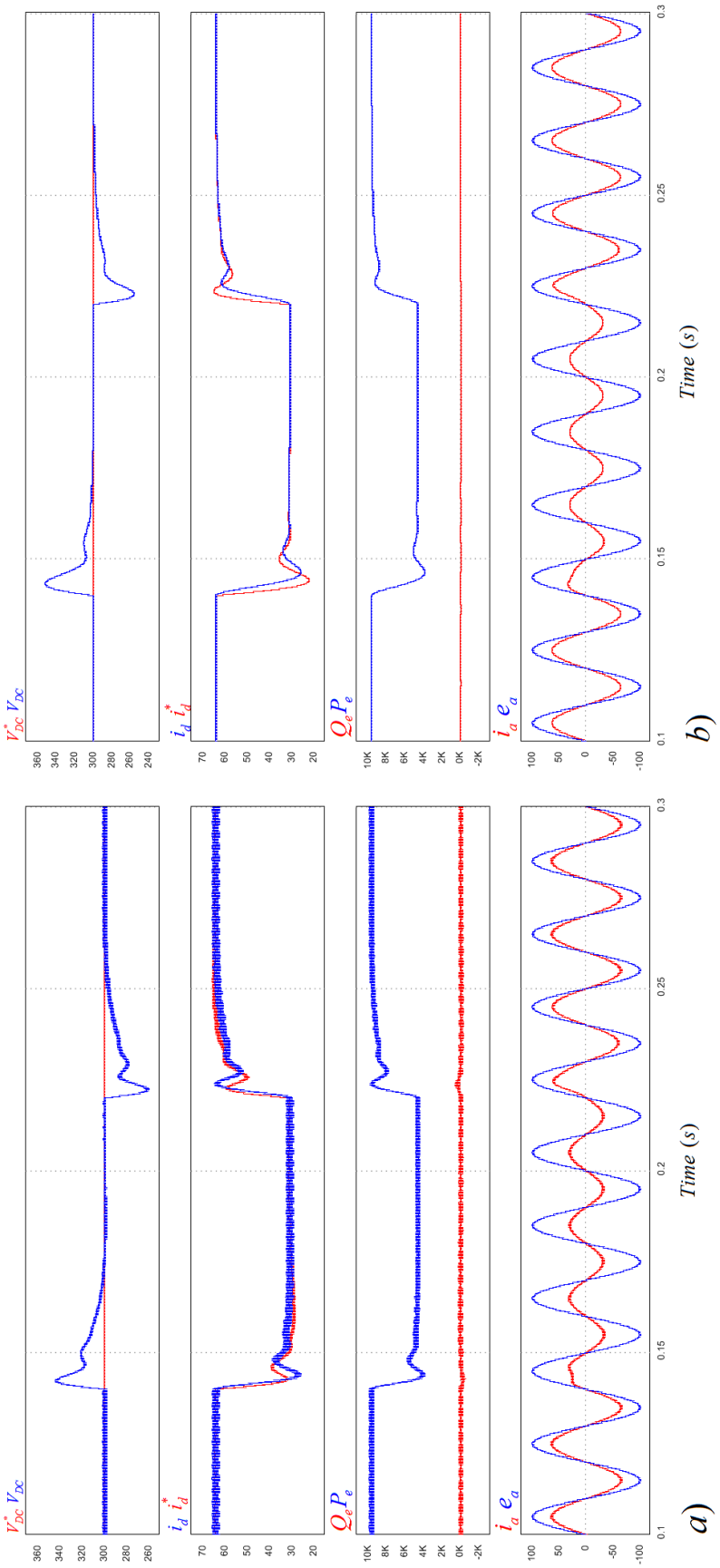

Figure 3.42 - Voltage controller simulation waveforms at a power step change maintaining V_{DC} constant

3.4 Conclusions

In this chapter are presented new three-phase VSC Laplace models in the dq frame. These models exclude the converter's carrier frequency signal but include real parameters associated to the line inductors and to the DC filter capacitor as they perform an important role on the system's dynamic and stability.

One of the main issues in designing vector controllers for power converter interconnection with the grid is the internal cross-coupling between d and q quantities that result from dq transformation. The Laplace model highlights VSC's internal cross-coupling.

An integrated decoupled current controller is designed. Analysis of both electrical and new Laplace models shows they have the same dynamic behavior apart from the switching frequency that is present in the electric model.

From the results it can be concluded that the model presents a good performance, thus proving the technical assumption of using Laplace modeling techniques to solve this issue.

3.5 References

[1] M. Malinowski, M. Jasinski, and M. P. Kazmierkowski, "Simple direct power control of three-phase PWM rectifier using space-vector modulation (DPC-SVM)," *Industrial Electronics, IEEE Transactions on,* vol. 51, pp. 447-454, 2004.

[2] Y. O. Jiang-Häfner, Rolf "HVDC with Voltage Source Converters – A Desirable Solution for Connecting Renewable Energies," presented at the Large-scale integration o wind power in power systems, Breman, Germany 2009, 2009.

[3] E. H. Koldby, Mats "Challenges on the Road to an Offshore HVDC Grid," presented at the Nordic Wind Power Conference 2009, Denmark, 2009.

[4] J. R. Rodriguez, J. W. Dixon, J. R. Espinoza, J. Pontt, and P. Lezana, "PWM regenerative rectifiers: state of the art," *Industrial Electronics, IEEE Transactions on,* vol. 52, pp. 5-22, 2005.

[5] B. Wilamowski and J. Irvin, *The Industrial Electronics Hanbook - Power Electronics Handbook*, Bogdan M. Wilamowski; J. David Irvin ed. vol. 2: CRC Press, 2011.

[6] M. Kazmierkowski, R.Krishnan, and F. Blaabjerg. (2002). *Control in Power Electronics - Selected Problems*.

[7] K. Bong-Hwan, Y. Jang-Hyoun, and L. Jee-Woo, "A line-voltage-sensorless synchronous rectifier," *IEEE Transactions on Power Electronics,* vol. 14, pp. 966-972, 1999.

[8] N. R. Zargari and G. Joos, "Performance investigation of a current-controlled voltage-regulated PWM rectifier in rotating and stationary frames," *Industrial Electronics, IEEE Transactions on,* vol. 42, pp. 396-401, 1995.

[9] V. Blasko and V. Kaura, "A new mathematical model and control of a three-phase AC-DC voltage source converter," *Power Electronics, IEEE Transactions on,* vol. 12, pp. 116-123, 1997.

[10] R. S. Pena, R. J. Cardenas, J. C. Clare, and G. M. Asher, "Control strategies for voltage control of a boost type PWM converter," in *Power Electronics Specialists Conference, 2001. PESC. 2001 IEEE 32nd Annual*, 2001, pp. 730-735 vol.2.

[11] W. C. Duesterhoeft, M. W. Schulz, and E. Clarke, "Determination of Instantaneous Currents and Voltages by Means of Alpha, Beta, and Zero Components," *American Institute of Electrical Engineers, Transactions of the,* vol. 70, pp. 1248-1255, 1951.

[12] M. Malinowski, "Sensorless Control Startegies for Three-Phase PWM Rectifiers," Ph. D. Thesis, Faculty of Electrical Engineering, Warsaw University of Technology, 2001.

[13] H. Akagi, Y. Kanazawa, and A. Nabae, "Instantaneous Reactive Power Compensators Comprising Switching Devices without Energy-Storage Components," *Ieee Transactions on Industry Applications,* vol. 20, pp. 625-630, 1984.

[14] M. Malinowski, M. P. Kazmierkowski, and A. M. Trzynadlowski, "A comparative study of control techniques for PWM rectifiers in AC adjustable speed drives," *Power Electronics, IEEE Transactions on,* vol. 18, pp. 1390-1396, 2003.

4
Pulse-width Modulation Techniques for Voltage Source Converters

4.1 Introduction

Figure 4.1 shows a three-phase VSC with the associated AC and DC sources/loads. This generic representation highlights the converter's reversibility. It can work as PWM Inverter or as PWM Boost Rectifier, i.e. the (Active) power can flow in both directions.

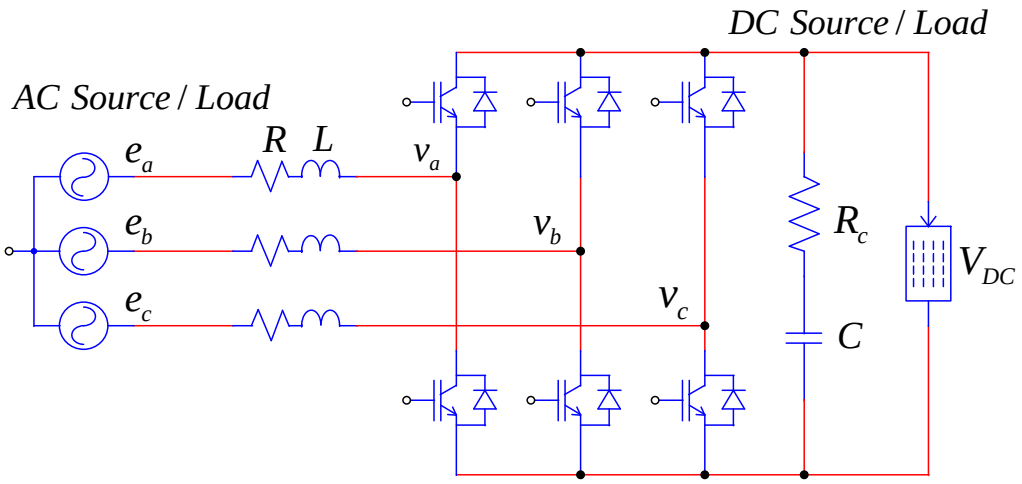

Figure 4.1 - Three-phase PWM Boost Rectifier/Inverter with AC and DC Sources/Loads

The goal of the VSC's control is to build v_a, v_b and v_c voltages up, which interacting with e_a, e_b and e_c voltages define the active power flow that crosses the converter from the AC to the DC side, or vice-versa, and the reactive power that flows (only) between the AC Source/Load and the converter's AC side.

The current controller is responsible for generating the signals that, after amplification inside the VSC by proper switching operation, produce v_a, v_b and v_c voltages. The switching modus operandi requires the adoption of a modulation technique [1, 2].

The most widely used, among others, are the Sinusoidal PWM (SPWM) and the Space Vector PWM (SVM). SPWM is popular because it is easy to implement. On the

other hand, SVM, a computation intensive technique, can deliver better results, namely:

- to provide a wider linear modulation range (15% higher than SPWM);
- to produce lower base-band harmonics than other regular PWM techniques[3];
- to prevent unnecessary switching hence less commutation losses.

In this chapter both SPWM and SVM modulation techniques are reviewed and compared. Two different SVM implementations addressed to PSIM are designed and compared.

4.2 Carrier Frequency and Harmonics

Ideally the v_a, v_b and v_c voltages should be sinusoidal waves but due to the VSC's operation principle, based on switching operation at high frequencies, the resultant v voltages exhibit complex waveforms instead. In addition to the fundamental (desired) frequency ω, those voltages have frequency-related harmonics with modulation-frequency sidebands in the form of

$$A\omega_c \pm B\omega \tag{4.1}$$

where ω_c is the modulator or carrier frequency, and A and B are integers as defined in [2] for SPWM. Figure 4.2 shows a summary of those harmonics for a carrier-to-modulation frequency ratio $\omega_c / \omega = 15$.

m	Harmonics
1	15ω
	15ω±2ω
	15ω±4ω
	⋮
2	30ω±ω
	30ω±3ω
	30ω±5ω
	⋮
3	45ω
	45ω±2ω
	45ω±4ω
	⋮
	⋮

Figure 4.2 - Output harmonics for sinusoidal PWM with $\omega_c / \omega = 15$ [2]

Figure 4.2 shows that harmonics exist around and above the carrier frequency ω_c.

Harmonics are undesirable as they originate supplementary losses to the conversion process. They are limited by the line inductors in the AC side and by the

capacitor attached to the DC side terminals. The line inductors act as low-pass filters limiting the amplitude of the line current harmonics while the DC side capacitor, with a low ESR, contributes to limit the harmonics present in the DC line voltage.

To reduce the amplitude of the harmonics and the size of inductances and capacitors, the carrier frequency ω_c must be set as distant as possible from the fundamental frequency ω.

On the other hand, since switches are not ideal, taking some time to turn on and off, switching losses, during the interval when switches' voltage and current are not zero, have to be taken into account. These are proportional to the number of switchings per unit of time and depend also on the particular features of the chosen switch, which can be a fast or slow switch. However, since when power increases switching speed decreases, the maximum carrier frequency ends up limited and determined mainly by the available power electronic switches and their associated costs.

Therefore, it is necessary to establish a compromise between carrier frequency and acceptable losses.

4.3 Modulation Indexes

4.3.1 The M Index

The equation (4.2) gives the modulation index M as function of v_d, v_q and V_{DC} [4]. M determines the limits allowed for v and V_{DC} relative amplitudes.

$$M = \frac{\pi}{2}\frac{v}{V_{DC}} = \frac{\pi}{2}\frac{\sqrt{v_d^2 + v_q^2}}{V_{DC}} \tag{4.2}$$

Theoretically M can take any value between 0 and 1. Values of M near 0 mean that v and V_{DC} have big relative voltage amplitudes, while when M is 1 the VSC is operated in six-step mode [5], resulting in square-wave v voltages.

In practice, M maximum values are limited by the modulation technique adopted taking into account that the harmonics should be around and above the carrier frequency, i.e. the VSC should operate in the linear zone.

The equation (4.3) shows the maximum M index value for SPWM in linear operation, while (4.4) shows the same limit for SVM [6]. Above $M_{\max}$ the converter operates in overmodulation (or saturation). In general, the overmodulation operation is not desirable mainly because of two factors:

- changes in v almost do not produce changes in V_{DC} and vice-versa;
- it generates undesirable low frequency current harmonics in the AC line.

$$M_{\max} = \frac{\pi}{4} = 0.7854 \tag{4.3}$$

$$M_{\max} = \frac{\pi}{2\sqrt{3}} = 0.9069 \tag{4.4}$$

From equation (4.2) it is clear that V_{DC} is always higher than the v voltage peak. As an example, for SVM and linear operation ($M \leq 0.9069$), $V_{DC} \geq \sqrt{3} v_{peak}$ or $V_{DC} \geq \sqrt{\frac{3}{2}} v_{rms}$, where v_{rms} is the single-phase RMS voltage at the VSC terminal. This means that the VSC only works as a Boost rectifier or as Buck inverter.

4.3.2 The *m* Index

The m index is another common definition for the modulation index [4] usually associated to the SPWM technique. It results from the quotient between the controller output $v_{control}$ and $v_{carrier}$ amplitudes as represented in (4.4). $v_{carrier}$ is usually a high-frequency (e.g. 20kHz), triangular wave. The intersection points between the two waveforms define the switching points used to control the power switches. m limits vary between 0 and 1. When $v_{control}$ equals $v_{carrier}$, $m = 1$, defining the upper limit of the linear zone. Above that is the overmodulation zone.

$$m = \frac{v_{control}}{v_{carrier}} \tag{4.4}$$

Note that when the (4.4) m index definition is applied to other modulation techniques besides SPWM, $v_{control}$ refers to the fundamental frequency of the used modulator waveform.

The relation between the converter voltage peak v and V_{DC} in the linear zone is expressed by equation (4.4).

$$m = 2\frac{v}{V_{DC}} = 2\frac{\sqrt{v_d^2 + v_q^2}}{V_{DC}} \tag{4.4}$$

The relationship between M and m modulation indexes is obtained from equations (4.2) and (4.4)

$$M = \frac{\pi}{4} m = 0.785m \tag{4.4}$$

For SVM the upper limit of m, i.e. the upper limit for the linear zone is $m_{\max} = 1.1547$. Thus, SVM improves the modulation index in the linear zone by about 15% comparatively to SPWM [4].

4.4 Fourier Analysis of Modulation Waveforms

Figure 4.3a) represents the carrier triangular waveform $v_{carrier}$ and the sinusoidal modulator waveform $v_{control}$ used in SPWM, while Figure 4.3b) represents the corresponding waveforms for SVM. In both cases the carrier has a frequency of 500Hz and the modulator 50Hz.

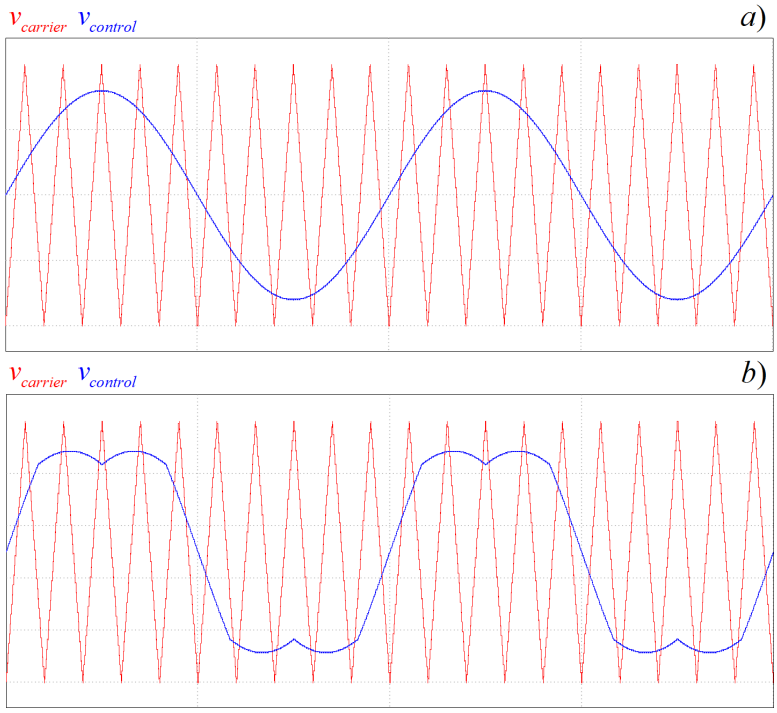

Figure 4.3 - a) Sinusoidal PWM and b) Space Vector PWM modulation techniques

By applying the Fast Fourier Transform (FFT) analysis to the SVM modulating waveform we get the frequency spectrum of Figure 4.4. The harmonics occur at specific frequencies: 150Hz, 450Hz, 750Hz, 1050Hz, 1350Hz, and so on, which corresponds to the odd triple harmonics.

Those triple harmonics have *null sequence* and only appear in the neutral wire of three-phase systems. In balanced three-phase systems, like three-phase motors and generators no neutral wire exists, and thus triple harmonics are not present in such systems. This explains why using this technique results in phase-current waveforms having (only) the fundamental sinusoidal frequency (and, of course the high-frequency harmonics around and above the carrier frequency due to switching). The low-frequency harmonics do not exist when VSCs are operated in the linear zone. (Note: low frequency harmonics may exist but are caused by the dead-time between IGBT outputs; this issue is addressed later is this document).

The sum of those triple harmonics results in a triangular waveform of 150Hz. Indeed, doing an FFT analysis to a triangular wave with such frequency, results in the odd harmonics 3x150=450Hz, 5x150=750Hz, 7x150=1050Hz, 9x150=1350Hz and so on.

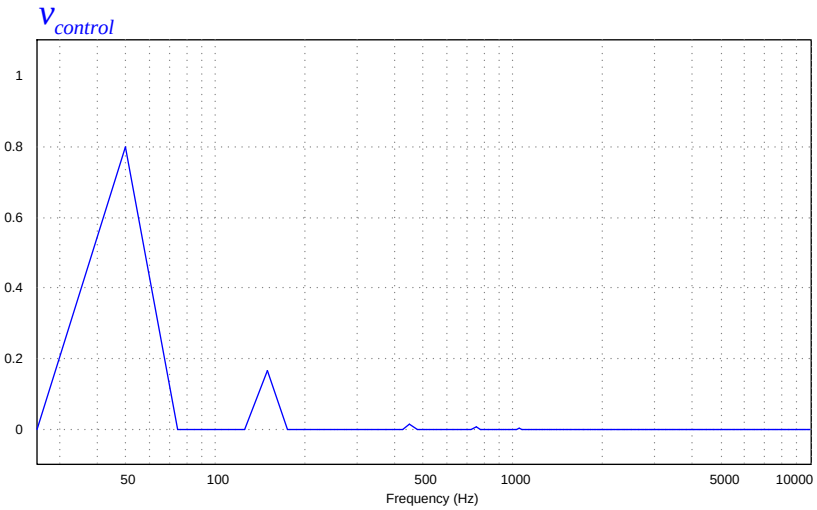

Figure 4.4 - FFT of the SVM waveform

In sum, the SVM modulator waveform results from adding a sinusoidal waveform and an appropriate triangular waveform with three times the frequency of the original sinusoid [1, 7-10] as shown in Figure 4.5.

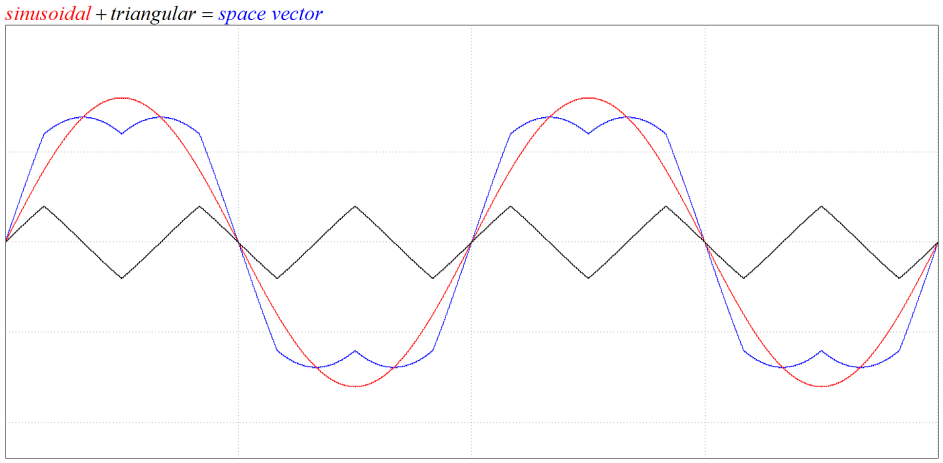

Figure 4.5 – Space vector waveform decomposition

4.5 Space Vector PWM Technique

The Space Vector Modulation technique is based on vector representation of the VSC's AC side voltages.

4.5.1 The Space Vector Voltage

The Space Vector voltage is defined as

$$\vec{V} = V_\alpha + jV_\beta \tag{4.5}$$

where v_α and v_β components are given by Clarke's transform from $v_a; v_b; v_c$ to $v_\alpha; v_\beta$ according to (4.6)

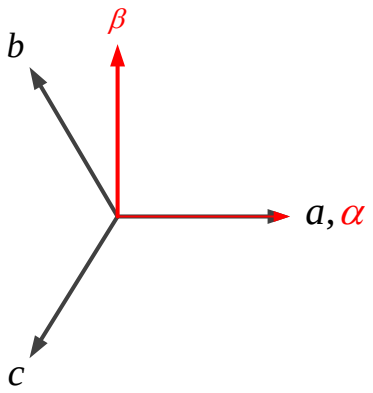

Figure 4.6 - abc and $\alpha\beta$ reference frames

$$\begin{bmatrix} \alpha \\ \beta \end{bmatrix} = \frac{2}{3} \begin{bmatrix} 1 & -\frac{1}{2} & -\frac{1}{2} \\ 0 & \frac{\sqrt{3}}{2} & -\frac{\sqrt{3}}{2} \end{bmatrix} \begin{bmatrix} a \\ b \\ c \end{bmatrix} \tag{4.6}$$

so

$$\begin{cases} v_\alpha = \frac{2}{3}\left(v_a - \frac{1}{2}v_b - \frac{1}{2}v_c \right) \\ v_\beta = \frac{2}{3}\left(+ \frac{\sqrt{3}}{2}v_b - \frac{\sqrt{3}}{2}v_c \right) \end{cases} \tag{4.7}$$

and then

$$\vec{V} = \frac{2}{3}\left(v_a + \left(-\frac{1}{2} + j\frac{\sqrt{3}}{2} \right) v_b + \left(-\frac{1}{2} - j\frac{\sqrt{3}}{2} \right) v_c \right) \tag{4.8}$$

The vector (4.8) can be viewed as:

$$\vec{V} = \frac{2}{3}\left((1)v_a + xv_b + x^2 v_c \right) \tag{4.9}$$

where $x = e^{j\frac{2\pi}{3}}$ and $x^2 = e^{-j\frac{2\pi}{3}}$

The parameters 1, x and x^2 can be interpreted as unity vectors aligned with phases v_a, v_b and v_c respectively, where the $a-axis$ is the reference.

4.5.2 Space Vector Voltages Generation

Let's consider the VSC of Figure 4.7 where Q1 to Q6 are the power switches.

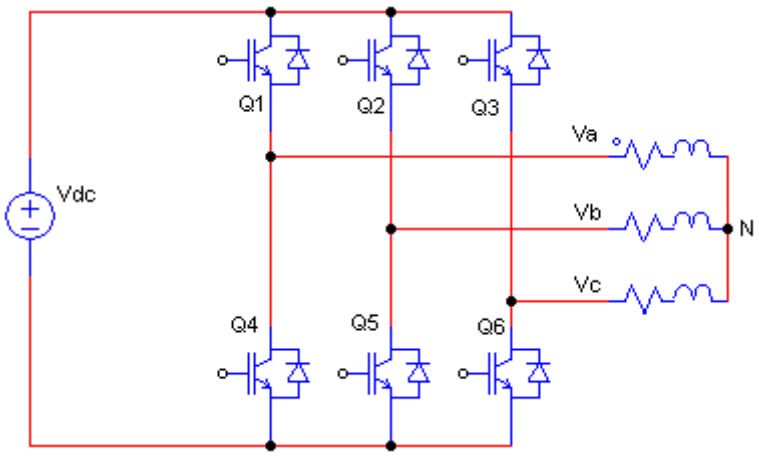

Figure 4.7 - Three-phase VSC

In each VSC's arm only one switch is ON at a time: Q1 or Q4; Q2 or Q5; Q3 or Q6. There are eight possible states, from U0 to U7, according to Figure 4.8 (note that $V_{DC} = U_{DC}$).

There are six (U1 to U6), active states and two (U0 and U7), NULL states. For the NULL states, $v_a = v_b = v_c = 0$, so there is not any coupling between the AC and the DC side.

Notice that even when all switches are OFF, power can flow by the VSC through the diodes.

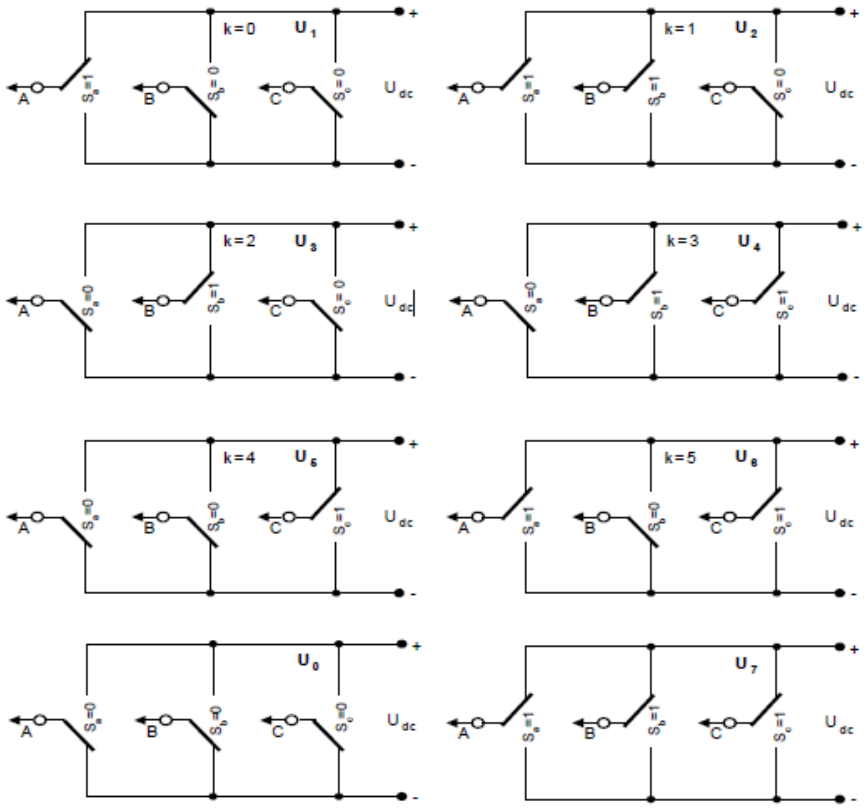

Figure 4.8 - The eight possible switching states

Let's analyze state U1. The equivalent circuit is represented in Figure 4.9.

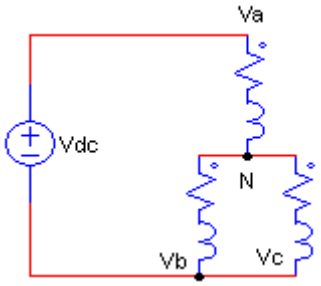

Figure 4.9 - Equivalent circuit for Space Vector state U1

In this case $v_a = \frac{2}{3}V_{DC}$ and $v_b = v_c = -\frac{1}{3}V_{DC}$

Taking into account the switches' state and following the notation displayed in Figure 4.8 where Sx=1 when a upper switch is ON and Sx=0 when a lower switch is ON, the Space Vector state notation for U1 is: $\vec{V}_1(100)$.

In the same way and considering now state U7, represented in Figure 4.10, the voltages are now $v_a = v_b = v_c = 0$, which corresponds to the Space Vector $\vec{V}_7(111)$.

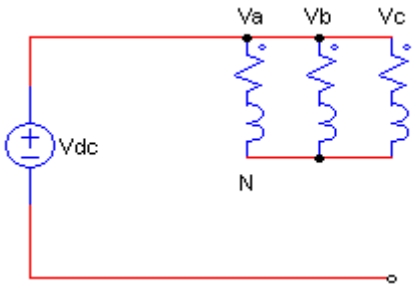

Figure 4.10 - Equivalent circuit for Space Vector state U7

Table 4.1 shows all possible Space Vector voltages.

State	Switches ON	v_a	v_b	v_c	Space Vector voltage
0	Q4 Q5 Q6	0	0	0	$\bar{V}0(000)$
1	Q1 Q5 Q6	2/3Vdc	-1/3Vdc	-1/3Vdc	$\bar{V}1(100)$
2	Q1 Q2 Q6	1/3Vdc	1/3Vdc	-2/3Vdc	$\bar{V}2(110)$
3	Q4 Q2 Q6	-1/3Vdc	2/3Vdc	-1/3Vdc	$\bar{V}3(010)$
4	Q4 Q2 Q3	-2/3Vdc	1/3Vdc	1/3Vdc	$\bar{V}4(011)$
5	Q4 Q5 Q3	-1/3Vdc	-1/3Vdc	2/3Vdc	$\bar{V}5(001)$
6	Q1 Q5 Q3	1/3Vdc	-2/3Vdc	1/3Vdc	$\bar{V}6(101)$
7	Q1 Q2 Q3	0	0	0	$\bar{V}7(111)$

Table 4.1 - Space Vector states

4.5.3 The Spatial V^* Vector

Taking into account equation (4.8) and Table 4.1, it is now possible to obtain the eight Space Vector voltages in the $\alpha\beta$ reference frame.

The NULL Space Vectors are:

$$\vec{V}_0(000) = \vec{V}_7(111) = \frac{2}{3}\left(0 + \left(-\frac{1}{2} + j\frac{\sqrt{3}}{2}\right)0 + \left(-\frac{1}{2} - j\frac{\sqrt{3}}{2}\right)0\right) = 0 + j0 = 0e^{j0}$$

The active Space Vectors are:

$$\vec{V}_1(100) = \frac{2}{3}\left(\frac{2}{3}V_{DC} + \left(-\frac{1}{2} + j\frac{\sqrt{3}}{2}\right)\left(-\frac{1}{3}V_{DC}\right) + \left(-\frac{1}{2} - j\frac{\sqrt{3}}{2}\right)\left(-\frac{1}{3}V_{DC}\right)\right) \Leftrightarrow$$

$$\Leftrightarrow \vec{V}_1(100) = \frac{2}{3}V_{DC} + j0 = \frac{2}{3}V_{DC}e^{j0}$$

and in the same way

$$\vec{V}_2(110) = \frac{1}{3}V_{DC} + j\frac{\sqrt{3}}{3}V_{DC} = \frac{2}{3}V_{DC}e^{j\frac{\pi}{3}}$$

$$\vec{V}_3(010) = -\frac{1}{3}V_{DC} + j\frac{\sqrt{3}}{3}V_{DC} = \frac{2}{3}V_{DC}e^{j\frac{2\pi}{3}}$$

$$\vec{V}_4(011) = -\frac{2}{3}V_{DC} + j0 = \frac{2}{3}V_{DC}e^{j\pi}$$

$$\vec{V}_5(001) = -\frac{1}{3}V_{DC} - j\frac{\sqrt{3}}{3}V_{DC} = \frac{2}{3}V_{DC}e^{j\frac{4\pi}{3}}$$

$$\vec{V}_6(010) = \frac{1}{3}V_{DC} - j\frac{\sqrt{3}}{3}V_{DC} = \frac{2}{3}V_{DC}e^{j\frac{5\pi}{3}}$$

Mathematically the eight Space Vectors can be condensed in the form

$$\vec{V}(k) = \begin{cases} \frac{2}{3}V_{DC}e^{j\frac{\pi}{3}(k-1)}, & 1 \le k \le 6 \\ 0, & k = 0,7 \end{cases} \tag{4.10}$$

The eight vectors are spatially represented in Figure 4.11

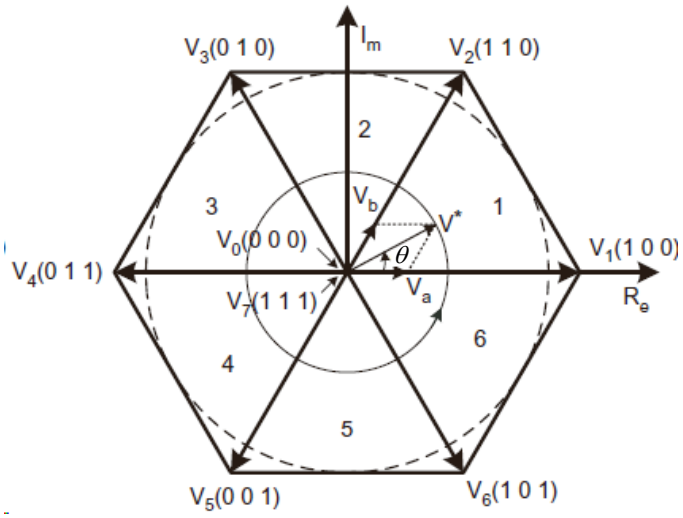

Figure 4.11 - Spatial representation of the eight vectors

The active vectors, $\vec{V}_1$ to $\vec{V}_6$ divide the plane in six sectors, $n = 1...6$, of 60^o each.

$$n \begin{cases} 1, & 0^o < \theta \le 60^o \\ 2, & 60^o < \theta \le 120^o \\ \dots & \dots \\ 6, & 300^o < \theta \le 360^o \end{cases} \tag{4.11}$$

The question now is how to obtain any $\vec{V}^*$ vector (see Figure 4.11) in the plan in addition to the eight already defined. This is done by switching alternately between

two adjacent vectors at the appropriate time. As $\vec{V}^*$ is placed in sector $n=1$ in the plan, the vectors $\vec{V}_a$ and $\vec{V}_b$ are components of $\vec{V}^*$ aligned with $\vec{V}_1$ and $\vec{V}_2$ respectively.

Vector $\vec{V}^*$ is used to compute which switches are ON and OFF at a given instant allowing to define later the voltage in each phase.

Considering that T_c is the time period in which the switchings should generate $\vec{V}^*$ expression (4.12) is deduced:

$$\vec{V}^* = \vec{V}_a + \vec{V}_b = \vec{V}_1 \frac{t_a}{T_c} + \vec{V}_2 \frac{t_b}{T_c} + \left(\vec{V}_0 \, or \, \vec{V}_7\right) \frac{t_0}{T_c} \tag{4.12}$$

where $t_a = \frac{\left|\vec{V}_a\right|}{\left|\vec{V}_1\right|} T_c$, $t_b = \frac{\left|\vec{V}_b\right|}{\left|\vec{V}_2\right|} T_c$ and $t_0 = T_c - \left(t_a + t_b\right)$

The time intervals t_a and t_b allow to obtain $\vec{V}^*$. The time interval t_0 fills the remaining time until T_c. Notice that $t_a + t_b + t_0 = T_c$. t_0 is filled with the null vectors $\vec{V}_0$ or $\vec{V}_7$.

Increasing or decreasing $\vec{V}^*$ implies to increase or decrease $\vec{V}_a$ and $\vec{V}_b$. Since $\vec{V}_1$, $\vec{V}_2$ and T_c are constants, this means to increase t_a and t_b adjusting later t_0 accordingly.

For a $\vec{V}^*$ with small amplitude the corresponding t_a and t_b are small when compared to t_0. For increasing amplitudes of $\vec{V}^*$, t_a and t_b may increase until $t_a + t_b = T_c$ and in this case, $t_0 = 0$. This amplitude corresponds to the maximum circle inside the Figure 4.11 hexagon, which defines the border of the so called linear working zone.

Figure 4.12 shows a symmetrical impulse pattern for two consecutive T_c periods.

Let's define $T_s = 2T_c = 1/f_s$ as the sampling period where f_s is the switching frequency.

Notice that in Figure 4.12, t_0 is added and equally distributed by $\vec{V}_0$ to $\vec{V}_7$ in order to create a symmetric pattern. Studies [1, 2] prove that by using a symmetric pattern the number of switchings is reduced, producing fewer harmonics.

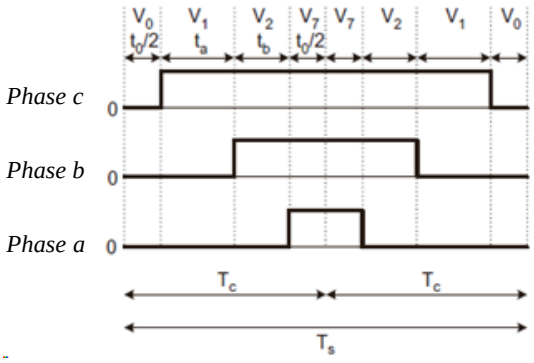

Figure 4.12 - Impulse pattern to apply to the switches for sector n=1

Based on Figure 4.12 the following correlation between ON and OFF times for each switch A, B and C (see Figure 4.8), is obtained.

$$\begin{aligned} T_{A_{ON}} &= \frac{t_0}{2} & T_{A_{OFF}} &= \frac{t_0}{2} + t_a + t_b \\ T_{B_{ON}} &= \frac{t_0}{2} + t_a & T_{B_{OFF}} &= \frac{t_0}{2} + t_b \\ T_{C_{ON}} &= \frac{t_0}{2} + t_a + t_b & T_{C_{OFF}} &= \frac{t_0}{2} \end{aligned} \tag{4.13}$$

These times are only valid for sector n=1 which is the one considered in this analysis.

In matrix form

$$\begin{bmatrix} T_{A_{ON}} \\ T_{B_{ON}} \\ T_{C_{ON}} \end{bmatrix} = \begin{bmatrix} 1 & 0 & 0 \\ 1 & 1 & 0 \\ 1 & 1 & 1 \end{bmatrix} \begin{bmatrix} t_0/2 \\ t_a \\ t_b \end{bmatrix} \tag{4.14}$$

By doing the same analysis for the remaining sectors, the matrix $A(n)$ is build.

$$A(n) = \overset{\text{sector } n}{\overset{1}{\begin{bmatrix} 1 & 0 & 0 \\ 1 & 1 & 0 \\ 1 & 1 & 1 \end{bmatrix}} \overset{2}{\begin{bmatrix} 1 & 0 & 1 \\ 1 & 0 & 0 \\ 1 & 1 & 1 \end{bmatrix}} \overset{3}{\begin{bmatrix} 1 & 1 & 1 \\ 1 & 0 & 0 \\ 1 & 1 & 0 \end{bmatrix}} \overset{4}{\begin{bmatrix} 1 & 1 & 1 \\ 1 & 0 & 1 \\ 1 & 0 & 0 \end{bmatrix}} \overset{5}{\begin{bmatrix} 1 & 1 & 0 \\ 1 & 1 & 1 \\ 1 & 0 & 0 \end{bmatrix}} \overset{6}{\begin{bmatrix} 1 & 0 & 0 \\ 1 & 1 & 1 \\ 1 & 0 & 1 \end{bmatrix}}} \tag{4.15}$$

4.5.4 Modulation Index *M* and Space Vector Pulse Width Modulation

Modulation index M is defined as the quotient between the vector $\vec{V}^*$ peak, i.e. $\hat{V}^*$, and the fundamental harmonic of a square wave with null average voltage, representative of the phase, i.e. $\hat{V}_{1st\_h}$.

$$M = \frac{\hat{V}^*}{\hat{V}_{1st\_h}} \tag{4.16}$$

The fundamental component, $\hat{V}_{1st\_h} = \frac{2}{\pi} V_{DC}$, is obtained using the Fourier analysis to decompose the square waveform. Thus

$$M = \frac{\hat{V}^*}{\frac{2}{\pi} V_{DC}} \tag{4.17}$$

As seen in (4.10) the peak value of any vector from $\vec{V}_1$ to $\vec{V}_6$ is $\frac{2}{3} V_{DC}$.

Observing now Figure 4.11, the maximum value that $\vec{V}^*$ can assume is

$$\hat{V}^* = \frac{2}{3} V_{DC} \cos\frac{\pi}{6} = \frac{2}{3} V_{DC} \frac{\sqrt{3}}{2} = \frac{1}{\sqrt{3}} V_{DC} = 0.577 V_{DC} \tag{4.18}$$

So the maximum value that Space Vector modulation can assume in the linear zone is

$$M = \frac{\frac{1}{\sqrt{3}} V_{DC}}{\frac{2}{\pi} V_{DC}} = \frac{\pi}{2\sqrt{3}} = 0.9069 \tag{4.19}$$

This means that 90.7% of the fundamental square wave harmonic is achieved in the linear zone.

The normalized Space Vector is now defined as

$$\vec{V}_n(k) = \begin{cases} \frac{\pi}{2\sqrt{3}} e^{j\frac{\pi}{3}(k-1)}, & 1 \le k \le 6 \\ 0, & k = 0, 7 \end{cases} \tag{4.20}$$

The overmodulation working zone occurs when $0.9069 < M \le 1$ which corresponds to Spatial Vectors $\vec{V}^*$ whose amplitude is located outside of the circle comprised inside the hexagon of Figure 4.11.

4.5.5 SVM Implementation in PSIM

To allow the comparison of Sinusoidal and Space Vector PWM techniques, the PSIM block SVM (M,a) RMB is used. This block allows the simulation of power converters using the Space Vector (Symmetric) PWM technique or SVM.

The block has two inputs: the modulation index M (the normalized amplitude of the Space Vector $\vec{V}^*$); and its angle θ, as represented in Figure 4.11. The PSIM block was designed to work in the linear zone only so M can only assume values between $0 \leq M \leq 0.9096$.

The three outputs are typical Space Vector PWM modulated waveforms, 120° out--of-phase.

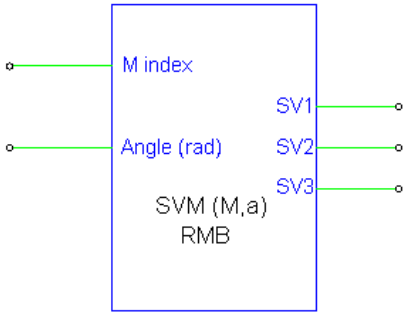

Figure 4.13 - SVM Block designed to PSIM

Figure 4.14 shows a three-phase VSC inverter PSIM circuit, with open-loop control, where the SVM block is applied.

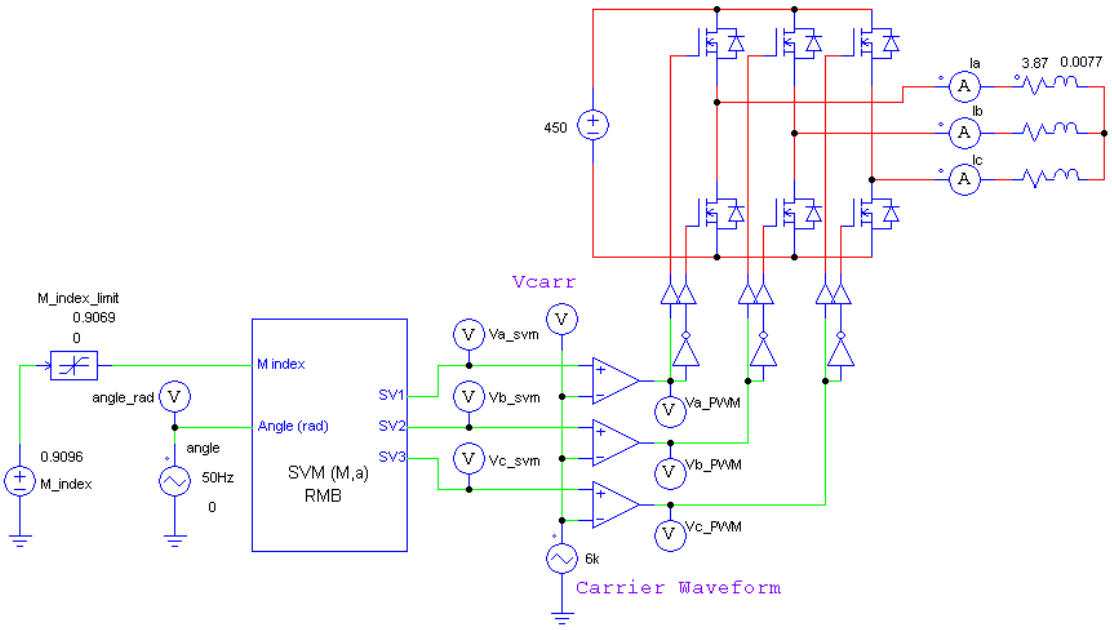

Figure 4.14 – Space Vector PWM block example with open-loop, three-phase inverter

Figure 4.15 shows the Space Vector waveforms for phase-a and phase-b, with $M = 0.9096$. The "angle_rad" is a sawtooth waveform with a peak value of 2π,

applied to the "Angle" SVM block input. The 6kHz carrier, not represented, is a triangular waveform with 2V peak-to-peak and i_a, i_b, i_c are the resulting line currents.

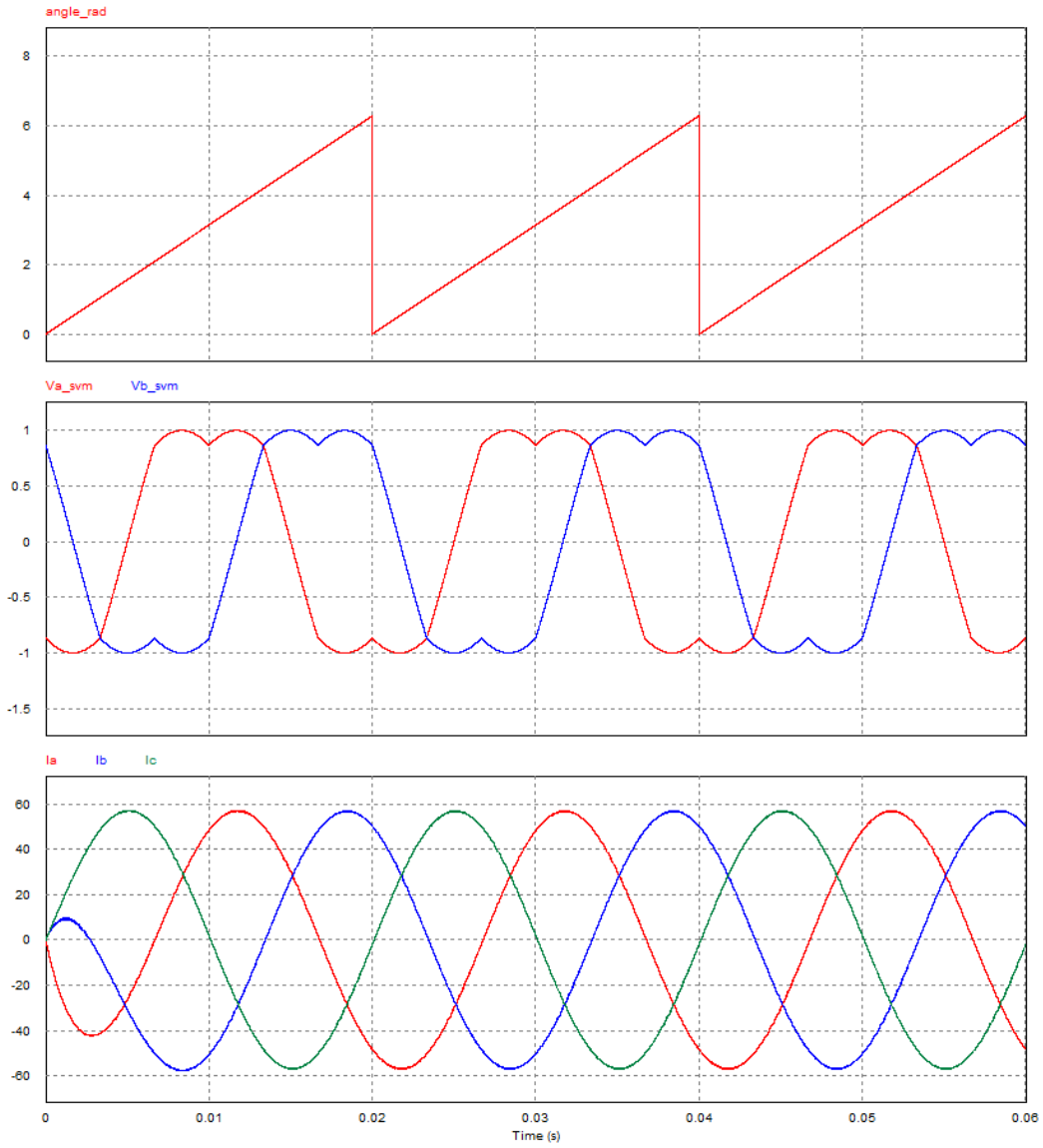

Figure 4.15 – Waveform results for the Space Vector PWM block with open-loop, three-phase inverter and M=0.9096

4.5.5.1 Detailed Description of the SVM (M, a) RMB PSIM Block

In order to implement Space Vector theory described in [3, 4, 11, 12], only equations valid for θ angles located in sector n=1 are considered. For θ angles located in other sectors, a translation to sector n=1 is previously computed before the application of those equations.

As seen before, the different sectors are delimited according to (4.11). The θ angle translated to sector n=1, i.e. θ_{1s} is given by

$$\theta_{1s} = \theta - (n-1)60^o \tag{4.21}$$

With the voltage vector in the first sector, times t_a, t_b and t_0 are calculated according to the following equations

$$\begin{gathered} K = M\,\frac{2\sqrt{3}}{\pi}T_s \\ t_a = K\sin(60^o - \theta_{1s}) \quad t_b = K\sin(\theta_{1s}) \quad t_0 = (T_s - t_a - t_b) \end{gathered} \tag{4.22}$$

These time calculations are implemented in PSIM as represented in Figure 4.16.

According to matrix $A(n)$ (4.15), different time calculations are computed according to the sector under study. To help performing those calculations, it is considered the binary variables R_1 to R_6. Taking into account that in all matrices the first column is all 1s, only the two remaining columns are considered, as represented in (4.23).

$$\begin{bmatrix} R_1 & R_2 \\ R_3 & R_4 \\ R_5 & R_6 \end{bmatrix} = f\left(n_{BIN}\right) = \overset{\text{Sector } n_{BIN}=A_2A_1A_0}{\overset{001}{\begin{bmatrix} 0 & 0 \\ 1 & 0 \\ 1 & 1 \end{bmatrix}} \overset{010}{\begin{bmatrix} 0 & 1 \\ 0 & 0 \\ 1 & 1 \end{bmatrix}} \overset{011}{\begin{bmatrix} 1 & 1 \\ 0 & 0 \\ 1 & 0 \end{bmatrix}} \overset{100}{\begin{bmatrix} 1 & 1 \\ 0 & 1 \\ 0 & 0 \end{bmatrix}} \overset{101}{\begin{bmatrix} 1 & 0 \\ 1 & 1 \\ 0 & 0 \end{bmatrix}} \overset{110}{\begin{bmatrix} 0 & 0 \\ 1 & 1 \\ 0 & 1 \end{bmatrix}}} \tag{4.23}$$

The binary simplified expression for each R_x output is obtained using Karnaugh maps, where the sector number in binary $n_{BIN} = A_2A_1A_0$ are the inputs. For example, for R_1 and R_2 the resulting simplified Boolean expressions are:

$$\begin{aligned} R_1 &= A_2\overline{A}_1 + A_1A_0 \\ R_2 &= \overline{A}_2A_1 + \overline{A}_1\overline{A}_0 \end{aligned} \tag{4.24}$$

Figure 4.17 shows a PSIM implementation of a decimal-to-binary converter and Figure 4.18 shows the PSIM implementation of normalized Space Vector modulators having a maximum of 2V peak-to-peak and with $M = 0.9096$.

Figure 4.19 shows the sector number as computed by the PSIM block and the Space Vector resulting waveforms, again with $M = 0.9096$.

Figure 4.20 shows a detail of the Space Vector PWM signals related to Sector n=1 which are similar to the ones of Figure 4.12.

The whole implementation of Space Vector theory uses simple PSIM discrete parts only to allow a better evaluation of the SVM block.

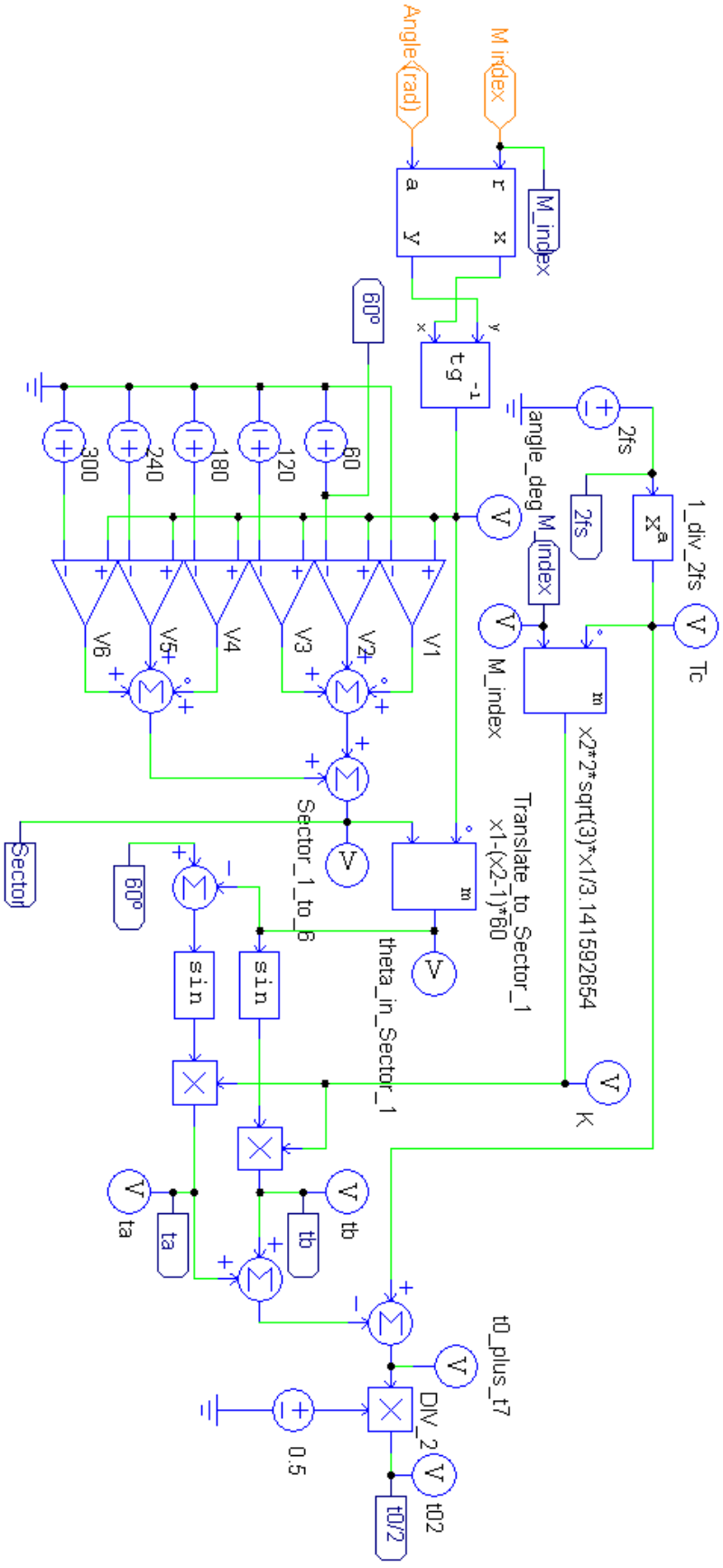

Figure 4.16 - Space Vector PWM implementation in PSIM – part 1

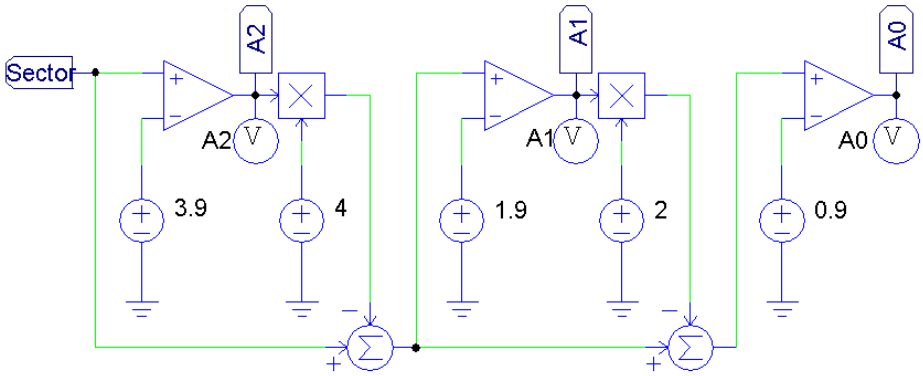

Figure 4.17 - Space Vector PWM implementation in PSIM – part 2

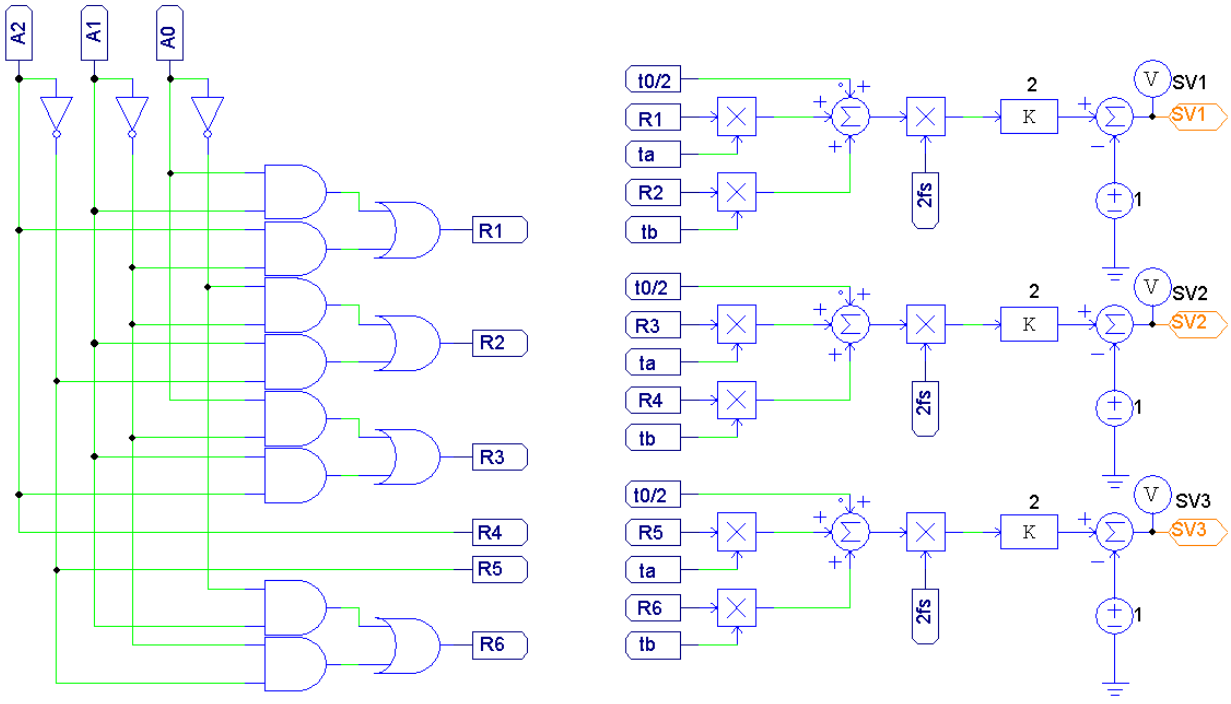

Figure 4.18 - Space Vector PWM implementation in PSIM – part 3

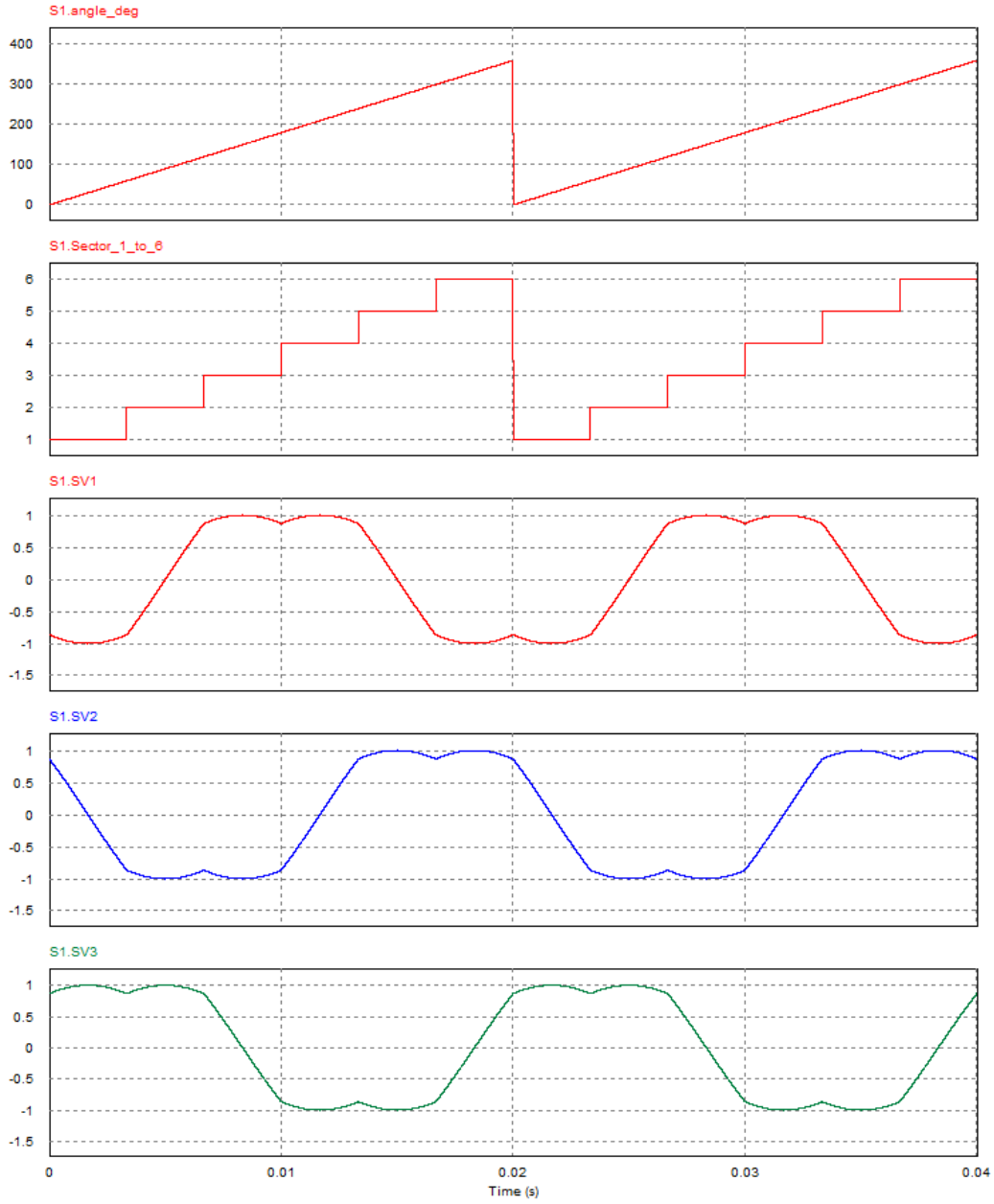

Figure 4.19 - PSIM Space Vector block internal waveforms for *M*=0.9096

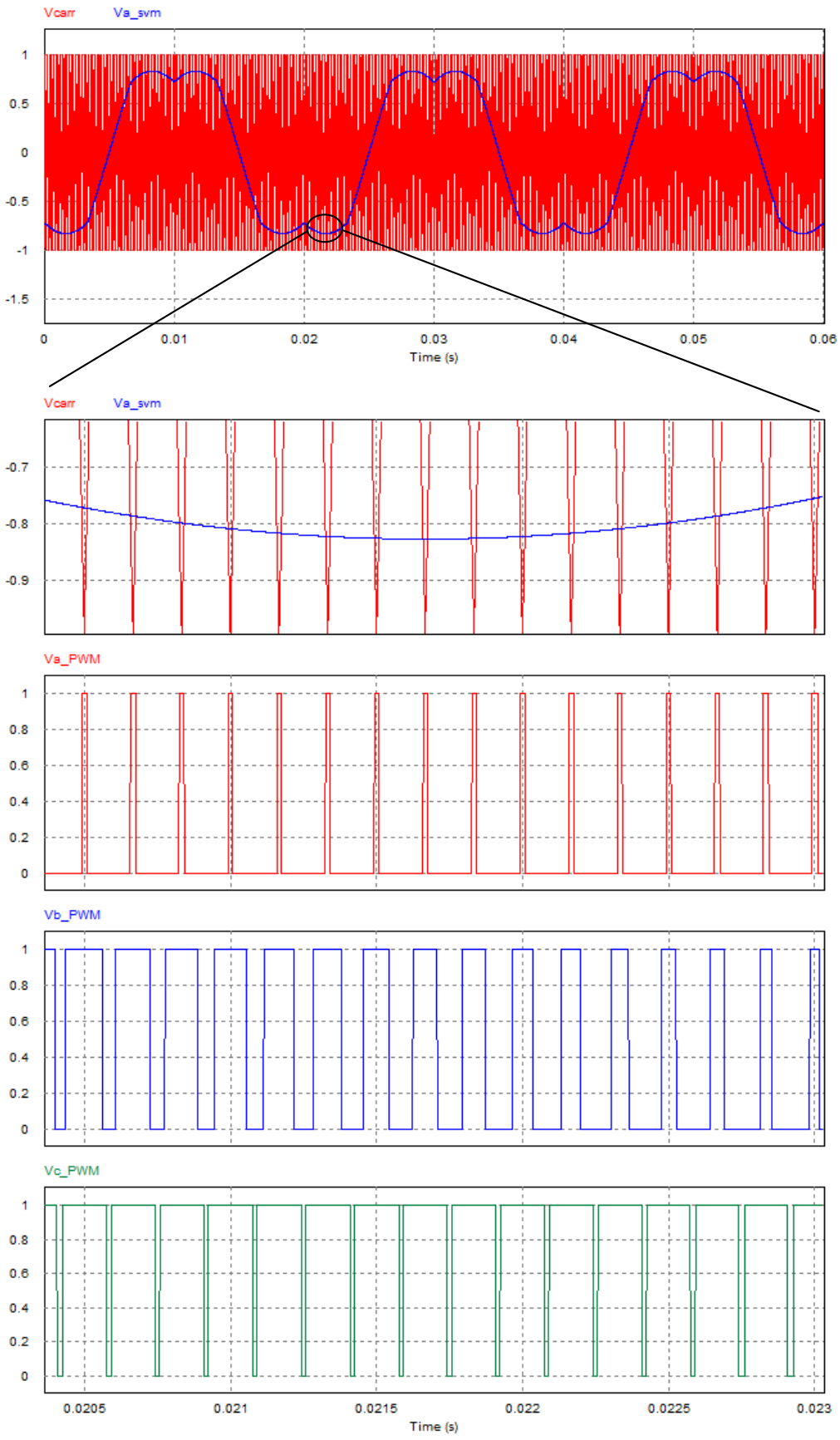

Figure 4.20 - Detail view of Sector 1 PWM waveforms for *M*=0.75

4.5.5.2 SVM (M, a) RMB PSIM Block Application Example

Figure 4.21 shows a three-phase VSC operated as rectifier that uses the SVM (M, a) RMB PSIM block in the control process. The DC load is a 10 Ohm resistance. A specific decoupled current controller (Figure 4.22) is designed taking into account the circuit characteristics. Two i_d reference levels - 64.5A and 122.5A - are applied at specified times resulting in two V_{DC} levels (300V and 400V).

Figure 4.23 shows the VSC dynamics for i_d steep changes, in particular the phase-a Space Vector modulator SV1, the phase-a voltage e_a and current i_a, and the DC voltage V_{DC}.

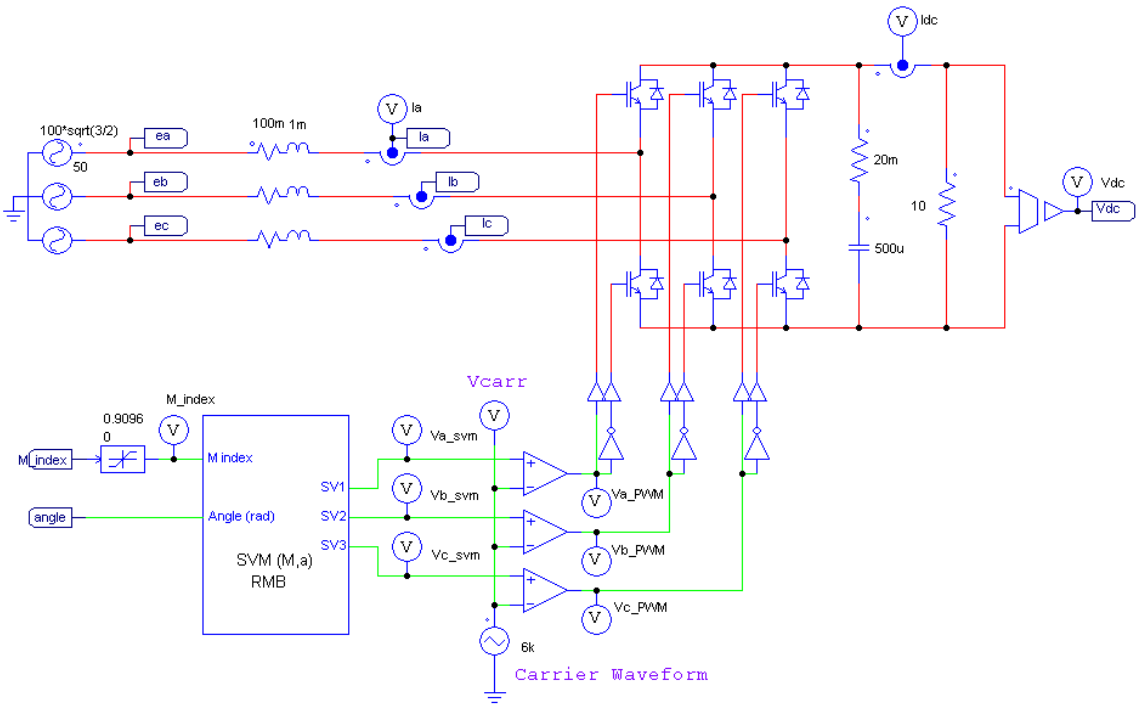

Figure 4.21 – SVM (M,a) RMB block example applied to a three-phase VSC operated as rectifier

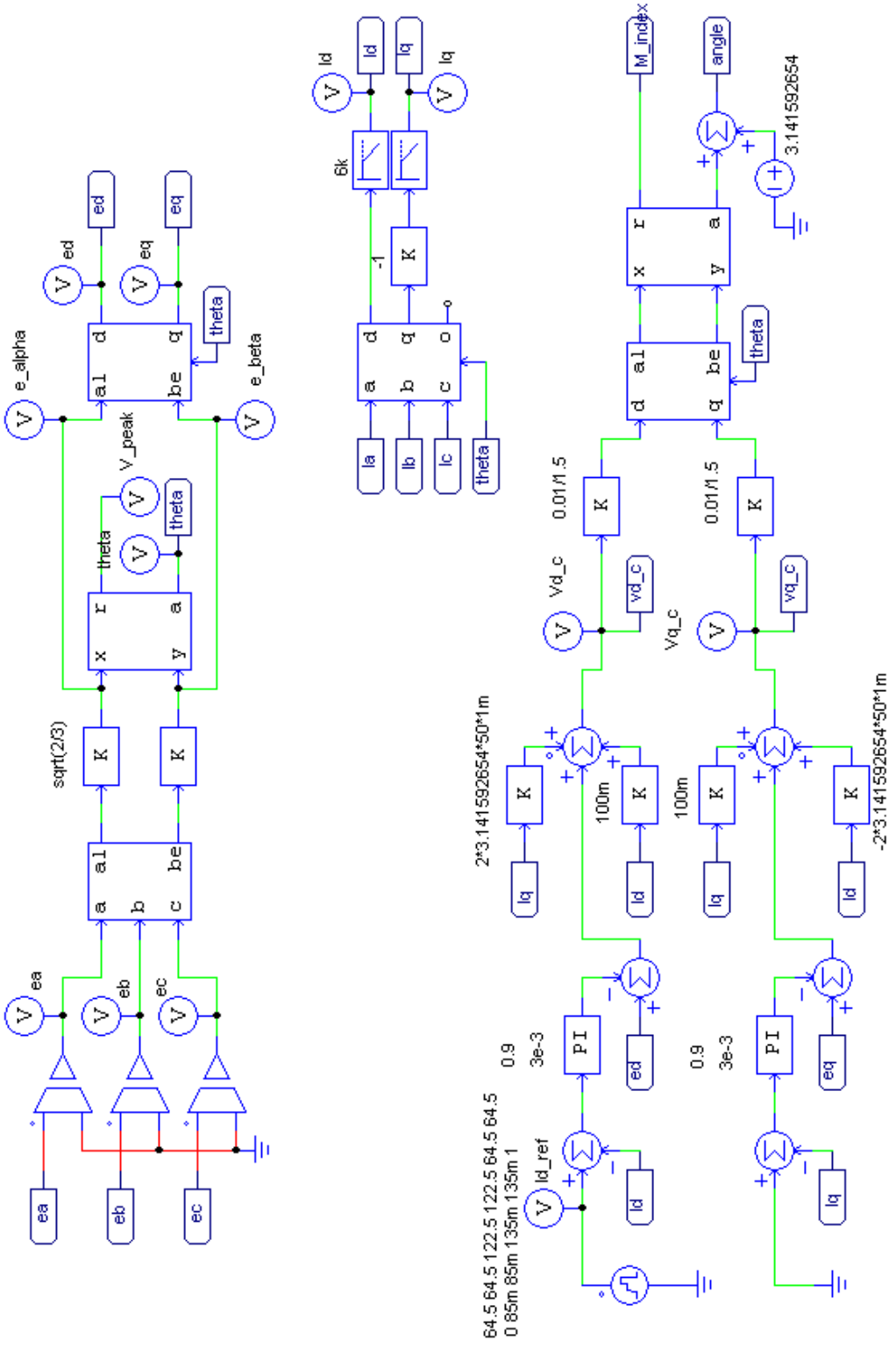

Figure 4.22 - Three-phase VSC decoupled current controller addressed to the PSIM SVM (M,a) RMB Block

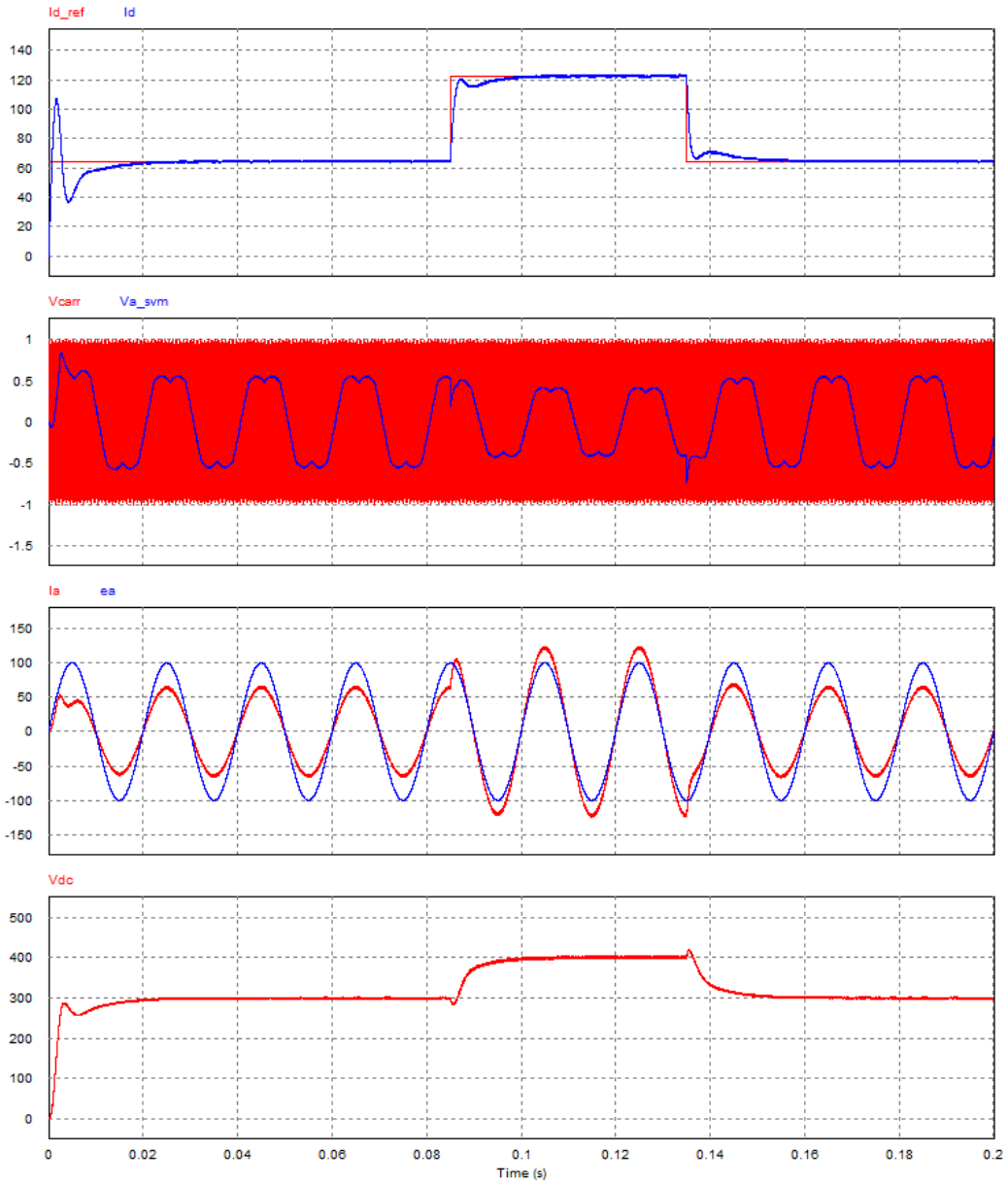

Figure 4.23 – Three-phase VSC operated as rectifier with decoupled current controller + SVM (M,a) RMB block, dynamics

4.6 Third Order odd Harmonic Injection PWM Technique

The third order odd harmonic injection PWM technique, described in the literature as THUPWM [13], consists in adding third order odd harmonics to the original sinusoidal modulators $v_{a\_\sin}, v_{b\_\sin}, v_{c\_\sin}$. The result is a new set of modulators $v_{a\_svm}, v_{b\_svm}, v_{c\_svm}$ with the same shape of the original SVM modulators, i.e. those obtained according to Space Vector theory.

The third order odd harmonics are generated according to (4.24) [13]. The resulting v_{inj} is a triangular waveform.

$$v_{inj} = -\frac{1}{2}\left(\max\left(v_{a\_\sin}, v_{b\_\sin}, v_{c\_\sin}\right) + \min\left(v_{a\_\sin}, v_{b\_\sin}, v_{c\_\sin}\right)\right) \quad (4.24)$$

This modulation technique has the same properties than conventional SVM.

Figure 4.24 shows a three-phase VSC inverter PSIM circuit, with open-loop control, where this modulation technique is applied. The original sinusoidal modulators have 80% of the carrier's amplitude (m index = 0.8).

Figure 4.25 shows the resulting waveforms, starting from the original sinusoidal modulators through the SVM modulators generation process and the line sinusoidal currents.

This technique is very simple to implement and gives fast results for tools such as PSIM or Matlab.

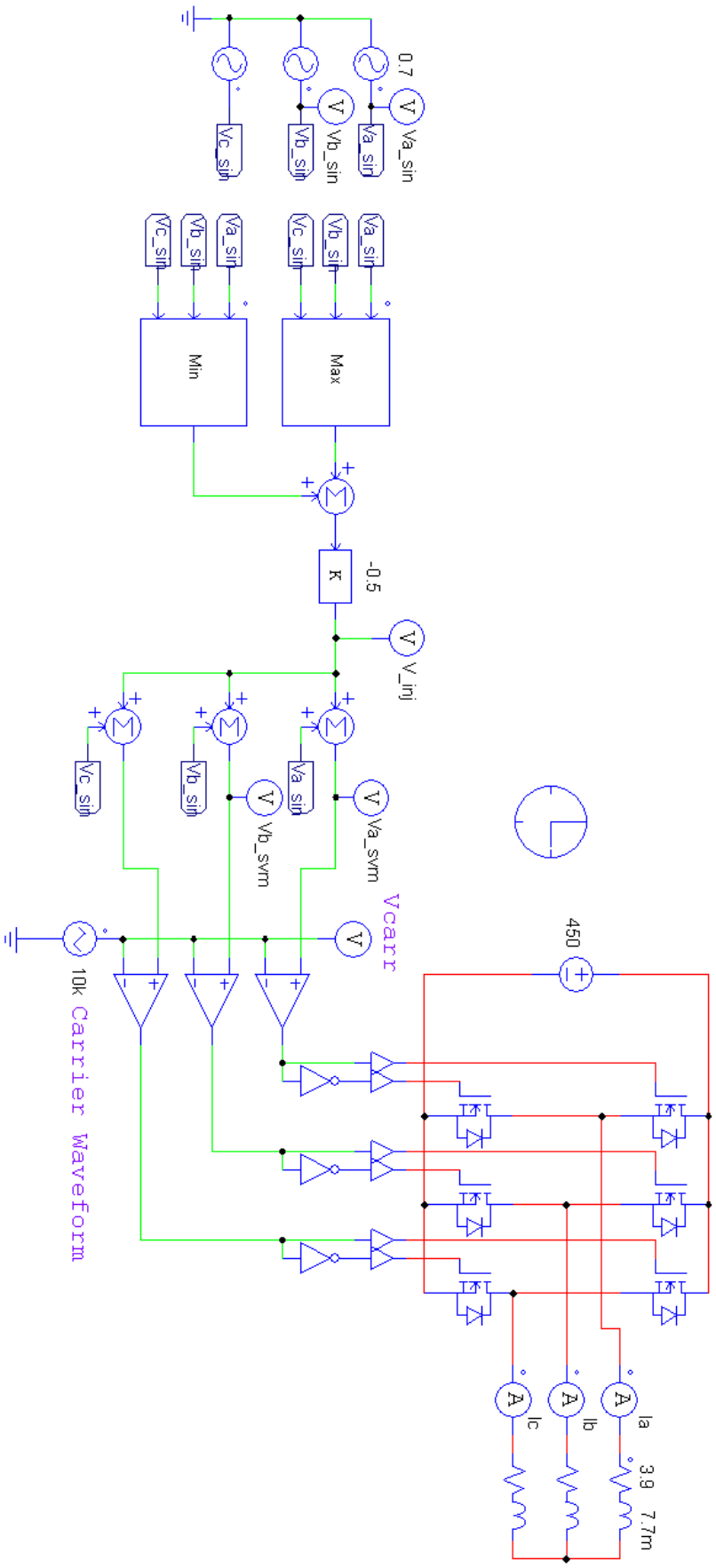

Figure 4.24 – Third order odd harmonic injection PWM technique - PSIM example

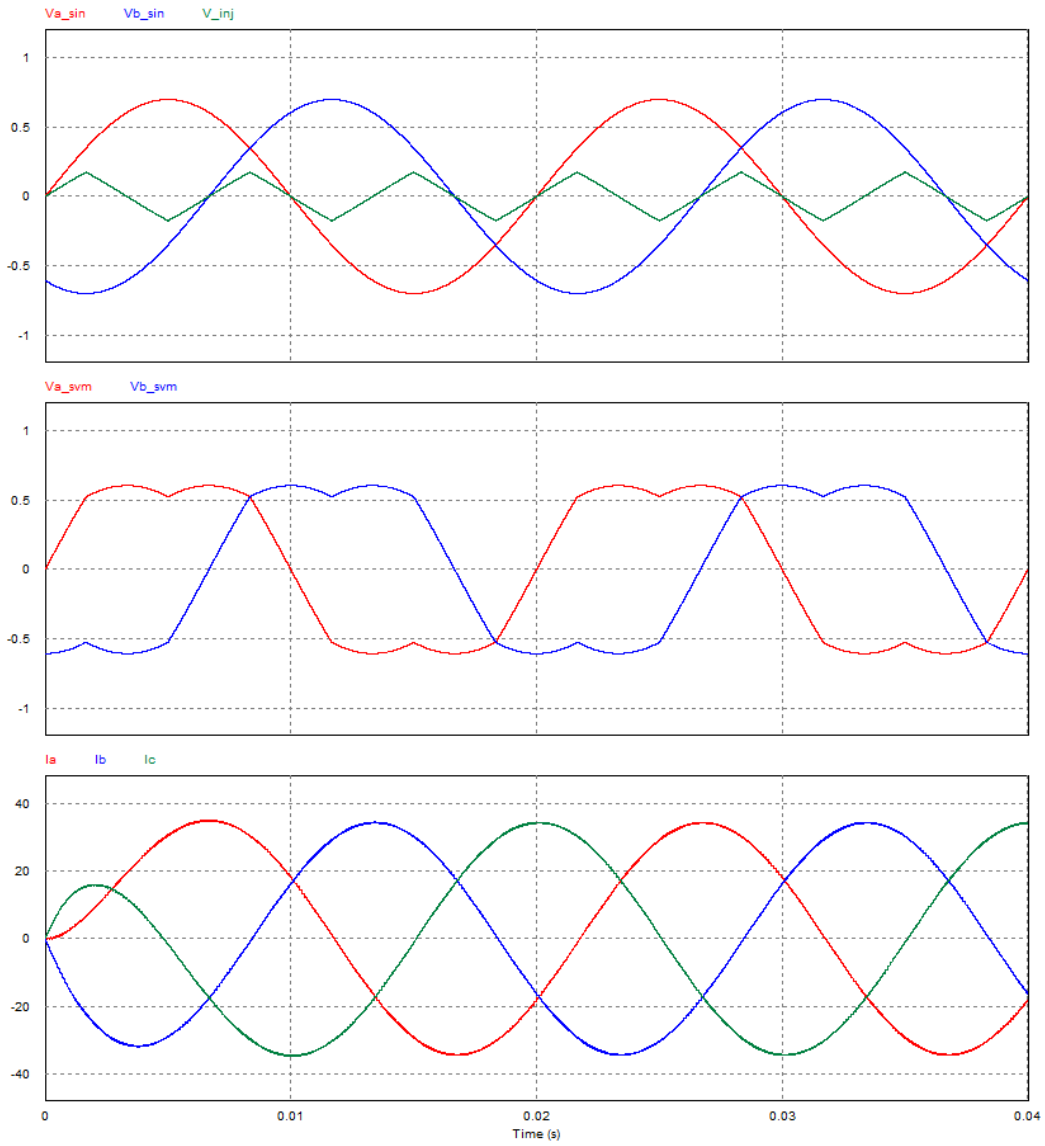

Figure 4.25 - Third order odd harmonic injection PWM technique - PSIM example waveforms

Figure 4.26 shows an adaptation of the third order odd harmonic injection PWM technique that behaves as the SVM (M, a) RMB block previously explained.

Figure 4.27 presents the resulting waveforms that are in fact equal to the ones shown in Figure 4.15.

Due to its lower complexity, this implementation can advantageously replace the SVM (M, a) RMB block in circuit analysis with PSIM or Matlab.

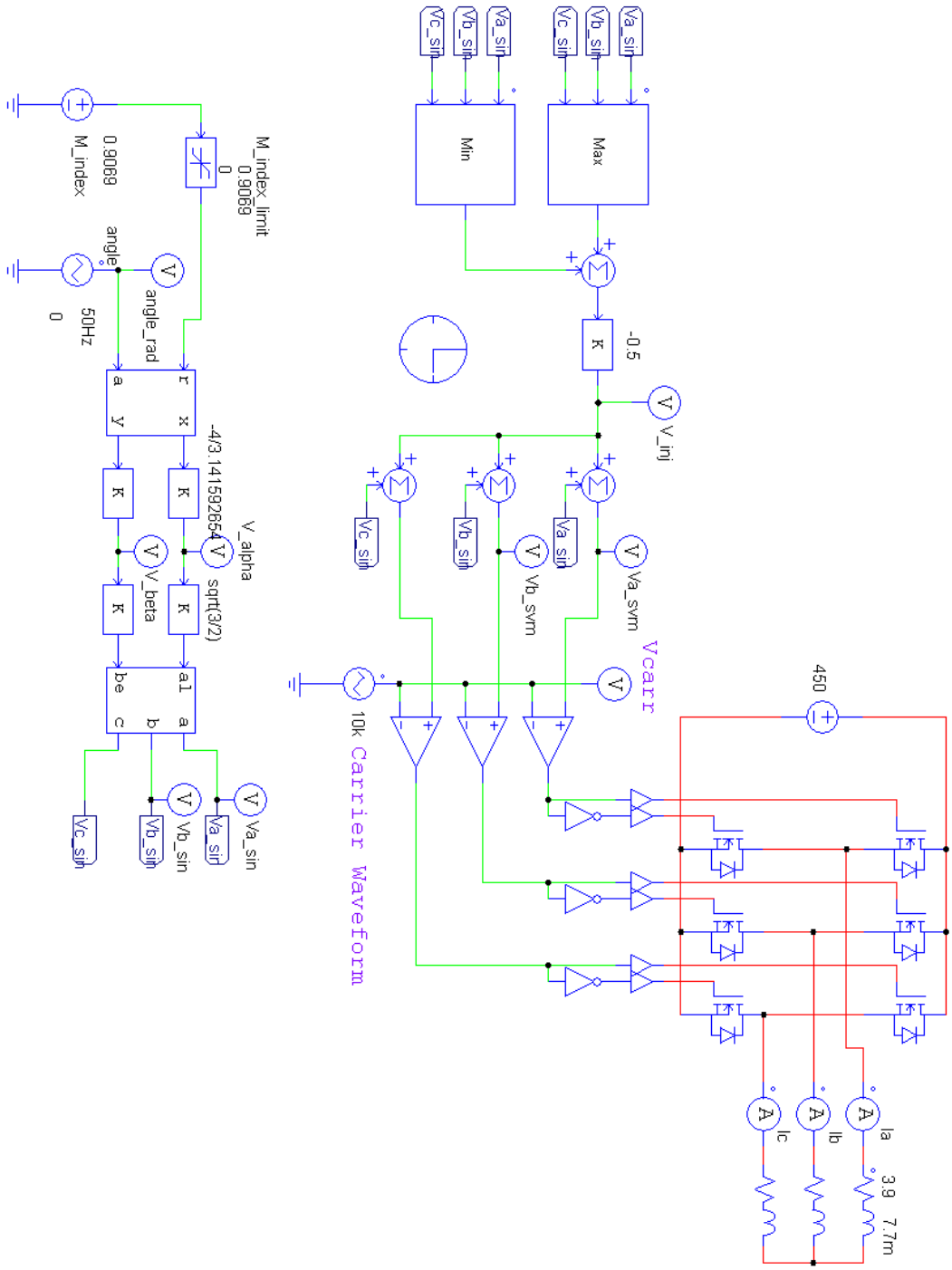

Figure 4.26 - Third order odd harmonic injection PWM technique with (M, a) control and behavior equal to SVM (M, a) RMB block

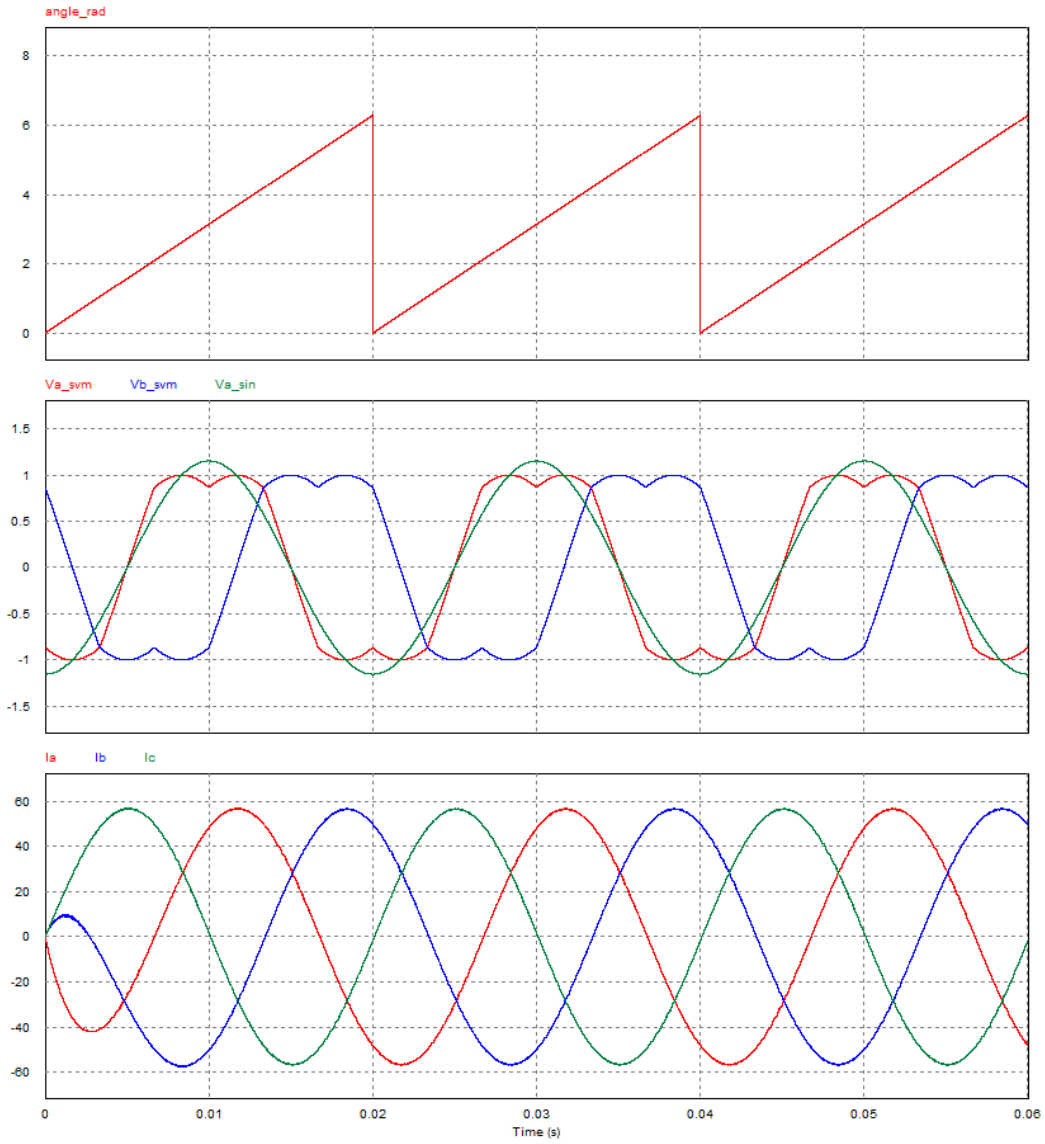

Figure 4.27 - Third order odd harmonic injection PWM technique with (M, a) control, resulting waveforms

4.7 Conclusions

In this chapter two of the most well-known modulation techniques, SPWM and SVM are analyzed in detail. It is shown that SVM improves the modulation index in the linear zone by about 15% comparatively to SPWM. This leads to an improvement on the VSC's dynamic response.

The modulation indexes M and m are defined and compared, and a new PSIM implementation example of SVM technique is developed step-by-step using exclusively PSIM blocks.

Another technique that has the same properties as conventional SVM, the third order odd harmonic injection PWM technique, is also described. When this technique is applied to the same application example, the results mimic the behavior obtained with the SVM technique.

4.8 References

[1] M. Kazmierkowski, R.Krishnan, and F. Blaabjerg. (2002). *Control in Power Electronics - Selected Problems*.

[2] B. K. BOSE, *Modern Power Electronics and AC Drives*, 2001.

[3] D. Rathnakumar, J. LakshmanaPerumal, and T. Srinivasan, "A new software implementation of space vector PWM," in *SoutheastCon, 2005. Proceedings. IEEE*, 2005, pp. 131-136.

[4] M. Malinowski, "Sensorless Control Startegies for Three-Phase PWM Rectifiers," Ph. D. Thesis, Faculty of Electrical Engineering, Warsaw University of Technology, 2001.

[5] M. Malinowski, M. Jasinski, and M. P. Kazmierkowski, "Simple direct power control of three-phase PWM rectifier using space-vector modulation (DPC-SVM)," *Industrial Electronics, IEEE Transactions on,* vol. 51, pp. 447-454, 2004.

[6] R. S. Pena, R. J. Cardenas, J. C. Clare, and G. M. Asher, "Control strategies for voltage control of a boost type PWM converter," in *Power Electronics Specialists Conference, 2001. PESC. 2001 IEEE 32nd Annual*, 2001, pp. 730-735 vol.2.

[7] A. Kwasinski, P. T. Krein, and P. L. Chapman, "Time domain comparison of pulse-width modulation schemes," *Power Electronics Letters, IEEE,* vol. 1, pp. 64-68, 2003.

[8] J. T. Boys and P. G. Handley, "Harmonic analysis of space vector modulated PWM waveforms," *Electric Power Applications, IEE Proceedings B,* vol. 137, pp. 197-204, 1990.

[9] S. R. Bowes and L. Yen-Shin, "The relationship between space-vector modulation and regular-sampled PWM," *Industrial Electronics, IEEE Transactions on,* vol. 44, pp. 670-679, 1997.

[10] D. G. Holmes and T. A. Lipo, *Pulse Width Modulation For Power Converters - Principle and Practice*, 2003.

[11] R. de Castro, R. E. Araujo, and H. Oliveira, "Design, development and characterisation of a FPGA platform for multi-motor electric vehicle control," in *Vehicle Power and Propulsion Conference, 2009. VPPC '09. IEEE*, 2009, pp. 145-152.

[12] R. de Castro, R. E. Araujo, and H. Oliveira, "Control in Multi-Motor Electric Vehicle with a FPGA platform," in *Industrial Embedded Systems, 2009. SIES '09. IEEE International Symposium on*, 2009, pp. 219-227.

[13] C. J. Ramos, "Modelação e Controlo de Conversores de Tensão Aplicados à Máquina Assincrona Duplamente Alimentada," PhD, FEUP- DEE, University of Porto, FEUP, 2010.

5
Synchronization Techniques for Sensorless Vector Control

5.1 Introduction

The vector control of permanent magnet synchronous machines is actually based on the synchronous dq reference frame. To implement it, is necessary to know rotor position (rotor angle) and its speed (angular frequency). They can be obtained through a shaft-mounted sensor, usually an encoder or a resolver, or alternatively though a sensorless methodology.

The implementation of a sensorless synchronization methodology for rotating machines is generically called a sensorless position controller. The methodology enables to synchronize the estimated dq frame with the actual machine frame.

The benefits of using a sensorless instead of a sensor based position controller can be summarized as:

- increased reliability (no rotating sensor, which can fail or get out of calibration);
- reduced price (no need for sensor and associated signal conditioning electronics);
- reduced weight and volume;
- reduced assembling time (no time needed to assemble and calibrate the sensor);
- no-maintenance solution.

Typically, however, the behavior of sensorless position controllers varies with rotor speed. In fact, sensorless position controllers present synchronization issues at zero or low frequencies bringing some problems, for example, when starting a PMSM operated as a motor. Similar problems can occur at high-speeds, e.g. 6000 r.p.m., when high-speed data acquisition and fast computing is required. To overcome those issues some new sensorless techniques have emerged. Those techniques that are discussed in this chapter can be divided into the following categories:

- Back-EMF estimators;
- State Observers;
- Sliding-mode observers;
- High-frequency signal injection;
- PLL-based estimators.

5.2 Sensorless Techniques Comparison

In this section are briefly describes the different sensorless techniques used to control PMSMs. Most of them require a sort of startup assistance in order to estimate the rotor's position and speed [1, 2], while others take advantage of a particular rotor configuration. Some combine two different techniques to achieve better results. That is the case presented in [3] where Back-EMF estimation is combined with High-frequency signal injection.

5.2.1 Back-EMF Estimator

This estimator requires two stator line voltages and currents measurements. The Clarke's reference frame transform is applied to obtain the corresponding $\alpha\beta$ voltages and currents. The stator flux vector is estimated according to the expression [2]:

$$\lambda_{\alpha\beta} = \int \left(v_{\alpha\beta} - R_s i_{\alpha\beta} \right) dt \tag{5.1}$$

where $\lambda_{\alpha\beta}$ is the flux, $v_{\alpha\beta}$ is the voltage, R_s is the phase resistance, and $i_{\alpha\beta}$ the current.

The stator flux module and angle are given by:

$$\begin{aligned} \left|\lambda_{\alpha\beta}\right| &= \sqrt{\lambda_\alpha^2 + \lambda_\beta^2} \\ \theta_\lambda &= \tan^{-1}\left(\frac{\lambda_\beta}{\lambda_\alpha}\right) \end{aligned} \tag{5.2}$$

The rotor position is assumed to be given by the stator flux angle and the speed by its derivative. The controller performance depends on the correct flux estimation, which in turn depends on the accuracy of four measurements and on the integration algorithm. Furthermore, the estimator does not take into account the rotor flux for the $\lambda_{\alpha\beta}$ flux estimation. Although many compensations are reported in the literature, the estimation is problematic at low speeds when the stator voltages are very small [4].

5.2.2 State Observer

State Observers are also known as closed-loop estimators. The idea is to estimate unknown parameters based on machine's measurements, using the estimated error to adjust the estimator response [5]. They usually consist in estimating rotor position by observing the variation in the inductance. This technique only applies to anisotropic rotors ($L_d \neq L_q$). An example is the INFORM technique proposed by [6], which is based on real-time inductance measurements using rotor saliency to estimate the flux angle [2]. According to [7] this technique must be combined with observer techniques to work properly in a wide speed range.

The Extended Luenberger Observer (ELO) and the Extended Kalman Filter (EKF) are also classified as State Observers.

- The ELO addresses non-linear, time-variant and deterministic systems [8];

- The EKF is a recursive optimum-state estimator providing measurement noise filtering if the covariance of the noise is known. Although it is classified a as viable candidate for on-line estimation of rotor position and speed, there are no practical industry applications using it due to the issues described in [2, 4]. However, a recent paper [9] presented a sensorless FPGA-based implementation addressed to a 100W PMSM using a Reduced-Order EKF with good results.

5.2.3 Sliding Mode Observer

Sliding Mode Observers (SMO) techniques are based on the state variables of the machine. A sliding surface is defined as well as two limits for that surface, creating a hysteresis window. The controlled variable is intended to track that surface and slide along it within the imposed limits. SMO has been recognized as one of the best techniques due to its robustness to disturbances and low sensitivity to machine parameters deviations [2]. In [10] the robustness of the technique is evaluated taking into account the effects of the variation of motor parameters, such as stator resistance and stator inductance, over a wide speed range.

A FPGA-based implementation-ready schema based on current measurements is presented in [11], clamming the feasibility of the proposed control system. An adaptive SMO, described on [12], uses the Lyapunov function to determine the observer gain. Experimental results show the validity of the proposed method.

5.2.4 High-frequency Signal Injection

High-frequency signal injection techniques take advantage of anisotropic rotor configurations ($L_d \neq L_q$). The rotor position is detected even at low and zero speed [13]. The technique consists in adding a high-frequency voltage to the stator voltage [14, 15]. The corresponding high-frequency stator current is affected by the rotor saliency and the rotor position is estimated based on current measurements [16, 17]. This technique requires fast and high precision current measurement and fast signal processing capability, which increases the complexity and cost of the solution [2].

Due to constraints related to the maximum PWM frequency and geometry of the rotor, this technique usually works within a limited speed range, from standstill to lower speeds [4].

5.2.5 Phase Locked Loop

Among others Phase Locked Loop (PLL) synchronization techniques are specially designed to sensorless vector control drives of rotating machines and grid connected converters, when other techniques cannot be implemented.

It was decided to investigate this technique specially addressed to PMSG sensorless drives due to previous studies that classify PLL-based sensorless as robust [2, 18-23].

5.2.5.1 The PLL Basic Structure

The PLL is a closed-loop control mechanism aimed to estimate the frequency and the phase-angle of a given input signal. Figure 5.1 shows a three-block diagram that describes the PLL operation: the phase detector; the low-pass filter (LPF); and the Voltage Controlled Oscillator (VCO).

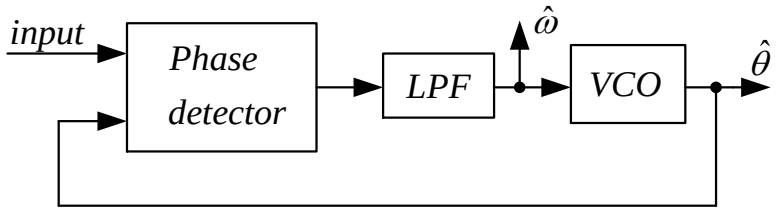

Figure 5.1 - PLL basic structure

The phase detector compares the input signal phase with the estimated phase and generates an error signal. The LPF guarantees the dynamic response of the PLL by removing the high-frequency components introduced by the phase detector. The LPF output gives the estimated frequency $\hat{\omega}$. The VCO can be seen as an integrator that determines the estimated phase-angle $\hat{\theta}$ from the estimated frequency.

The PLL mechanism can be described according to the following expressions [24]

$$\begin{aligned} \hat{\omega}(t) &= \omega_{ff} + k_v u_f(t) \\ \hat{\theta}(t) &= \int \hat{\omega}(t), \quad 0 \le \hat{\theta}(t) \le 2\pi \end{aligned} \tag{5.3}$$

where k_v is the DC gain and $u_f(t)$ is the control signal of the LPF. When a phase error occurs, the phase detector calculates it and the LPF reacts adjusting the estimated frequency $\hat{\omega}$ and cancelling the error. If the error is null, the LPF output is the natural frequency ω_{ff}.

5.2.5.2 PLL Schemas Comparison

Different PLL synchronization schemas emerged in recent years, most of them addressed to grid connected converters. Some of them can be advantageously applied to vehicular industry and in particular to PMSGs sensorless drives as discussed herein.

The performance of a PLL synchronization technique can be quantified according to the following parameters:

- fast dynamic response – synchronization and convergence;
- accurate output data - angle, frequency (and amplitude) of the output signals;
- robustness;
- insensitivity to input signal's magnitude changes;
- immunity and insensitivity to disturbances, harmonics, unbalances, sags/swells, notches and other types of distortions in the input signals;
- high-speed data acquisition;

- processor time or computing time required;
- implementation simplicity.

Table 5.1 shows a comprehensive review of twelve PLL-based schemas analyzed in [25]. According to this reference the "T" stands for "theoretical feasibility" as the corresponding research articles did not provide those results or verifications.

	Design Simplicity	Frequency adaptive & range	Distortion insensitivity	Unbalance insensitivity	Single-phase utilization
SF-PLL	Good	Average	Average	Poor	
PQ-PLL	Average	Average	Average	Poor	
DSF-PLL	Average	Average	Good	Good	
SSI-PLL	Average	Average	Good	Good	Good
DSOGI-PLL	Average	Average	Good	Good	Good
EPLL	Average	Average	Good	Good	Good
3MPLL	Average	Average	Good	Good	
Q-PLL	Average	Average	Good	T	Good
RPLL	Average	Average	Good	T	Good
PPLL	Average	Good	Good	Good	Good
ALC-PLL	Average	Average	Good	T	Good
MR-PLL	Average	Average	Good	T	Good
APLL	Average	Average	Good	Good	Good
ZCD	Good	Poor	Poor	Poor	Good
SV	Average	Poor	Average	Poor	
WLSE	Average	Average	Good	Good	

Table 5.1 - PLL-based sensorless techniques comparison [25]

The PLL schema adopted for a specific PMSG sensorless application has a decisive impact on the overall drive performance. Therefore, it should be chosen based on the specific application requirements.

According to [25], for PMSG drives the simplest PLL-based schema is the Synchronous Reference frame (SRF-PLL or SF-PLL). This schema is discussed in detail in the following section.

5.2.5.3 Synchronous Reference Frame PLL

The Synchronous Reference Frame PLL (SRF-PLL) derives the phase angle from a three-phase voltage source by completing a reference frame transformation from the stationary abc to the rotational dq. The reference frame transform can be done in two steps: applying the Clarke's $abc-to-\alpha\beta$ followed by the Park's $\alpha\beta-to-dq$ reference frame transformations.

The Clarke's transform assumes that

$$\begin{aligned} V_a &= V\cos(\theta) \\ V_b &= V\cos\left(\theta-\frac{2\pi}{3}\right) \\ V_c &= V\cos\left(\theta+\frac{2\pi}{3}\right) \end{aligned} \tag{5.4}$$

The Clarke's transform is given by

$$\left[T_{\alpha\beta}\right]=\frac{2}{3}\begin{bmatrix}1 & -\frac{1}{2} & -\frac{1}{2}\\ 0 & \frac{\sqrt{3}}{2} & -\frac{\sqrt{3}}{2}\end{bmatrix} \tag{5.5}$$

Doing $\left[V_{\alpha\beta}\right]=\left[T_{\alpha\beta}\right]\left[V_{abc}\right]$ leads to

$$\begin{bmatrix}V_{\alpha}\\ V_{\beta}\end{bmatrix}=\begin{bmatrix}V\cos\theta\\ V\sin\theta\end{bmatrix} \tag{5.6}$$

The phase-angle can be detected by synchronizing the V_a voltage vector with the direct or quadrature axis. By choosing the synchronization with the direct axis where $V_d=V$ and $V_q=0$, the Park's transform is given by

$$\left[T_{dq}\right]=\begin{bmatrix}\cos\hat{\theta} & -\sin\hat{\theta}\\ \sin\hat{\theta} & \cos\hat{\theta}\end{bmatrix} \tag{5.7}$$

where $\hat{\theta}$ is the estimated phase-angle that is the PLL output. Then the product $\left[V_{dq}\right]=\left[T_{dq}\right]\left[V_{\alpha\beta}\right]$ leads to

$$\begin{bmatrix}V_d\\ V_q\end{bmatrix}=\begin{bmatrix}\cos\hat{\theta} & -\sin\hat{\theta}\\ \sin\hat{\theta} & \cos\hat{\theta}\end{bmatrix}\begin{bmatrix}V\cos\theta\\ V\sin\theta\end{bmatrix}\Leftrightarrow$$
$$\Leftrightarrow\begin{bmatrix}V_d\\ V_q\end{bmatrix}=\begin{bmatrix}V\cos\left(\hat{\theta}-\theta\right)\\ V\sin\left(\hat{\theta}-\theta\right)\end{bmatrix}=\begin{bmatrix}V\cos\left(\Delta\theta\right)\\ V\sin\left(\Delta\theta\right)\end{bmatrix} \tag{5.8}$$

From the synchronous referential V_q is set to be zero. When the error $\Delta\theta$ is null the estimated dq frame is synchronized with the machine/grid abc frame. Figure 5.2 shows the structure of the SRF-PLL method.

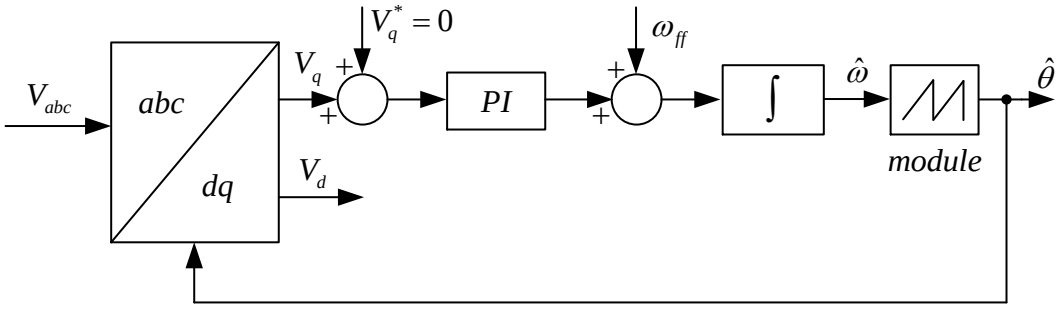

Figure 5.2 - Synchronous Reference Frame PLL model

In steady state $\hat{\theta} \approx \theta$ so $\Delta\theta$ is very small and the term $\sin(\Delta\theta)$ varies linearly, i.e., $\sin(\Delta\theta) \approx \Delta\theta$. The PLL can thus be treated as a linear control system where

$$V_q = V\left(\hat{\theta} - \theta\right) \tag{5.9}$$

Figure 5.3 shows the block diagram of a SRF-PLL model built on equation (5.9).

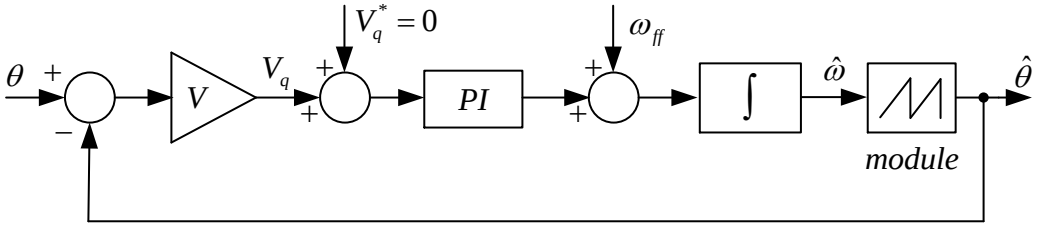

Figure 5.3 - Synchronous Reference Frame PLL comprehensive model

The angular frequency ω_{ff} is the source angular frequency. For near constant frequency sources, like the grid frequency, it may be easily specified, $\omega_{ff} = 2\pi 50\ rads^{-1}$, but for variable frequency sources, e.g. a PMSG operating in different regimes, ω_{ff} is unknown. The ω_{ff} speeds up the PLL synchronizing process. If unknown it can be set to zero and the PI controller integral part will compensate its value over time. The practical consequence is that the synchronizing process will take longer.

Based on [26] the PLL schema is described as an integrator with gain V, as represented in Figure 5.3, which includes a 1st order delay system that traduces the sampling of the input signals, with sampling period T_s.

$$H(s) = \frac{V}{s}\frac{1}{1+sT_s} \tag{5.10}$$

The Symmetrical Optimum (SO) PI tuning method is proposed with the goal of maximizing system's phase-margin. The resulting tuning parameters are given according to (5.11), where ω_c is the cross-over frequency and a is an operator that defines the phase-margin of the system. The cross-over frequency should be the angular frequency, when dealing with grid connected converters.

$$a = \frac{1}{\omega_c T_s} \qquad K_p = \frac{1}{aVT_s} \qquad T_i = a^2 T_s \tag{5.11}$$

The SO method puts in evidence that the PI parameters depend on the following variables:

- input signal's magnitude V;
- input signal's frequency, which influences the choice of ω_c;

- the sampling period T_s.

So apparently this method is not adequate to synchronize signals that vary not only with frequency but also in magnitude as it is the case of PMSGs sensorless drives. Later in this chapter this issue is discussed in detail.

5.2.5.4 PSIM SRF-PLL Dynamic Evaluation

Figure 5.4a) shows a PSIM implementation of the SRF-PLL. The source is a three-phase voltage system with a single-phase magnitude of 1V and a frequency of 250Hz. The phase-angle is obtained by synchronizing the V_a voltage vector with the d axis, thus getting the V_q signal used in the close-loop control. The ω_{ff} angular frequency is set to zero meaning that there is not an initial estimation for the line frequency. As expected when $\theta = 0$, V_a is at is positive maximum as shown in Figure 5.5. The "-1" multiplier is necessary to have a correct $abc-to-dq$ reference frame transform in PSIM, as explained in detailed in Annex 1.

It is also possible to synchronize the V_a vector with the q axis using the V_d signal, as represented in Figure 5.4b). The difference is that the resulting phase-angle is now synchronized with the beginning of the sinusoid instead of with its positive maximum, as it can be observed in Figure 5.5.

Figure 5.4a) circuit should be for control systems using reference frame transformations because it respects the original reference frame statements where the three-phase system is represented as a function of cosines (see eq. (5.4)).

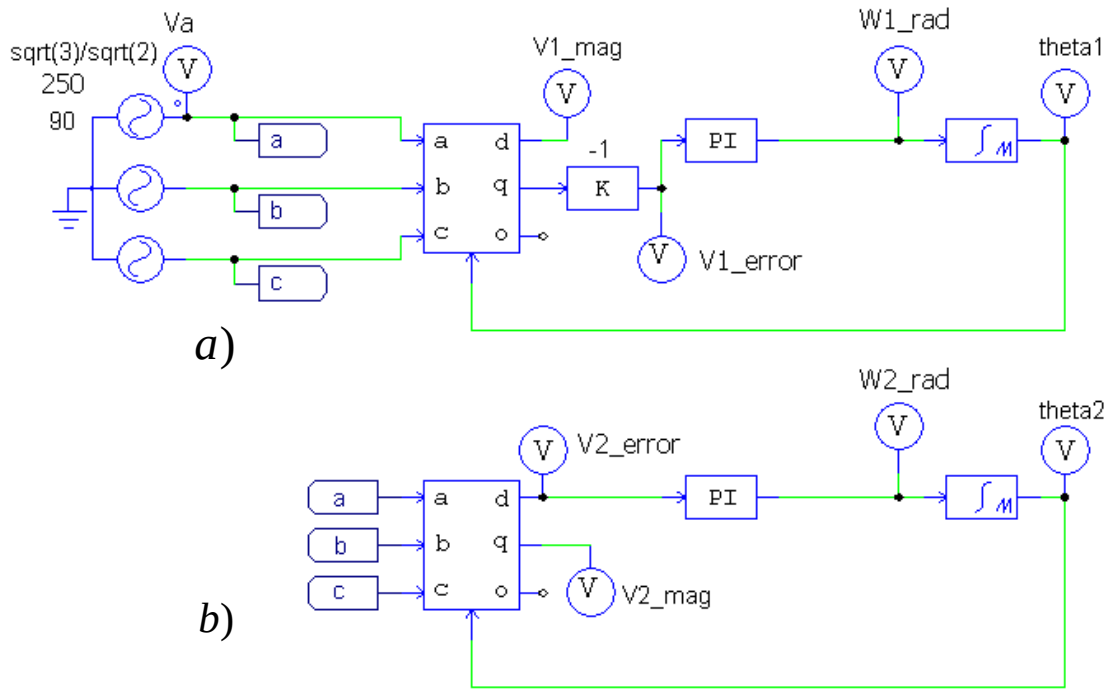

Figure 5.4 - PSIM SRF-PLL synchronization test circuits using a) *Vq* or b) *Vd* as synchronization signal

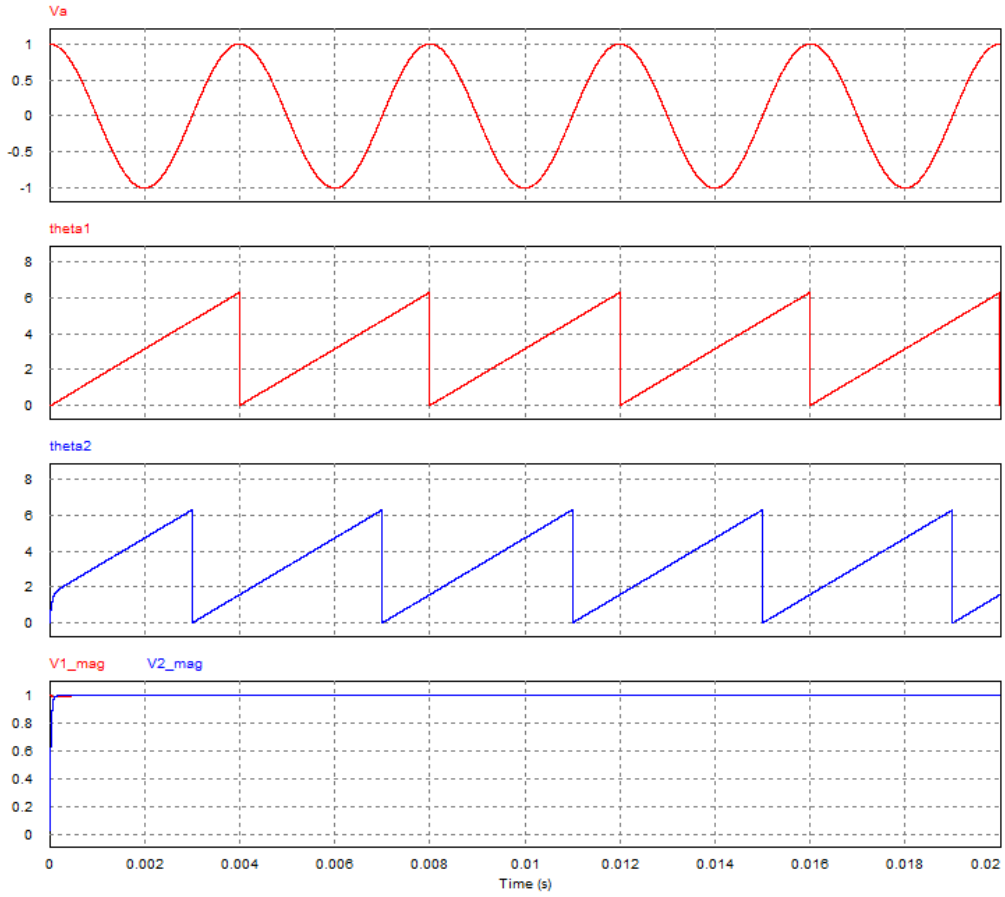

Figure 5.5 - PSIM SRF-PLL synchronization test circuits - waveforms

As seen before, the dynamic behavior of the SRF-PLL synchronization method depends on the input signal's magnitude and frequency. Figure 5.6 shows a SRF-PLL test circuit based on current instead of voltages measurements. It aim is to evaluate the PLL dynamics and robustness in harmonic polluted environments, and its response to steep instantaneous variation in current's magnitude.

The three-phase power source is built adding 10V peak square-wave sources (with frequencies of 800Hz; 900Hz and 1000Hz, respectively), to 100V peak, 250Hz, single-phase sinusoids thus creating distorted voltages. An example of this distorted voltage, Va_noise, is shown in Figure 5.7.

Additionally a 330 Ohm star load is permanently attached to the source while a 5 Ohm is commutated according to the frequencies imposed by the switches (match those of the switches - 16Hz and 1.5kHz). Accordingly the line current peak varies between 0.3A and 20.3A. In percentage, 0.3A is 1.5% of the maximum.

With this arrangement the SRF-PLL operation is stressed out enabling the evaluation of its behavior in the presence of distorted voltages and currents.

The use of those specific signal frequencies is chosen intentionally. As frequency analysis results shown (presented in the next chapter), the harmonic content of a VSC line current with a fundamental frequency of 250Hz are located at specific frequencies. Harmonics from 1 kHz to 5 kHz are present, mainly associated to the

IGBTs dead-time. Higher frequencies, around the switching frequency and around twice the switching frequency, e.g. 20kHz and 40kHz, are also present.

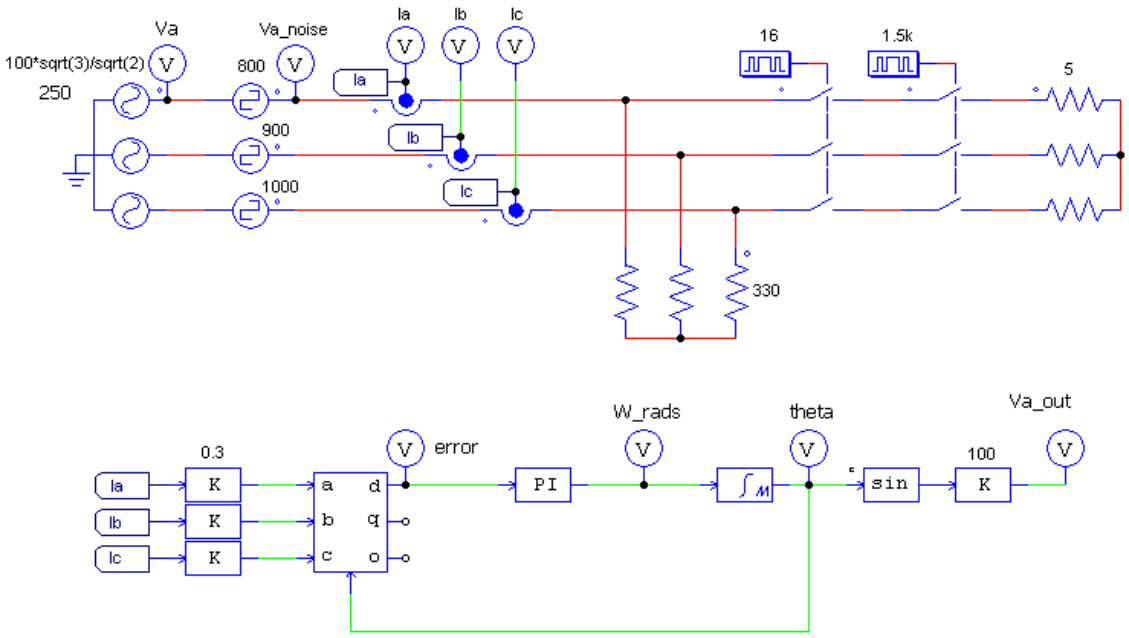

Figure 5.6 – PSIM SRF-PLL current based evaluation circuit

As low frequency components cause higher influence on: a) the PLL synchronization; and b) its steady state operation, the chosen frequencies injected into the main power source worsens the real PLL operation.

In Figure 5.7, Ia is the phase-a current, W_rads is the estimated angular frequency ω in rad/s and theta is the estimated angle related to phase-a. Va is the original phase-a sinusoid while Va_out is the estimated one. Both sinusoids are represented in the same graphic window to allow their comparison.

Notice that the signal inputs of the SRF-PLL are i_a, i_b, and i_c, i.e., highly distorted and magnitude varying currents. However, it can be seen that the PLL synchronization occurs in less than two periods, albeit low harmonic polluted currents or high-magnitude current variations.

Figure 5.8 shows detailed waveforms for a specific time instant, when the 5 Ohm star load starts to be switched ON and OFF at 1.5 kHz. Only slight variations in the phase-angle are observed even for huge (from 1.5% to 100%), current amplitude variations (see Va and Va_out).

The 330 Ohm star load is permanently connected to guarantee, in the absence of any (bigger) load (all switches OFF), the PLL does not lose synchronism.

What this simulation (Figure 5.7 and Figure 5.8) does not show is what occurs if the PLL operation is started with the 330 Ohm star load only (all switches OFF). In this case the SRF-PLL takes a much longer time to synchronize. This is because the error signal at the input of the PI controller has only 1.5% of the previous error magnitude.

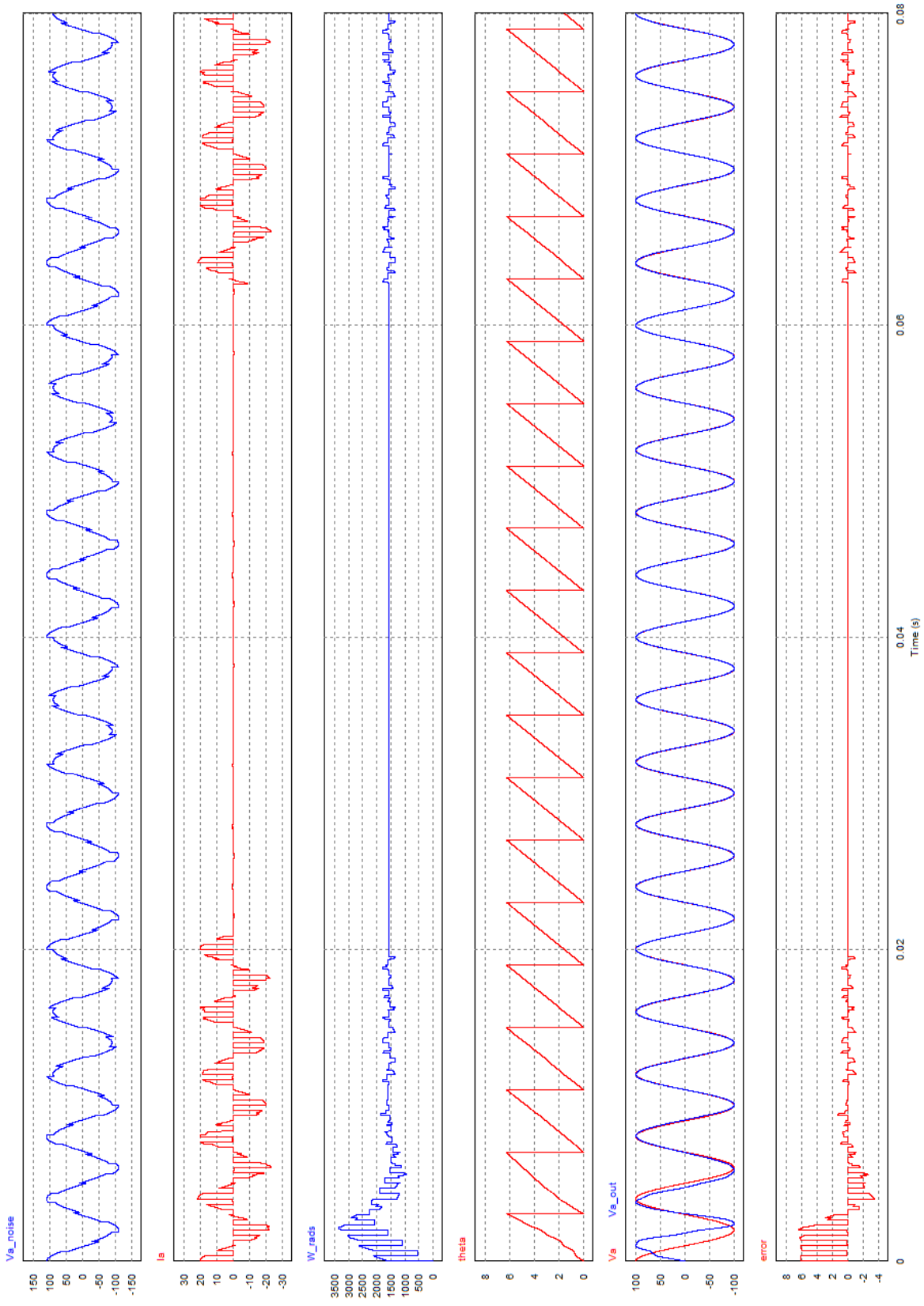

Figure 5.7 – PSIM SRF-PLL current based evaluation circuit - waveforms

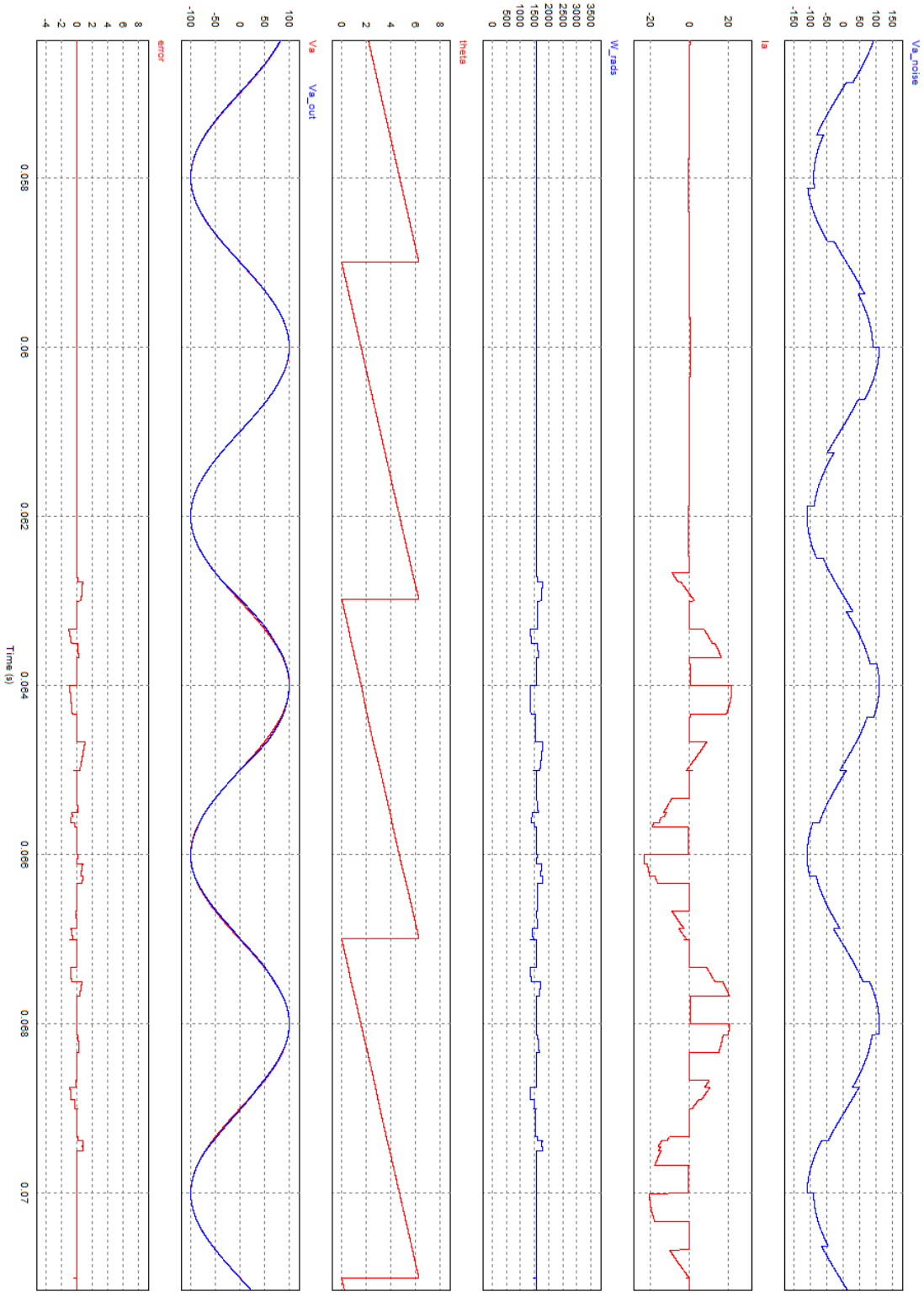

Figure 5.8 – PSIM SRF-PLL current based evaluation circuit - detail waveforms

Apart it, after the initial phase-lock time period, the synchronization is no longer broken even if high-magnitude variations in the input current's magnitude occur.

The phase-lock time period is not a limitation for the application herein described. This issue is addressed again in the next chapter.

As conclusion, the SRF-PLL is a robust method to estimate the phase-angle even under stressful test conditions. Still, depending on the application the initial phase-lock time period can be an issue. This PLL method is quite simple requiring a very small computational effort.

Figure 5.9 shows a digital implementation block of the SRF-PLL described in Figure 5.6. Only two currents are required calculate the Pak's transform as voltage source and load are balanced systems. The currents are acquired at 40kHz rate $(T_s = 25\mu s)$, which means that there are 40k/250=160 samples, per period of the source frequency.

The "0.3" input block multipliers represent current transducers. An average of three readings is made to minimize the error related to current samplings.

The code is written in C language and a new estimative of the phase-angle is obtained each $25\mu s$ (40kHz).

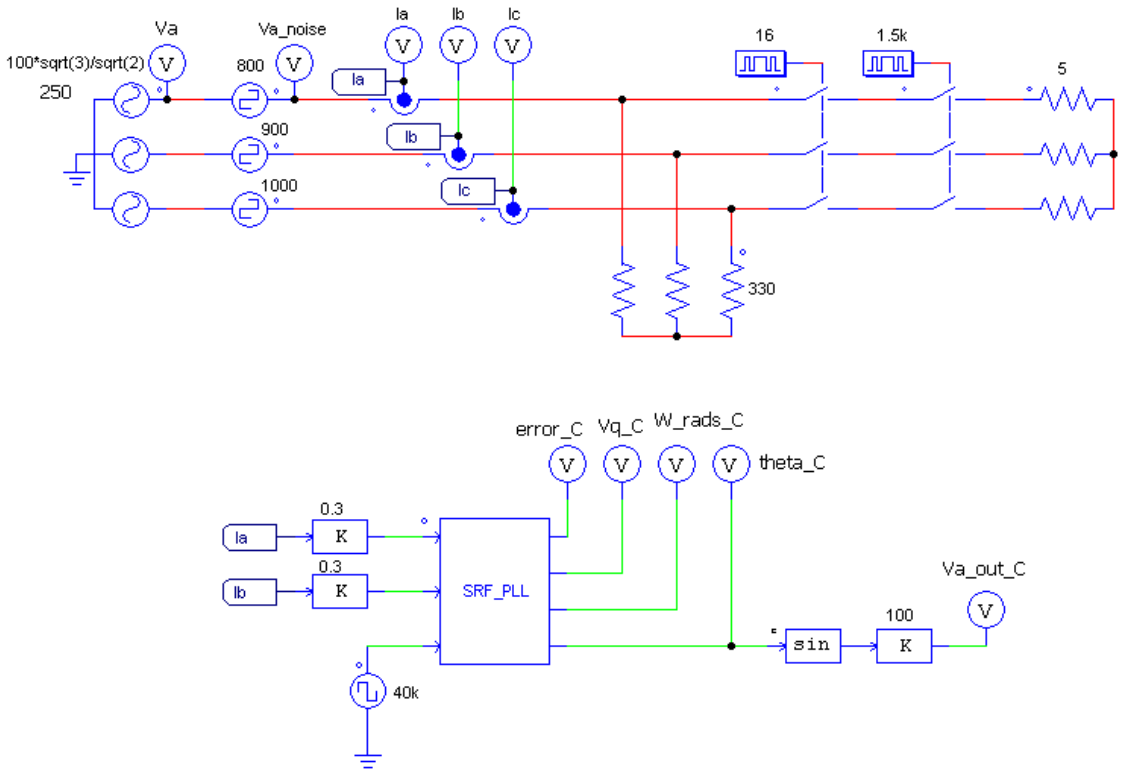

Figure 5.9 - PSIM SRF-PLL current based evaluation circuit – digital implementation

Figure 5.10 and Figure 5.11 show the simulation results. Due to the delay imposed by the acquisition rate and by the average currents related calculations, some degree of instability is added to the PLL control. This is mainly observed while the PLL does not achieve the phase-lock (it takes one more cycle than in the previous circuit). After the phase-lock time period, the PLL's behavior is nearly the same. Figure 5.12 shows the error of the estimated Va_out_C phase in contrast with the original Va phase. In the worst case the error is less than 0.1%.

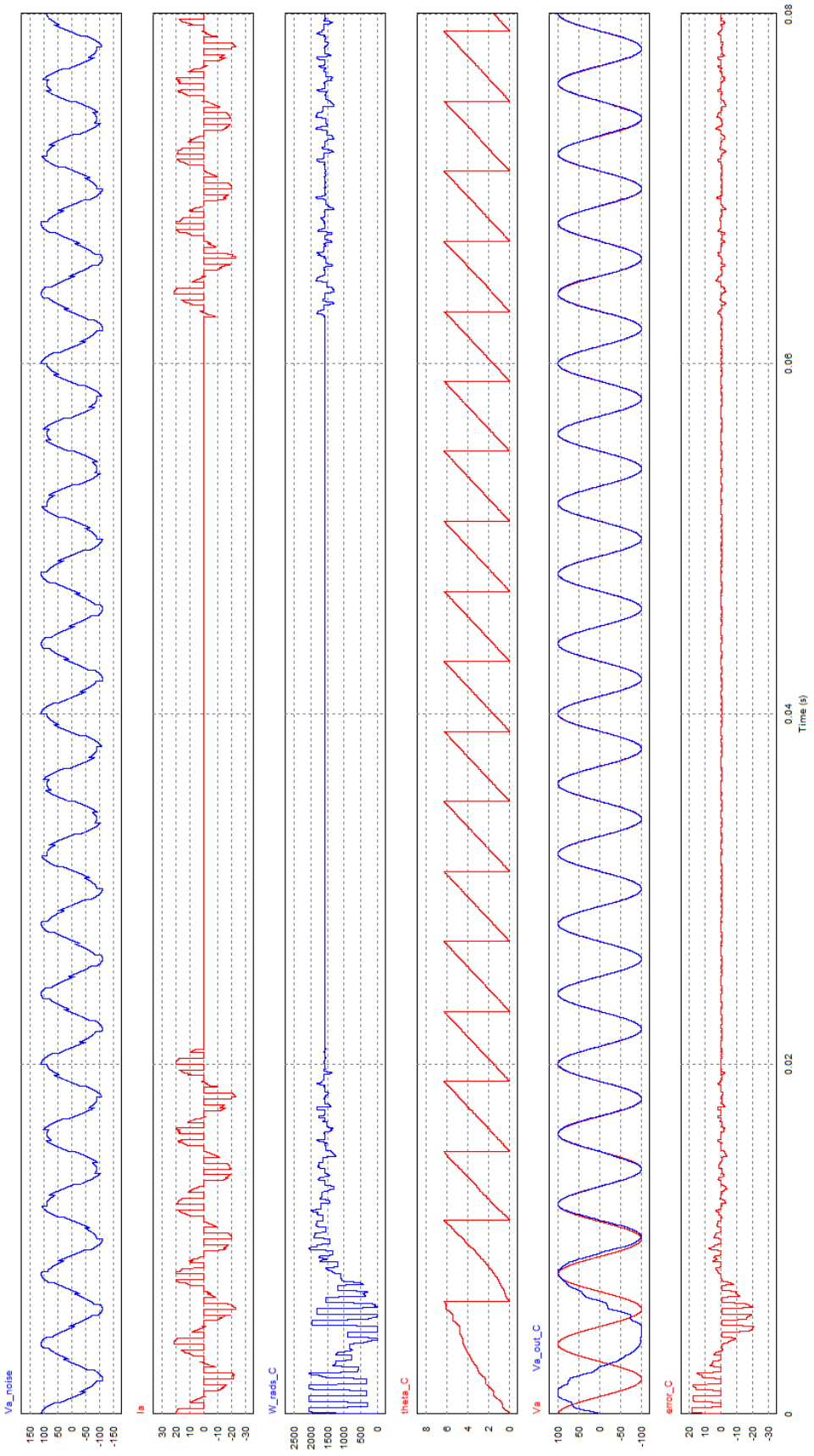

Figure 5.10 - PSIM SRF-PLL current based evaluation circuit – digital implementation - waveforms

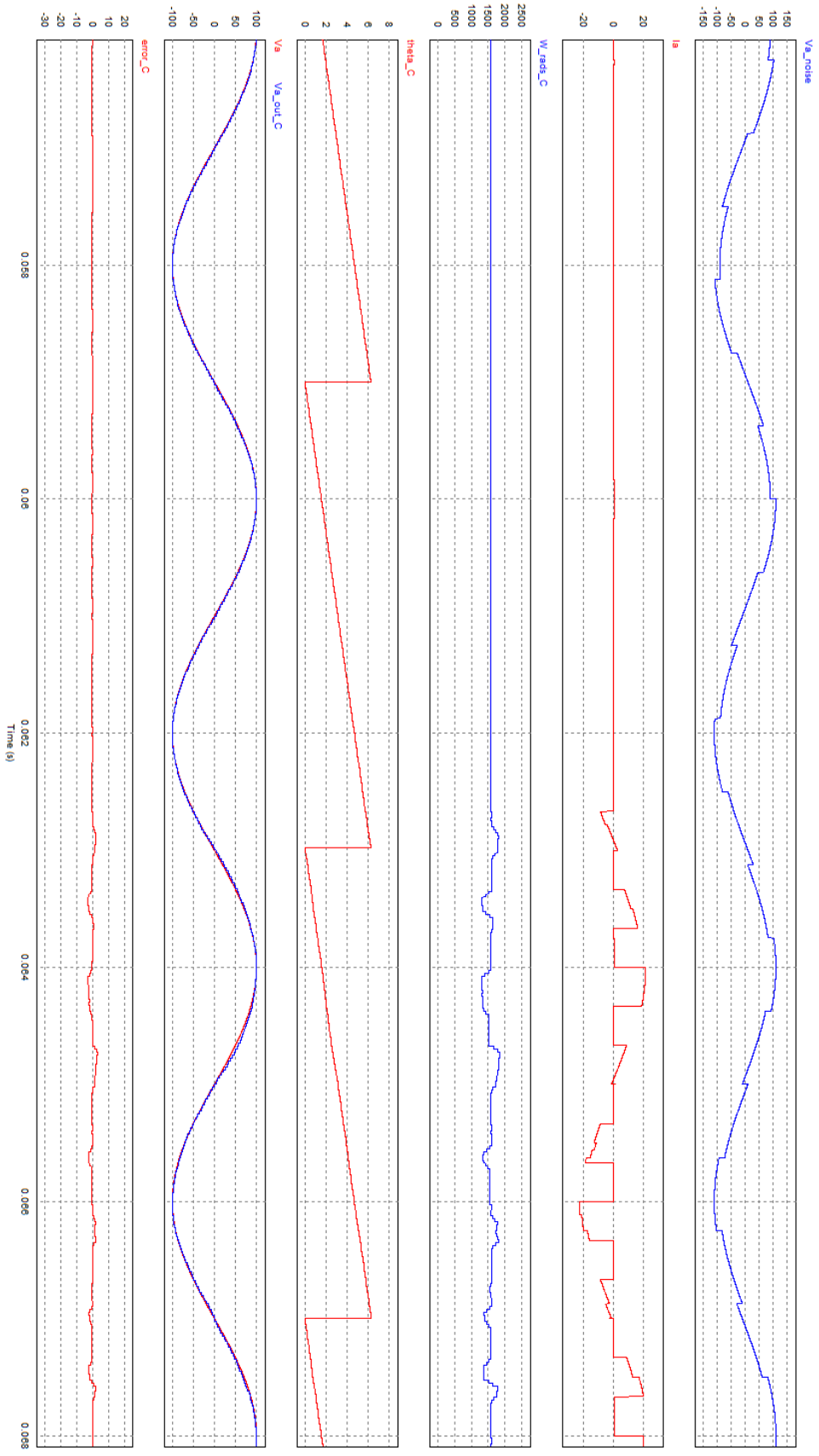

Figure 5.11 - PSIM SRF-PLL current based evaluation circuit – digital implementation – detail waveforms

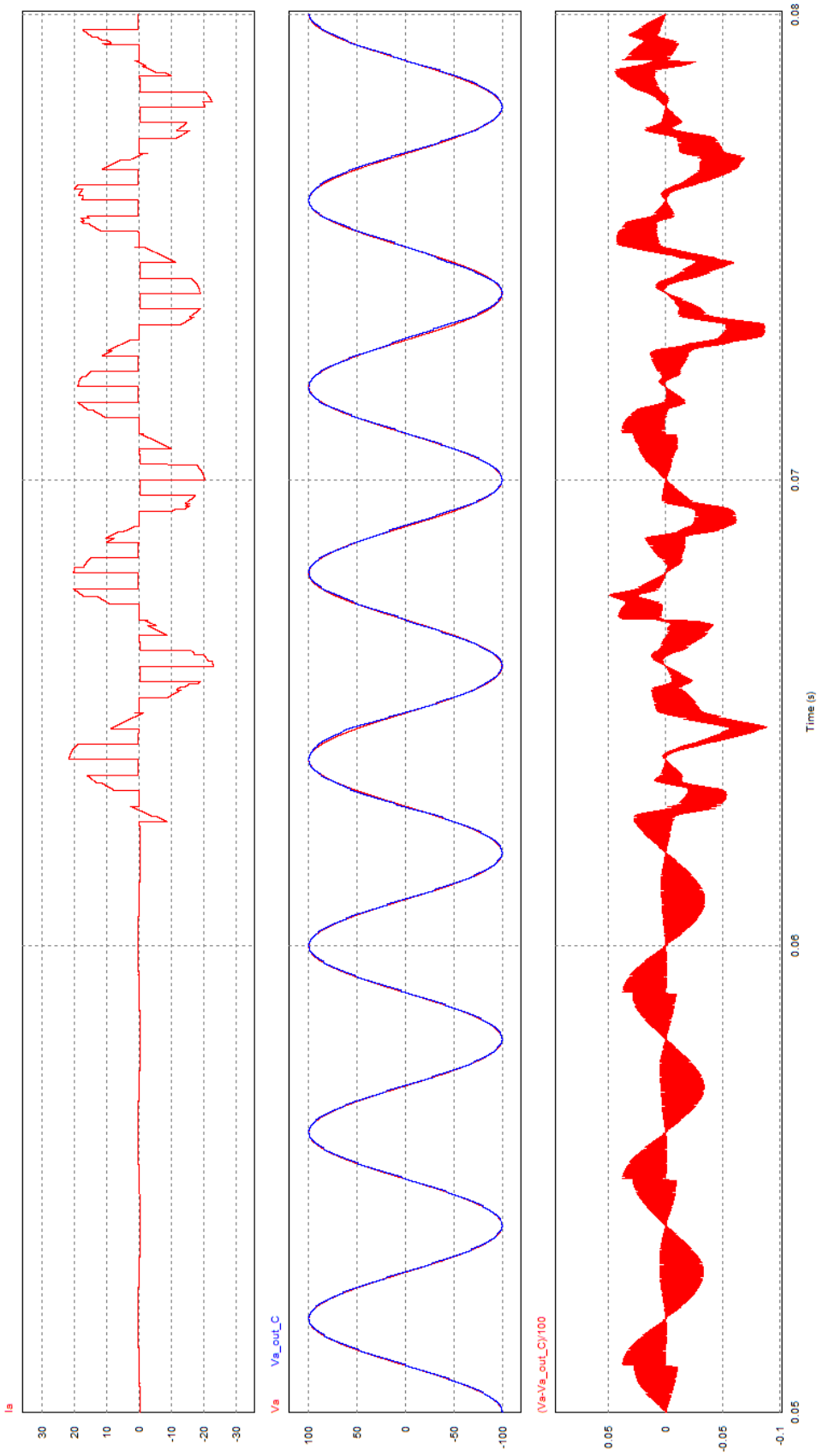

Figure 5.12 - PSIM SRF-PLL current based evaluation circuit – digital implementation – error evaluation

5.2.5.5 Tuning the SRF-PLL PI Controller

Tuning the PI controller is not an easy task because for each specific working point there is a set of ideal k_p and k_i parameters. A specific working point comprises: the signals (currents) magnitudes and frequency, and the sampling time period T_s. In here the unique variable than can be considered constant is the sampling time.

For a PMSG sensorless drive application whose control is based on line currents, it is necessary to specify the line currents and rotor speed ranges. Based on the range, the PI parameters chosen must guarantee that:

- the PLL achieves the phase-lock state, in more or less time (up to 500ms), within the specified limits for the current magnitude and speed;
- after the initial phase-lock time period, the stable operation is maintained along the entire operation range.

Initial PI parameters can be obtained according to (5.11) equations (for specific working points). PSIM and its SimCoupler interface to Matlab Simulink also helped in tuning PI. Nevertheless, the better results were achieved with a trial-error method.

5.3 Conclusions

In this chapter a comprehensive set of synchronization techniques focused on sensorless vector control is described, with emphasis on the PLL technique. Indeed, the PLL technique offers several advantages over other techniques namely with machines with isotropic rotors where other techniques cannot be applied.

The simplest PLL-based schema, the SRF-PLL, is evaluated using a test circuit based exclusively on line current measurements where both phase voltages and currents are intentionally harmonic polluted. Moreover the current's amplitude varies from 1.5% to its maximum 100%. Results showed that the SRF-PLL correctly estimates angle and speed.

This technique is used later in the experimental setup described in Chapters 6 and 7, where its robustness is proved.

5.4 References

[1] S.-K. Sul, *Control of Electric Machine Drive Systems*: WILEY, 2011.

[2] T. Sá, "Traction Control in Electric Vehicles," Master, FEUP - Porto University, Porto, 2012.

[3] O. Wallmark, "On Control of Permanent-Magnet Synchronous Motors in Hybrid-Electric Vehicle Applications," Licentiate, Chalmers University of Technology, 2004.

[4] Song Chi, "Position-sensorless control of permanent magnet synchronous machines over wide speed range," PhD, The Ohio State University, USA, 2007.

[5] P. Vas, *Sensorless Vector and Direct Torque Control*: Oxford University Press, 1998.

[6] M. Schroedl, "Sensorless control of AC machines at low speed and standstill based on the INFORM method," in *Industry Applications Conference, 1996. Thirty-First IAS Annual Meeting, IAS '96., Conference Record of the 1996 IEEE*, 1996, pp. 270-277 vol.1.

[7] P. Thiemann, C. Mantala, J. Hordler, A. Trautmann, D. Groppe, R. Strothmann*, et al.*, "New sensorless rotor position detection technique of PMSM based on direct flux control," in *Power Engineering, Energy and Electrical Drives (POWERENG), 2011 International Conference on*, 2011, pp. 1-6.

[8] T. Pana and O. Stoicut, "Design of an extended luenberger observer for sensorless vector control of induction machines under regenerating mode," in *Optimization of Electrical and Electronic Equipment (OPTIM), 2010 12th International Conference on*, 2010, pp. 469-478.

[9] Q. Nguyen Khanh, H. Nguyen Trung, and Q. P. Ha, "FPGA-Based Sensorless PMSM Speed Control Using Reduced-Order Extended Kalman Filters," *Industrial Electronics, IEEE Transactions on,* vol. 61, pp. 6574-6582, 2014.

[10] H. Yoon-Seok, C. Jung-Soo, and K. Young-Seok, "Sensorless PMSM drive with a sliding mode control based adaptive speed and stator resistance estimator," *Magnetics, IEEE Transactions on,* vol. 36, pp. 3588-3591, 2000.

[11] Q. Nguyen Khanh, V. Doan Quang, N. D. That, and Q. P. Ha, "Observer-based integral sliding mode control for sensorless PMSM drives using FPGA," in *Control, Automation and Information Sciences (ICCAIS), 2013 International Conference on*, 2013, pp. 218-223.

[12] E. Wesub, K. ImYong, and L. Jangmyung, "Enhancement of the speed response of PMSM sensorless control using an improved adaptive sliding mode observer," in *Industrial Electronics, 2008. IECON 2008. 34th Annual Conference of IEEE*, 2008, pp. 188-191.

[13] B. Wilamowski and J. Irvin, *The Industrial Electronics Hanbook - Power Electronics Handbook*, Bogdan M. Wilamowski; J. David Irvin ed. vol. 2: CRC Press, 2011.

[14] K. Hyunbae, M. C. Harke, and R. D. Lorenz, "Sensorless control of interior permanent-magnet machine drives with zero-phase lag position estimation," *Industry Applications, IEEE Transactions on,* vol. 39, pp. 1726-1733, 2003.

[15] S. Sato, H. Iura, K. Ide, and S. Seung-Ki, "Three years of industrial experience with sensorless ipmsm drive based on high frequency injection method," in *Sensorless Control for Electrical Drives (SLED), 2011 Symposium on*, 2011, pp. 74-79.

[16] A. Consoli, G. Scarcella, G. Tutino, and A. Testa, "Sensorless field oriented control using common mode currents," in *Industry Applications Conference, 2000. Conference Record of the 2000 IEEE*, 2000, pp. 1866-1873 vol.3.

[17] S. Bolognani, S. Calligaro, R. Petrella, and M. Sterpellone, "Sensorless control for IPMSM using PWM excitation: Analytical developments and

implementation issues," in *Sensorless Control for Electrical Drives (SLED), 2011 Symposium on*, 2011, pp. 64-73.
[18] J. Wang, J. Liang, F. Gao, L. Zhang, and Z. Wang, "A Method to Improve the Dynamic Performance of Moving Average Filter Based PLL," *Power Electronics, IEEE Transactions on,* vol. PP, pp. 1-1, 2014.
[19] V. Kaura and V. Blasko, "Operation of a phase locked loop system under distorted utility conditions," *Industry Applications, IEEE Transactions on,* vol. 33, pp. 58-63, 1997.
[20] R. P. Burgos, P. Kshirsagar, A. Lidozzi, J. Jihoon, F. Wang, D. Boroyevich*, et al.*, "Design and Evaluation of a PLL-Based Position Controller for Sensorless Vector Control of Permanent-Magnet Synchronous Machines," in *IEEE Industrial Electronics, IECON 2006 - 32nd Annual Conference on*, 2006, pp. 5081-5086.
[21] E. Robles, S. Ceballos, J. Pou, J. Zaragoza, and I. Gabiola, "Grid synchronization method based on a quasi-ideal low-pass filter stage and a phase-locked loop," in *Power Electronics Specialists Conference, 2008. PESC 2008. IEEE*, 2008, pp. 4056-4061.
[22] S. K. Panda and B. Chitti Babu, "Improved phase detection technique for grid synchronization of DG systems during grid abnormalities," in *Engineering and Systems (SCES), 2013 Students Conference on*, 2013, pp. 1-6.
[23] K. Young and R. A. Dougal, "SRF-PLL with dynamic center frequency for improved phase detection," in *Clean Electrical Power, 2009 International Conference on*, 2009, pp. 212-216.
[24] G. F. Pla and A. G. Matias, "Control of Grid Side Inverter for Wind Turbine," INSTITUTE OF ENERGY TECHNOLOGY, Aalborg, 2010.
[25] X.-Q. GUO, W.-Y. WU, and H.-R. GU, "Phase locked loop and synchronization methods for grid interfaced converters: a review," *Elektrotechniczny,* 2011.
[26] A. Lopes, "Controlo Avançado de Conversores para Sistemas FotoVoltaicos," Master, DEE, Porto, FEUP, 2013.

6
Permanent Magnet Synchronous Generator Control

6.1 Introduction

For a HEV with an ICE acting as Range Extender (RE) the main goal of the RE subsystem is to convert the maximum available torque provided by the ICE shaft to DC power at the vehicle DC bus. As explained in Chapter 2, the solution adopted to perform the power conversion takes advantage of the superior characteristics of a PMSM operated as a generator, i.e. a PMSG. Those characteristics can be enumerated as: high power density, lower volume, less weight and higher efficiency over other electrical generators.

Converting the AC power provided by the PMSG to DC power is not a difficult task and has been done for many years with basic power converters based on diodes and thyristors. But this technique presents many drawbacks, the main being the very low efficiency since there is no control over the conversion process. The solution is to adopt a vector control method that allows to independently control torque and rotor flux.

The most significant vector control methods used with PMSM are described in literature as Direct Torque Control (DTC) and Field Oriented Control (FOC) [1-4]. These methods are shortly described and compared.

In this work the FOC method is adopted to control the PMSG. A sensorless synchronization technique based on SFR-PLL and current measurements is added to FOC.

The final result is a PMSG FOC sensorless control exclusively based on SRF-PLL and current measurements, where the SVM technique is adopted. Current transducers measurements are simulated at 40 kHz rate and control actions are performed at 20 kHz. Switches dead-time are added to the simulation process. Data acquisition and control is performed using a PSIM C-block, microcontroller-ready, C code.

6.2 FOC vs DTC Methods

The FOC method, originally introduced by F. Blaschke [5], is a widely used control method addressed to, among others, Induction Motors (IM) and PMSMs. It is based on the dynamic modeling of the machine and requires coordinate transformation (from $abc-to-dq$). Both torque and rotor flux can be controlled independently by

reorienting the stator current components i_q and i_d, respectively. Two PI controllers are employed to control both torque and rotor flux. The control process needs to accurately know the machine parameters, where L_d and L_q inductance values are crucial to design precise decoupled current controllers. Also required are the shaft position and speed, thus the need to use a position sensor in the shaft or to adopt a sensorless position/speed estimator method.

The PMSM modeling process is presented in Chapter 2 and the PMSM FOC method is presented in detail later is this chapter.

The DTC method was initially proposed by I. Takahashi and T. Noguchi [6] and is considered an improvement of the Direct Self Control (DSC) [7] method, able to compete with FOC [1]. In its first version, the DSC method is quite simple to implement using standard analog and logic devices [1, 7].

Figure 6.1 shows an example of a DTC method addressed to an IM.

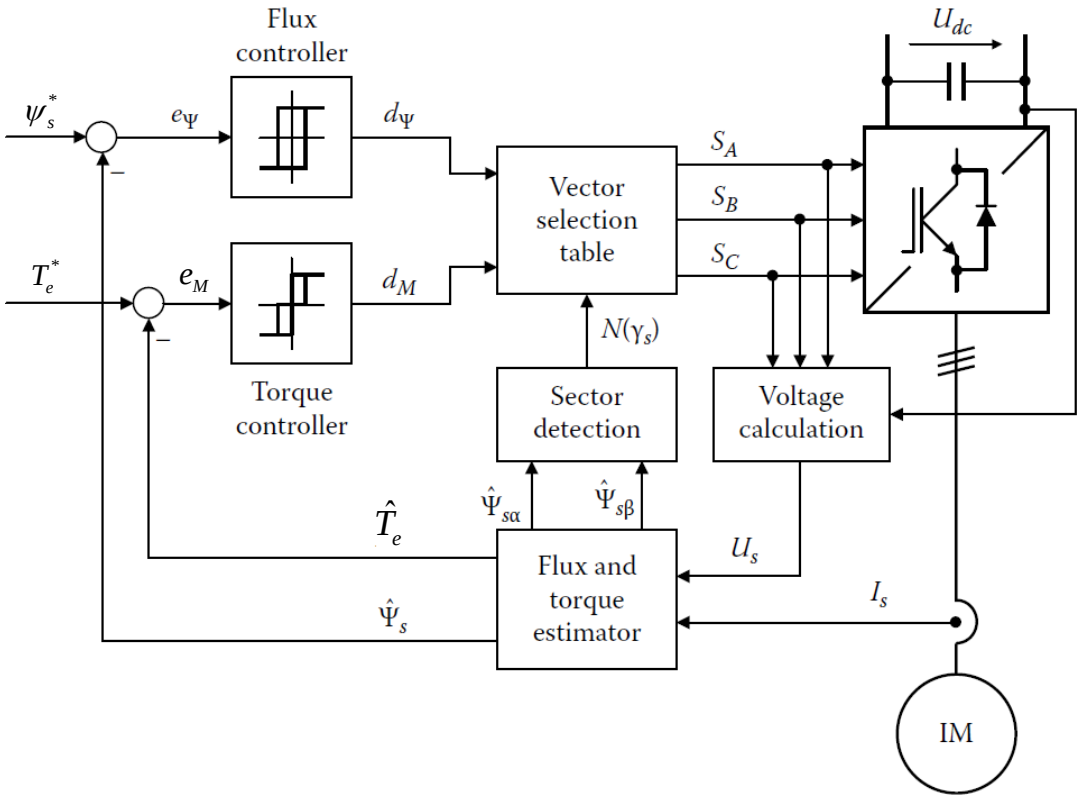

Figure 6.1 - Scheme of switching table based DTC method addressed to an IM [4]

The DTC is based on qualitative rules derived from the stator equation

$$v_s = R_s i_s + \frac{d\psi_s}{dt} \tag{6.1}$$

If the stator resistance is neglected, which is a valid approximation at medium/high speeds, then the variation of the stator flux is directly proportional to the stator voltage. On the other hand, the electromagnetic torque T_e can be controlled by

changing the relative angle between stator flux ψ_s and rotor flux ψ_f vectors (see Chapter 2). Therefore, controlling the stator voltage, and thus varying the stator flux vector position, it is possible to regulate the torque.

The decoupled control of stator flux and torque is achieved by acting on the $\alpha\beta$ components of the stator flux vector, by means of hysteresis regulators [1, 2].

A second generation of DTC oriented to digital implementation is computation intensive and incorporate predictive models of the machine, thus requiring the knowledge of the machine parameters. The advantages are an improved torque harmonic distortion and control of the switching frequency.

Table 6.1 shows a comparison between FOC and DTC methods. DTC has a faster dynamic response than FOC, and is a robust method simply to implement even in the presence of machine model uncertainties [1]. On the other hand, the hysteresis imposes a dynamic variation of the converter frequency that is function of torque and rotor speed. At low speed operation that frequency may descend to a few tens of Hz causing high intensity audible noise and low frequency torque harmonics that may stress the mechanical parts causing premature failure [1].

FOC method has a good dynamic response (but slower than DTC), smoother operation, fixed high frequency operation, low noise, low torque ripple and improved efficiency. A high degree of decoupling from torque and flux is achieved if the correct machine parameters are known. Traditionally the FOC method has been pointed as complex and requiring high performance MCUs. But with the continuing innovation in MCU technology FOC has become extremely affordable. This issue is reviewed with more detail in Chapter 7.

	DTC	FOC
Dynamic response for torque	Quicker	Slower
Steady-state behaviour for torque, stator flux and currents	High ripple and distortion	Low ripple and distortion
Parameter sensitivity	• For a sensorless estimator: R_s • For a non-sensorless estimator: L_{sd}, L_{sq} and Ψ	Decoupling depends on L_{sd}, L_{sq} and Ψ
Requirement of rotor position	No	Yes
Current control	No	Yes
PWM modulator	No	Yes
Coordinate transformation	No	Yes
Switching frequency	Variable, depending on the operating point and during transients	Constant
Audible noise	Spread spectrum, high noise especially at low speed	Low noise at a fixed frequency
Control tuning	Hysteresis bands	PI gains
Complexity and processing requirements	Lower	Higher

Table 6.1 - Summary of the comparison between FOC and DTC methods [2]

Choosing between DTC, FOC or other control method depends basically on the specific application and machine type. As an example, the lower inductance of the PMSM when compared to the IM results in higher torque harmonics due to faster current variation when DTC is employed. This is one of the main reasons to choose the FOC method over DTC to control the PMSG in the current application.

6.3 Field Oriented Control of a PMSM

The FOC is a vector control method that tries to orient the stationary flux or "stator" flux vector to a specific angle relative to the rotor flux vector. The optimal orientation angle depends basically on the characteristics of the PMSM rotor, i.e. its anisotropy, and on the parameters that needs to be maximized or minimized, i.e. the control strategy.

As exposed in Chapter 2, the interaction between stator flux ψ_s and rotor flux ψ_f can alternatively be viewed as the interaction between rotor flux and stator current i_s, as represented in Figure 6.2. In this "friendly" representation, the i_d component of i_s is responsible to strengthen ($i_d > 0$) or weaken ($i_d < 0$) the rotor flux (field), and the i_q component is responsible mainly for controlling the magnitude of the electromagnetic torque. Furthermore, a positive i_q refers to motoring operation, while a negative one refers to generator operation. In sum the FOC method aims to reorient the stator current i_s to follow its i_d^* and i_q^* desired component references.

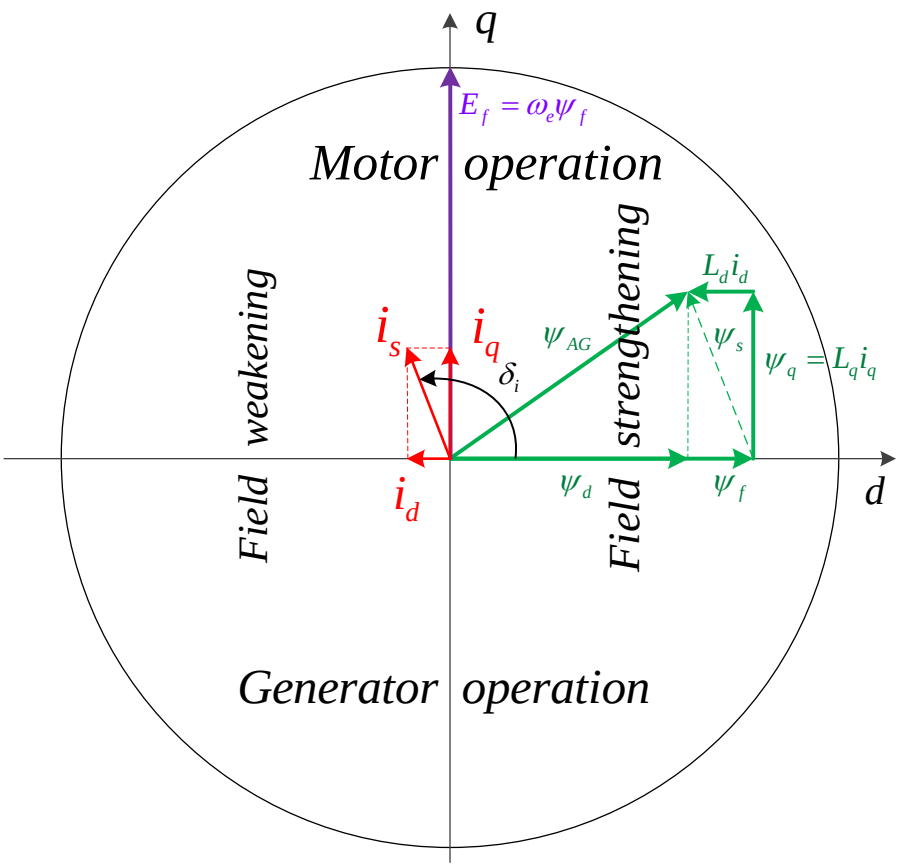

Figure 6.2 – The four PMSM operation modes as a function of the stator current i_s

6.3.1 Control Strategies Addressed to PMSMs

The main control strategies addressed to PMSM are [4, 8, 9]:

- Maximum Torque-per-Ampere Control (MTPA)
- Constant Torque-Angle Control ($\delta_i = 90^o \Rightarrow i_d^* = 0$)
- Flux-Weakening Control;
- Maximum Torque-per-Voltage Control (MTPV);
- Maximum Efficiency Control;
- Unity-Power-Factor Control;
- Constant-Mutual-Flux-Linkages Control.

Each control strategy is achieved by setting a pair of ($i_d^*; i_q^*$) current references to the FOC current-controller. The FOC current-controller is analyzed in detail in this chapter. The listed control strategies are detailed in the following sub-chapters.

6.3.1.1 Maximum Torque-per-Ampere Control

The most common use of FOC is to maximize the PMSM's Torque-per-Ampere (MTPA). This control strategy achieves the maximum power transfer (maximum torque), with minimum copper losses.

The PMSM electromagnetic torque is given by

$$T_e = \frac{3}{2} pp\left(\psi_f i_q + (L_d - L_q) i_d i_q\right) \tag{6.2}$$

where L_d and L_q are the PMSM characteristic inductances and pp is the number of pole pairs.

The maximum torque is achieved for the torque angle $\delta_{i\max}$ (see Chapter 2)

$$\delta_{i\max} = \cos^{-1} \frac{-\psi_f \pm \sqrt{\psi_f^2 + 8\left(L_d - L_q\right)^2 i_s^2}}{4\left(L_d - L_q\right) i_s} \tag{6.3}$$

where the i_s components are given by

$$\begin{aligned} i_d &= i_s \cos\delta_i \\ i_q &= i_s \sin\delta_i \end{aligned} \tag{6.4}$$

For Anisotropic PMSM rotors where $L_d < L_q$ the MTPA operation is achieved with a (small) negative i_d, which corresponds to a flux weakening operation region. The MTPA control strategy is exemplified in Figure 6.3 for a PMSG.

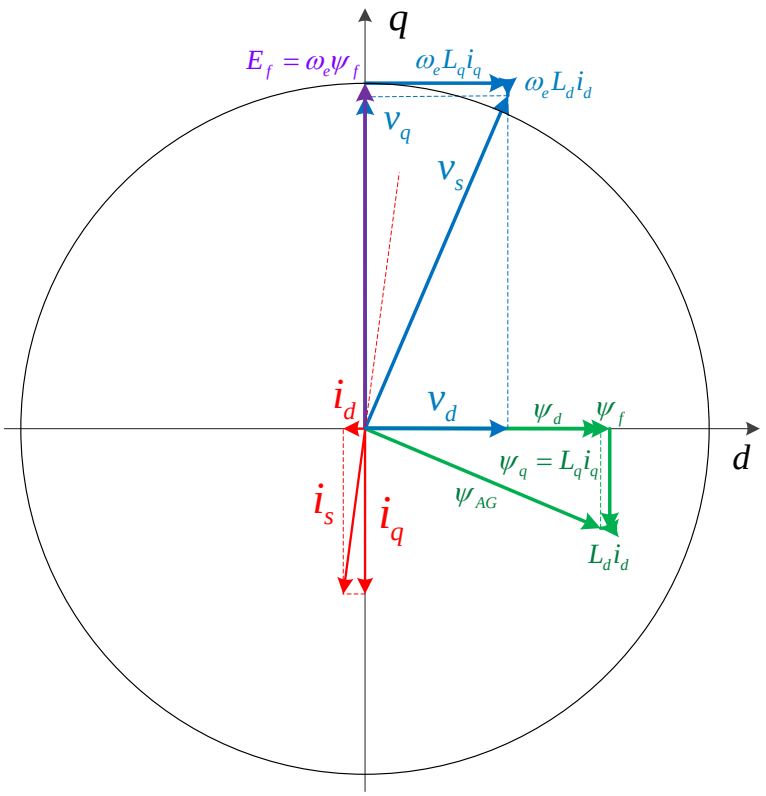

Figure 6.3 - PMSG with MTPA control – example

6.3.1.2 Constant-Angle Control ($\delta_i = 90^o \Rightarrow i_d^* = 0$)

In the Constant-Angle Control strategy, the torque angle is maintained at 90 degrees ($\delta_i = 90^o$), so the i_d current is set to be zero. In this case the electromagnetic torque is simply given by

$$T_e = \frac{3}{2} pp \psi_f i_q \tag{6.5}$$

The electromagnetic torque is a function of i_q only. With this strategy the control is simplified (as only one parameter, i_q, has to be set), by wasting the reluctance torque that is given by

$$T_{rel} = \frac{3}{2} pp(L_d - L_q) i_d i_q \tag{6.6}$$

For PMSM Isotropic rotors, $L_d = L_q$, and the general torque expression (6.2) simplifies to (6.5). The MTPA control strategy becomes the Constant-Angle Control strategy. This is the control strategy used in many PMSM drives for speeds lower than the nominal one.

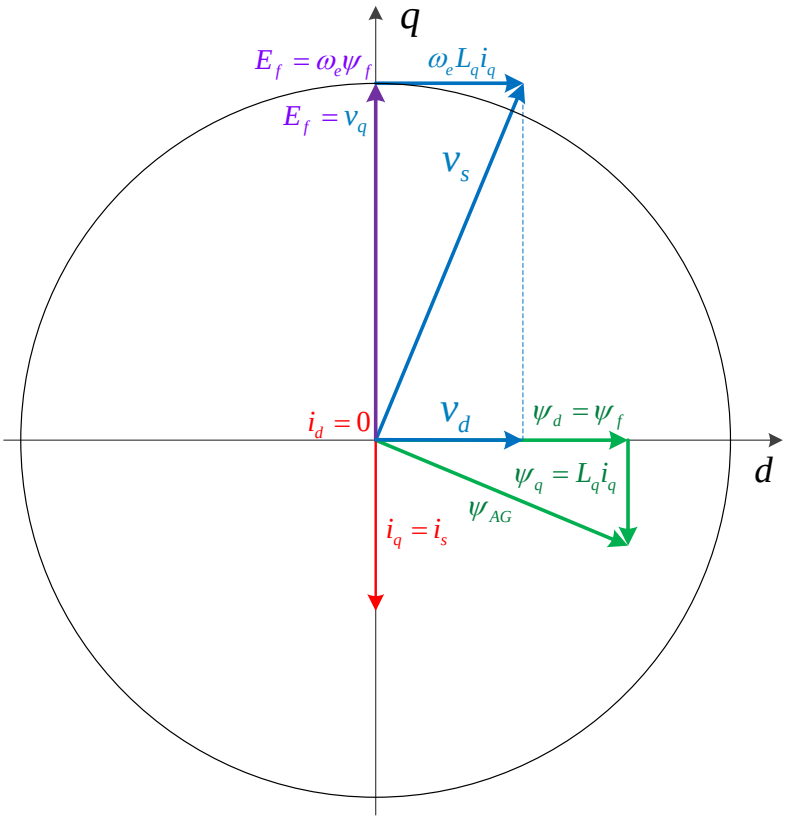

Figure 6.4 - PMSG with Constant-Angle Control ($\delta_i = 90^o \Rightarrow i_d^* = 0$)

6.3.1.3 Flux-Weakening Control

The flux-weakening control is a strategy used mainly to control PMSMs operated as motors at speeds higher than the nominal one. Above the nominal speeds the electromotive-force $E_f = \omega_e \psi_f$ exceeds the maximum input voltage v_s, making the current flow into the machine phases impractical. To overcome this issue the solution is to weak the air-gap flux linkages by increasing the negative i_d current component. Figure 6.5 exemplifies this control strategy for a PMSM where the $\omega_e L_d i_d$ voltage is the main responsible to reduce the voltage v_s needed at the machine terminals.

Normally the flux-weakening is controlled to be inversely proportional to speed. The immediate consequence of this strategy is that the available torque decreases as the rotor speed increases.

As viewed before, some degree of flux-weakening is desirable to achieve the MTPA control strategy for PMSMs with anisotropic rotors, even for speeds below the nominal one. The UPF control is another strategy that takes advantage from the flux weakening even for speeds below the rated one as it can be seen later is this chapter.

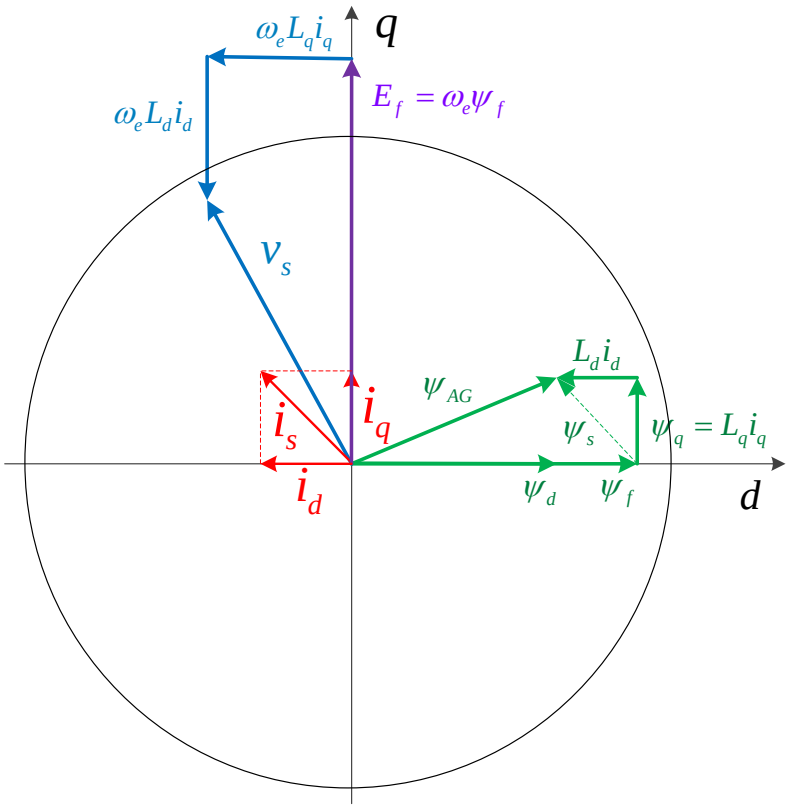

Figure 6.5 - PMSM operated as a motor with Flux-Weakening control

6.3.1.4 Unity-Power-Factor Control

In UPF control the power factor at the PMSM terminals is one. No reactive energy flows between the PMSM and the power converter. The VA rating of the power converter is fully used.

This control strategy does not allow achieving the maximum electromagnetic torque or, from another point of view, to transfer the maximum power from or to, the PMSM. As Figure 6.6 and Figure 6.7 show, whether the PMSM is operated as a generator or motor, this control strategy is achieved in the flux weakening zone.

6.3.1.5 Maximum Torque-per-Voltage Control

For a given electromagnetic torque there is an optimal operating point that minimizes the air-gap flux ψ_{AG}. This can be viewed as the Maximum Torque-per-Flux (MTPF) [4] or, in other words, the Maximum Torque-per-Voltage control (MTPV) [10]. This control strategy minimizes iron losses and gives optimum control for PMSMs when the maximum PMSM terminal voltage is reached [4].

6.3.1.6 Maximum Efficiency Control

The Maximum Efficiency Control strategy aims at minimizing PMSM copper and iron losses. As viewed before the MTPA control strategy minimizes the copper losses and the MTPV minimizes the iron losses, so the total losses are minimized at an optimal power angle between MTPA and MTPV [4]. This corresponds to the Maximum Efficiency Control.

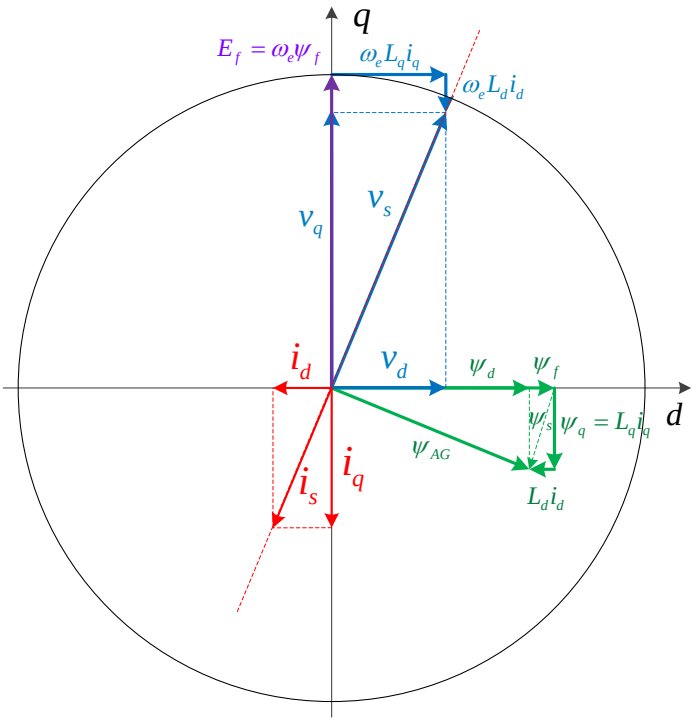

Figure 6.6 - PMSG with UPF control

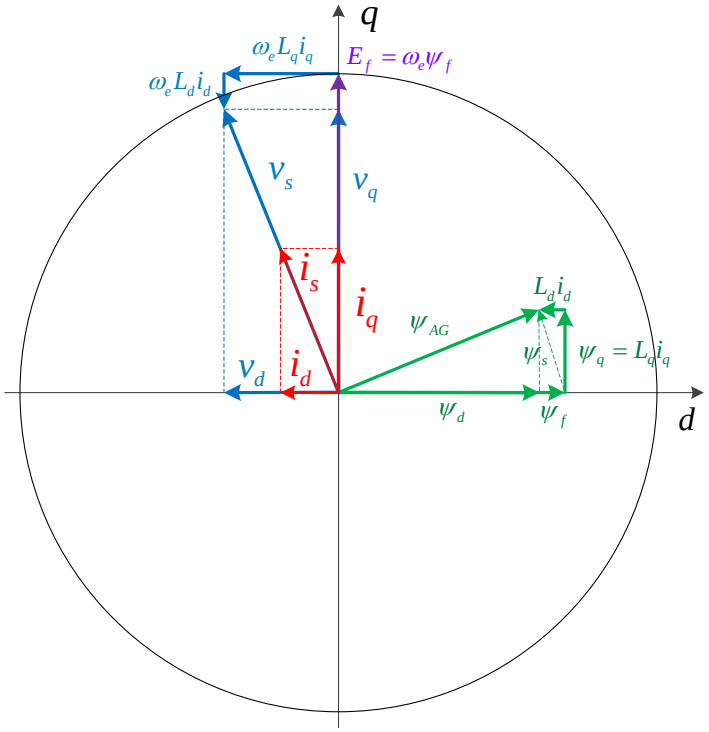

Figure 6.7 - PMSM operated as a motor with UPF control

To calculate the PMSM total losses a more accurate PMSM model, including the iron (or core losses), is required. An example of that model is described in Figure 6.8. A new resistance R_c is included representing the iron losses.

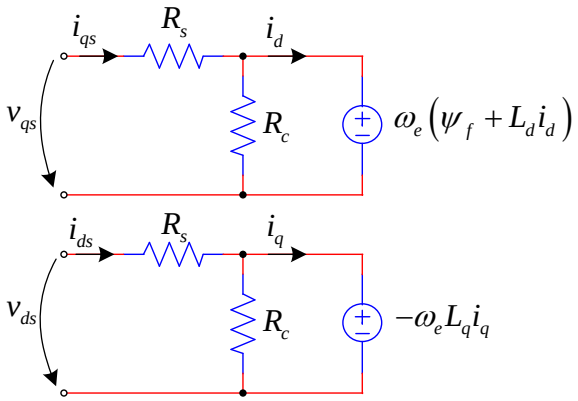

Figure 6.8 - PMSM model including stator and iron loss resistances

According to [9] the total PMSM power losses, including both copper and iron losses can be described by

$$P_{losses} = \frac{3}{2} R_s \left(i_{ds}^2 + i_{qs}^2\right) + \frac{3}{2} \frac{\omega_e^2}{R_c} \left(\left(L_q L_q\right)^2 + \left(\psi_f + L_d L_d\right)^2\right) \tag{6.7}$$

The difficulty in applying such models is that normally the data related to iron losses is not made available at the manufacturer's datasheets.

6.3.2 PMSM FOC Current-controller

As viewed in the previous subchapter, implementing whatever desired PMSM control strategy implies to reorient the current vector i_s to a specific position relative to the rotor flux. This is achieved by adjusting i_d and i_q components of i_s though a current-controller. The current-controller is also known as a Flux and Torque controller.

As described in Chapter 2 the equations that characterize PMSM dynamic behavior in the dq frame, excluding the iron losses, are

$$\begin{aligned} v_d &= R_s i_d + \frac{d\psi_d}{dt} - \omega_e L_q i_q \\ v_q &= R_s i_q + \frac{d\psi_q}{dt} + \omega_e \left(L_d i_d + \psi_f\right) \end{aligned} \tag{6.8}$$

and since $\psi_d = L_d i_d + \psi_f$ and $\psi_q = L_q i_q$

$$
\begin{aligned}
v_d &= R_s i_d + \frac{d}{dt}\left(L_d i_d + \psi_f\right) - \omega_e L_q i_q \\
v_q &= R_s i_q + \frac{d}{dt} L_q i_q + \omega_e \left(L_d i_d + \psi_f\right)
\end{aligned}
\tag{6.9}
$$

which leads to

$$
\begin{aligned}
v_d &= R_s i_d + L_d \frac{d}{dt} i_d - \omega_e L_q i_q \\
v_q &= R_s i_q + L_q \frac{d}{dt} i_q + \omega_e \left(L_d i_d + \psi_f\right)
\end{aligned}
\tag{6.10}
$$

And, in the frequency domain,

$$
\begin{aligned}
v_d &= \left(R_s + sL_d\right) i_d - \omega_e L_q i_q \\
v_q &= \left(R_s + sL_q\right) i_q + \omega_e \left(L_d i_d + \psi_f\right)
\end{aligned}
\tag{6.11}
$$

which can take the form

$$
\begin{aligned}
i_d &= \left(v_d + \omega_e L_q i_q\right) \frac{1}{R_s + sL_d} \\
i_q &= \left(v_q - \omega_e L_d i_d - \omega_e \psi_f\right) \frac{1}{R_s + sL_q}
\end{aligned}
\tag{6.12}
$$

where $E = \omega_e \psi_f$, i.e. the internal voltage (EMF or Back-EMF).

Combining equations (6.12) and (6.2), leads to the Laplace PMSM model presented in Figure 6.9

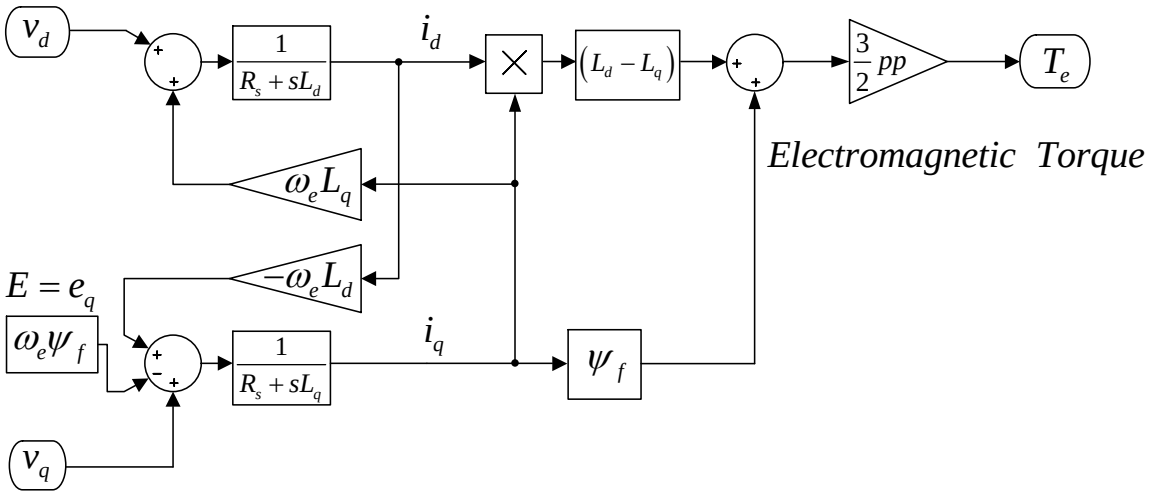

Figure 6.9 - PMSM Laplace model

To design a suitable decoupled current-controller and following the same reasoning described in Chapter 3, the transformer voltages of equation (6.8):

$$\frac{d\psi_d}{dt};\ \frac{d\psi_q}{dt} \tag{6.13}$$

are replaced by PI controllers, resulting in

$$\begin{aligned} v_d &= R_s i_d + \Delta v_d - \omega_e L_q i_q \\ v_q &= R_s i_q + \Delta v_q + \omega_e \left(L_d i_d + \psi_f \right) \end{aligned} \tag{6.14}$$

where Δv_d and Δv_q are the control actions of the PI controllers, given by

$$\begin{cases} \Delta v_d = k_p \left(i_d^* - i_d \right) + k_i \int \left(i_d^* - i_d \right) dt \\ \Delta v_q = k_p \left(i_q^* - i_q \right) + k_i \int \left(i_q^* - i_q \right) dt \end{cases} \tag{6.15}$$

The i_d^* and i_q^* are the current references according to control strategy adopted. The current-controller receives the currents i_d and i_q from the PMSM phases after proper reference frame transformation and generate v_d and v_q command output voltages that are the correspondent inputs of the power converter modulator.

A suitable decoupled current-controller is presented in Figure 6.10. The current-controller decoupling paths are $\omega_e L_d$ and $-\omega_e L_q$. Notice that these controller decoupling paths cancel the same coupling paths observed inside the PMSM model of Figure 6.9.

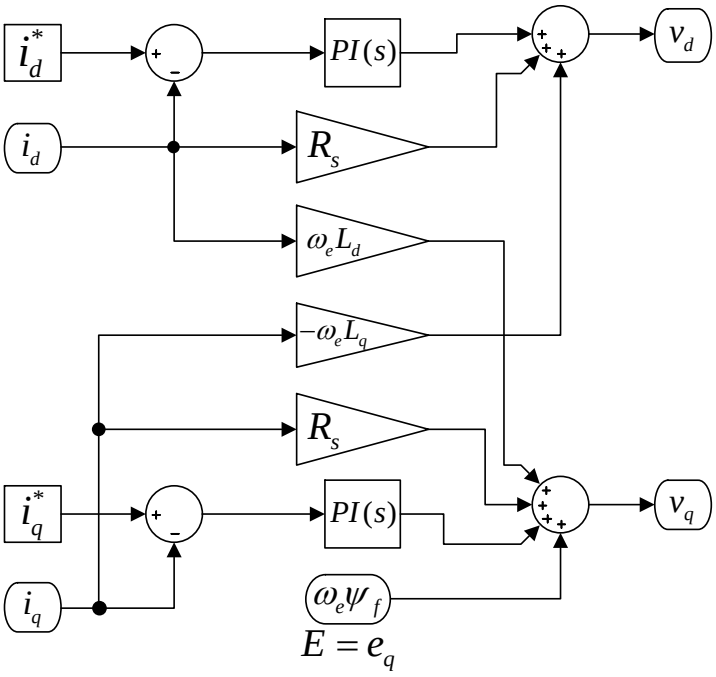

Figure 6.10 - PMSM decoupled current-controller or Flux and Torque controller

To achieve an effective control over the PMSM the following machine parameters have to be known:

- the direct and quadrature inductances L_d, L_q;
- the stator phase resistance R_s;
- the PM flux or field flux ψ_f;
- the machine pole pairs pp.

Also the following measurements have to be performed at a specific rate:

- the phase currents $i_{ab(c)}$ to obtain the currents i_d, i_q;
- the electric angle θ_e to perform reference frame transformations;
- the electrical speed ω_e;

The velocity and rotor position can be measured by means of a sensor placed on the shaft (normally a resolver or an encoder), or by estimating these variables as described in Chapter 5.

Figure 6.11 shows a sensor based FOC control block schema and Figure 6.12 shows its sensorless equivalent, exclusively based on current measurements.

As discussed before, the PMSM can be operated either as a motor or generator.

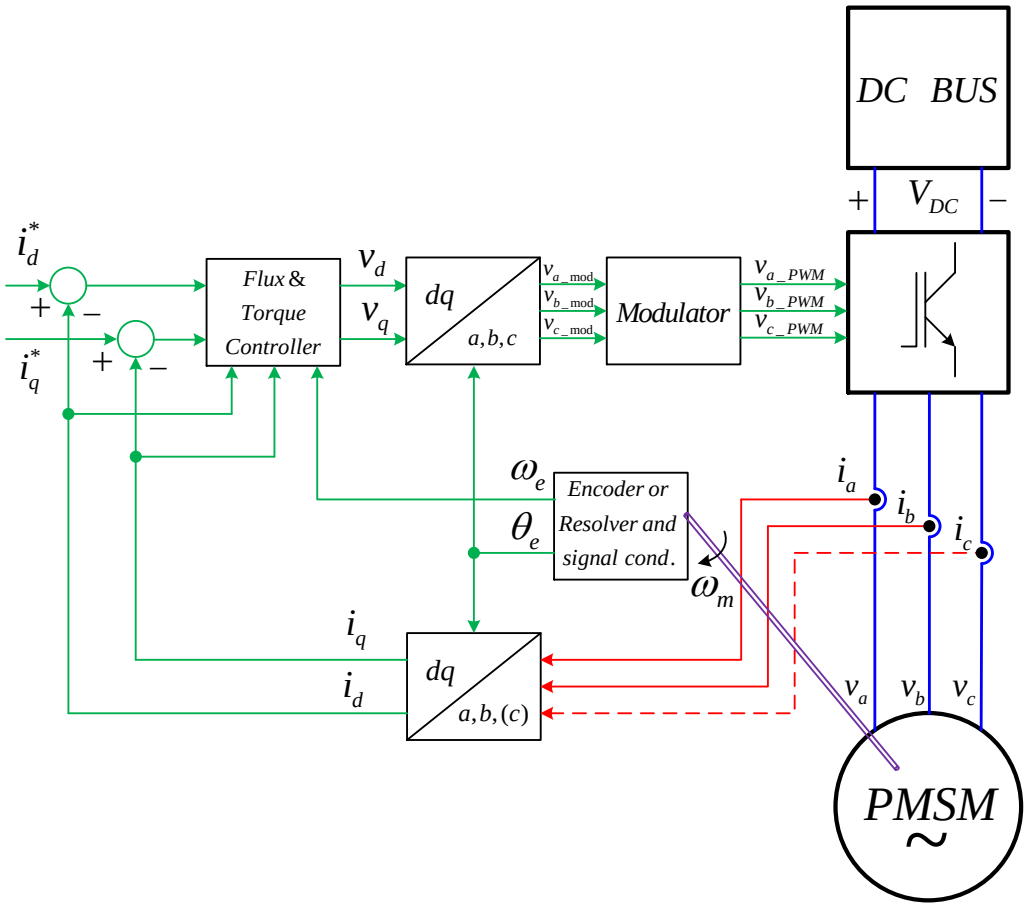

Figure 6.11 - PMSM sensor based FOC control schema

6.4 The EMRAX 228 High Voltage PMSM

The PMSM EMRAX 228 High Voltage (2013 version) was made available to perform practical experimental analysis within this work.

The EMRAX 228 High Voltage (shown in Figure 6.13), originally designed for avionics industry, is a Patented Pancake axial flux PMSM that can be operated as motor or generator. It is characterized by having high-power, high-torque, high power density (extremely light), high-speed and low noise. Its efficiency achieves 96% according to the manufacturer [11] (see Figure 6.15). The 2013 version, used in the experimental part of this work, presents a Permanent Magnet's flux magnitude (field flux) of 0.053 Wb (current version has 0.0542 Wb).

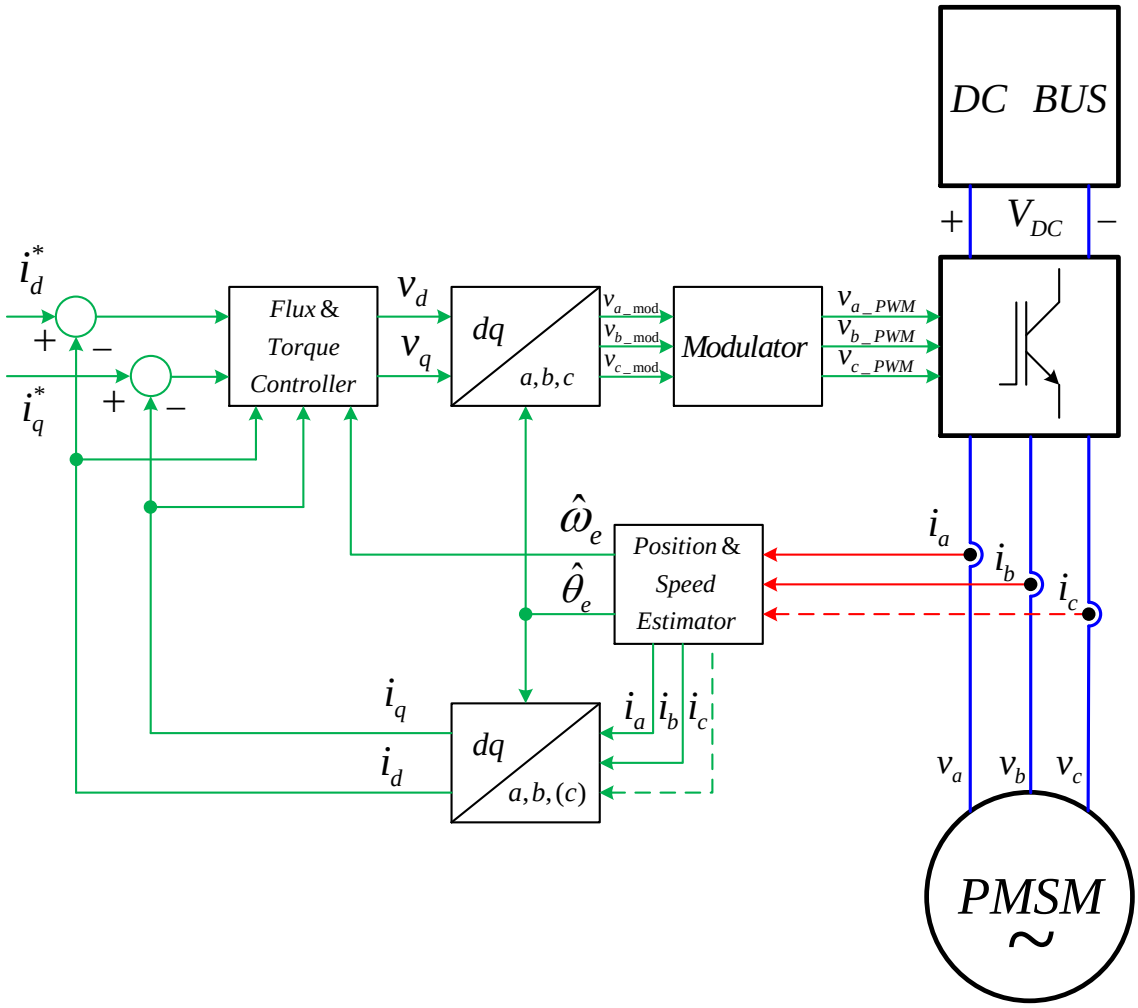

Figure 6.12 - PMSM sensorless FOC control schema based on current measurements

Figure 6.13 - The EMRAX PMSM 228 High Voltage [11]

Some relevant characteristics provided by EMRAX's manufacturer are shown in Figure 6.14, Figure 6.15, Figure 6.16 and Figure 6.17.

According to the manufacturer the EMRAX can be operated with a Liquid Cooling (LC) circuit or without it, i.e. Air Cooled (AC). In this latter case, the continuous power shown on Figure 6.14 must be reduced by 20%.

Figure 6.13 shows a picture of an EMRAX 228 HV. Power terminals, liquid cooling circuit, temperature sensor terminals, and a shaft position sensor are shown. However, the EMRAX used in this work does not have the shaft position sensor.

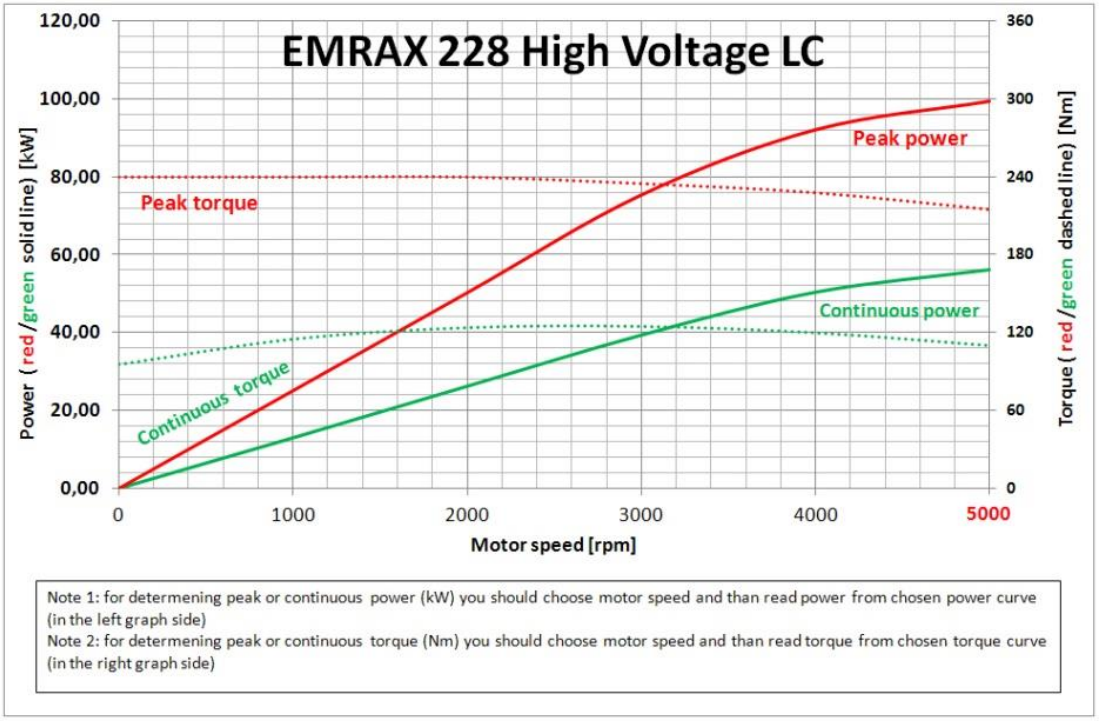

Figure 6.14 - EMRAX 228 High Voltage LC – Torque, Power and Speed curves [11]

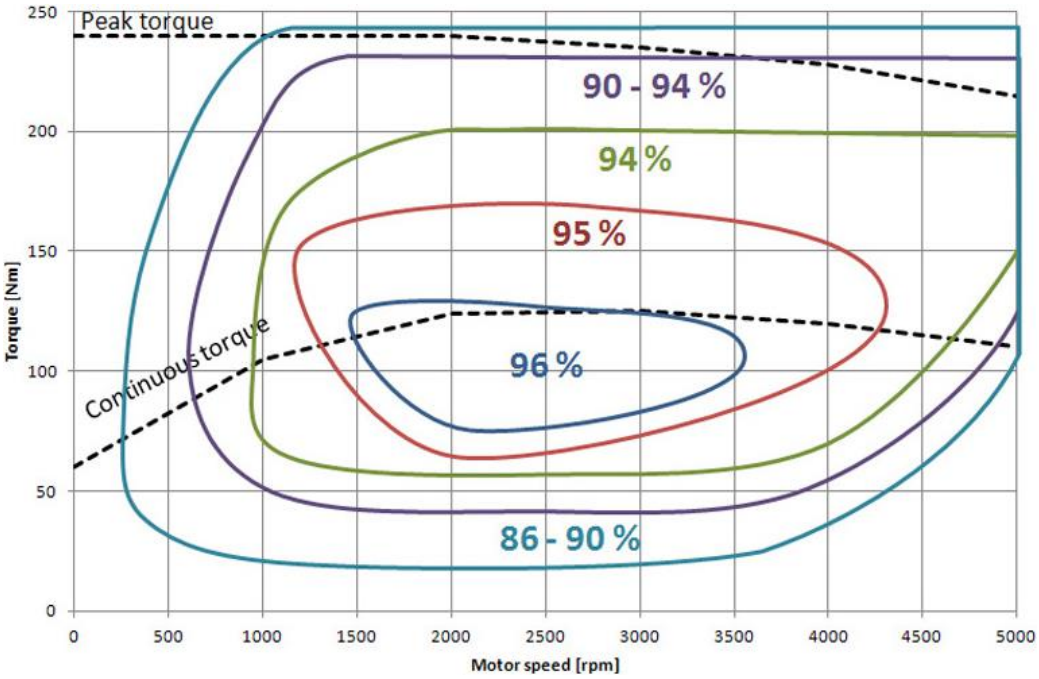

Figure 6.15 - EMRAX 228 High Voltage Liquid Cooled - Efficiency Map [11]

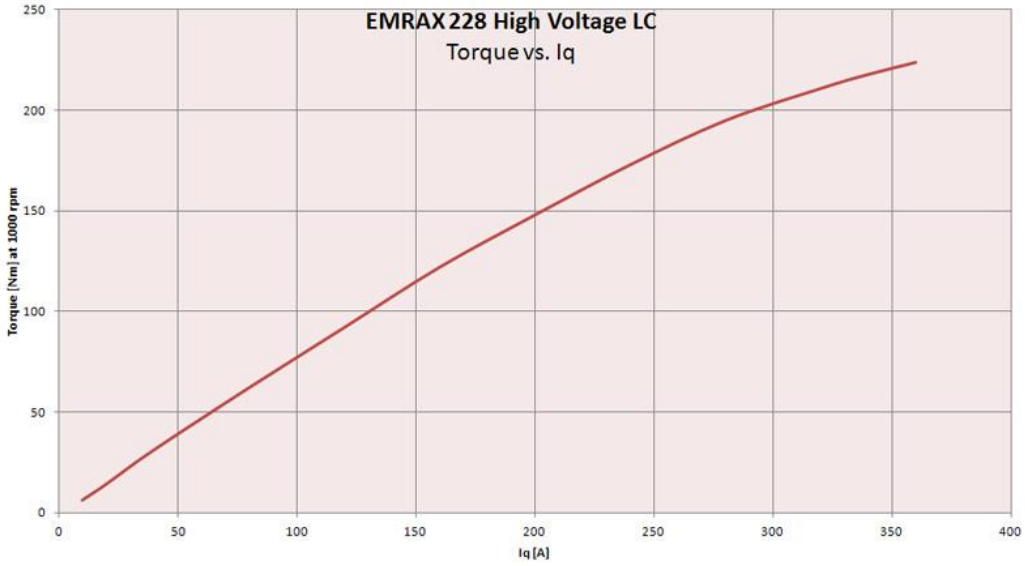

Figure 6.16 - EMRAX 228 High Voltage Liquid Cooled - Torque vs *Iq* [11]

To perform the experimental part of this work with the EMRAX PMSM some relevant data is extracted from the datasheet [11]:

- $L_d = 175 \mu H$;
- $L_d = 180 \mu H$;
- Number of pole pairs $pp = 10$;
- Field flux $\psi_f = 0.053\ Wb$ (from the 2013 version datasheet).

Type / Technical data	EMRAX 228 High Voltage		EMRAX 228 Medium Voltage		EMRAX 228 Low Voltage	
Cooling (AC – Air Cooled; LC – Liquid Cooled)	LC	AC	LC	AC	LC	AC
Cooling medium spec.	water flow speed 0,2 l/s; 20 °C	air flow speed 25 m/s; 20 °C	water flow speed 0,2 l/s; 20 °C	air flow speed 25 m/s; 20 °C	water flow speed 0,2 l/s; 20 °C	air flow speed 25 m/s; 20 °C
Weight [kg]	12,3	12,0	12,3	12,0	12,3	12,0
Diameter ø / width [mm]	228 / 86					
Battery voltage range [Vdc]	50 – 400 (*600)		50 – 350 (*450)		24 – 100 (*140)	
Peak motor power (few min at cold start / few seconds at hot start) [kW]	**100**					
Continuous motor power (depends on the motor RPM) [kW]	30 - 50	25 - 40	30 - 50	25 - 40	30 - 50	25 – 40
Maximal rotation speed [RPM]	4000 (*5000) (**6000)					
Maximal motor current (for 2 min if cooled as described in Manual for EMRAX) [Arms]	240		320		900	
Continuous motor current [Arms]	115		160		450	
Maximal motor torque (for a few seconds) [Nm]	240					
Continuous motor torque [Nm]	125					
Torque / motor current [Nm/1Aph rms]	**1,1**		**0,75**		**0,27**	
Maximal temperature of the copper windings in the stator and also max. temp. of the magnets [°C]	120					
Nominal motor efficiency [%]	93 - 96					
Internal phase resistance at 25 °C [mΩ]	18		8,0		1,12	
Input phase wire cross-section [mm²]	10,2		15,2		38	
Induction in d/q axis [µH]	Ld=175 Lq=180		Ld=75 Lq=80		Ld=10,6 Lq=11,2	
Controller / motor signal	sine wave					
Specific idle speed (no load RPM) [RPM/1Vdc]	9,8		14		40	
Specific load speed (depends on the controller settings) [RPM/1Vdc]	8 – 9,8		11 – 14		34 – 40	
Magnetic field weakening (for higher RPM at low torque) [%]	up to 20					
Magnetic flux – axial [Vs]	0,0542		0,0355		0,0131	
Temperature sensor in the motor	kty 81/210					
Number of pole pairs	10					
Rotor inertia (mass dia=175mm, m=5,5kg) [kg*cm²]	421					
Bearings SKF _ FAG	R/R 6206/6206 or R/AR 6206/7206 or AR/AR 7206/7206 (»O« orientation)					
Ingress protection	IP21 / IP54***	IP21	IP21 / IP54***	IP21	IP21 / IP54***	IP21

*Tested in Enstroj for a few minutes.
**Tested in Enstroj for a few seconds.
*** We can also make IP54, but load time is shorter and continuous power is approximately 20 to 30% lower compared to IP21. Peak

Figure 6.17 - EMRAX 228 Technical Data Table [11]

6.5 Design of the Experimental Setup

The experimental setup is designed in order to extract the maximum torque available at the Internal Combustion Engine (ICE) shaft converting it to power available at the DC bus.

A generic experimental setup should include:

- an Internal Combustion Engine (ICE);
- a three-phase PMSG;
- a power electronics converter;
- a DC bus.

Selecting an ICE is out of the scope of this work. However, to know the ICE basics is very helpful in defining system parameters and control strategies. Figure 6.18 shows power, torque and fuel consumption typical curves for a Daewoo Matiz F8C engine chosen as an example. To extract the maximum torque with affordable fuel consumption, the shaft speed must be located around $4200\ rpm$.

The engine torque peak and power peak are respectively 7 Kgm (68.7 Nm) and 52 PS (38.8 kW). At $4200\ rpm$ the torque is almost 7 Kgm (68.7 Nm) and the power is near 41.5 PS (31 kW).

To have minimal mechanical losses, it is assumed a direct coupling (no gear box), between the ICE and the PMSM. In this way, the PMSM would also work, at this speed with minimal losses (copper and iron losses).

Consulting the EMRAX LC curves some relevant information is obtained: the PMSM can be operated at up to $5000\ rpm$; At $4200\ rpm$ the torque can be up to $120Nm$ at 52kW of continuous power, having 95% efficiency (96% is the maximum).

In short, for this couple running at $4200\ rpm$, the EMRAX LC would be used at (31kW/52kW)=60% of its rated power for this speed or at (31kW/(0.8x52kW))=75% of its rated power if air cooled is adopted.

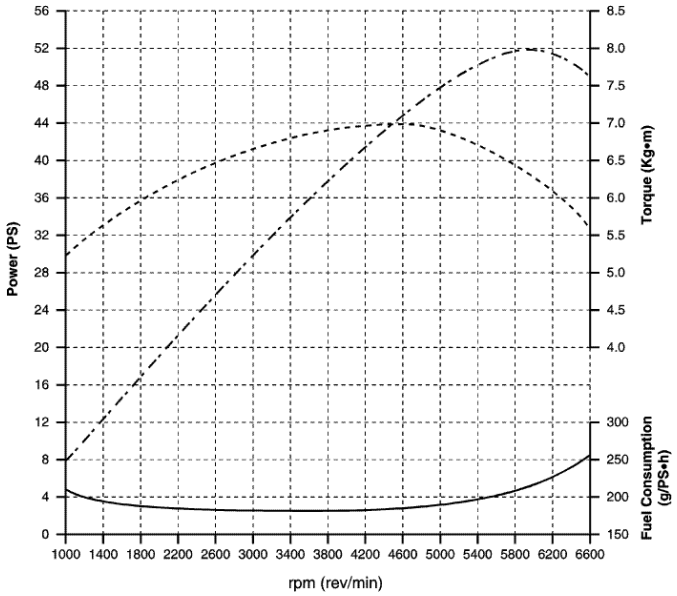

Figure 6.18 - Daewoo Matiz F8C ICE – Power, Torque and Fuel curves [12]

6.5.1 DC Bus Considerations

The DC bus has to be specified according to many factors where the ICE and PMSG characteristics are probably the less significant part. The DC bus voltage is more likely to be defined in accordance to the traction motors adopted. Voltages between 300V and 600V are currently used with the 600V DC bus rapidly becoming a standard in the automotive industry.

The question to answer now is: which is the minimum DC bus voltage to work with this experimental setup?

The answer depends on some variables, of which the control strategy and the modulation technique adopted are the more relevant.

The PMSM internal voltage vector is given by $E = \omega_e \psi_f$. As $\omega_m = 4200\ rpm$ corresponds to $\omega_e = 4398$ rad/s, then $E = 4398x0.053 = 233.1V$ (physically E is the single-phase peak voltage measured at the machine terminals at no-load condition).

If a MTPA control strategy is adopted, the PMSG single-phase terminal voltage vector is $V = 241.4V$ @ P=31KW as it can be seen in Table 6.2.

If a space vector modulation is adopted ($M \leq 0.9069$), then the minimum DC bus voltage must be

$$V_{DC} \geq \frac{\pi}{2}\frac{V}{M} = \frac{\pi}{2}\frac{241.4}{0.9069} = 419V \tag{6.16}$$

For higher speeds a higher DC bus voltage is required.

If a 600V DC bus is adopted, the modulation index for this particular operating point is

$$M = \frac{\pi}{2}\frac{v}{V_{DC}} = \frac{\pi}{2}\frac{241,4}{600} = 0.63 \tag{6.17}$$

EMRAX 228 PMSM working as a generator (current vector "I" is negative)										
Field flux	0,053									
Rs	0,018									
Ld	0,000175				Vd	70,21				
Lq	0,00018				Vq	230,94				
Pole pairs	10				V=sqrt(Vd^2+Vq^2)	241,37				
Wm (rpm)	4.200,00	Shaft speed			(V is the PMSM terminal voltage vector)					
We (rad/s)	4.398,23	Electrical speed			E=We.Field flux	233,11				
I (current vector)	-88,700	I=sqrt(Id^2+Iq^2)			(E is the PMSG Internal voltage vector)					
Control strategie: MTPA					Active and Reactive Power at PMSM terminals					
Id and Iq to maximize the torque per ampere					P=3/2(VdId+VqIq)	-30.803,43				
Torque angle (rad)	-1,5791632				Q=3/2(VdIq-VqId)	-9.083,54	Capacitive			
Torque angle (deg)	-90,479									
Id	-0,742				Active and Reactive Power referred to the PMSM internal voltage E					
Iq	-88,697				P=3/2(Eiq)	-31.013,69				
Torque (electrical)	-70,519				Q=-3/2(Eid)	259,49	Inductive			

Table 6.2 - Calculations for an EMRAX PMSG w/ MTPA Control and 31KW @ 4200rpm

6.5.2 Experimental Setup Adopted

The experimental setup adopted for this work includes:

- a two-pole pair Induction Motor (IM) that replaces the ICE, controlled by an autotransformer, rotating at speeds up to near $1500\ rpm$;
- an EMRAX 228 High Voltage (2013 version), directly coupled to the IM;
- a DC bus with a battery bank of $300V / 400m\Omega$;
- a three-phase IGBTs power module;

- a $500\mu F / 1m\Omega$ ESR capacitor;
- two LEM current sensors with a transformation ratio of $30mV / A$.

The complete experimental setup is described in more detail in Chapter 7. For now this is the relevant data needed to perform simulation analysis of the system.

Figure 6.19 shows a PSIM model of the adopted experimental setup. Figure 6.20 lists the PMSG parameters. All electrical parameters can be obtained directly from the EMRAX datasheet except the $Vpk / krpm$ voltage. The $Vpk / krpm$ voltage is the phase-to-phase peak voltage at no load condition when the shaft speed is $1000\ rpm$. Since $\omega_m = 1000\ rpm$ corresponds to $\omega_e = 1047.2\ rad/s$, then the phase peak voltage is $E = \omega_e \psi_f = 1047.2x0.053 = 55.5V$ leading to a phase-to-phase peak voltage $Vpk / krpm = \sqrt{3}E = 96.13137V$. This value was experimentally confirmed by measuring the voltage terminals when the PMSG is running at $1000\ rpm$.

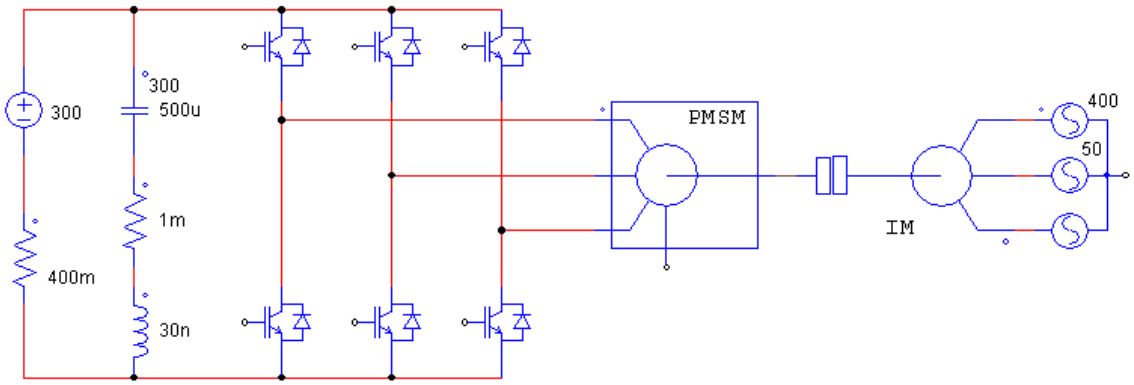

Figure 6.19 - PSIM representation of the setup used to perform system's analysis

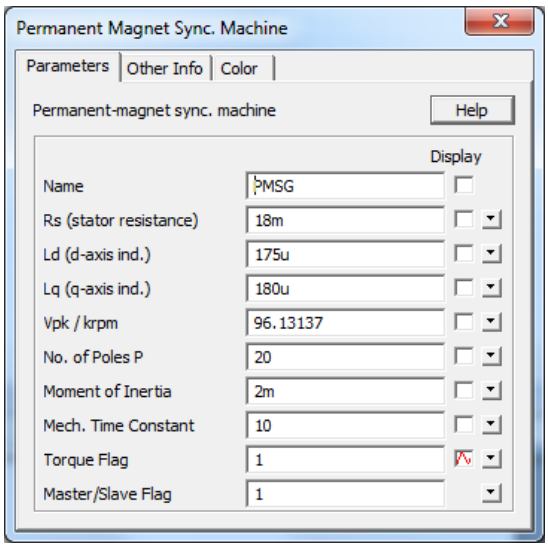

Figure 6.20 - PSIM parameters used to simulate the EMRAX PMSG

6.6 Sensor-Based FOC of a PMSM

A basic FOC controlled PMSM is presented in Figure 6.23. It includes the above described experimental setup of Figure 6.19 and a sensor attached to the shaft outputting rpm speed. The mechanical speed ω_m is then converted in electrical speed ω_e which, after integration, gives θ_e.

The phase currents are acquired, filtered and a Park's transform applied to obtain the currents in the dq frame. Those currents are compared with their references and the errors applied to PI controllers, which are parts of the decoupled current-controller (see Figure 6.10). The current-controller outputs v_d and v_q are, after inverse Park's transform, the modulator signals applied to the SPWM with a 20kHz carrier. The SPWM outputs are the switching signals applied to the IGBT's gates.

The schema includes two additional circuits to improve system's observability: (1) the machine internal voltages e_a, e_b, e_c are obtained through the circuit of Figure 6.21. Knowing that $E = \omega_e \psi_f$, then an inverse Park's transform is applied to obtain those voltages; (2) a $10k\Omega$ three-phase star resistive load (see Figure 6.22) is attached to the PMSG terminals to observe phase-to-neutral terminal voltages $v_a v_b v_c$, as well as the phase-to-neutral filtered voltage v_{a_filt}. This last voltage gives an idea (not the exact value) of the phase angle and phase amplitude to be compared with the internal voltage e_a and with the line current i_a.

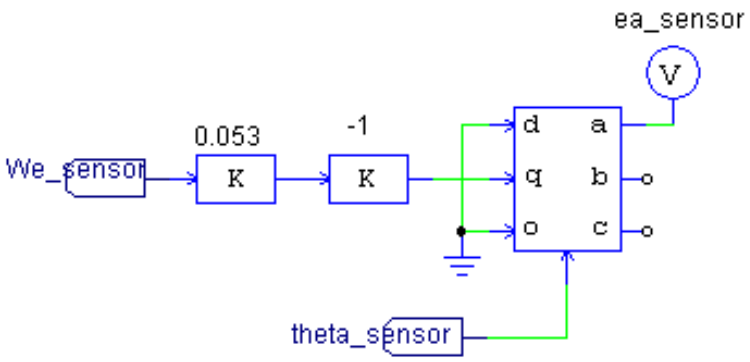

Figure 6.21 - PMSM internal voltages generation

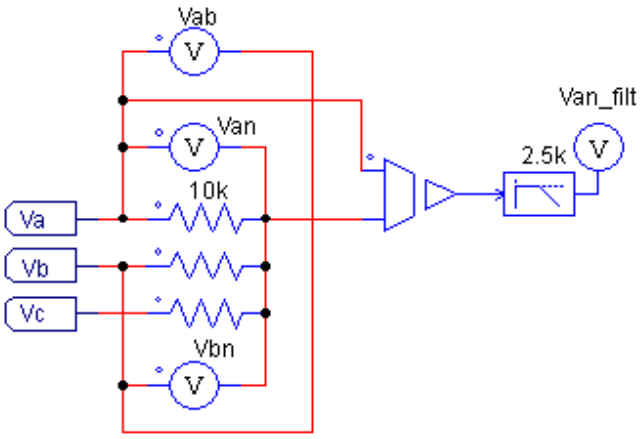

Figure 6.22 - PMSM terminal voltages measurements

The PI controllers were initially adjusted with the help of MATLAB Simulink through PSIM SimCoupler's interface to MATLAB.

The control strategy adopted for this analysis is the constant-angle-control where $i_d^* = 0$ (the field flux is maintained as constant). The current i_q is the only one responsible for counteract the torque generated by the IM that, in this particular case, is given by $T_e = \frac{3}{2} pp\psi_f i_q$.

While the IM does not achieve its nominal speed, (a little less than $1500\ rpm$, which corresponds to a line frequency of 250Hz), the i_q^* reference is set at -4A and later, at specific times, -21A, -40A and again back to -4A. The "-" sign denotes that the PMSM is controlled as a generator.

The simulation results presented on Figure 6.24 show the dynamic behavior of this arrangement. The i_d and i_q currents accurately follow its references i_d^* and i_q^* with no overshoots or undershoots. The internal single-phase e_a is in phase with i_a, as expected, and when step changes on i_q^* are introduced an almost instantaneous adjustment in the phase current's magnitude is observed. The V_{DC} voltage includes some high frequency harmonics related to switching operation that the $500\mu F$ capacitor is unable to filter. The small increase in V_{DC} is due to the battery's internal voltage drop when the i_{DC} charging current increases.

A zoom over the zone where the i_q^* step changes occur is presented on Figure 6.25 to better show the system's dynamics, particularly the i_a current dynamics.

This sensor based FOC has optimum dynamics and therefore is excellent to be used as a reference model in comparison with other equivalent sensorless implementations.

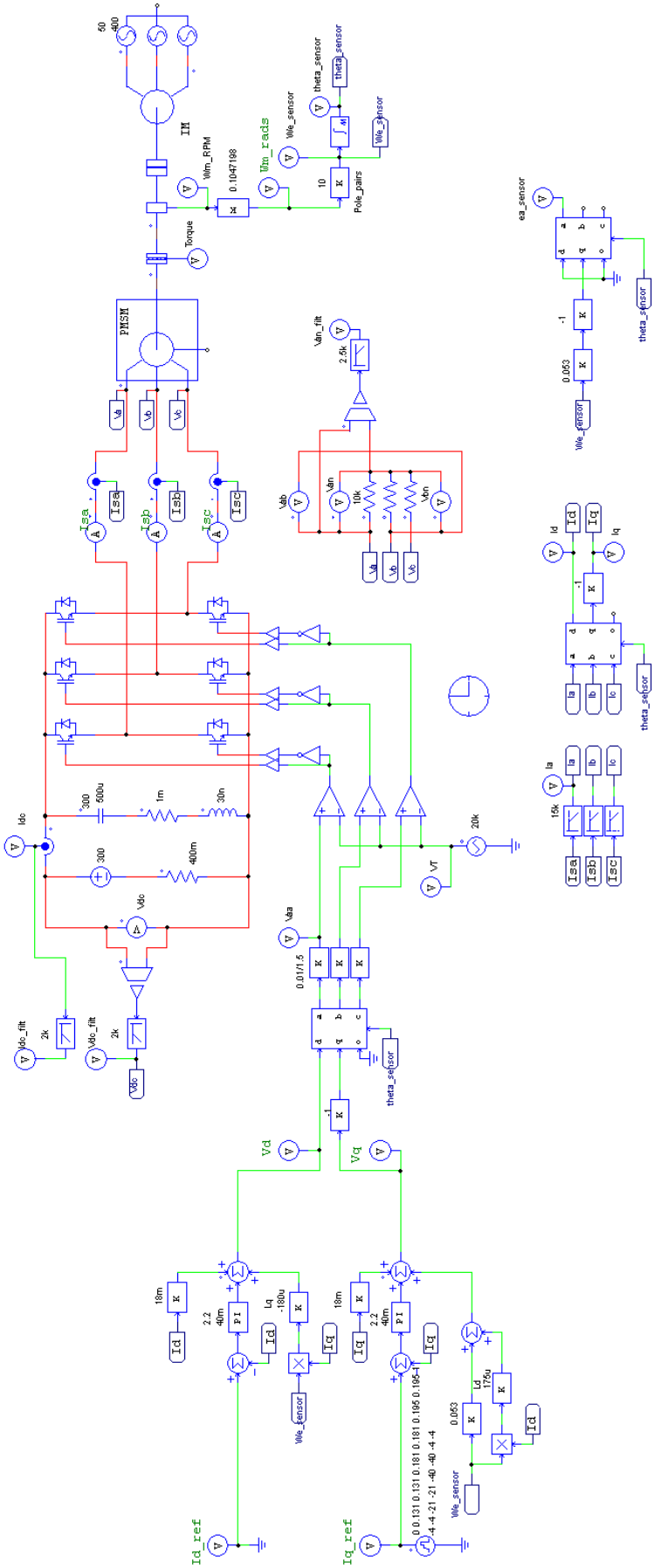

Figure 6.23 - PMSG FOC control with speed sensor in the Shaft – sinusoidal PWM modulation

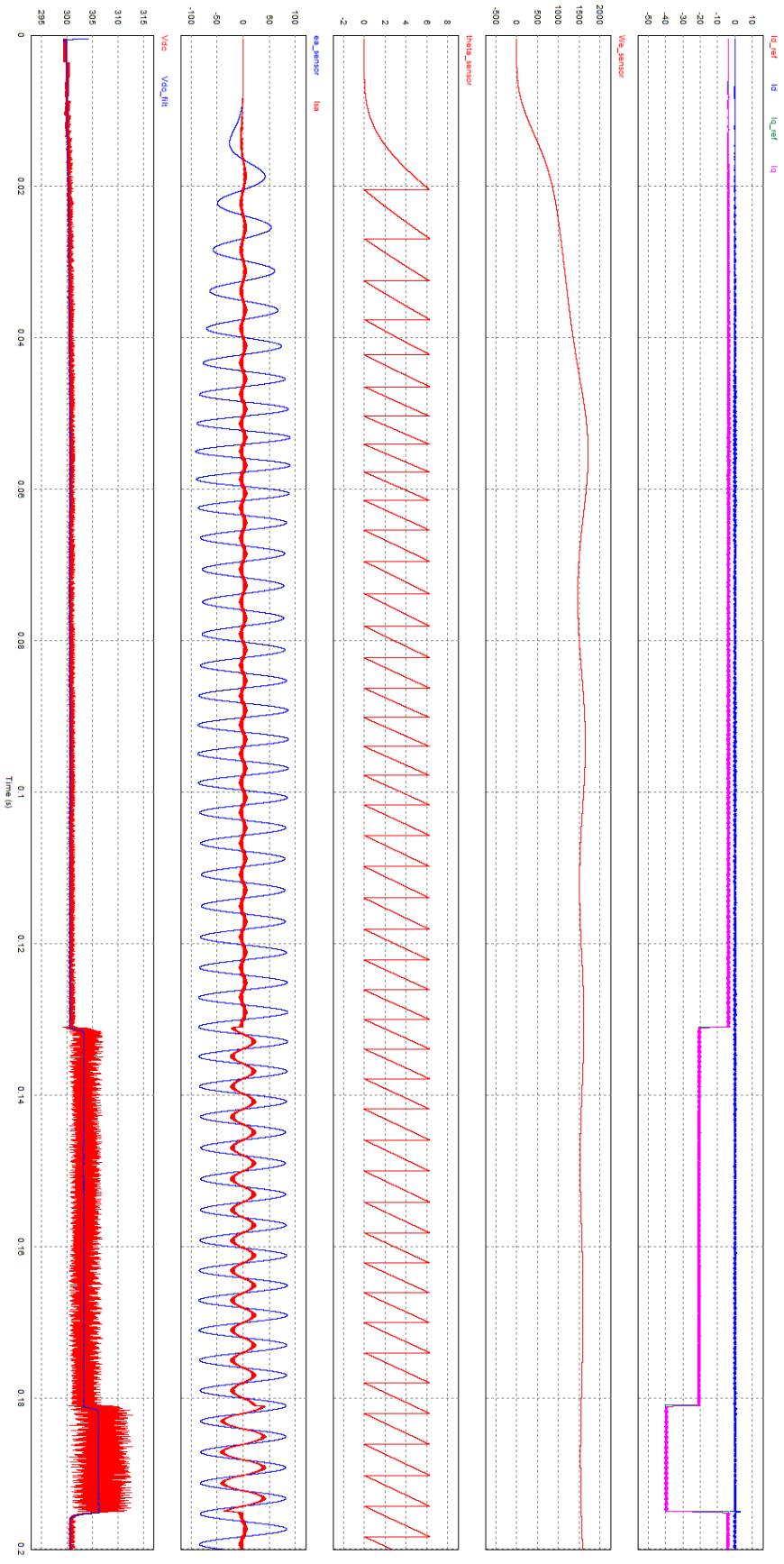

Figure 6.24 - PMSG FOC control with speed sensor in the shaft – waveforms 1

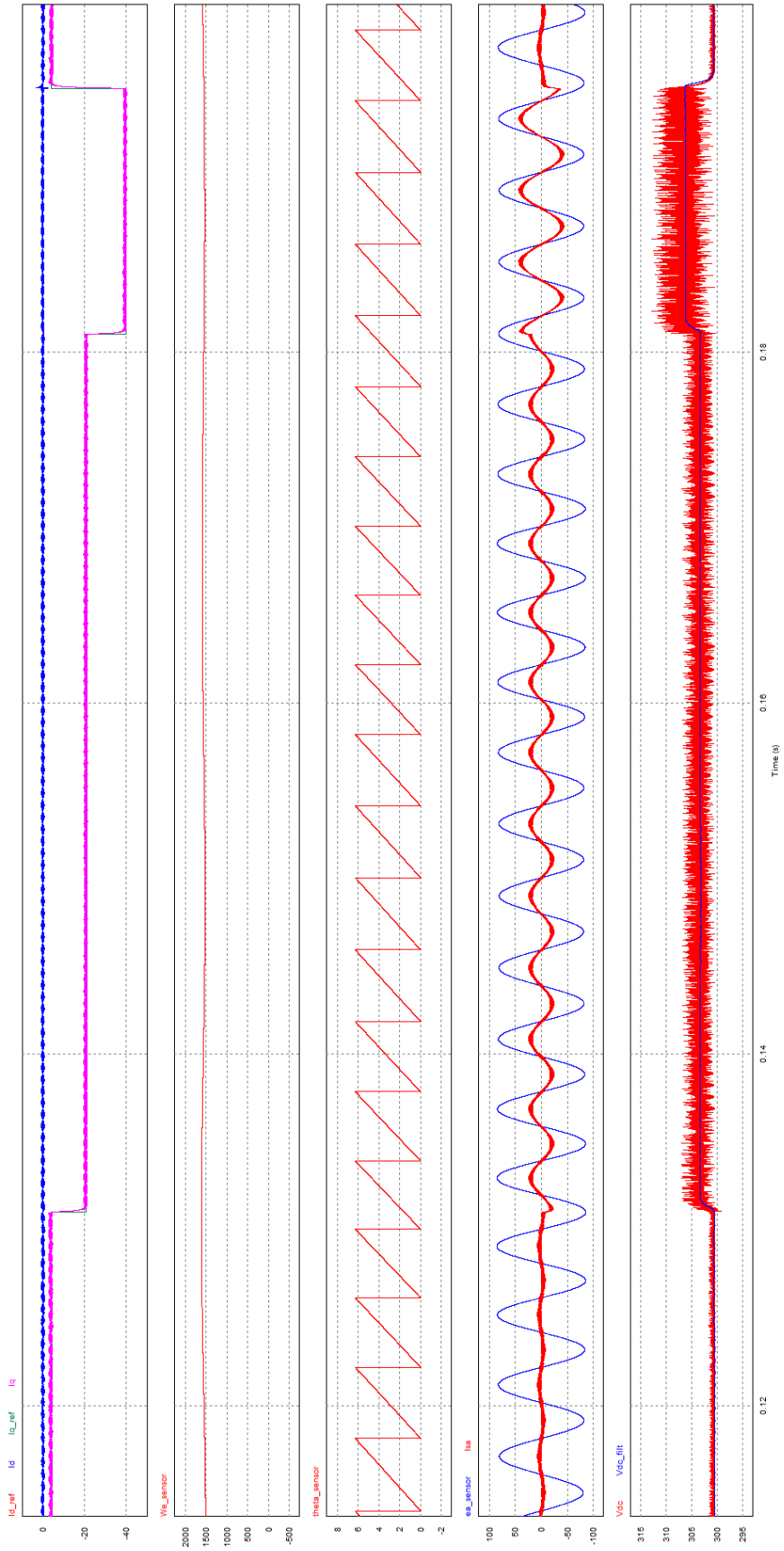

Figure 6.25 - PMSG FOC control with speed sensor in the shaft – waveforms 2

6.7 Sensorless FOC of a PMSM

Figure 6.28 shows a sensorless implementation of the circuit previously described (see Figure 6.23). To obtain the electrical speed ω_e and angle θ_e, instead of a speed sensor placed on the shaft, a SFR-PLL is used. Figure 6.26 shows a SFR-PLL schema that estimates the electrical speed $\hat{\omega}_e$ and angle $\hat{\theta}_e$. As shown in Chapter 5, the angle estimation is a very robust process even in the presence of distorted voltages and currents while the speed estimation is very sensitive to those distorted signals. Furthermore, the fast dynamics that the SFR-PLL must have compared to the FOC dynamics requires a PI controller with a high proportional k_p gain and a low time constant $T = k_p / k_i$ which leads to huge fluctuations at the PI output (see Figure 6.27), i.e. the electrical speed estimation. To overcome this issue and achieve a robust control over the PMSM, a proper low-pass filter (LPF) must be added to the SFR-PLL as shown in Figure 6.26.

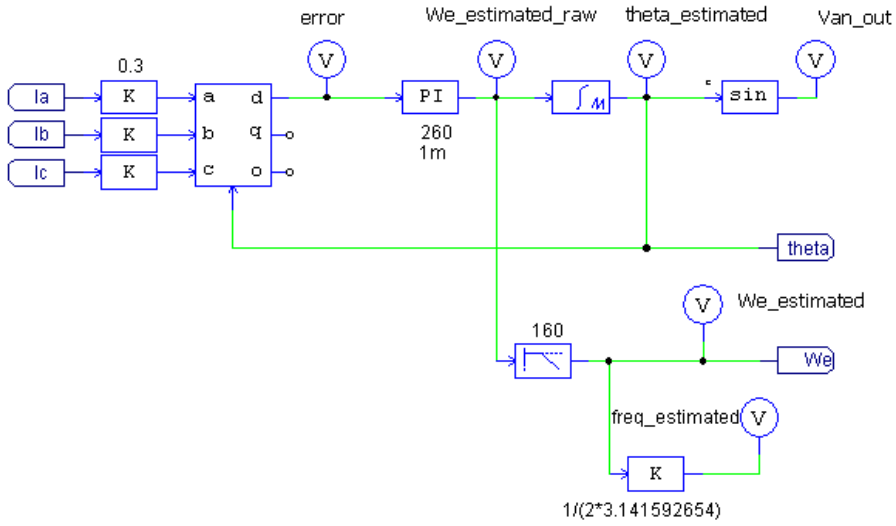

Figure 6.26 - SRF-PLL - speed, angle and line frequency estimator

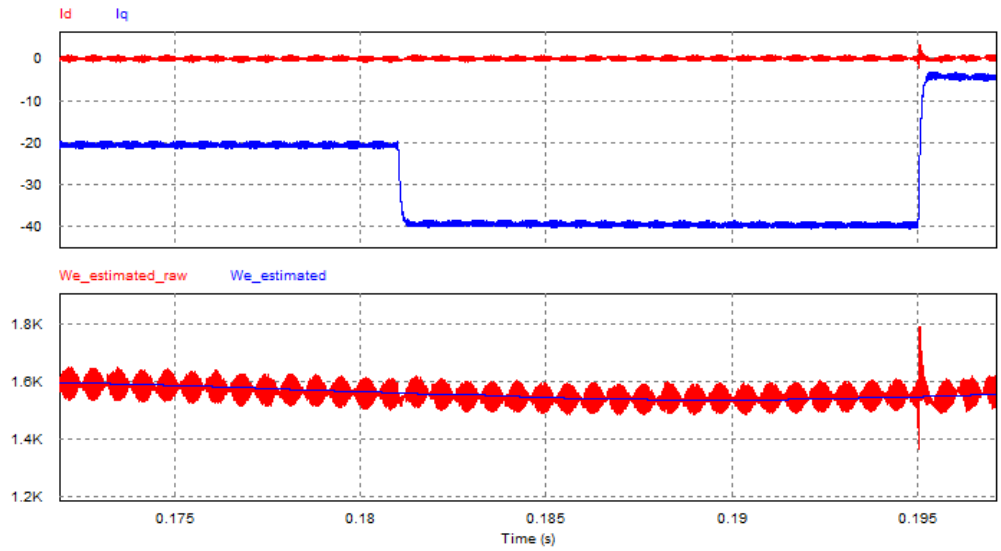

Figure 6.27 – SFR-PLL - Electrical speed estimation waveforms

Notice however that since the estimator works exclusively based on current measurements, if the FOC do not impose any line current on the circuit it is not possible to perform the estimation of speed $\hat{\omega}_e$ and angle $\hat{\theta}_e$. To overcome this issue a simple but innovative solution is proposed on this work, which will be discussed in Chapter 7.

The simulation results for this arrangement are globally presented in Figure 6.28 and with more detail in Figure 6.29 and Figure 6.30. When the IM starts spinning the SFR-PLL finds an initial difficulty to achieve the phase-lock. This is because the initial currents are very week as very week are the PMSM terminal voltages. After this period, that has no consequences namely over the line currents, the system's behaves just like the previously analyzed sensor based system.

A comparison between estimated speed and angle and the same values given by the shaft sensor, show that estimated and real values are equal, as well as the system's dynamics proving the robustness of this solution.

6.8 Sensorless Control Strategy based on SRF-PLL and two *dq* frames

The previous circuit used a constant-angle control strategy where the i_d^* reference is set to zero. From a control point of view, this corresponds to operating points where, the PMSM internal voltages $e_a e_b e_c$ are in phase (motor operation), or 180^o out of phase (generator operation), with line currents $i_a i_b i_c$. In a Steinmetz representation this operating points are located on the $q-axis$ (see Figure 6.4). Note that the E internal voltage vector is collinear with i_s current vector. The SFR-PLL works fine for both motor and generator operation, because it is not affected by the sign of i_q. The only important restriction is i_d that must be zero.

If an i_d different from zero is required as represented in Figure 6.32, then the current vector i_s is not collinear with the internal voltage vector E and the angle given by the SFR-PLL, let's call it θ_i, is not the angle θ_e needed to perform Park's and inverse Park's transforms within FOC.

To overcome this issue and obtain θ_e, a new technique is proposed based on two dq frames. The first one is the dq_{PLL} frame associated to i_d and i_q currents, whose angle θ_i is provided by the SFR-PLL output. The second dq frame is the traditional one associated to the rotor position and internal voltage E, referenced by θ_e.

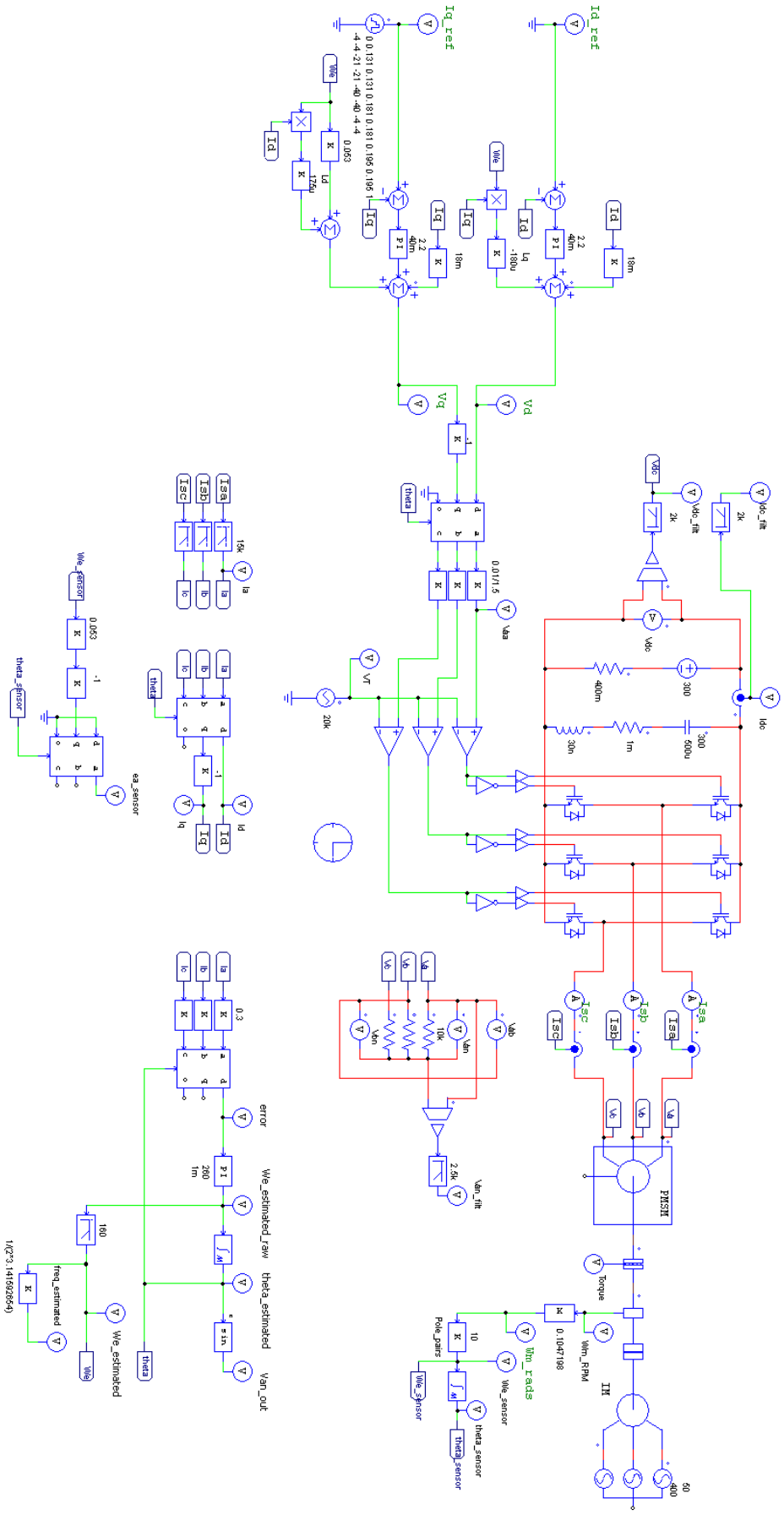

Figure 6.28 - PMSG sensorless FOC based on current measurements – *Id*=0

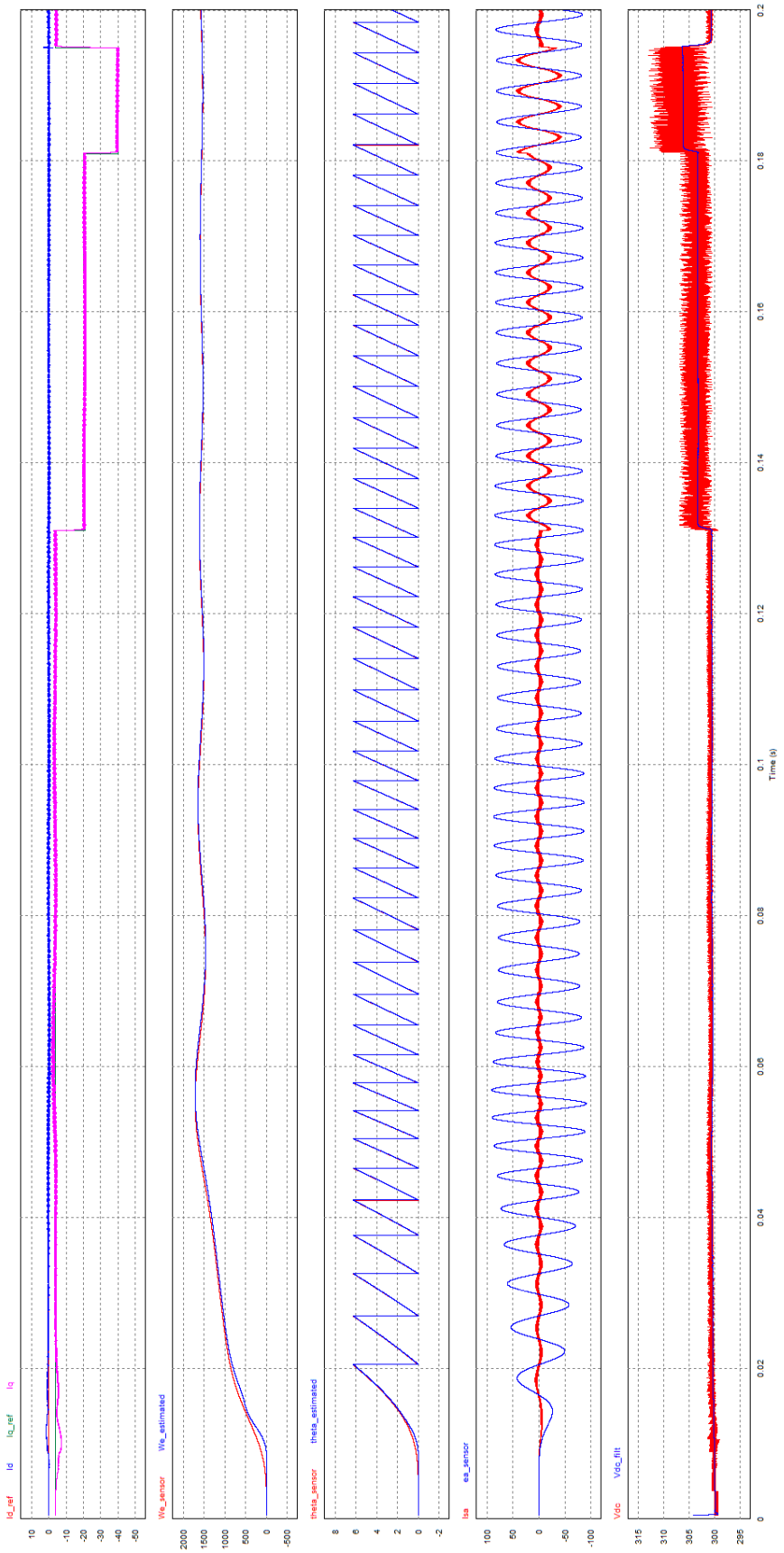

Figure 6.29 - PMSG sensorless FOC based on current measurements – *Id*=0 – waveforms 1

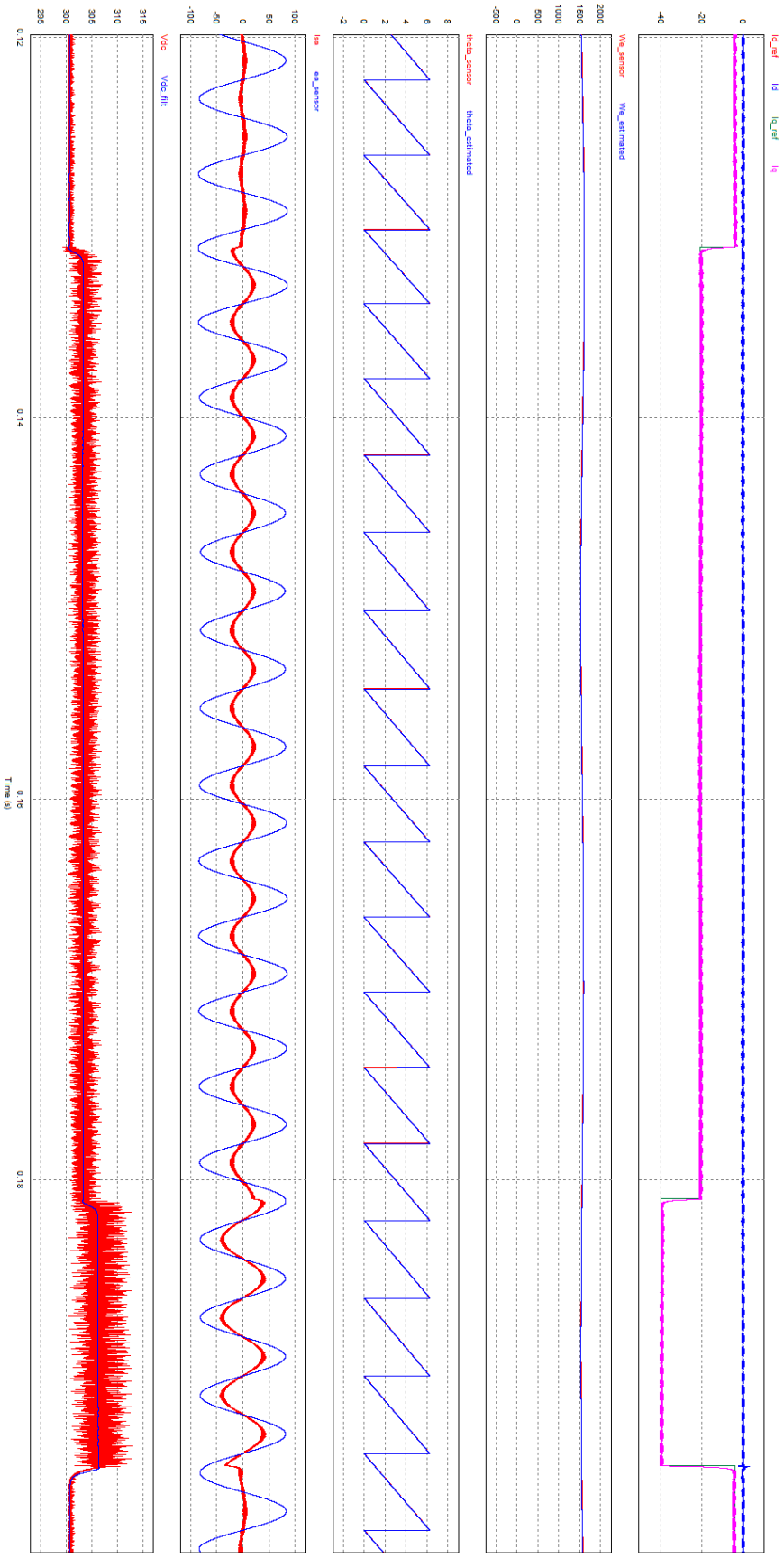

Figure 6.30 - PMSG sensorless FOC based on current measurements – *Id*=0 – waveforms 2

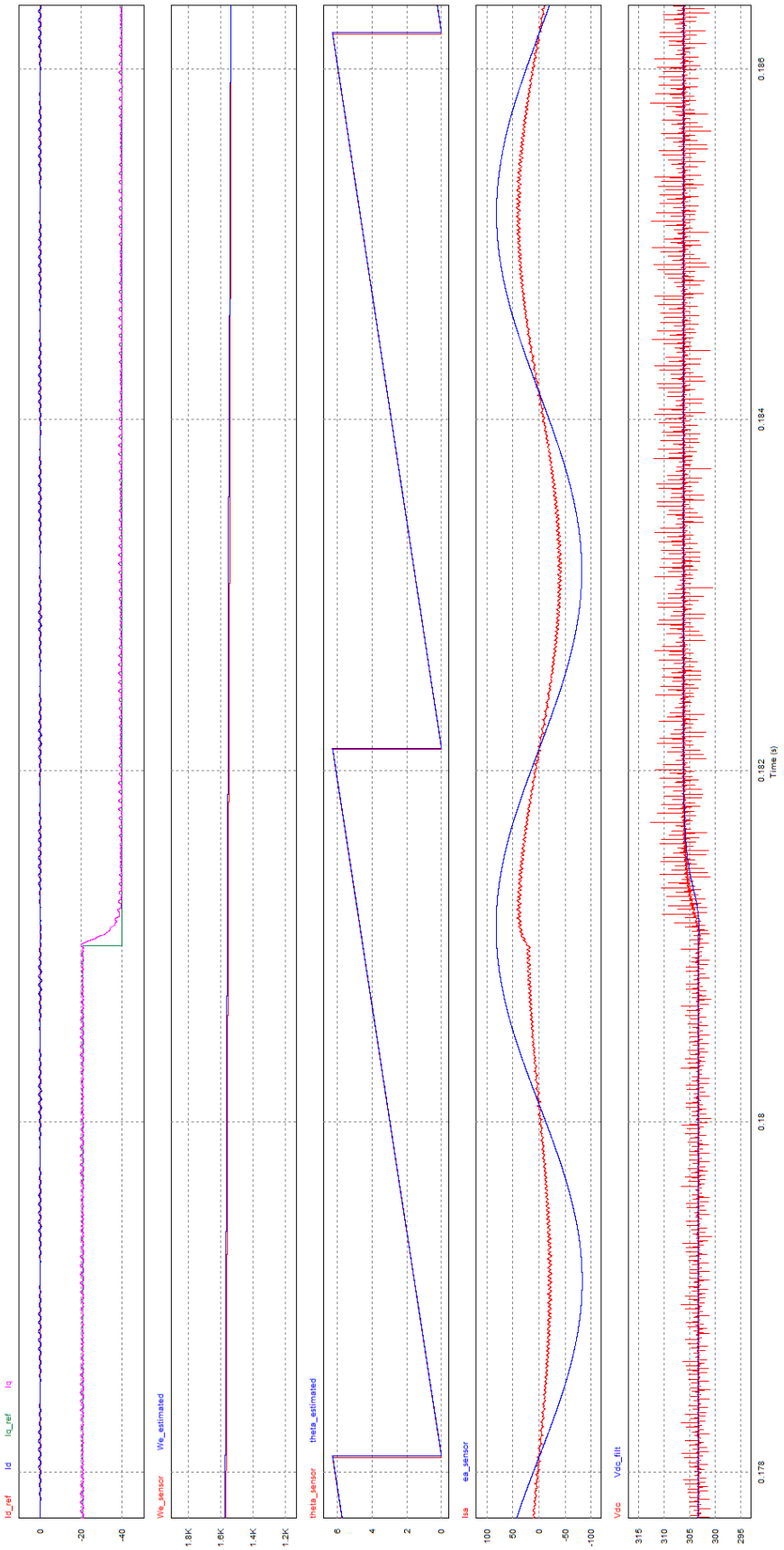

Figure 6.31 - PMSG sensorless FOC based on current measurements – *Id*=0 – waveforms 3

The new technique aims to estimate θ_e from θ_i or in other words, to achieve the dq frame from the dq_{PLL} frame. One possible answer is described graphically in the example of Figure 6.32. With the θ_i angle provided by the SFR-PLL: (step 1), subtract π, and; (step 2) add θ_{REF}. θ_{REF} is the angle between i_d and i_q references, provided by

$$\theta_{REF} = \tan^{-1}\left(\frac{i_d^*}{i_q^*}\right) \tag{6.18}$$

In this case,

$$\theta_e = \theta_i - \pi + \theta_{REF} \tag{6.19}$$

The PSIM circuit that performs these calculations is presented in Figure 6.33.

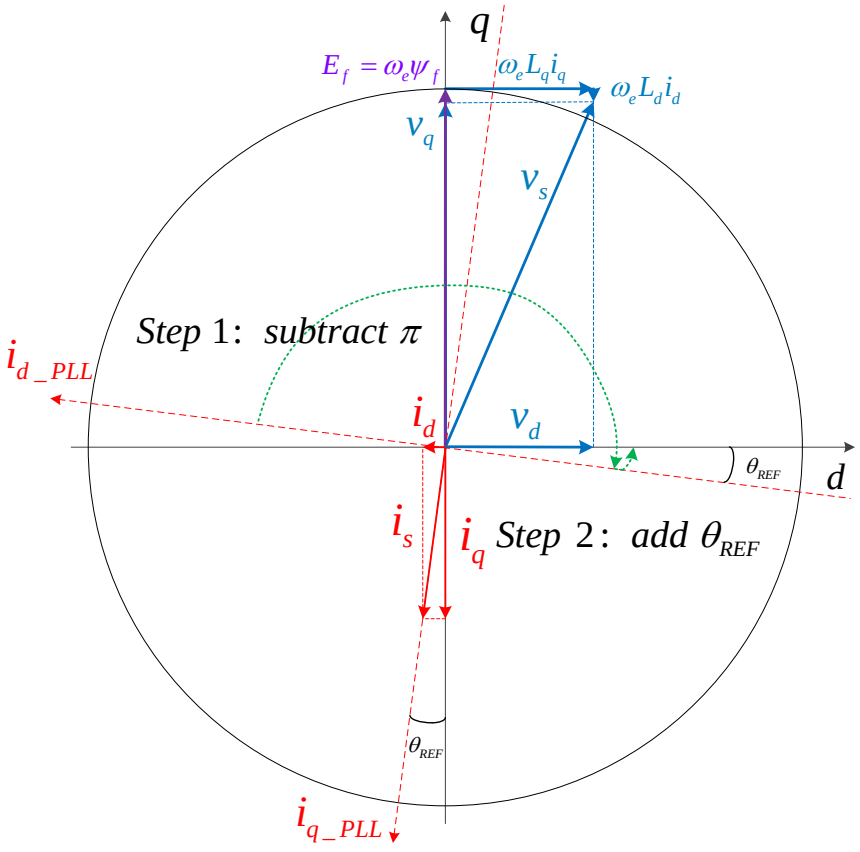

Figure 6.32 – Voltage and current *dq* reference frames

The PSIM simulation results are presented in Figure 6.34. Initially $i_d^* = 0$ and $i_q^* = -4A$. When i_q reference changes to $i_q^* = -21A$, the estimator dynamics behavior is excellent as no perturbation is observed in the estimated speed $\hat{\omega}_e$ and angle $\hat{\theta}_e$. Then, the i_d reference changes to $i_d^* = -21A$ which is a step change of the same magnitude of i_q. Usually i_d never achieves such magnitudes compared to

i_q but this test is made to stress the estimator and observe its dynamics and robustness.

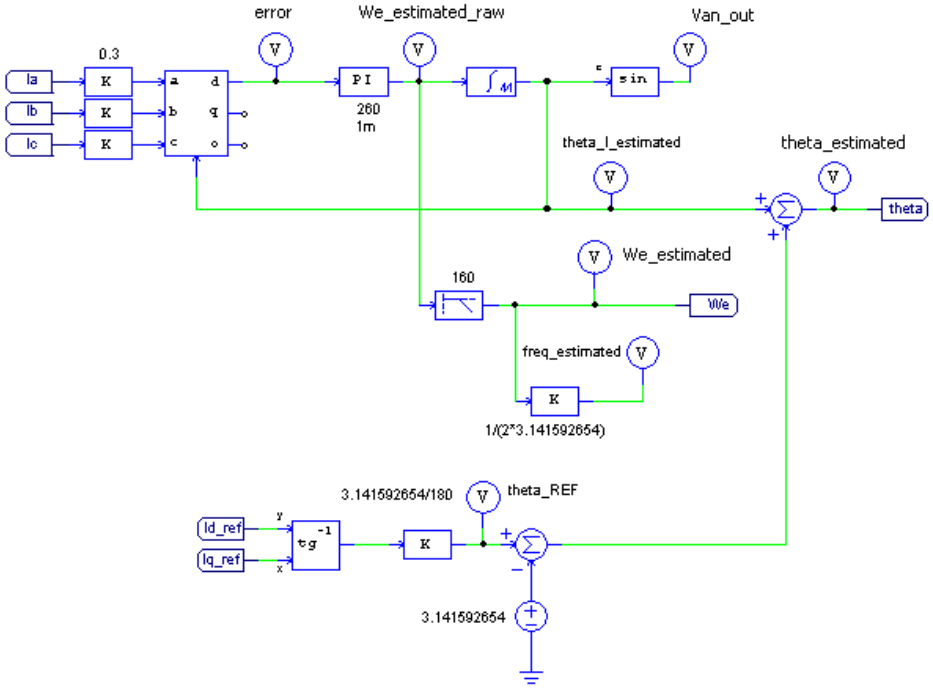

Figure 6.33 – PMSG sensorless speed and position estimator addressed to any *Id*

When the i_d reference suffers a step change, a $\theta_{REF} = 45^O$ is generated and a perturbation is introduced in the estimated angle $\hat{\theta}_e$ according to equation (6.19). This is clearly observed in Figure 6.34. The FOC also has to achieve a new operating point according to its new i_d reference. It has to perform this change with a wrong estimation of $\hat{\theta}_e$ resulting on inaccurate control signals. Fortunately the superior dynamics of the estimator compared to FOC quickly corrects $\hat{\theta}_e$ (it takes less than a quarter of the period in this example). However, the estimated speed $\hat{\omega}_e$ takes a longer time to stabilize (one period in this example) due to the delay introduced by the LPF. As a result, the FOC decoupling paths $\hat{\omega}_e L_d$ and $-\hat{\omega}_e L_q$ (see Figure 6.10) are not estimated accurately leading to an inefficient decoupling between d and q quantities that is reflected later on i_d and i_q currents.

In an attempt to solve these issues a LPF is added to the estimator as shown in Figure 6.35, in order to introduce a smooth change in the reference angle $\hat{\theta}_e$. The benefits of this strategy are quite evident and can be shown on Figure 6.36. The estimated angle $\hat{\theta}_e$ is now close to its real θ_e while the estimated speed continues having those undesirable undershoots and overshoots. In spite of that, the overall results are better than the previous ones as proved by i_d and i_q currents behavior.

In sum, albeit the proven stability and robustness of the estimator is certainly possible to improve it, overcoming some of the identified weaknesses.

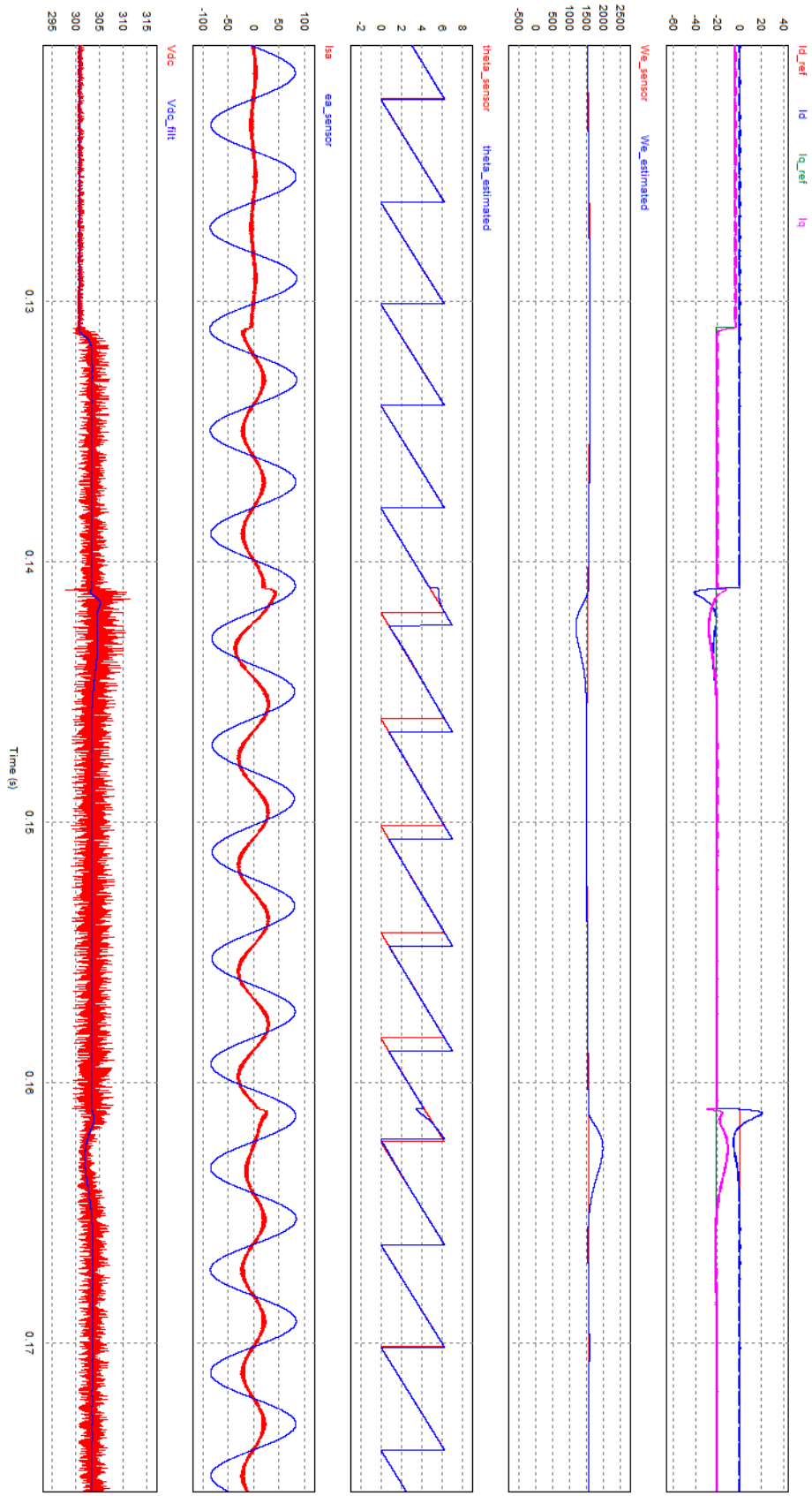

Figure 6.34 - PMSG FOC sensorless control based on current measurements and addressed to any *Id*

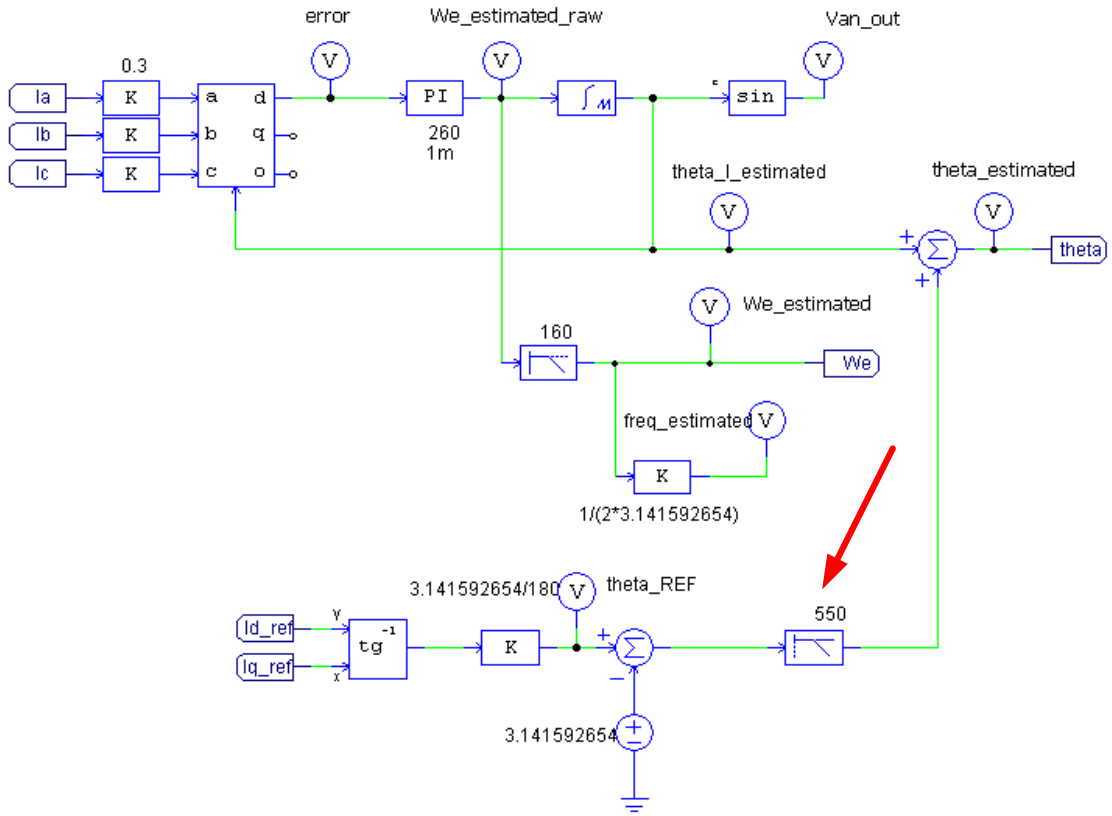

Figure 6.35 - PMSG sensorless speed and position estimator, addressed to any Id and with additional LPF

In C code the calculus of the tg^{-1} function needed to estimate θ_e and speed is a time-consuming operation. The function ATAN2(y, x) is preferred, because it does not require a previous argument division, thus leading to a faster execution time.

The estimator presented in Figure 6.33 and Figure 6.35 is suited to work with a PMSM operating as a generator.

With the ATAN2(y, x) function in order to obtain θ_e for generator operation, use

$$\theta_e = \theta_i - \frac{\pi}{2} - ATAN2\left(i_q^*,\ i_d^*\right) \tag{6.20}$$

and for motor operation, use

$$\theta_e = \theta_i + \frac{\pi}{2} - ATAN2\left(i_q^*,\ i_d^*\right) \tag{6.21}$$

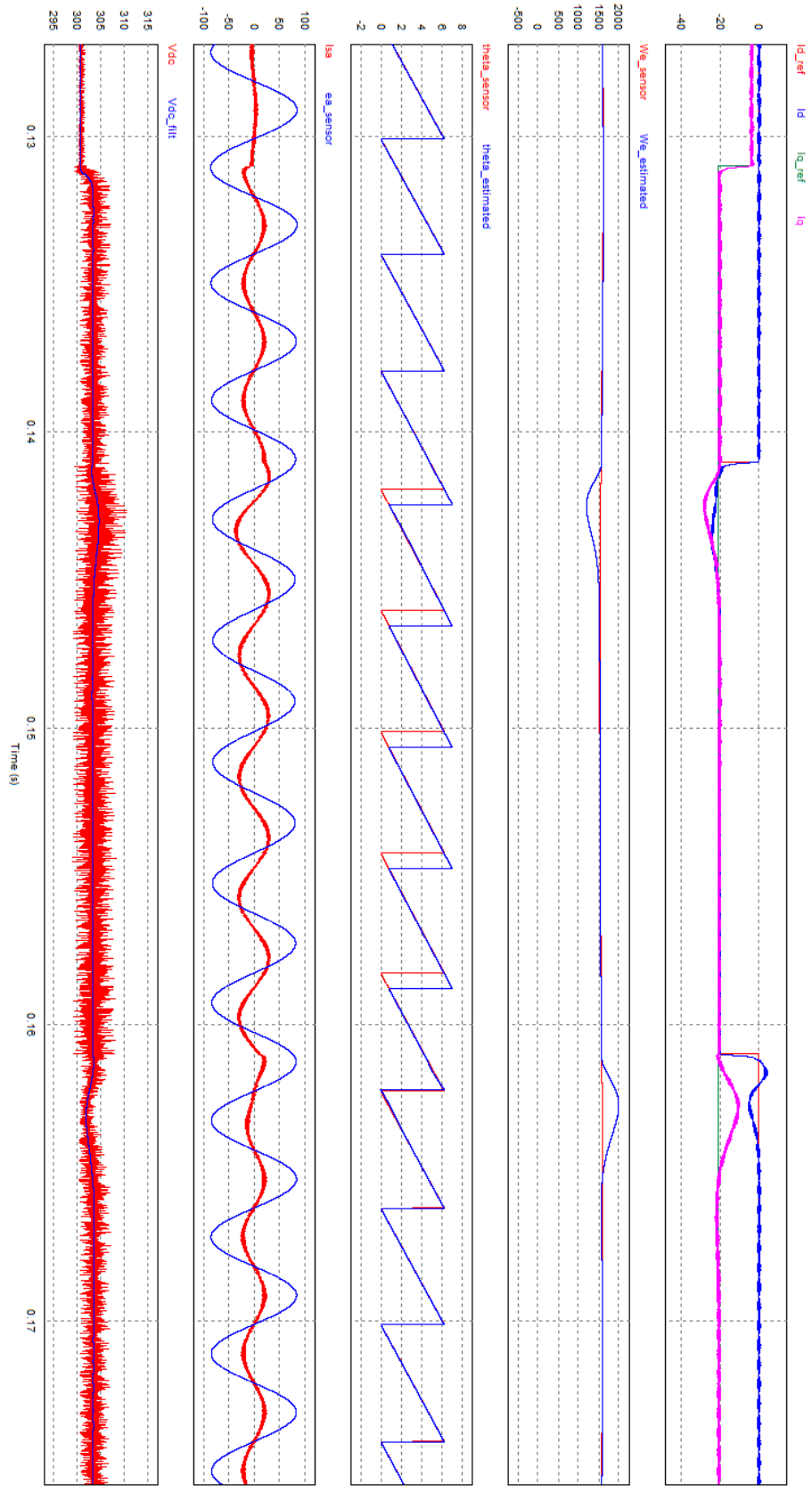

Figure 6.36 - PMSG FOC sensorless control based on current measurements, addressed to any Id and with additional LPF – waveforms

6.9 Adopting a Control Strategy

To extract the maximum power from the EMRAX 228 High Voltage, the MTPA control strategy must be adopted, as it allows to extract the maximum power (or torque) from the PMSG, with minimal copper losses.

As shown before, for isotropic rotors (where $L_d = L_q$), the control strategies MTPA and constant-angle control coincide, as the MTPA is achieved when $i_d = 0$. Taking into account that the EMRAX has near equal L_d and L_q inductances, the following analysis evaluates the differences in adopting one strategy or the other. To complement it a UPF control strategy is also evaluated. The setup used consists on an EMRAX running at $1500\ rpm$ with $i_s = 100A$, and operating as generator.

PMSM working as generator (Current "I" is negative)					
Rotor flux	0,053				
Rs	0,018				
Ld	0,000175				
Lq	0,00018				
Pole pairs	10				
Wm (rpm)	1500	Shaft speed			
We (rads-1)	1570,796327	Electrical speed			
I (vector amplitude)	-100	I=sqrt(Id^2+Iq^2)			
Control strategies:					
	MTPA		Id=0 and Iq=I		UPF
Torque angle (rad)	-1,58022875		-1,57079633		-1,91616267
Torque angle (deg)	-90,540		-90,000		-109,788
Id	-0,943		0,000		-33,854
Iq	-99,996		-100,000		-94,095
Torque (electrical)	-79,504		-79,500		-75,045
Vd	28,256		28,274		25,995
Vq	81,193		81,452		72,252
V (vector amplitude)	85,969		86,220		76,786
V -> PMSM terminal voltage					
E (vector amplitude)	83,252		83,252		83,252
E -> PMSG Internal voltage					
Active and Reactive Power at PMSM terminals					
P=3/2(VdId+VqIq)	-12.218,386		-12.217,831		-11.517,971
Q=3/2(VdIq-VqId)	-4.123,351		-4.241,150		0,000
Active and Reactive Power referred to the PMSM internal voltage E					
P=3/2(Eiq)	-12.487,275		-12.487,831		-11.750,443
Q=-3/2(Eid)	117,789		0,000		4.227,648

Table 6.3 - EMRAX control strategy comparison for $\omega_m = 1500rpm$ and $i_s = 100A$

The Table 6.3 shows the control strategy comparison results. As it can be seen, the torque and power for both MTPA and constant-angle control ($i_d = 0$) are equal, while for UPF the torque and power are reduced respectively in 5.6% and 5.7%. Using MTPA /constant-angle control, a reactive power (capacitive) appears at the converter/PMSG terminals. One the other hand the UPF strategy achieves 11% lower converter/PMSG terminal voltage in comparison with constant-angle control.

In sum, from the previous analysis to control the EMRAX with MTPA, i_d must be set to zero. Fortunately setting $i_d = 0$ simplifies the overall control process:

- the speed and angle estimator becomes as simple as the one described in Figure 6.26 requiring much less computational effort than the "full" version of Figure 6.35;
- instead of two, only one reference, i_q^*, has to be set to control torque and power;
- the torque becomes proportional to i_q (see equation (6.5));
- the active power at PMSM/converter terminals P_v is almost proportional to i_q, if some constraints are observed.

Indeed the active power at PMSM/converter terminals P_v is given by

$$P_v = \frac{3}{2}\left(v_q i_q + v_d i_d\right) = \frac{3}{2}\left(v_q i_q + v_d 0\right) = \frac{3}{2} v_q i_q \tag{6.22}$$

which can assume the form

$$P_v = P_e - P_{losses} = \frac{3}{2} E i_q - \frac{3}{2} R i_q^2 = \frac{3}{2} \omega_e \psi_f i_q - \frac{3}{2} R i_q^2 \tag{6.23}$$

where P_{losses} are the copper losses. This expression highlights that (1) P_v is not directly proportional to i_q and (2) the copper losses may be relevant when the PMSM is running at low speeds.

Considering the example of Table 6.3, where $i_s = i_q = -100A@1500rpm$, results show: $P_e = 12.488W$; $P_v = 12.218W$; $P_{losses} = 270W$ which leads to $P_{losses} / P_e =$ 2.16%. Taking another example where: $i_s = i_q = -200A@3000rpm$, results show $P_e = 49.951W$; $P_v = 48.871W$; $P_{losses} = 1.080W$ leading to $P_{losses} / P_e =$ 2.16% (the same value from the previous example).

In sum, the copper losses can be properly controlled and maintained at a low level by controlling the ω_e / i_q rate.

6.10 Discrete Time Control Process Implementation

The overall control process using PSIM blocks of an EMRAX operating as generator with $i_d = 0$ was already described and analyzed in this Chapter (see Figure 6.28). The next goal was to get a digital implementation in C language, "microcontroller-ready", including SVM and dead-times needed for proper IGBT's operation and using only two current measurements.

The C code developed for this PSIM implementation is 99% of the code used in the experimental setup described in Chapter 7. The results of this PSIM implementation are later compared to the ones of the physical implementation.

The target microcontroller is an ARM XMC4500 from Infineon and the target board is an "XMC4500 Lite Relax Kit" from the same brand. The control software was designed according to and targeting that board.

The manufacturer provides a set of optimized Software Applications (Apps) addressed to motor control as is the case of the SVM block. To take advantage of this block, the control routine must be executed at a specific rate. According to Infineon this rate is the adopted switching frequency. With a switching frequency of $f_c = 20kHz$, an interrupt is generated each $T_c = 1/20kHz = 50\mu s$. Within this cycle period, data acquisition (currents measurement), and a new set of control variables $(v\_mag,\ \theta_v)$ must be computed. These control variables are used to perform the SVM operation in the next cycle period. According to Figure 6.37, the control variables are given by

$$\begin{aligned} v_s &= \sqrt{v_d^2 + v_q^2} \\ \theta_v &= \theta_e - tg^{-1}\left(\frac{v_d}{v_q}\right) \end{aligned} \tag{6.24}$$

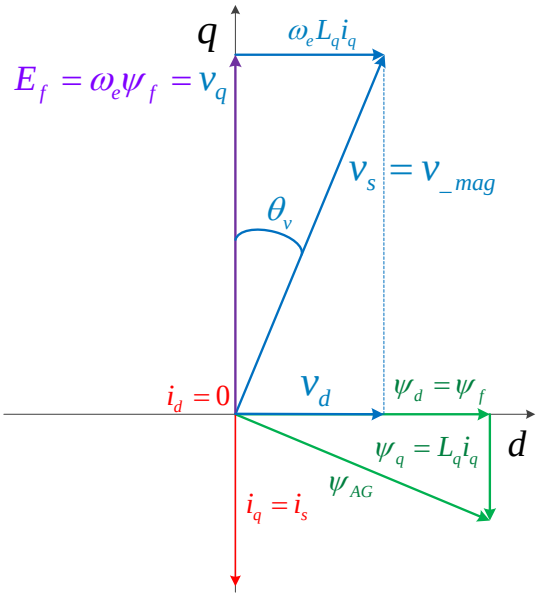

Figure 6.37 – PMSG θ_v and v_mag control variables

Figure 6.38 shows a block diagram describing the overall control process. All non-power blocks interconnected by green lines are implemented in C-code with exception of the space-vector modulator. In order to emulate the Infineon's SVM implementation (optimized and targeted to the XMC4500 microcontroller), a SVM technique known as "third order odd harmonic injection PWM technique", is adopted and implemented using PSIM blocks. This technique is described in Chapter 4.

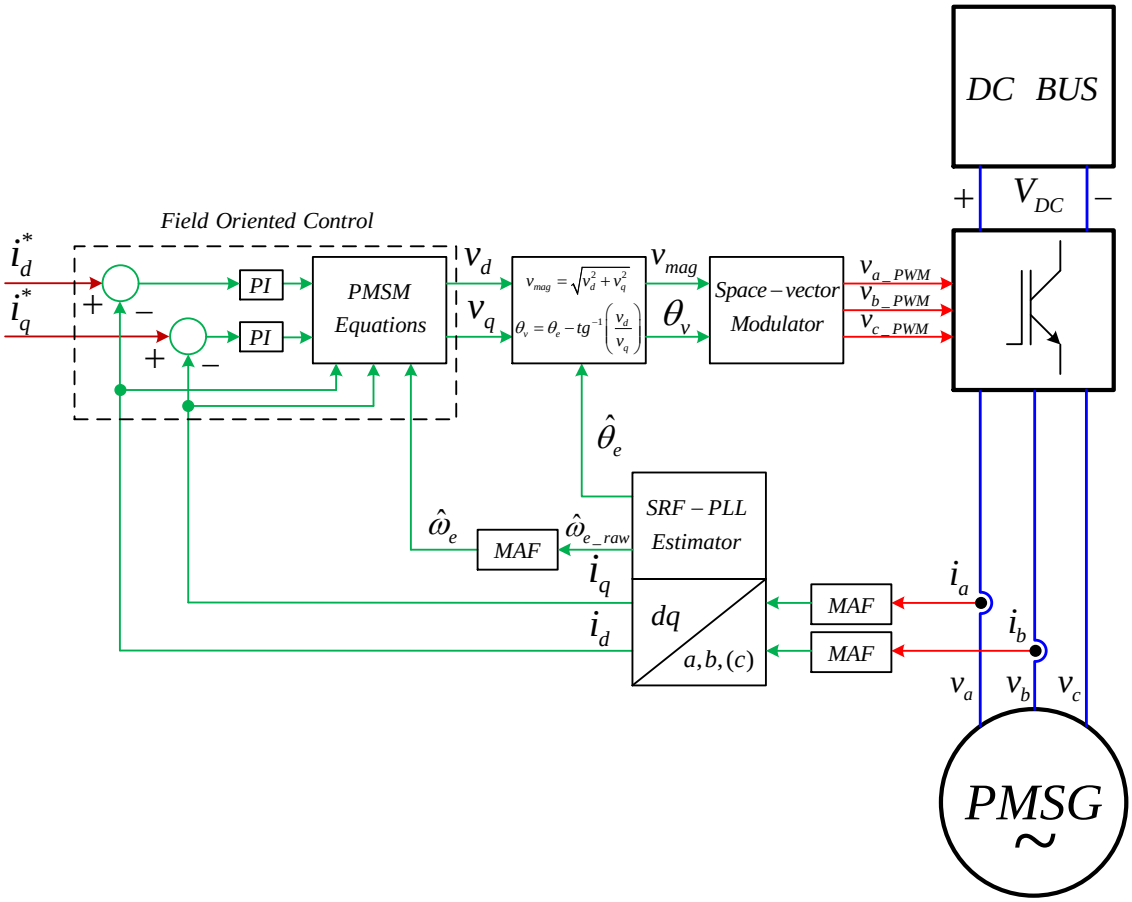

Figure 6.38 – PMSG's overall control process using SFR-PLL and FOC

In computational terms, controlling a process comprises, in its basic form, three steps performed within an infinite loop: data acquisition, data processing and output commands. The cycle period results from the sum of the execution times of each individual step and determines the computational effort needed.

As seen before, in this implementation the cycle period is 50us. As described in Chapter 7, this time is more than enough to perform the necessary control operations, leaving time for other auxiliary operations.

To guarantee the SRF-PLL dynamics and robustness that free time is used to more accurately estimate θ_e and ω_e. The result is that two current acquisitions and θ_e, ω_e estimations are performed within each cycle period as detailed in Figure 6.39. The currents acquisition rate is $1/25\mu s = 40kHz$.

In order to perform these control operations in PSIM, a $40kHz$ clock is connected to one of the PSIM C-block inputs. The code is executed only at positive rising edge of the clock and new control variables are provided at the C-block outputs at each two clock periods.

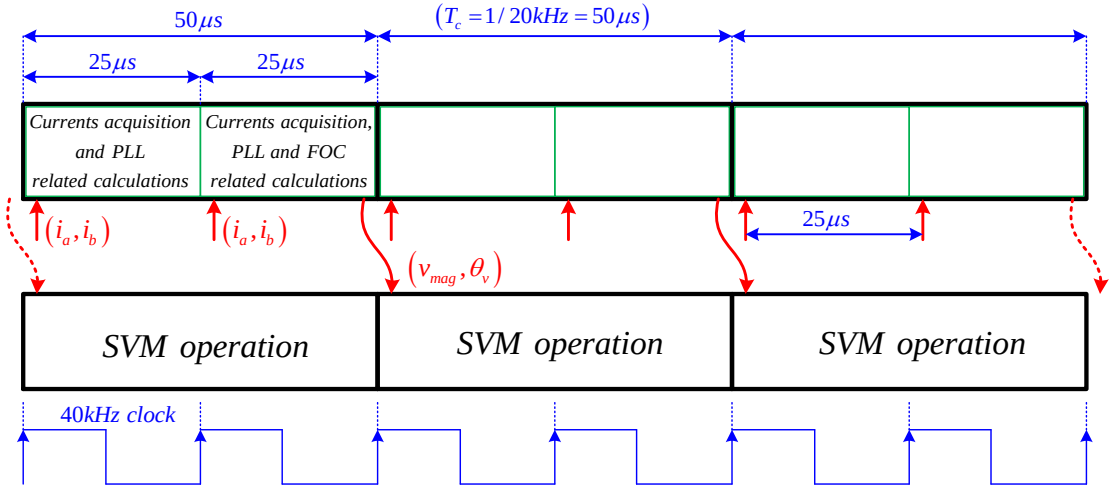

Figure 6.39 – C-block Execution Timing

One question that naturally arises is if the currents acquisition rate or in other words, if the sampling frequency of $40kHz$ is enough to accurately characterize the current signal.

In this case, the generator shaft is spinning at $1500\ rpm$ which gives a current frequency of $250Hz$. This results on $40k/250=160$ samples per period.

If the shaft speeds up to its maximum, $5000\ rpm$, it gives a current frequency of $833.3Hz$, leading to $40k/833.3=48$ samples per period.

According to the Nyquist–Shannon sampling theorem, the sampling frequency must be greater than $1.7kHz$ which is definitely guaranteed. On the other hand, a sampling frequency of $40kHz$ ensures that currents whit a harmonic spectrum up to $20kHz$ are reconstructed.

6.11 Dead-time Between IGBT Outputs

The dead-time between IGBT outputs is achieved in PSIM by using the circuit shown in Figure 6.40. The dead-time value is specified inside the monostable block. A dead-time of $3\mu s$ is set according to the characteristics of the IGBT drivers used in the experimental setup. This issue is detailed in Chapter 7.

6.12 Moving Average Filter

In addition to the low-pass filter needed for proper electrical speed estimation (see Figure 6.26), two more LPFs are required to filter the line currents after their acquisition by the ADCs. Errors can result from the acquisition process itself, but can also result from having acquisitions taking place at the wrong time. And, in this case, a wrong time is the time instant in which a commutation takes place. Filtering those disturbances leads to a smooth operation and to a robust control.

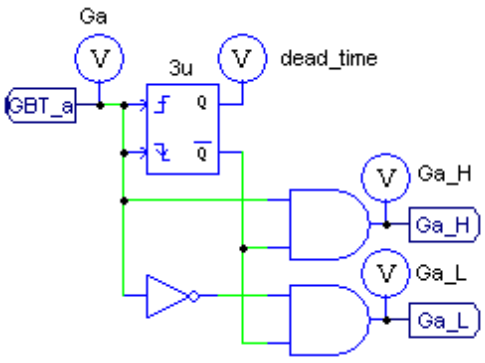

Figure 6.40 - Dead-time generator circuit in PSIM

A possible digital implementation of an LPF is the Moving Average Filter (MAF). The MAF transfer function in Z domain is given by [13]

$$MAF(Z) = \frac{1}{N}\left(\frac{1-Z^{-N}}{1-Z^{-1}}\right) \tag{6.25}$$

The filter parameters are the sampling frequency f_s and the cutoff frequency f_c. The filter order N is given by

$$N = \frac{f_s}{f_c} \tag{6.26}$$

The MAF implementation requires a first-in-last-out memory (FILO) of N positions, (a circular array in C-code). At each interaction a new sample is inserted into the memory replacing the oldest one. The filtered quantity is given by the average value of the N samples. In C-code this implementation requires a subtraction, a sum and a division operation. Furthermore, the execution time is independent of the number of samples.

Filtering the line currents is a tricky task. Like any filter the MAF introduces a delay or phase that in this particular case can compromise accurate θ_e and ω_e estimations and thus the overall system's stability. For that reason a MAF of order $N = 3$ is considered for currents, giving a cutoff frequency of

$$f_{c\_currents} = \frac{40k}{3} = 13.33kHz \tag{6.27}$$

Unlike what happens with currents, the delay introduced by the MAF associated to the SRF-PLL for electrical speed estimation $\hat{\omega}_e$ is not really a problem as this speed, related to the shaft speed ω_m, since it varies too slowly when compared to the SRF-PLL dynamics. Hence, a MAF of order $N = 200$ is considered, giving a cutoff frequency of

$$f_{c\_\omega_e} = \frac{40k}{200} = 200Hz \tag{6.28}$$

6.13 Discrete-time PI Controller and Integrator

The s-domain transfer function of the PI controller represented in Figure 6.41 is given by

$$\frac{U(s)}{E(s)} = k_p + \frac{k_i}{s} \tag{6.29}$$

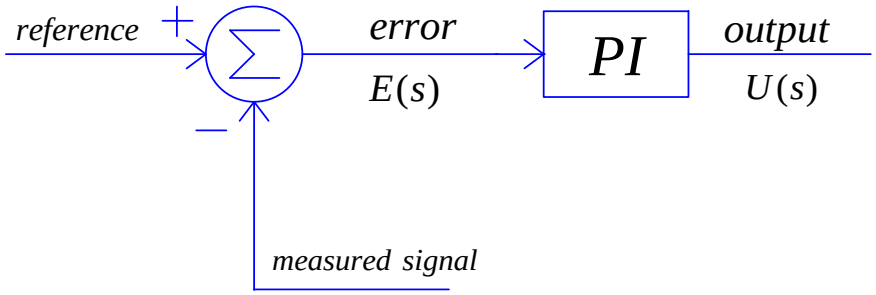

Figure 6.41 – Discrete-time PI controller

According to [14] the best discrete-time approximation of continuous time is given by the Trapezoidal Approximation, also known as Bilinear Transformation or Tustin's Approximation. It is given by

$$s \to \frac{2}{T_s}\frac{Z-1}{Z+1} \tag{6.30}$$

with T_s as the sampling period, the transfer function in Z-domain becomes

$$U(Z) = k_p E(Z) + k_i \frac{T_s}{2}\frac{Z+1}{Z-1}E(Z) \tag{6.31}$$

By developing (6.31) gives

$$\begin{aligned} &\left(U(Z) - k_p E(Z)\right)(Z-1) = k_i \frac{T_s}{2}(Z+1)E(Z) \Leftrightarrow \\ &ZU(Z) - U(Z) - k_p\left(ZE(Z) - E(Z)\right) = k_i \frac{T_s}{2}\left(ZE(Z) + E(Z)\right) \Leftrightarrow \\ &U(Z) = Z^{-1}U(Z) + k_p\left(E(Z) - Z^{-1}E(Z)\right) + k_i \frac{T_s}{2}\left(E(Z) + Z^{-1}E(Z)\right) \end{aligned} \tag{6.32}$$

And since $Z --> n$ and $Z^{-1} --> n-1$, gives

$$u[n] = u[n-1] + k_p\left(e[n] - e[n-1]\right) + k_i \frac{T_s}{2}\left(e[n] + e[n-1]\right) \tag{6.33}$$

or

$$out = prev\_out + k_p\left(error - prev\_error\right) + k_i \frac{T_s}{2}\left(error + prev\_error\right) \tag{6.34}$$

Following the same reasoning for an integrator,

$$u[n] = u[n-1] + \frac{T_s}{2}\left(e[n] + e[n-1]\right) \tag{6.35}$$

or

$$out = prev\_out + \frac{T_s}{2}\left(error + prev\_error\right) \tag{6.36}$$

According to Figure 6.39, the sampling period associated to both SRF-PLL's PI and integrator is $25\mu s$ and to the PIs associated to FOC, $50\mu s$.

6.14 Sin, Cos and Square-root Implementations

To speed up code execution, sin and cos functions are implemented using look-up tables and the square-root is implemented through an approximation provided by IAR Systems – Application Note G-002 - "Fast square root in C". The aim is to guarantee that the C code used in PSIM analysis is the same used in the experimental setup.

6.15 Discrete-time Control Analysis in PSIM

The overall control schema in PSIM is presented in Figure 6.43. Figure 6.42 highlights the C-block. The inputs are the line currents, the control references i_d^* and i_q^* and the clock that defines the code execution rate. Of the many outputs, almost all are used to make the system observable, with only two being used to perform control: $v_{\_mag}$ and θ_v (theta_V).

Simulation results are presented in Figure 6.44, Figure 6.45 and Figure 6.46. These results have to be compared with results of Figure 6.29, Figure 6.30 and Figure 6.31, obtained for ideal time domain conditions described in Figure 6.28.

The comparison shows very similar results regarding the speed and theta angle estimation an even on the line current and DC voltage shape. The most notorious difference is in the i_d current that incorporates low level frequencies around $1.5kHz$ A more detailed analysis of the current shape (Figure 6.47) and frequency spectrum (Figure 6.48), shows that frequencies are located from $1.5kHz$ to $6kHz$. Figure 6.49 shows the Total Harmonic Distortion (THD).

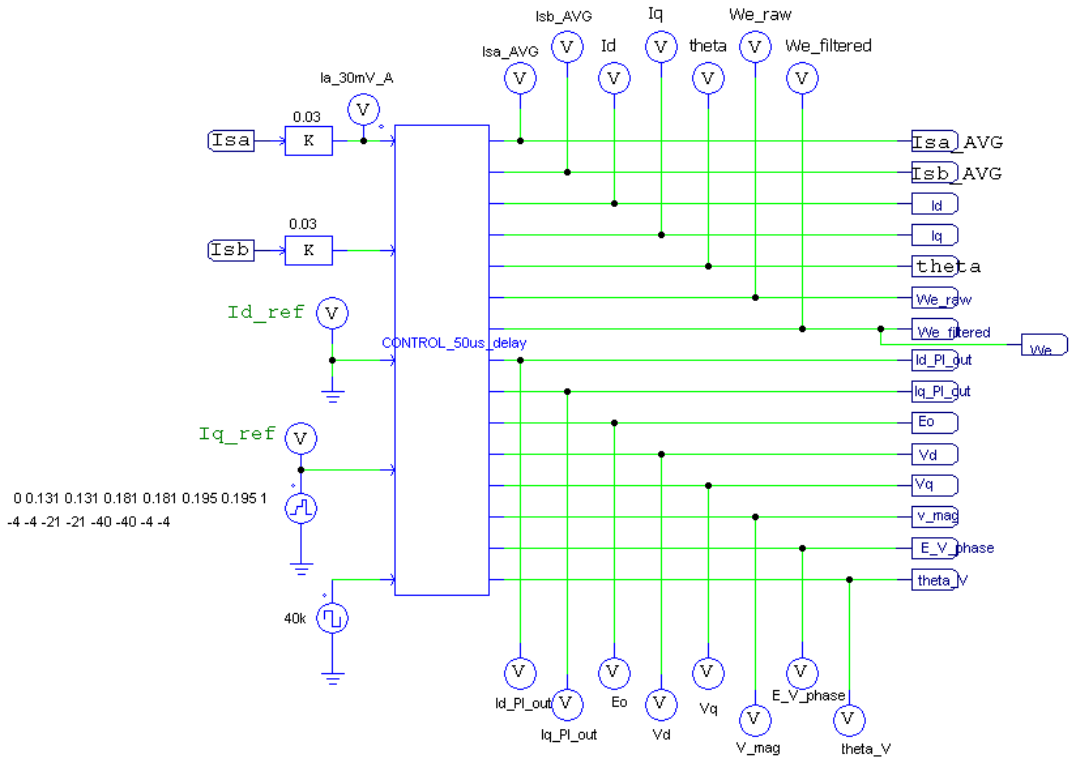

Figure 6.42 - PSIM C-block

In an attempt to find an explanation for this, the IGBTs dead-time was changed back to zero. Figure 6.50, Figure 6.51 and Figure 6.52 show the simulation results that confirm it is the introduction of a dead-time that causes the injection of those low level frequencies in the line phase currents.

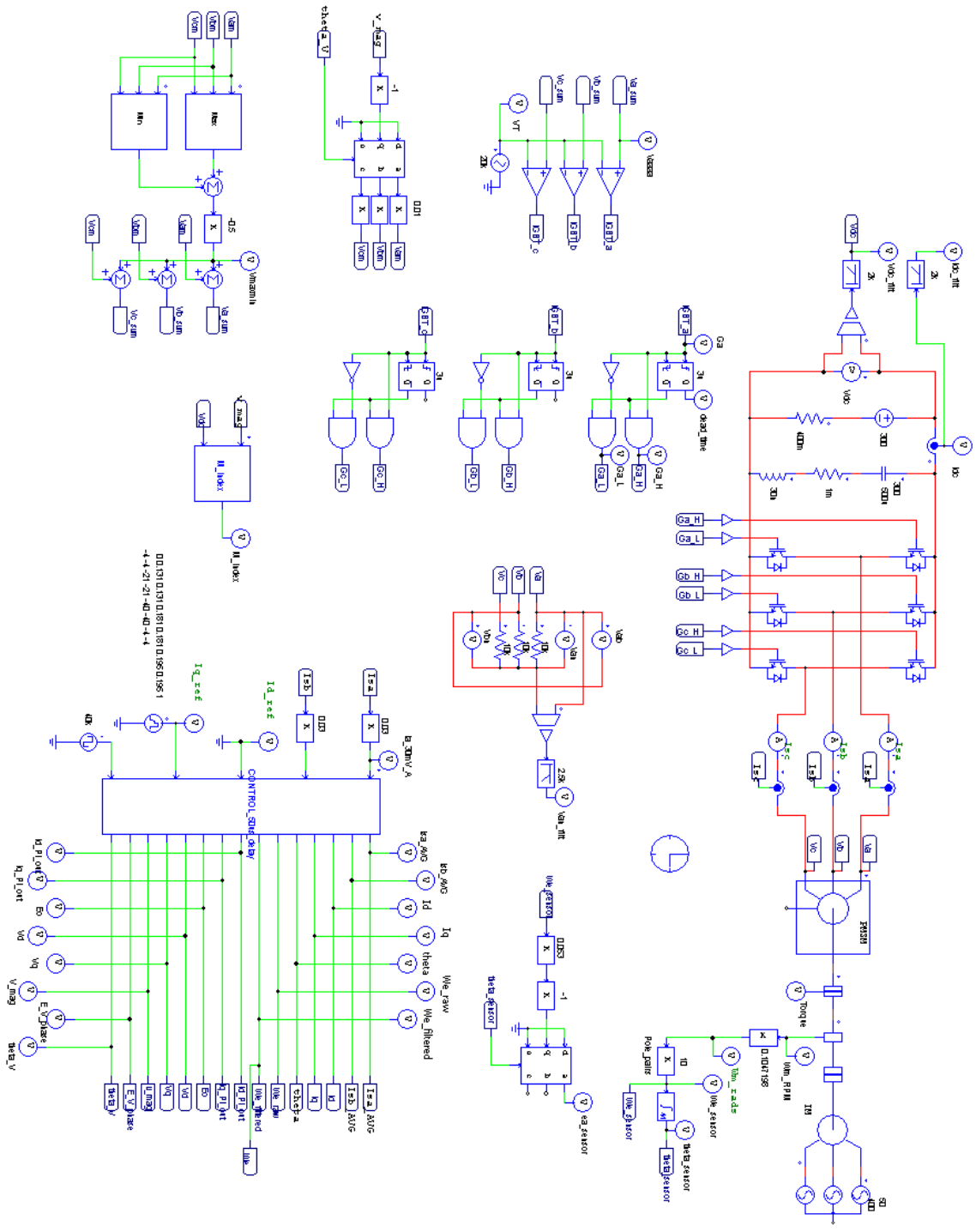

Figure 6.43 - PMSG sensorless FOC – Discrete-time implementation – Microcontroller ready C Code - Performs two current acquisitions at 40KHz rate and control actions at 20kHz rate – Space Vector Modulation - Dead-time of 3µs

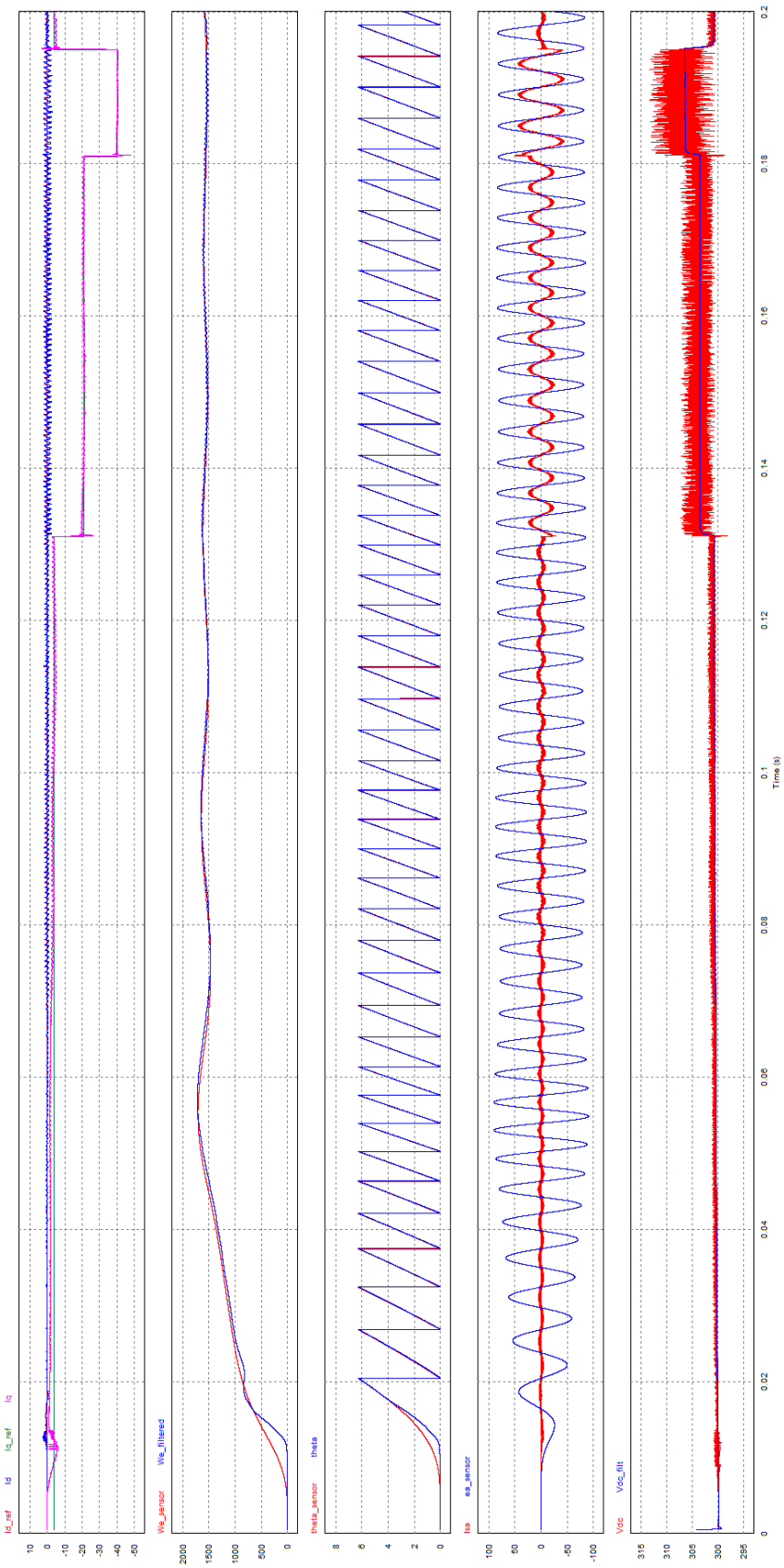

Figure 6.44 - PMSG sensorless FOC – Discrete-time implementation - Dead-time 3µs – waveforms 1

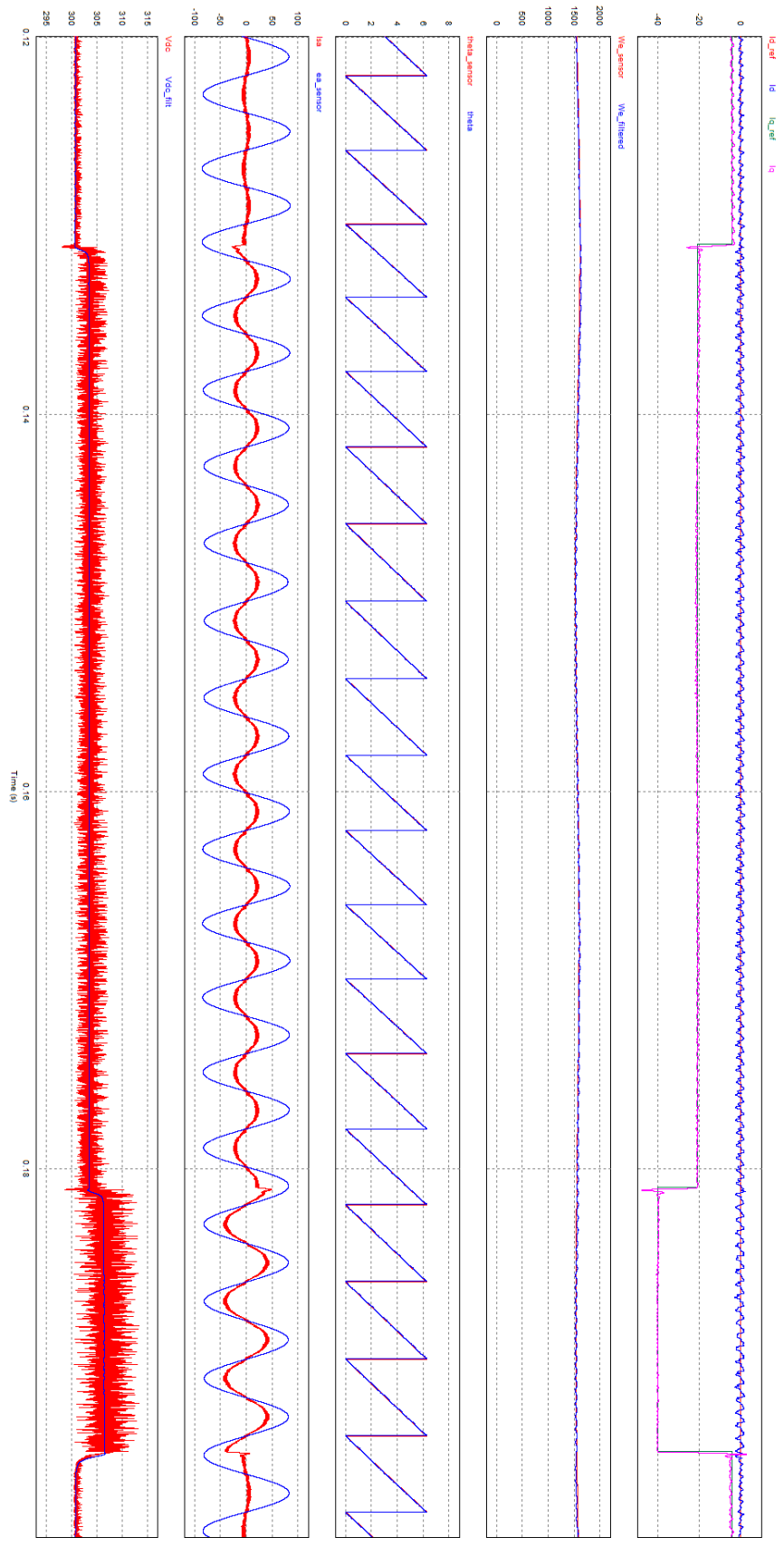

Figure 6.45 - PMSG sensorless FOC – Discrete-time implementation - Dead-time 3µs – waveforms 2

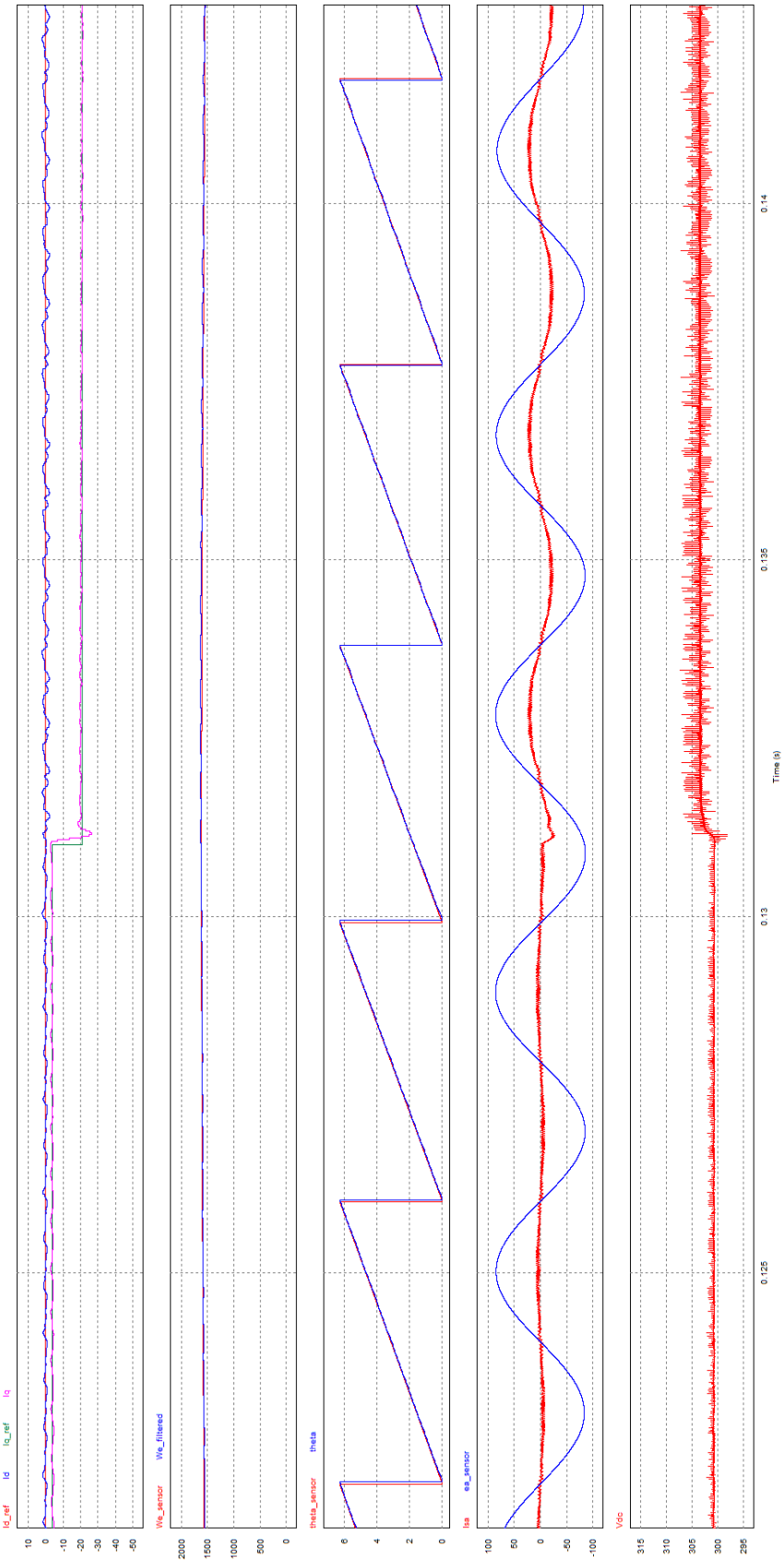

Figure 6.46 - PMSG sensorless FOC – Discrete-time implementation - Dead-time 3µs – waveforms 3

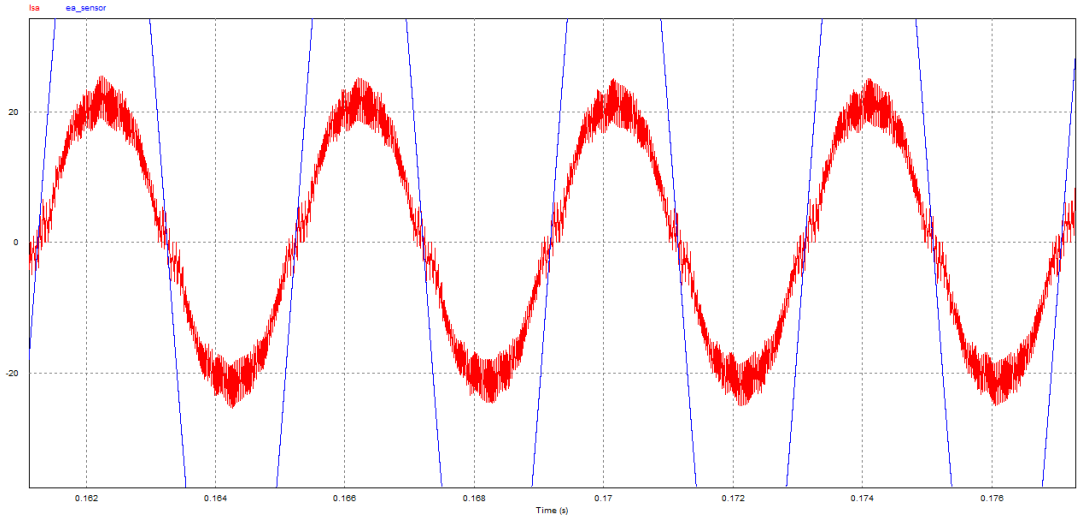

Figure 6.47 - PMSG Sensorless FOC - PSIM discrete-time implementation – Phase-a current waveform detail – Dead-time 3µs

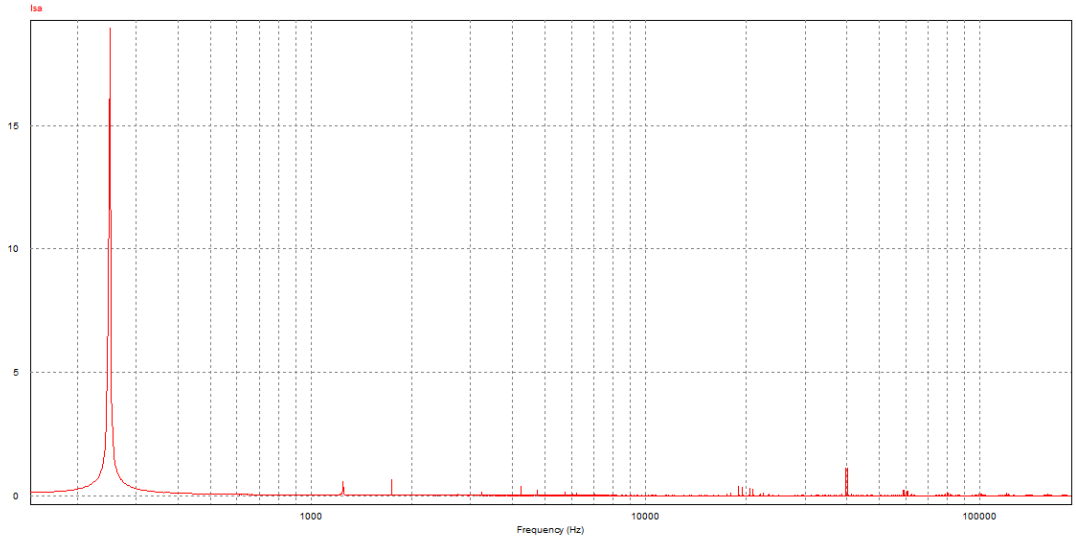

Figure 6.48 - PMSG sensorless FOC – PSIM discrete-time implementation - Dead-time 3µs - Frequency spectrum of Phase-*a* current

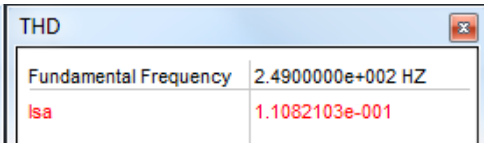

Figure 6.49 - PMSG sensorless FOC - PSIM discrete-time implementation – Dead-time 3µs - THD of phase-*a* current

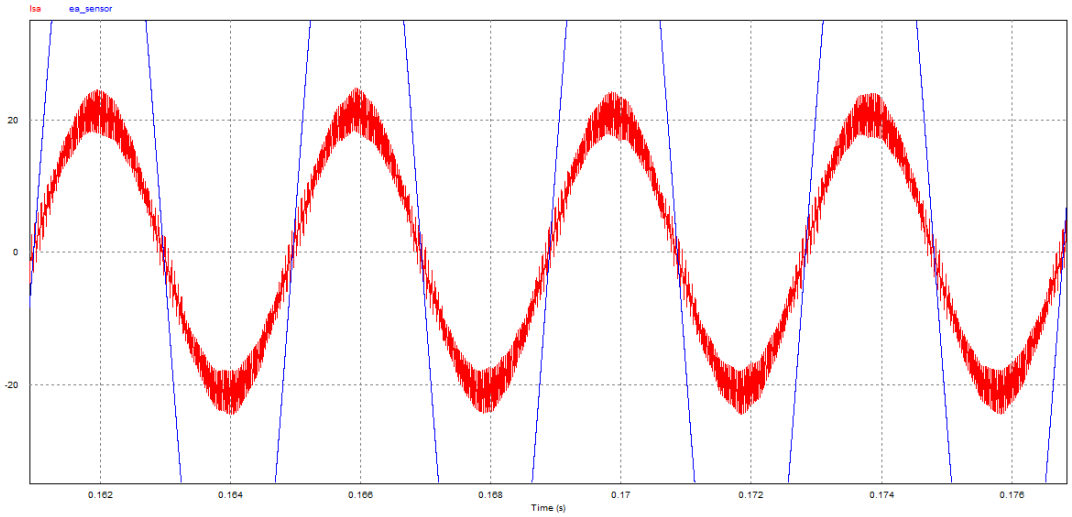

Figure 6.50 - PMSG sensorless FOC - PSIM discrete-time implementation – Dead-time 0μs - Phase-a current waveform detail

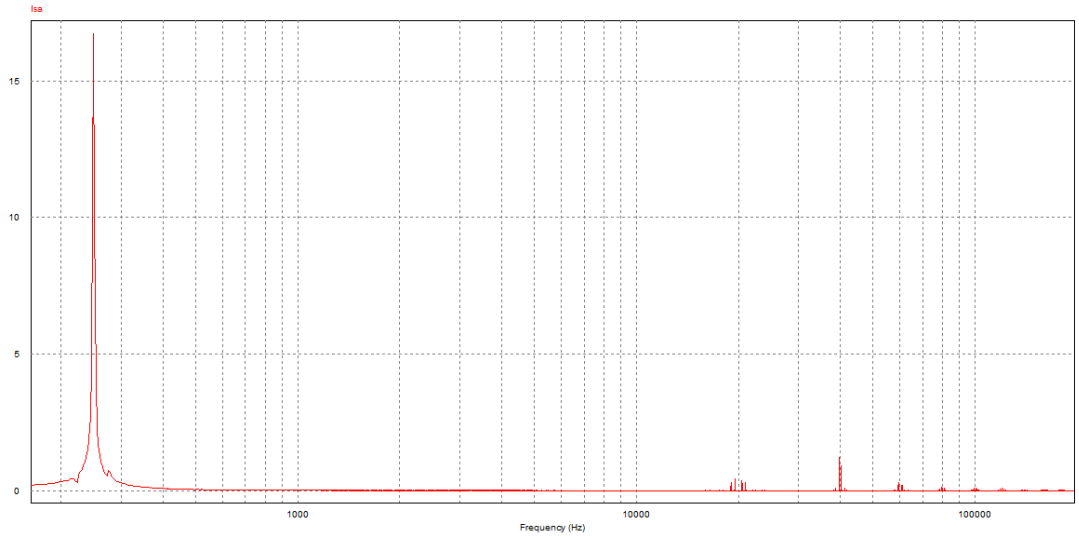

Figure 6.51 - PMSG sensorless FOC – PSIM discrete-time implementation - Dead-time 0μs - Frequency spectrum of phase-a current

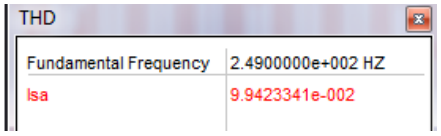

Figure 6.52 - PMSG sensorless FOC - PSIM discrete-time implementation – Dead-time 0μs - THD of phase-a current

6.16 Conclusions

In this chapter the two main vector control methods addressed to PMSMs, FOC and DTC, are described and compared.

Based on the PMSM equations in dq frame (Chapter 2) and on the modeling concepts (Chapter 3), a suitable current controller is derived in dq frame.

The design of the experimental setup is done taking into account the ICE, PMSG, and DC bus characteristics.

Sensor and sensorless (SFR-PLL) FOC with constant angle control strategy are evaluated and compared with the help of PSIM. Results show a very similar behavior and a very good dynamic response to step changes in the i_q control reference.

A new sensorless control strategy, applied to PMSM and based on SRF-PLL and two dq frames (one for flux and voltages, and the other for currents), is presented. Results show a good dynamic response and a good estimation of the rotor angle and speed.

For the PMSM adopted in this work, three control strategies are compared. Due to the PMSM anisotropy, results show MTPA and constant angle control produce the same results. For the sake of simplicity the control strategy sets $i_d = 0$ and thus the PMSM is controlled only by the i_q reference.

The PMSM control in discrete-time is implemented in PSIM using "microcontroller-ready" C-code. The control loop is executed at the same rate (40kHz/20kHz), as is in the experimental setup whose implementation is described in Chapter 7.

The simulation analysis shows that discrete-time and continuous-time produce similar results. Laboratorial results (see Chapter 7) confirm the robustness of the solution.

6.17 References

[1] C. A. Martins and A. S. Carvalho, "Technological trends in induction motor electrical drives," in *Power Tech Proceedings, 2001 IEEE Porto*, 2001, p. 7 pp. vol.2.

[2] X. d. T. Garcia, B. Zigmund, A. A. Terlizzi, R. Pavlanin, and L. Salvatore, *Comparison between FOC and DTC Strategies for Permanent Magnet Synchronous Motors* vol. 5, 2011.

[3] P. Vas, *Sensorless Vector and Direct Torque Control*: Oxford University Press, 1998.

[4] B. Wilamowski and J. Irvin, *The Industrial Electronics Hanbook - Power Electronics Handbook*, Bogdan M. Wilamowski; J. David Irvin ed. vol. 2: CRC Press, 2011.

[5] F. Blaschke. (1972) The Principle of Field Orientation as Applied to the New Transvector Closed Loop Control Systems for Rotating Machines. *Siemens Review*.

[6] I. Takahashi and T. Noguchi, "A New Quick-Response and High-Efficiency Control Strategy of an Induction Motor," *Industry Applications, IEEE Transactions on,* vol. IA-22, pp. 820-827, 1986.

[7] U. Baader, M. Depenbrock, and G. Gierse, "Direct self control (DSC) of inverter-fed induction machine: a basis for speed control without speed measurement," *Industry Applications, IEEE Transactions on,* vol. 28, pp. 581-588, 1992.

[8] R. Krishnan, *Permanent Magnet Synchronous and Brushless DC Motor Drives*: CRC Press, 2010.

[9] M. Kazmierkowski, R.Krishnan, and F. Blaabjerg. (2002). *Control in Power Electronics - Selected Problems*.

[10] S. Morimoto, Y. Takeda, T. Hirasa, and K. Taniguchi, "Expansion of operating limits for permanent magnet motor by current vector control considering inverter capacity," *Industry Applications, IEEE Transactions on,* vol. 26, pp. 866-871, 1990.

[11] ENSTROJ. (2014, 2015-02-07). *EMRAX 228 High Voltage PMSM datasheet - 2013 version [Online]*. Available: http://www.enstroj.si

[12] D. M. F8C. (2015, 22-04-2015). *Daewoo Matiz F8C - Power, Torque and Fuel curves [Online]*. Available: http://www.suzukituning.com/SuzukiTuning/AltoTuning/Pictures/Daewoo%20Matiz%20F8C%20Power%20Output.GIF

[13] A. Lopes, "Controlo Avançado de Conversores para Sistemas FotoVoltaicos," Master Thesis, DEE, Porto, FEUP, 2013.

[14] H. Peng and G. Chiu. (2008). *Design of Discrete Time Controller - Input/Output Approaches - Chapter 6 (Purdue University ed.)*.

7
Physical Setup and Practical Experiments

7.1 Introduction

In this chapter is described the physical setup design and its implementation and the practical experiments performed to validate the theoretical approach developed in the previous chapters and already verified by simulation.

The conclusions derived from the comparison between those two set of results, those obtained by simulation with the experimental ones, confirm the effectiveness of the proposals developed along this work.

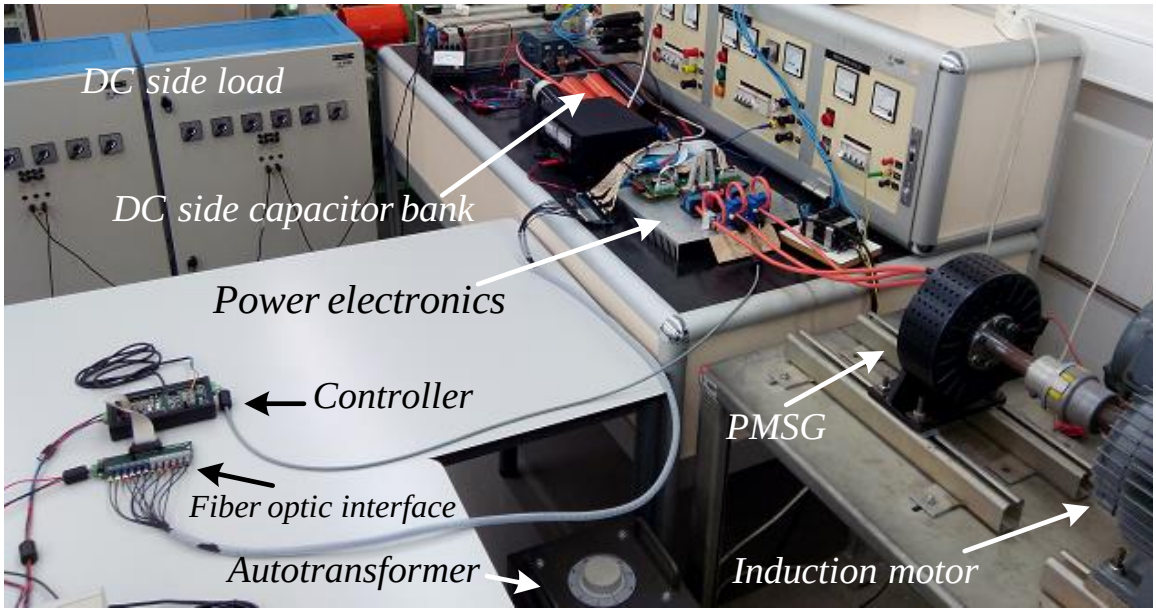

Figure 7.1 - Physical setup overview

7.2 Hardware Description

The physical setup comprises (see Figure 7.1 and Figure 7.2):

- an EMRAX PMSG direct driven by a 4.5kW induction motor;
- a power electronics converter;
- a DC Bus having a 9900uF/650V capacitor bank and two load resistor boxes;
- the system controller;
- Fiber optic interface.

A shielded cable carries the current transducers signals to the controller and twelve fiber optics cables carry the command/fault signals between controller and power electronics converter. All they have about one meter long.

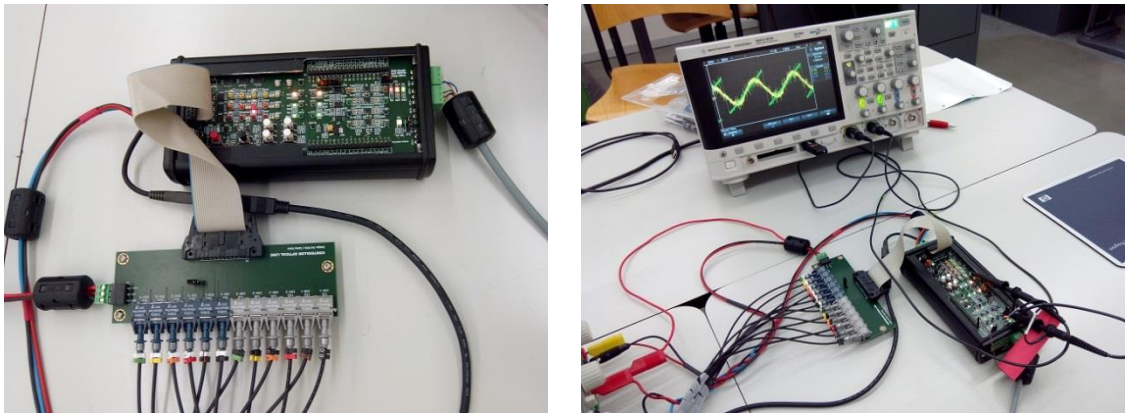

Figure 7.2 - Physical setup – control side overview

7.2.1 The Controller Central Processing Unit

A controller Central Processing Unit (CPU) guarantees that data acquisition, data processing, and control commands are performed or provided at the intended rate.

A first approach to choose a CPU is centered on its architecture. Different CPU architectures were considered:

- Field-Programmable Gate Array (FPGA);
- Digital Signal Processor (DSP);
- Microcontroller (MCU).

The FPGA is the fastest CPU unit as it is based on parallel processing and on low level programming language. The DSP are specially optimized to signal processing, particularly audio and video, where some relevant tasks are performed directly by hardware allowing some degree of parallel processing.

The Microcontroller core does not allow parallel processing in the strict sense of the word. However microcontrollers integrate a set of peripheral devices, e.g. ADC, DAC, PWM and others that after properly programmed can perform their tasks and communicate between them independently of the processor unit. In this sense some degree of parallel processing is also achieved by microcontrollers.

After the first approach the question that arose was: which CPU / CPU-board should be adopted that ensuring the computation effort needed, also provide:

- the less learning effort;
- an integrated development system;
- the less cost.

The answer to the previous question resulted in the adoption of Infineon's "XMC4500 Relax Lite Kit" (see Figure 7.4), a low cost but powerful evaluation board based on the Infineon's XMC4500 32-bit ARM Cortex M4 microcontroller, running at 120MHz. The XMC4500 belongs to the Infineon's 32-bit XMC4000 family of microcontrollers specially designed to motor drive systems. Furthermore, Infineon provides a free integrated development environment called DAVE 3 which has a set

of plug-and-play Software Applications (Apps) that allows to speed up the development of motor/generator control systems. The SVM, PWM, ADC and DAC are only a few Apps examples. DAVE 3 is also a compiler debugger, flash loader and automatic code generator.

The Figure 7.3 shows a comparative table of the Infineon's 32-bit XMC4000 family of microcontrollers. The XMC4500 [1] is the Infineon's most performant microcontroller actually made available in a low-cost kit format. Currently, the "XMC4500 Relax Lite Kit" [2] costs €10.00.

		Low-end				High-end
* Under definition		XMC4100	XMC4200	XMC4400	XMC4500	XMC4700*
System Performance	Core	ARM® Cortex™-M4				
	CPU frequency (at 125 °C)	80 MHz	80 MHz	120 MHz	120 MHz	180 MHz
	Co-proc	Floating Point Unit				
	Flash size	128 kB	256 kB	512 kB	1 MB	2.5 MB
	RAM size	20 kB	40 kB	80 kB	160 kB	512 kB
	Cache	4 kB	4 kB	4 kB	4 kB	6 kB
Timers	POSIF	1x	1x	2x	2x	2x
	CCU4 (4ch)	2x	2x	4x	4x	4x
	CCU8 (4ch)	1x	1x	2x	2x	2x
	High-resolution PWM (150ps)	1x	1x	1x		
Signal Pro-cessing	ADC 12-bit	2x	2x	4x	4x	4x
	Delta/Sigma Demodulator			4x	4x	4x
	DAC	2x	2x	2x	2x	2x
Communication	IEEE 1588 Ethernet MAC			1x	1x	2x
	USB	FS DEV	FS DEV	FS OTG	FS OTG	HS OTG
	SD/MMC				✓	✓
	Serial channels (UART, SPI, I²C, I²S)	4x	4x	4x	6x	6x
	Ext. Memory I/F				✓	✓
	CAN	1x	1x	2x	3x	3x
	Touch Button	✓	✓	✓	✓	✓

Figure 7.3 - Infineon's ARM Cortex M4 microcontrollers [1]

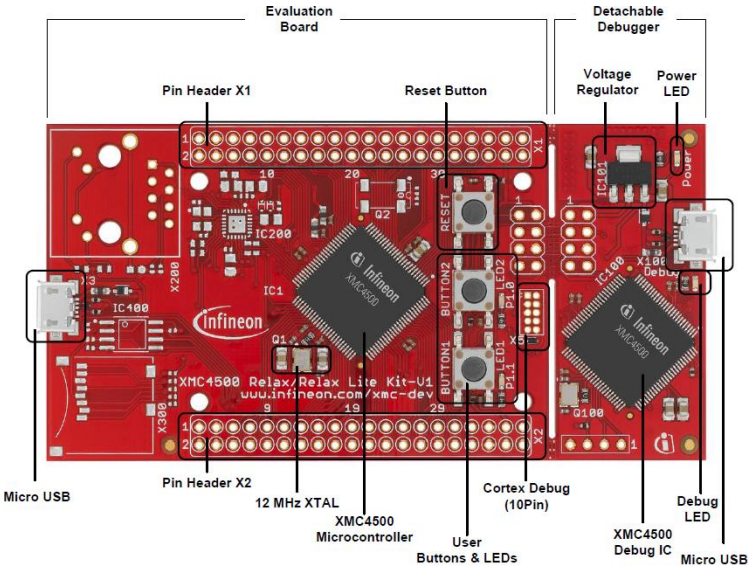

Figure 7.4 - Infineon's XMC4500 Relax Lite Kit [2]

The most important "XMC4500 Relax Lite Kit" features are presented in Figure 7.5. An integrated detachable on-board debugger allows on-site programming and

debugging. Furthermore, up to 17xADC (12 bit) and 2xDAC are available among many other features.

Feature	XMC4500 Relax Kit-V1	XMC4500 Relax Lite Kit-V1
XMC4500 Microcontroller (ARM® Cortex™-M4F based)	✓	✓
Detachable on-board Debugger	✓	✓
Power over USB	✓	✓
2 x User Button and 2 x User LED	✓	✓
Reset Button	✓	✓
Power Regulator from 5 V to 3.3V	✓	✓
4 x SPI-Master, 3x I2C, 3 x I2S, 3 x UART, 2 x CAN, 17 x ADC (12 bit), 2 x DAC, 31x PMW mapped on 2 Pin Headers 2 x 20	✓	✓
USB-OTG (Micro USB Plug)	✓	✓
Ethernet PHY and RJ45 jack	✓	
Real Time Clock Crystal	✓	
32 Mbit Quad-SPI Flash Memory	✓	
microSD Card Slot	✓	

Figure 7.5 - Infineon's XMC4500 Relax (Lite) Kit Features [2]

7.2.2 The Three-Phase IGBT Module

The three-phase IGBT module available for this work is the Infineon's FS200R07A1E3 HybridPACK™ 1 module [3] (see Figure 7.6). This is an automotive qualified power module designed for Hybrid Electric Vehicle applications for a power range up to 20–30kW.

The FS200R07A1E3 main features are:

- IGBT DC-collector current 200A;
- IGBT repetitive peak collector current 400A;
- IGBT collector-emitter voltage 650V;
- Maximum turn-off delay time 390ns;
- Minimum turn-on delay time 50ns.

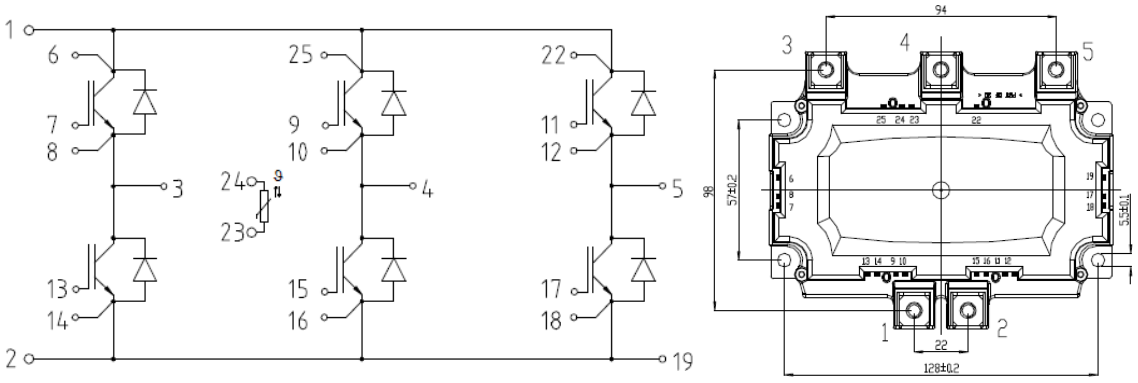

Figure 7.6 – Infineon's FS200R07A1E3 HybridPACK™ 1 module [3]

7.2.3 The IGBT Driver Module

The IGBT driver module available for this work is the Concept plug-and-play dual-channel IGBT driver 2SP0115T2A0-17 [4] shown in Figure 7.7.

Figure 7.7 - Concept plug-and-play dual-channel IGBT driver 2SP0115T2A0-17 [4]

The main IGBT driver features are:

- Supports IGBT modules up to 1700V;
- Gate resistors are assembled by the user according to specific IGBT requirements;
- Turn-on driver delay 75ns;
- Turn-off driver delay 65ns;
- IGBT's can be operated either in "direct mode" or in "half-bridge mode" (in the "direct mode" the dead-times are generated by the control circuit) ;
- In "half bridge mode" the dead-time is 3us;
- Fault condition outputs, activated when either the driver's power supply is undervoltage or when a short-circuit in a particular IGBT is detected.

7.2.4 Dead-time Discussion and Interface Board Between the IGBT Module and IGBT Drivers

In order to guarantee the IGBT module maximum protection, the "half-bridge mode" of operation is adopted. This mode of operation is selected by setting an appropriate command to the IGBT drivers. In this mode the dead-time between IGBT outputs is 3μs.

The Infineon's Application Note AN2007-04 [5] explains in detail how to calculate a proper dead-time that depends on a set of variables. Nevertheless a first approach to the dead-time calculation is given by the expression

$$t_{dead} = \left(\left(t_{D\_OFF\_MAX} - t_{D\_ON\_MIN}\right) + \left(t_{PDD\_MAX} - t_{PDD\_MIN}\right)\right)1.2 \qquad (7.1)$$

where:

- $t_{D\_OFF\_MAX}$ is the maximal turn-off delay;
- $t_{D\_ON\_MIN}$ is the minimal turn-on delay;
- t_{PDD_MAX} is the maximal propagation delay of driver;

- t_{PDD_MIN} is the minimal propagation delay of driver;
- 1.2 is the safety margin to be multiplied.

Because Infineon's IGBT module and Concept driver datasheet only gives typical values it is difficult to find the dead-time in this way. Nevertheless, this expression gives an order of magnitude for the dead time.

Computing the times from both IGBT module and driver gives

$$t_{dead} = \left(\left(390n - 50n\right) + \left(75n - 65n\right)\right)1.2 = 420ns \tag{7.2}$$

Taking this dead-time estimative it becomes clear that the Concept driver's dead-time of 3µs is too long. A dead-time of 1µs would be more appropriate. The consequences of having a long dead-time were already discussed in Chapter 6.

To interface the IGBT module and the three driver boards (one for each arm), a PCB shown on Figure 7.8 was designed.

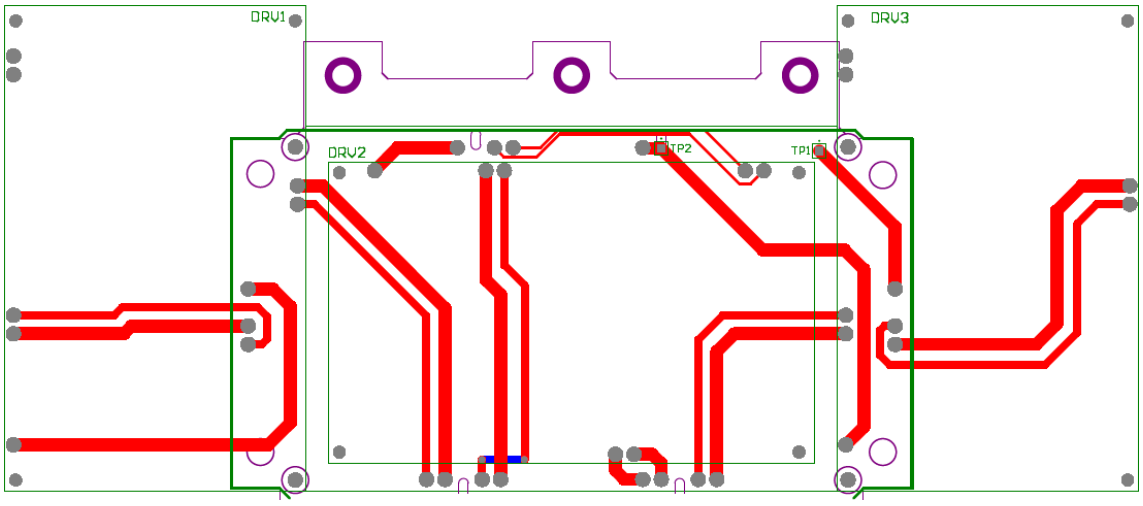

Figure 7.8 - PCB to interface IGBT module and drivers

7.2.5 DC side Capacitor

A DC side capacitor with low ESR directly attached to the DC side IGBT module terminals is required for proper operation of the VSC, as discussed in Chapter 3. The Capacitor available for this purpose is an EPCOS B25655 [6]. Its main features are:

- Capacity 500uF;
- Voltage 450V;
- Series inductance 15nH;
- ESR 1mΩ;
- I_{rms} current 120A.

Figure 7.9 – Capacitor EPCOS B25655 [6]

7.2.6 Current Transducers

To perform currents acquisition, two current transducers LEM 205-S [7] (see Figure 7.10) are adopted. They main features are:

- Primary nominal RMS current $I_{PN} = 100A$;
- Primary current, measurement range $I_{PM} = \pm 200A$;
- Secondary nominal RMS current $I_{SN} = 100mA$;
- Conversion ratio K_N 1:1000;
- Frequency Bandwidth (-3db): $DC\ to\ 100kHz$;
- Closed loop type.

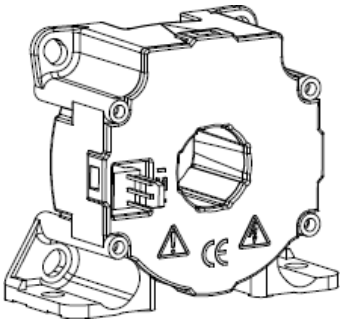

Figure 7.10 - Current transducer LEM 205-S [7]

7.2.7 The Controller Board

To interface the XMC4500 microcontroller with the "external world" it is developed a controller board that supports the "XMC4500 Relax Lite Kit" as a piggyback board (see Figure 7.11 and Figure 7.12).

The controller interface board's main features are:

- Current acquisition of two phases and signal conditioning;
- DC BUS voltage acquisition and signal conditioning;
- PMSG / IGBT module temperature acquisition and signal conditioning;
- Controller interface to three IGBT drivers, allow choosing "direct control" or "half-bridge control" and to deal with the driver's fault condition outputs;
- Power circuit protection, by hardware, on these events: positive or negative maximum current detection; maximum DC BUS voltage detection; fault

condition send by IGBT's drivers; if one of this events occur all control actions are disabled; for each IGBT fault condition, there is a Flip-flop and an individual LED that signalizes the event;

- One push-button to reset all six IGBT fault condition status;
- A bicolor LED that visually shows the SRF-PLL synchronization status;
- A PANIC push-button to stop, by hardware, all control actions;
- Four push-buttons to set/perform control actions;
- Power supply to current and voltage transducers, and temperature sensor;
- Independent power supply to analog and digital circuits;
- 32 test points that allow to observe internal signals (e.g.: measured currents; conditioned currents; SVM waveforms; code execution time; estimated theta angle; estimated speed and others);

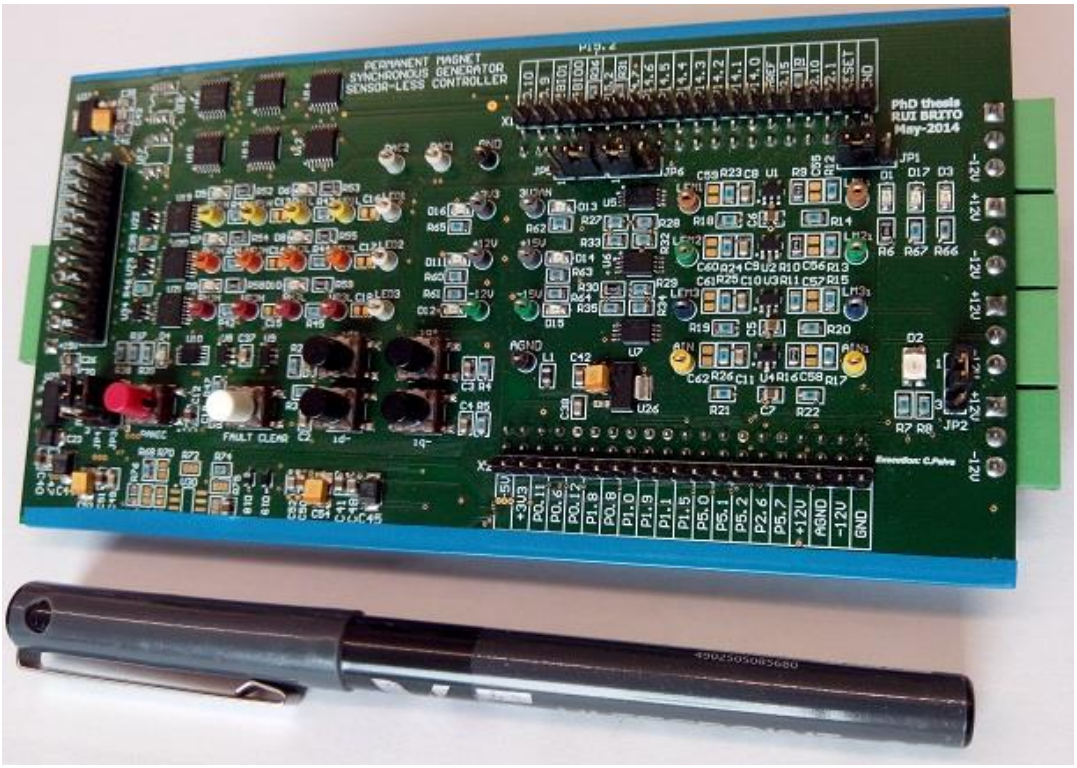

Figure 7.11- Controller interface Board - front side

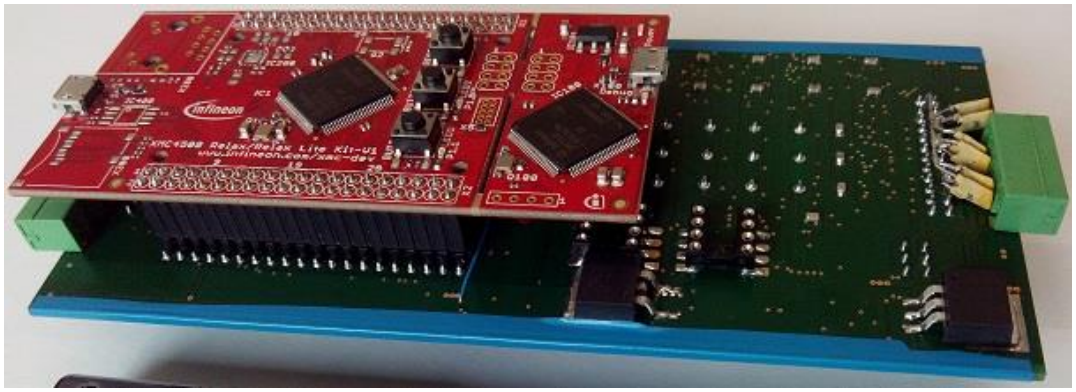

Figure 7.12 - Controller interface board - back side with piggybacked XMC4500 kit

7.2.8 Currents Acquisition

In this work the maximum acquired current is set to $I_P = \pm 55A$.

In order to double the sensibility of the current's acquisition, the power cable (that interconnects PMSG and converter), gives two turns around the transducer. In this way an $I_P = \pm 55A$ leads to an $I_S = \pm 110mA$.

The XMC4500 12-bit ADCs have a full scale of 3.3V. Thus, a resistance of

$$R_{LEM} = \frac{3.3V}{2x110mA} = 15\Omega \tag{7.3}$$

is placed between the LEM output and the ground, giving a current to voltage transducer relation of: $\pm 55A \rightarrow \pm 110mA \rightarrow \pm 1.65V$. This leads to a current to voltage conversion ratio of:

$$\frac{1.65V}{55A} = 30mV / A \tag{7.4}$$

Figure 7.13 shows the signal conditioning circuit that adds an offset of $1.65V$ to the voltage signal for proper ADC operation. For this circuit

$$V_o = 2V_{aux} - V_i \tag{7.5}$$

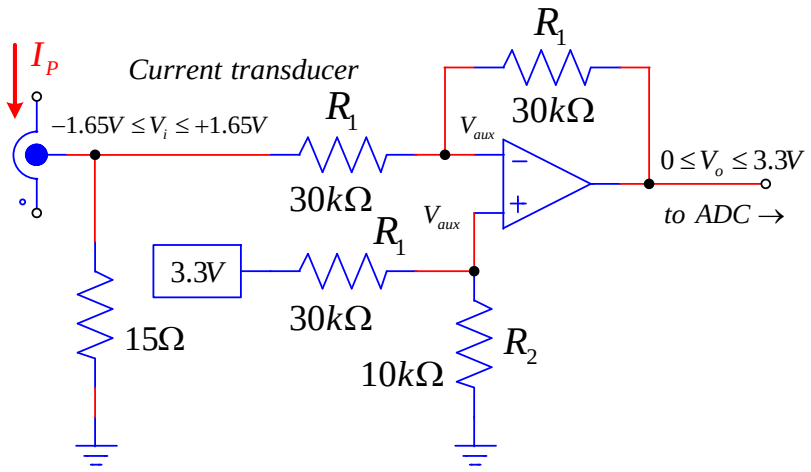

Figure 7.13 - Current signal conditioning

where $2V_{aux}$ is the offset added to the input signal V_i. In this case $2V_{aux} = 1.65V$ leads to $V_{aux} = 1.65V / 2$, which is a quarter of the XMC4500 power supply (V_{DD}=3.3V). In this case the ratio between resistors is $3R_2 = R_1$

In the equation (7.5) the "-" operator can be converted to "+" by inverting the direction of the current measurement in the transducer, as represented in Figure 7.13. The operational amplifier is a rail-to-rail type, supplied with a voltage $V_{DD} = 3.3V$ The output voltage achieves the entire range $0 \le V_o \le 3.3V$.

7.2.9 Overcurrent protection

To detect and protect the system against overcurrents is designed the circuit shown in Figure 7.14. The input signal is Figure 7.13 circuit's output signal. The comparators outputs are open-drain type. The output goes at low level condition whenever $V_i > 3.2V$ or $V_i < 0.1V$. In this way the circuit detects when the current goes over

$$I_{P_{\max}} = \frac{(3.2-1,65)*I_P}{3.3-1,65} = \frac{(3.2-1,65)*55}{3.3-1,65} = +51,7A \tag{7.6}$$

or below

$$I_{P_{\min}} = \frac{(0.1-1,65)*I_P}{3.3-1,65} = \frac{(0.1-1,65)*55}{3.3-1,65} = -51,7A \tag{7.7}$$

For a perfect sinusoidal current with $51.7A$ peak this corresponds to: $I_{P_{RMS}} = 36.5A$.

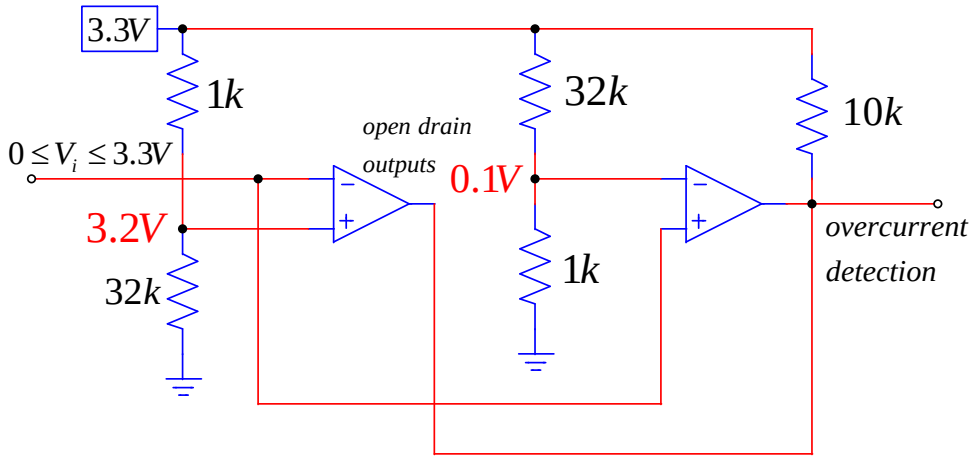

Figure 7.14 - Overcurrent circuit detection

7.2.10 Fiber Optics Interface to IGBT Drivers

The control system was originally designed to interconnect both the controller interface board and the IGBT driver's board by means of an 8cm flat cable. Although the drivers isolate both signals and power, experimental tests have shown that the drivers injected high frequency, commutation related signals on the control board making control impossible.

The solution was to isolate the boards using an optic link. A couple of optical fibers interface boards were designed. The optical fiber interface have six command signals for IGBTs and six more for IGBTs fault condition signals. The optical fiber circuits can be seen on Annex 2. The optical fibers' emitter/receiver are from Avago's HFBR-xT21Z family, with a typical propagation delay of 5ns/m of fiber optic cable. The twelve fiber optic cables used in this interface have a meter long.

7.3 Control Software

To take advantage of the DAVE 3 [8] Space Vector PWM App, the structure of the control software has to be drawn around this App.

Figure 7.16 shows a global view of all DAVE 3 Apps used in this project where the SVM App is highlighted. Figure 7.15 shows the SVM App (PWMSVM01) main interface, where the PWM frequency is set to $20kHz$. This setting implies that an interrupt is generated every $1/20k = 50us$ and all control code, as well as other auxiliary code, must run within this time frame.

At the beginning of each interrupt, the control variables previously set by the command "PWMSVM01_SVM(&PWMSVM01_Handle0, Amplitude, Angle)" are loaded and the SVM operation is performed accordingly. The (Magnitude, Angle) are respectively the variables $(v\_mag,\ \theta_v)$ (see Chapter 6).

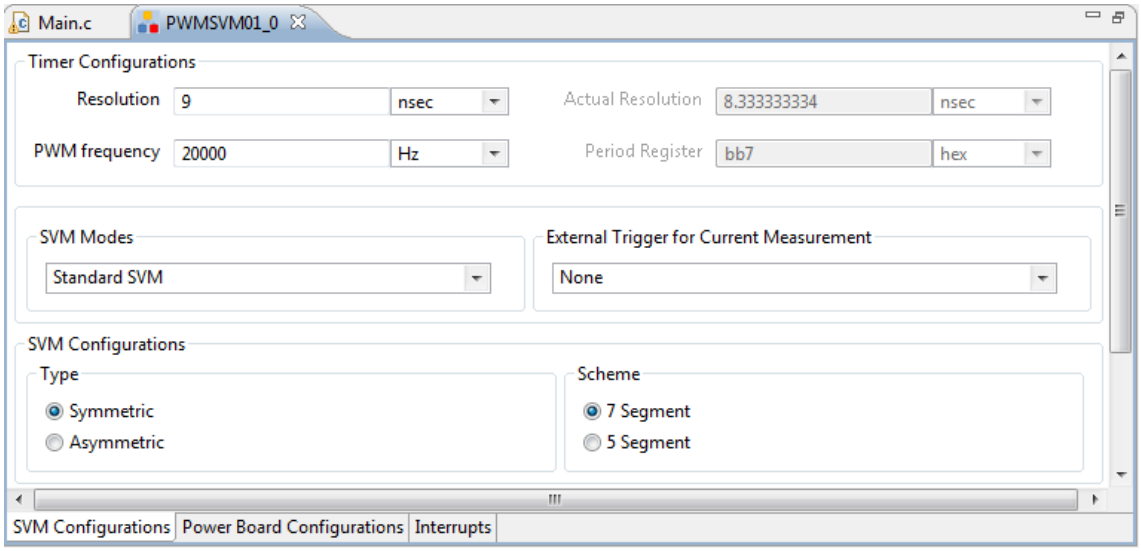

Figure 7.15 - DAVE 3 SVM App's main interface [8]

In order to guarantee a better θ_e and ω_e estimation, two current acquisitions are performed within the $50\mu s$ period. This process is achieved by dividing the $50\mu s$ time period in two time slots of $25\mu s$. Refer to Chapter 6 for more details.

The Figure 7.17 shows a flowchart of the control and auxiliary operations performed within the $50\mu s$ time period.

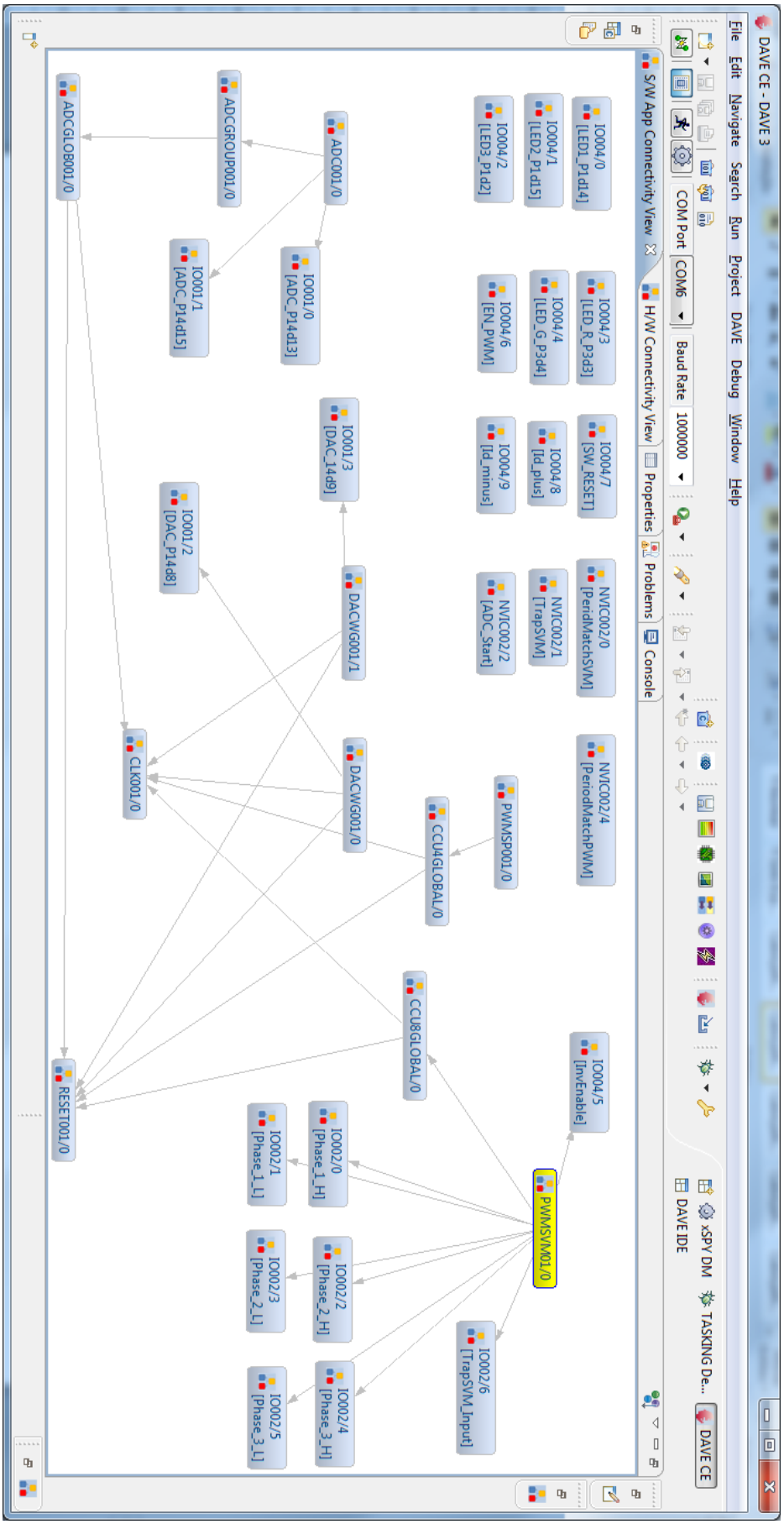

Figure 7.16 - Infineon's DAVE 3 project [8]

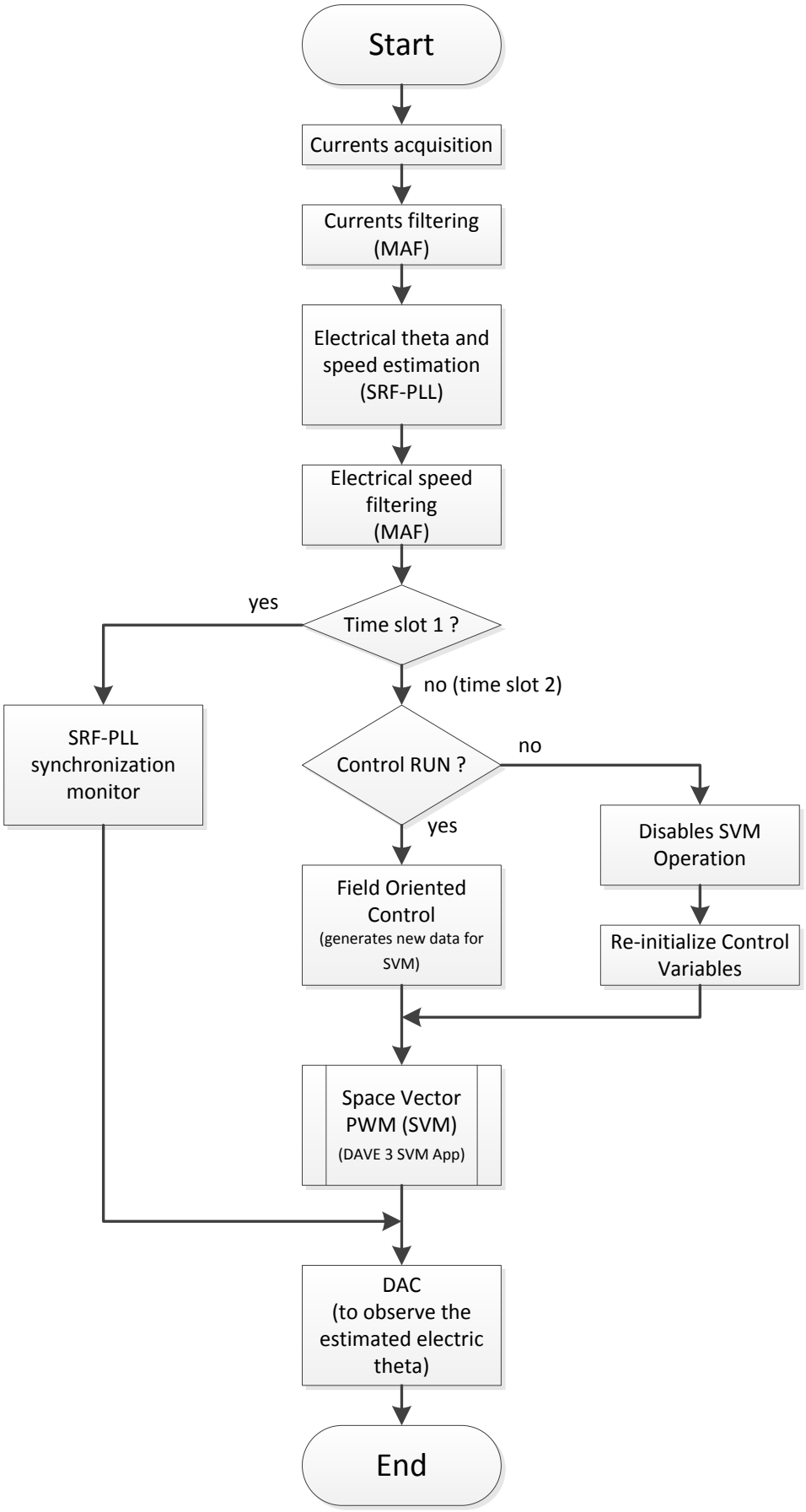

Figure 7.17 - Interrupt control routine

7.4 Timing Issues

The Figure 7.18 shows a real time diagram of the SVM interrupt. The waveform one (in yellow), shows a period of $50\mu s$ delimited by two interrupt events. The DAVE 3 SVM App itself takes about $6.4\mu s$ to be executed on the "XMC4500 Relax Lite Kit". This is the time it takes to reconfigure de XMC4500 peripherals according to the new variables $(v\_mag,\ \theta_v)$. The remaining time is free to be used by the user's C code.

The waveform two (in green), shows the $50\mu s$ divided in two time slots of $25us$, were the SVM App run time is included in the slot two. Each $25\mu s$ slot is divided in turn in two time zones related to currents acquisition and code execution. The interval reserved to currents acquisition has $5us$ fixed time. Each ADC conversion takes $0.55\mu s$ so up to nine ADC conversions can be performed within this time frame. The ADCs are operated in "background mode" which means that the ADCs' conversion is triggered by hardware. In this way the $5\mu s$ window can be used to run auxiliary code. For now this window is reserved to implement a communications system.

The "Control and Auxiliary C Code" time frames are the time space where the operations (C code) described in the flowchart of Figure 7.17 are performed. Figure 7.19 shows in detail which operations are executed and how much time they last.

The system's bottleneck is shown in Figure 7.18. The "Control and Auxiliary C Code" time duration in slot 2 is limited by the next SVM interrupt event. Thus, if needed, extra auxiliary C code should be allocated to slot 1.

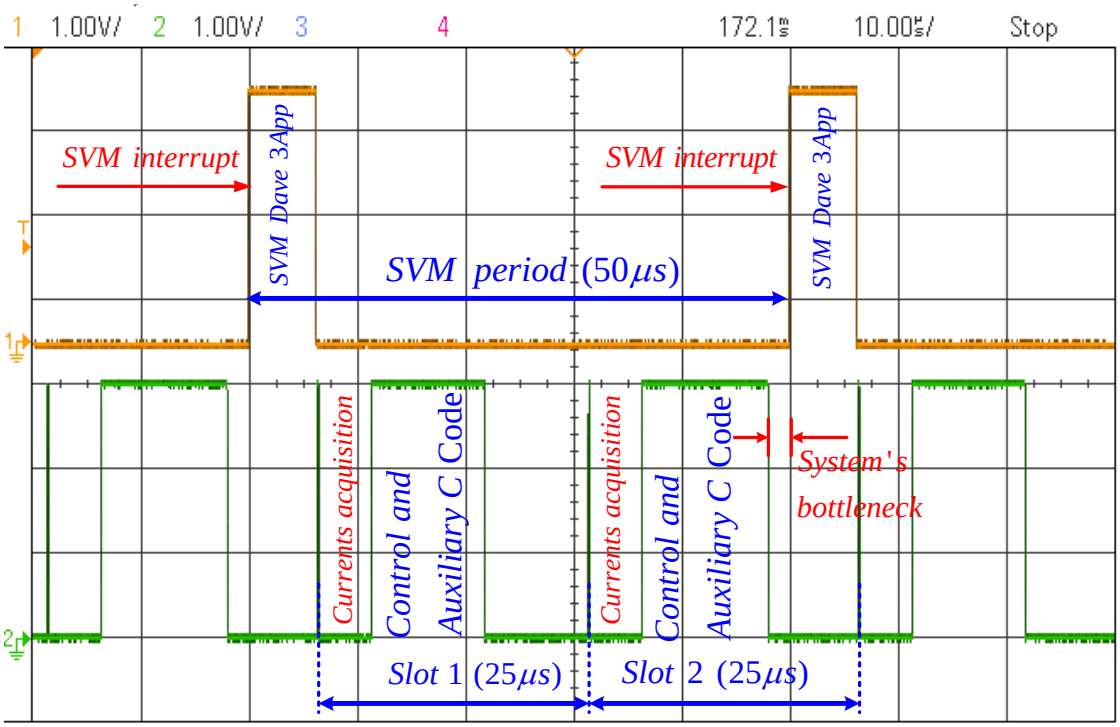

Figure 7.18 - DAVE 3 SVM App interrupt - time diagram

Numbers from 1 to 5 in Figure 7.19 identify the time frames where the following list of user programed operations (C code) are performed within one $50\mu s$ period interrupt:

1) refers to all operations needed to estimate θ_e and ω_e; it includes to get real current values, current filtering (MAF), SRF-PLL related calculations and ω_e filtering (MAF); Depending on where these operations are performed, in slot 1 or 2, they can last up to $4.9\mu s$;
2) are auxiliary operations to get the maximum and minimum magnitude of the currents; They run in slot 1 and last $1.4\mu s$;
3) are auxiliary operations to monitor the PLL synchronization through a bicolor LED (red and green); They run in slot 1 and last $4.1\mu s$;
4) are auxiliary operations to deliver the estimated θ_e at one of the XMC4500's DAC outputs; They run in both slots and last $2.2\mu s$;
5) refers to all operations related to FOC, including PI digital implementations square root and ATAN calculations; They run on slot 2 and last $4.3\mu s$.

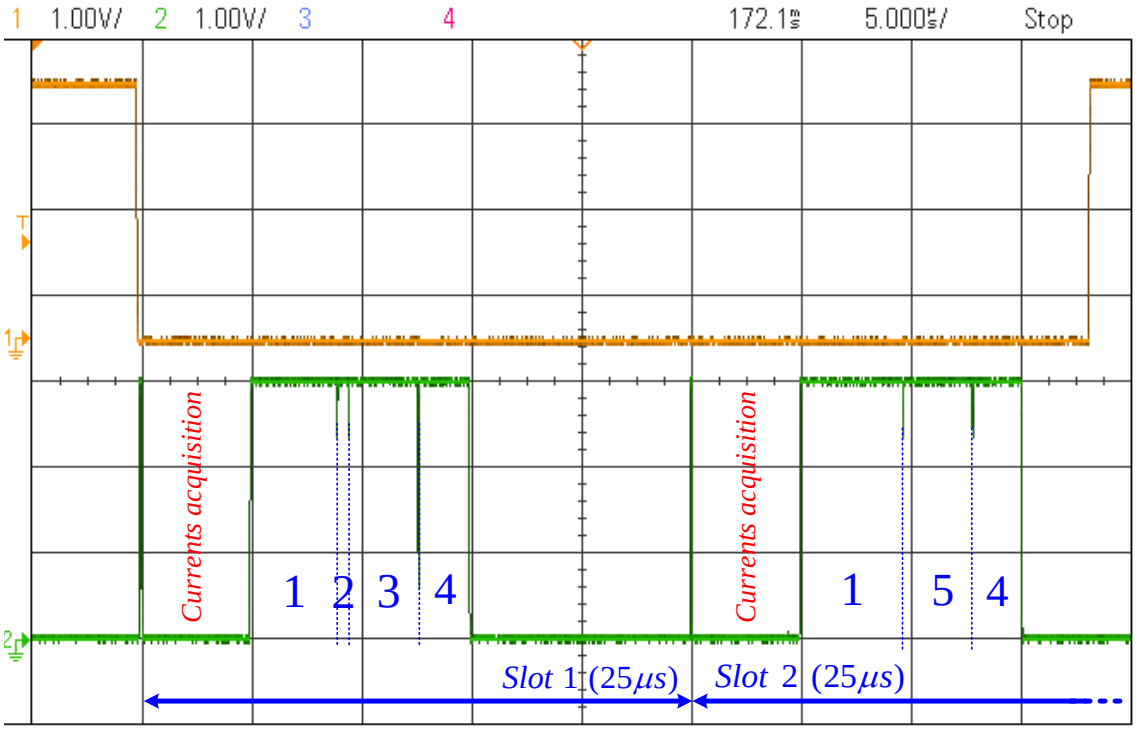

Figure 7.19 - DAVE 3 SVM App interrupt - detailed time diagram

The Table 7.1 shows additional operation's runtimes as a reference.

Operation	Runtime
To get ADC acquisitions (after ADC conversion), apply offsets and convert to real magnitude currents	1.7us
Moving Average Filter (MAF)	0.5us
Square Root calculation	0.6us
ATAN calculation	1.9us
PMSG equations (calculations in order to obtain V_d and V_q)	0.35us
Digital output port toggle (read-modify-write operation)	0.15us
Digital output port Set or Reset	0.05us

Table 7.1 - XMC4500 operation's runtime

7.5 Laboratory Experiments

To provide a smooth startup of the couple IM and PMSG, an autotransformer is used to feed the IM. The autotransformer allows to vary the machine speed by varying the supply voltage magnitude.

The IM is a two pair-pole machine so its speed, depending on the load, can achieve up to near $1500rpm$. Measurements made at no load condition gave $\omega_m = 1498rpm$ that corresponds to the electrical PMSG speed of $\omega_e = 1568rad/s$.

7.5.1 Experiment 1

The first experiment aims to confirm the PMSG field flux magnitude, which is, according to the EMRAX datasheet, $\psi_f = 0.053Wb$. At no load condition the phase-to-phase rms voltage measured at the PMSG terminals is $101.4V@1498rpm$. This leads to a single-phase peak voltage of $v_{\_mag} = 82.8V$.

On the other hand, at no load condition $v_{\_mag} = E$ (Internal EMF) and

$$E = \omega_e \psi_f = 1568 \times 0.053 = 83.1V \tag{7.8}$$

A little variation of 0.3% is observed. This confirms the field flux magnitude.

7.5.2 Experiment 2

A second experiment is performed by setting $i_q^* = -3A$ and $i_d^* = 0A$ and by starting the IM from zero to its maximum speed (when feed at its nominal voltage). Since the angle and speed estimation process started from zero speed, the system quickly achieves stability and the behavior observed is equal to the simulations presented in Chapter 6.

However, the process of extracting power from a generator has normally three steps: (1) start the primary mover, (2) let the primary mover to reach the steady-state speed and (3) start the generation process.

In this case the estimation process is initialized only at point (3) when phase currents start flowing. So both estimation and control processes start at the same time. In this way, despite stability being reached after some time periods, the initial phase currents can easily reach instantaneous peaks that trigger the overcurrent protections.

In an attempt to solve this issue 330Ω sensing resistors connected in a star-shape are placed at the IGBTs' power module terminals (as described in Chapter 5), shown in Figure 7.20. The resultant residual currents are used to estimate the electrical angle and speed.

The sinusoidal current flowing in each resistor is given by

$$I_{R_{peak}} = \frac{81.3}{330} = 246mA$$
$$I_{R_{rms}} = \frac{81.3/\sqrt{2}}{330} = 174mA \quad (7.9)$$

The power dissipated by these resistors is

$$P_R = 3\frac{V_{R_{rms}}^2}{R} = 3\frac{\left(83.1/\sqrt{2}\right)^2}{330} = 31.4W\ @1498rpm \quad (7.10)$$

which represents 0.16% of the EMRAX continuous power ($20kW$) at this speed.

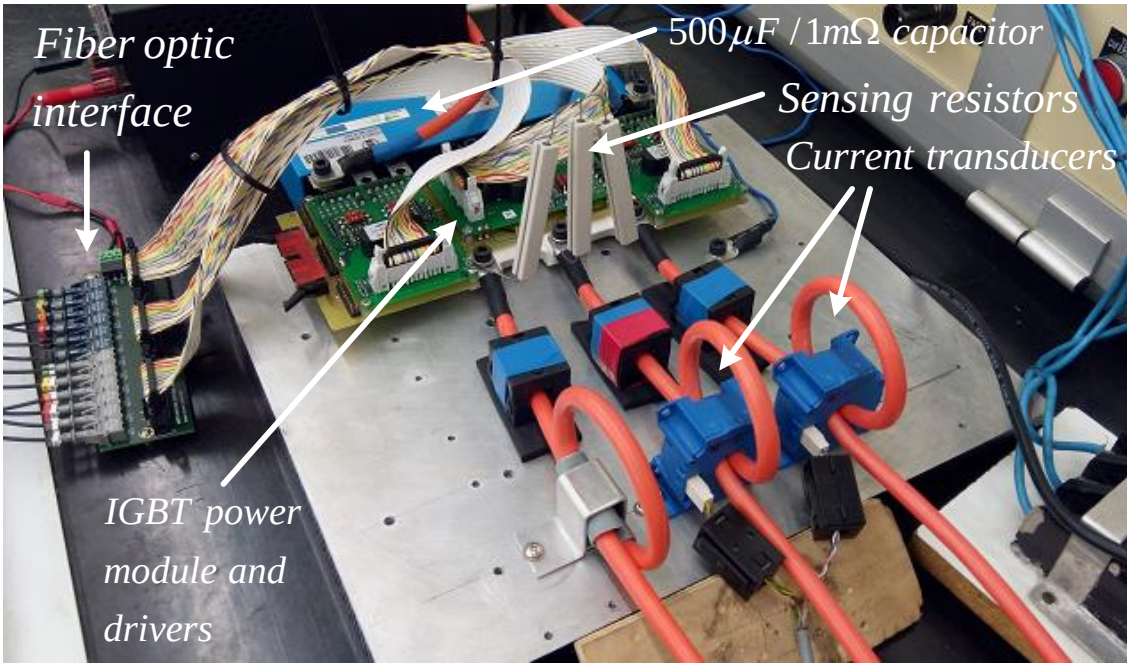

Figure 7.20 - Sensing Resistors Placed at the IGBT Module Terminals

Experiments are made considering only these resistors as the PMSG load, (after proper offset correction of the acquired currents).

The Figure 7.21 shows experimentally obtained waveforms of the:

- phase-a voltage given by an isolated voltage probe, in blue;
- phase-a current at one XMC4500 12-bit ADC input, in yellow;
- electrical angle θ_e in one XMC4500 12-bit DAC output, in green.

Notice that at the ADC input there are only a few mV over a full scale of 3.3V.

This experiment confirms the theoretical approach and the simulation analysis done in Chapter 5 where the 330Ω sensing resistances are used to estimate angle and speed.

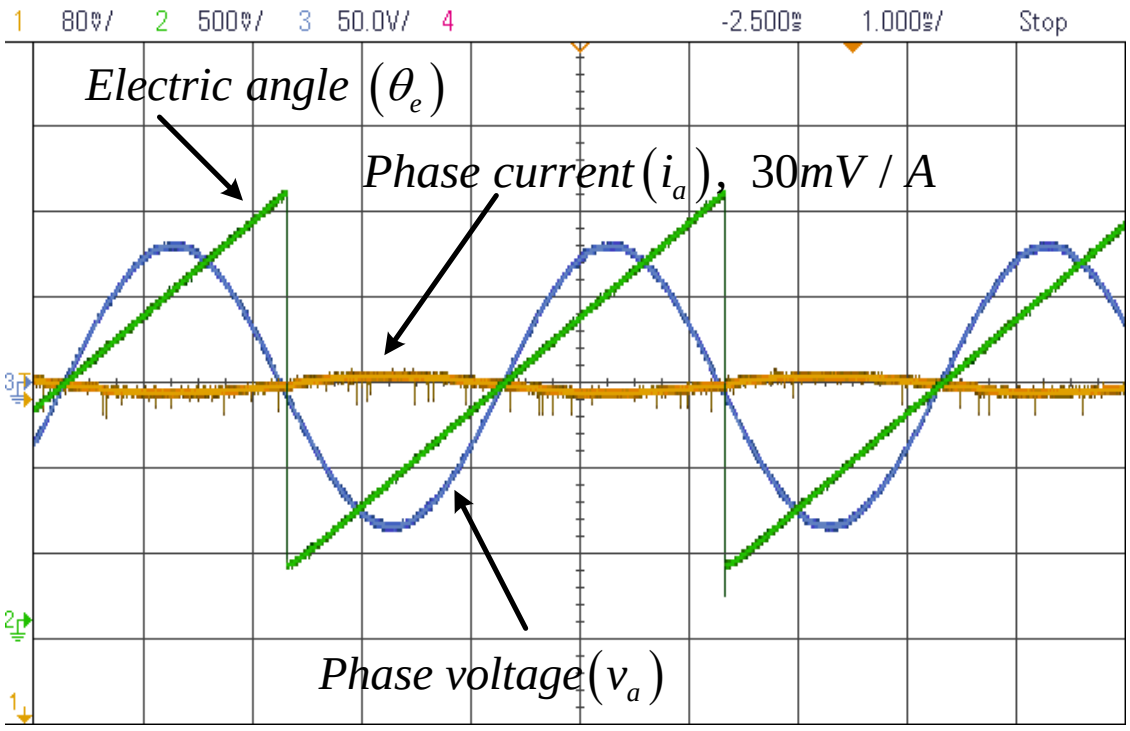

Figure 7.21 - PMSG phase-a voltage and current, and estimated electrical angle based uniquely on the current that flows through the 330Ω sensing resistors

7.5.3 Experiment 3

In this experiment the DC BUS, a $9900\mu s$ capacitor bank in parallel with a 45Ω resistor bank, was connected to the converter's DC-side.

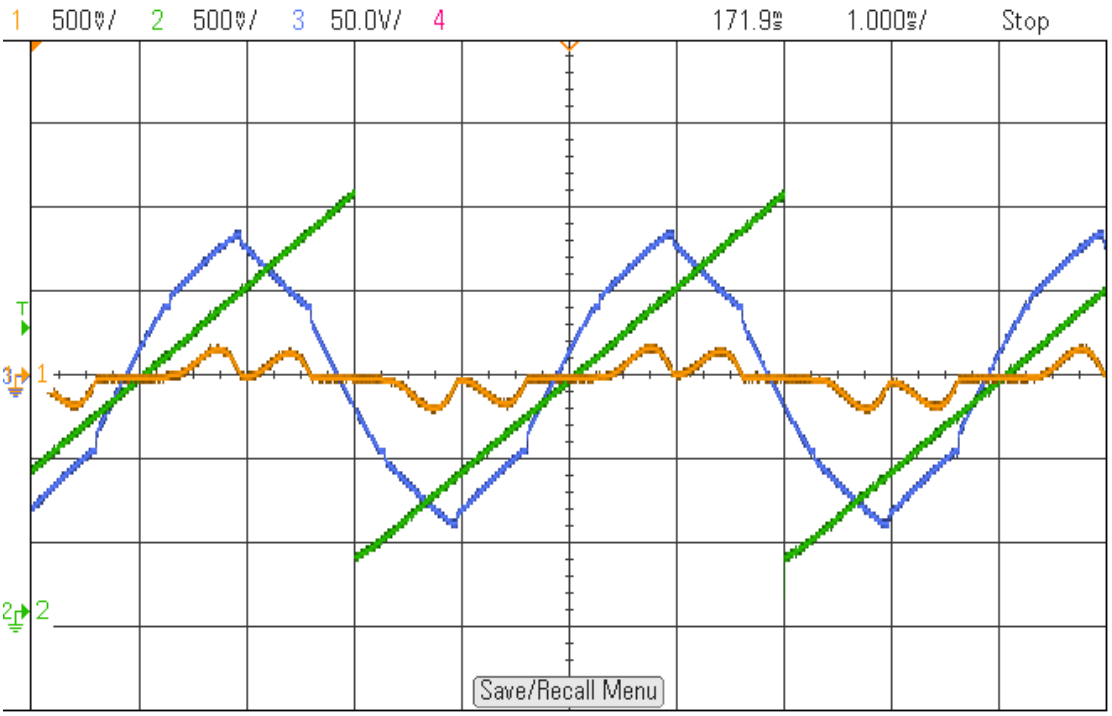

Figure 7.22 – PMSG Phase-a voltage and current, and estimated electrical angle - FOC is disabled (all IGBTs off giving full-bridge rectifier operation with RC load)

With the PMSG running at $1498rpm$ and with FOC disabled, the IGBT power module behaves as a three-phase full-bridge rectifier resulting in characteristic waveforms for this arrangement (see Figure 7.22).

The estimated electrical angle shows a phase delay relative to the phase-a voltage. The V_{DC} voltage is in this case close to the phase-to-phase voltage peak which is $81.3\times\sqrt{3}=140.8V$.

When FOC operation is enabled (with $i_q^*=-21A$ and $i_d^*=0A$), the system behaves as shown in Figure 7.23. After an initial transient peak of $40A$, the current assumes a sinusoidal shape with descending magnitude. Notice that within this time frame the estimated angle waveform shows a slight correction.

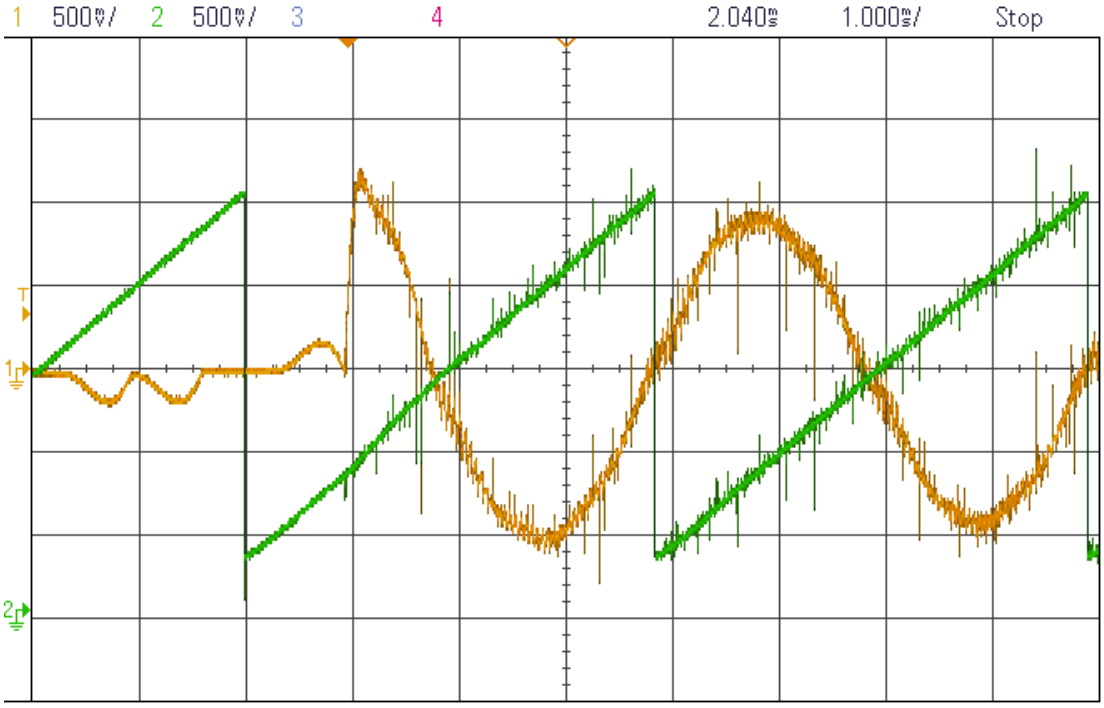

Figure 7.23 - PMSG phase-a current and estimated electrical angle when FOC is enabled (Iq reference of -21A)

Figure 7.24 shows the phase-a current behavior for a wider time frame of $200ms$. After the initial peak, the current tends to its reference peak of $21A$. In this transient time the DC BUS voltage is increased from $140.8V$ to its final value $308V$.

At this time the power dissipated in the resistive load is

$$P_{DC_{LOAD\_1}} = \frac{(308)^2}{45} = 2.1kW \tag{7.11}$$

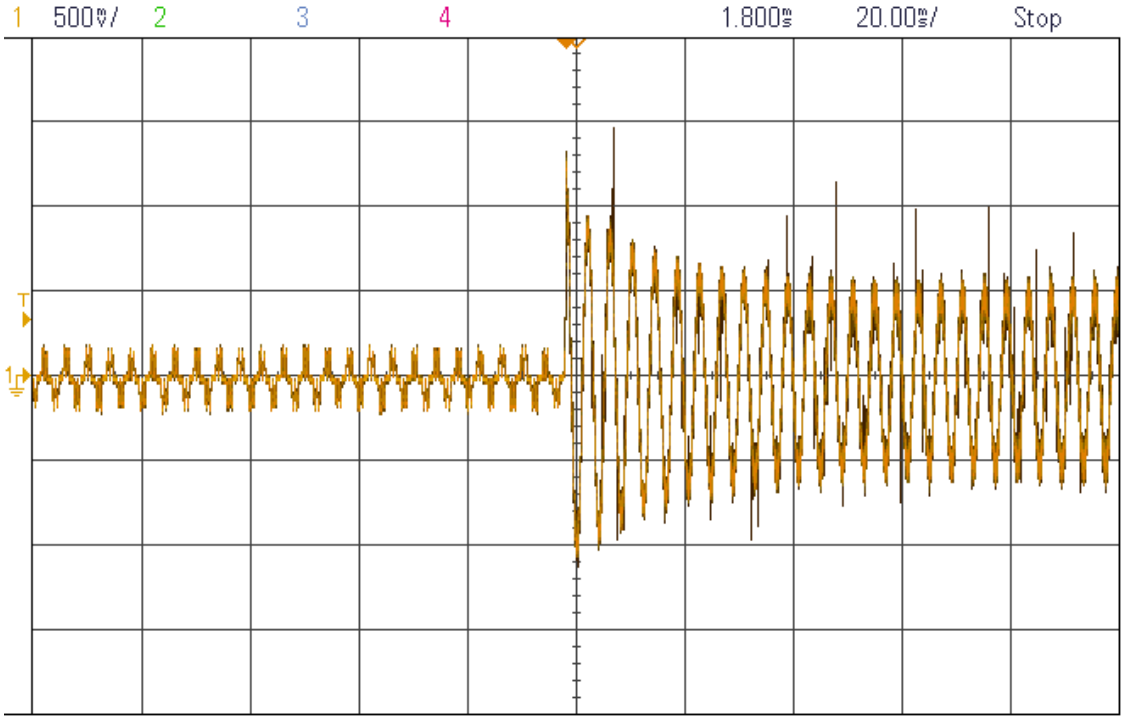

Figure 7.24 - PMSG phase-a current when FOC is turned on (*Iq* reference of -21A) – 200ms analysis

When FOC control is disabled all IGBTs are turned off. This time instant is reproduced in Figure 7.25. At this point the DC BUS voltage starts decreasing from $308V$ to $140.8V$. The current flowing through the 330Ω sensing resistors ensures that angle and speed continue to be correctly estimated.

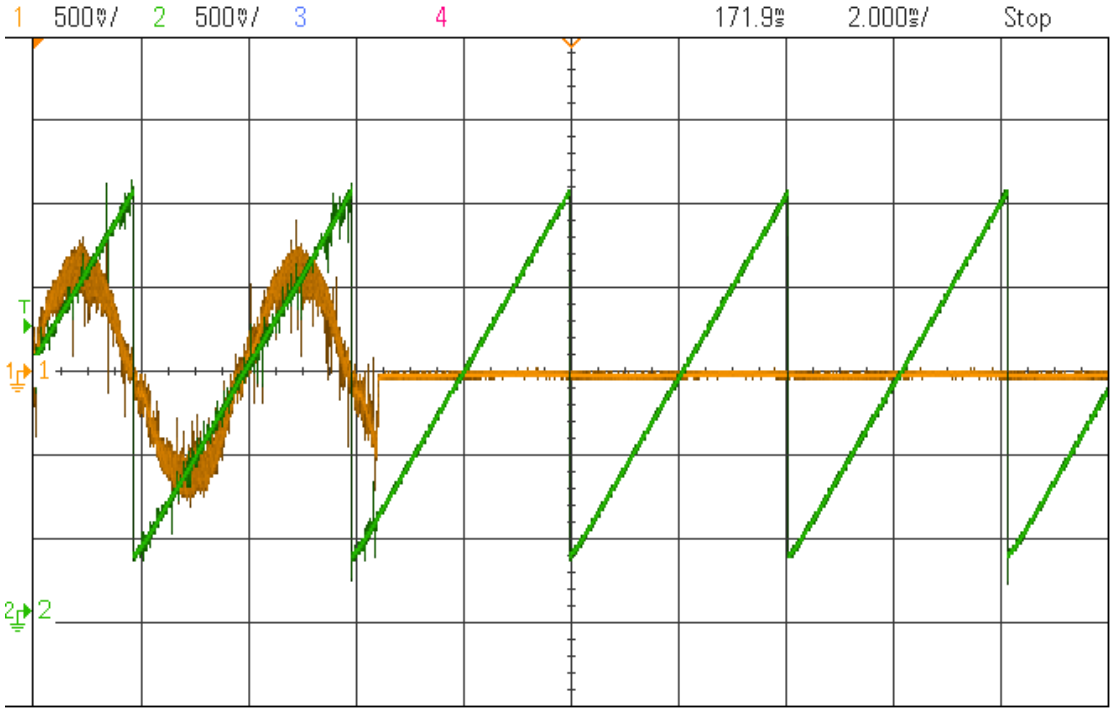

Figure 7.25 - PMSG phase-a current when FOC is disabled

Figure 7.26 shows the time instant were FOC is enabled. This is similar to Figure 7.23 but now the phase-a voltage is also shown. Notice that contrary to what can be seen in Figure 7.23 there is not a correction on the estimated angle. This is because the previous phase-a voltage was already synchronized with the estimated angle.

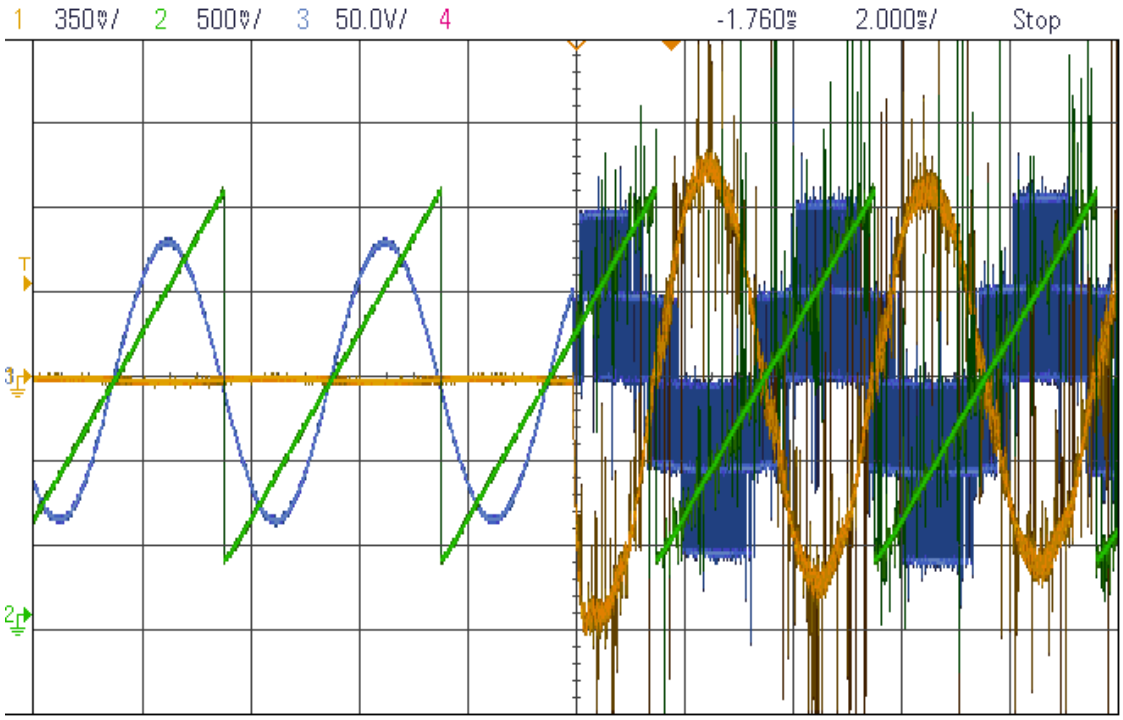

Figure 7.26 - PMSG Phase-a voltage and current, and estimated electrical angle when FOC is enabled with *Iq*=-21A

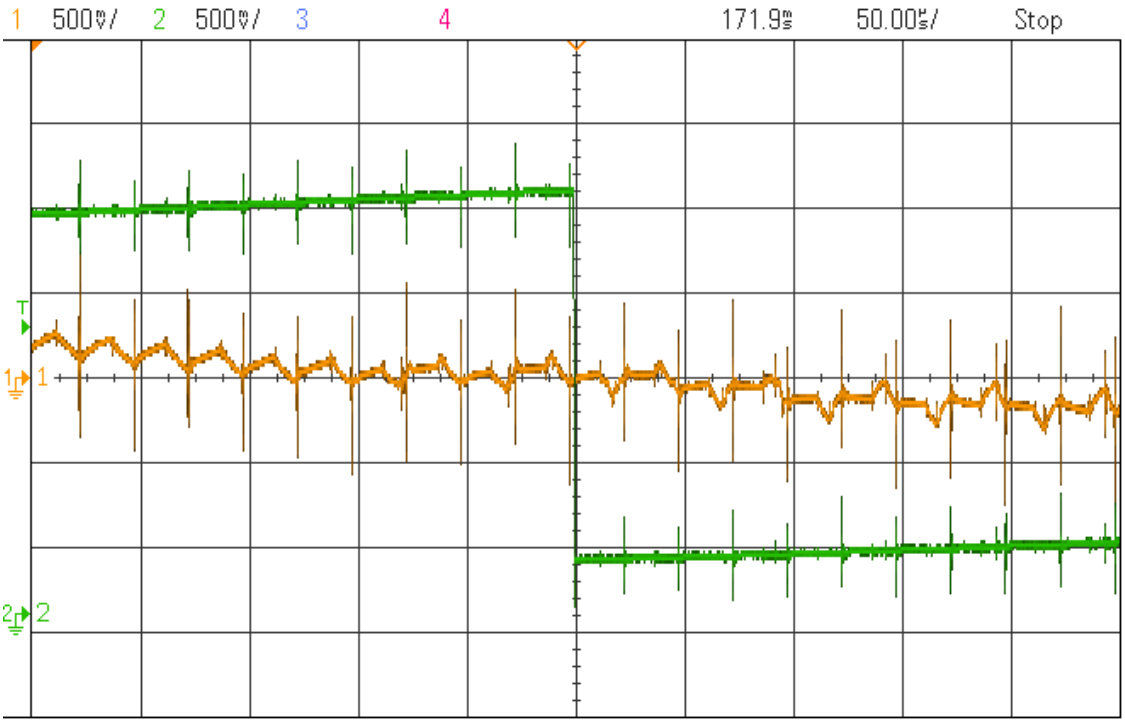

Figure 7.27 - PMSG detail of phase-a current and estimated electrical angle detailed view (*Iq*=-21A)

Figure 7.27 shows a detailed waveform of the phase-a current where the commutations become visible.

Figure 7.28 shows the FFT of the phase-a current. The scale of the frequency is linear. Harmonics can be shown in three different zones: (1) up to 5kHz; (2) around 20kHz; (3) around 40kHz. This image confirms the previous harmonic analysis done in Chapter 6.

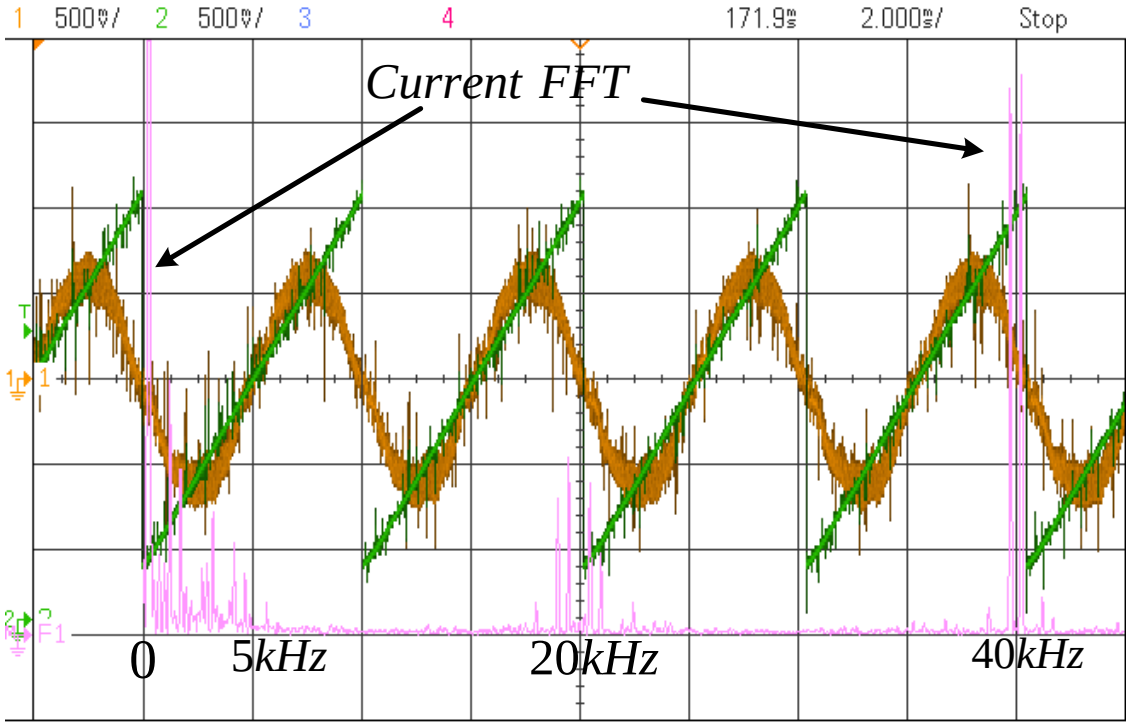

Figure 7.28 - PMSG phase-a current waveform and its FFT

7.5.4 Experiment 4

In order to test system's robustness it was set in continuous operation for three hours at $2.1kW$ DC power ($i_q^* = -21A$ and $i_d^* = 0A$). During this period no incidents were recorded.

Thermal analysis results are shown in Figure 7.29, Figure 7.30 and Figure 7.31. A computer fan was used to cool down the power electronics converter.

This experiment confirmed the system's robustness for the described conditions.

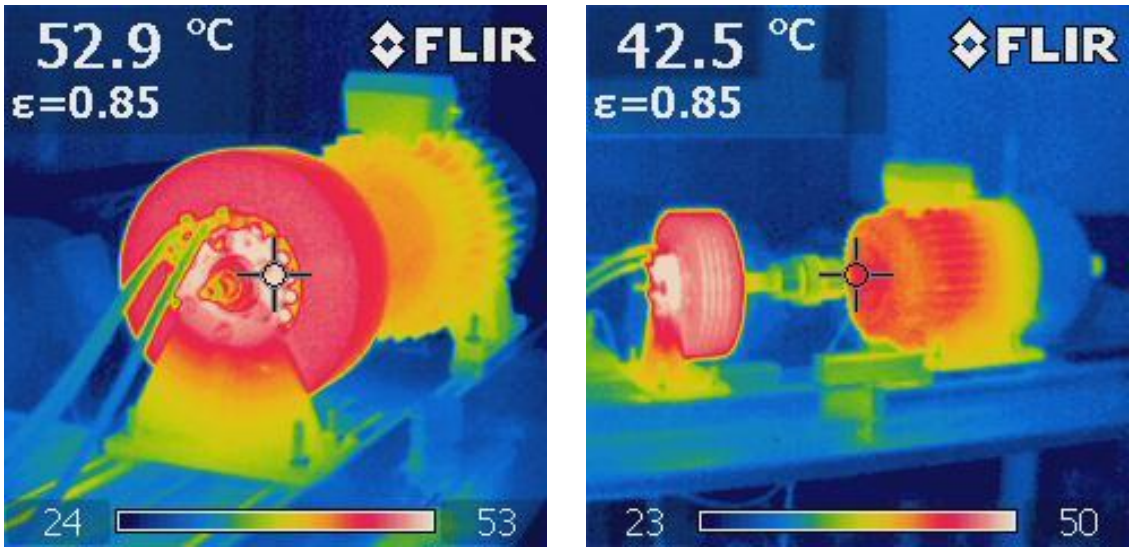

Figure 7.29 - EMRAX and IM set thermal pictures

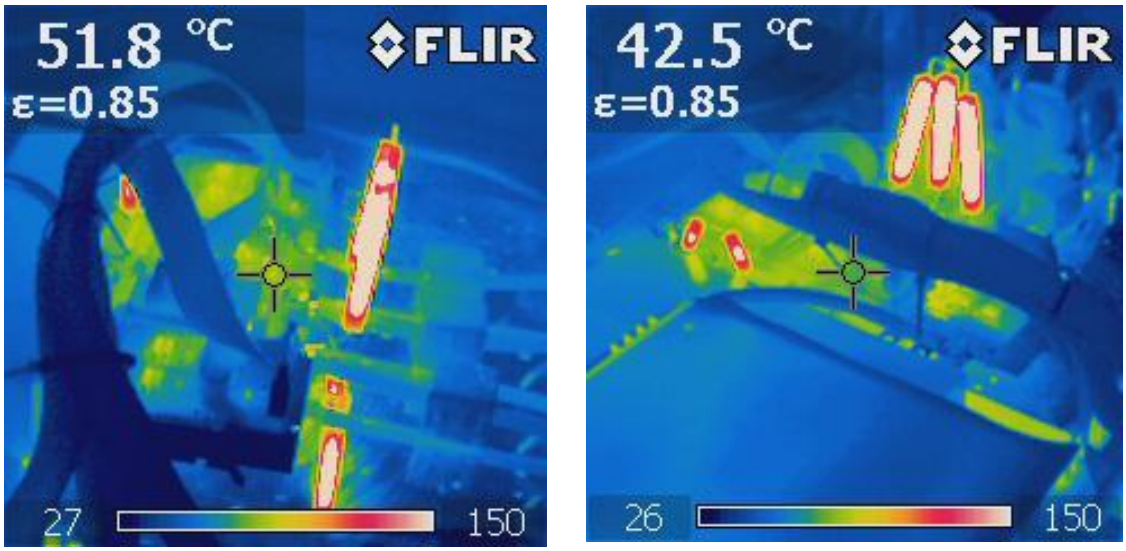

Figure 7.30 - IGBT module, drivers and sensing resistors thermal pictures

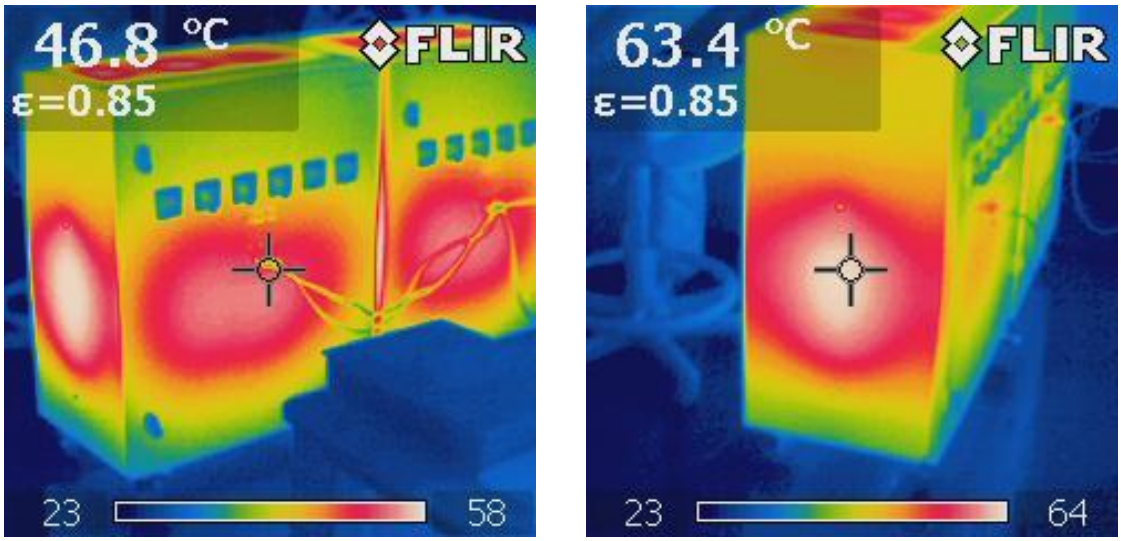

Figure 7.31 - Resistor bank thermal pictures

7.6 Conclusions

The first part of this chapter is related to the physical setup design and its implementation. The design is made around the XMC4500 microcontroller and of the XMC4500 Relax Lite kit.

The PSIM circuits described and analyzed in the previous chapters 5 and 6 were in fact designed at the same time and taking into account the physical setup design. Indeed, the current-to-voltage conversion ratio (of the current transducer), the code execution rate, the issues imposed by the SVM App and the dead-time between IGBT outputs were, among others, reflected on the simulation analysis. Furthermore, the C code running in the PSIM's C Block is the same code running in the XMC4500 microcontroller.

The second part of the chapter describes the four practical experiments executed to validate the theoretical approach and the simulation results.

Experiment 1 confirmed the flux field value given by the PMSM manufacturer.

Experiment 2 shows the sensor resistors placed on the terminals of the AC side of the VSC are adequate to accurately estimate the electrical angle and speed and therefore are a suitable and robust solution, since the experimental results confirm the theoretical and simulation analysis.

Experiment 3 shows the sensorless FOC dynamic response to steep changes (no ramp), in the i_q current reference (from 0 to -21A and back to 0). The angle and speed estimation, uniquely based on currents, are not affected by these steep changes. Again, the experimental results confirm the simulation analysis performed in chapter 6.

The phase harmonic content is also analyzed and again the experimental results confirm those previously obtained by simulation – the existence of three harmonic zones: (1) up to 5kHz due to the IGBT's dead-time; (2) around 20kHz, due to the switching frequency and (3) around twice this same frequency.

Experiment 4 consists of three hours of continuous operation to test the system's robustness as well as to perform thermal analysis. During this period no incidents were recorded, thus confirming the system's robustness under the defined test conditions.

7.7 References

[1] infineon-XMC4500. (2015). *infineon XMC 4500 [Online]*. Available: http://www.infineon.com/cms/en/product/microcontroller/32-bit-industrial-microcontroller-based-on-arm-registered-cortex-registered-m/32-bit-xmc4000-industrial-microcontroller-arm-registered-cortex-registered-m4/channel.html?channel=db3a30433580b3710135a03abaf9385e

[2] XMC4500RelaxKit. (2015). *XMC4500 Relax Kit [Online]*. Available: https://www.infineon.com/cms/en/product/evaluation-boards/KIT_XMC45_RELAX_V1/productType.html?productType=db3a30443784920501381 3b23ac17763

[3] infineon-FS200R07A1E3. (2015). *FS200R07A1E3 IGBT module [Online]*. Available: http://www.infineon.com/dgdl/Infineon-FS200R07A1E3-DS-v03_01-en_de.pdf?fileId=db3a304325afd6e001261d03d4e36001

[4] CONCEPT-2SP0115T2A0-17. (2015). *2SP0115T2A0-17 IGBT driver [Online]*. Available: http://igbt-driver.power.com/products/scale-2-plug-and-play-drivers/2sp0115t/

[5] infineon-AN2007-04. (2015). *How to calculate and minimize the dead time requirement for IGBTs properly [Online]*. Available: https://www.infineon.com/dgdl/Infineon-AN2007_04_Deadtime_calculation_for_IGBT_modules-AN-v1.0-en.pdf?fileId=db3a30431a5c32f2011a5daefc41005b

[6] EPCOS-B25655. (2015). *EPCOS B25655 500uF capacitor [Online]*. Available: http://en.tdk.eu/tdk-en/530192/products/product-catalog/film-capacitors/power-capacitors/search-results---power-capacitors?so={%22seriesname%22:%22B25655%22}

[7] LEM-205-S. (2015). *LEM 205-S current transducer [Online]*. Available: http://www.lem.com/docs/products/lf%20205-s%20sp1.pdf

[8] DAVE-3. (2015). *infineon DAVE 3 Development Platform [Online]*. Available: http://www.infineon.com/cms/en/product/microcontroller/development-tools-software-and-kits/dave-tm-%E2%80%93-free-development-platform-for-code-generation/channel.html?channel=db3a30433580b37101359f8ee6963814

8
Conclusions and Future Work

8.1 Conclusions

This thesis focus on the efficient control of the power delivered from an ICE to the DC bus in a series hybrid electric vehicle with range extender.

The conversion between mechanical and electrical energy is performed by a PMSG and a VSC. The strategy is to extract the maximum power from the ICE, minimizing losses. Furthermore, the controller has to show a good dynamic response to steep changes on the reference control parameters or load conditions.

The efficient control requires an in-depth knowledge of the different subsystems. Therefore, this work addresses: PMSG modeling process, VSC modeling, PWM techniques, PMSG sensorless synchronization techniques, PMSG control techniques and PMSG control strategies.

Three-phase VSC models are used to efficiently control the PMSG. These models enable a better understanding of the VSC dynamics and to extract the knowledge needed to design suitable current controllers. Usually the complexity of these models is high, mainly due to the consideration of the carrier frequency. In this work new Laplace VSC models in *dq* frame are designed which exclude the carrier frequency. It is shown that this inclusion is unnecessary resulting in less complex, albeit equally accurate, models. Furthermore, in these models the cross-coupling between *d* and *q* quantities is highlighted, enabling the design of current controllers able to deal with this *dq* interdependency. Simulation analysis shows that electrical PSIM models and new Laplace equivalent have the same dynamic behavior.

The new Laplace models are on the basis of the design of the decoupled current controller used to control the PMSG. A comparison between this decoupled current controller and a non-decoupled one enables to highlight the improvement in the system dynamics, with the non-decoupled controllers showing longer transients, higher instability and lower dynamics.

In order to achieve smooth operation and taking into account the low L_d and L_q PMSG inductances, the FOC technique is adopted in detriment of DTC. As a vector control technique, it requires to know rotor position and speed. These variables can be acquired either via a shaft-sensor or can be estimated using a sensorless technique.

In this work a new sensorless position and speed estimator is designed. It is based on PLL and synchronous reference frame (*abc*-to-*dq*, Park's transform) and on current measurements instead of voltages. Furthermore, sensing resistors added to

the VSC AC terminals guarantee the PLL synchronization even before FOC operation is enabled. Experimental results show the correct SRF-PLL operation when currents vary from 1.5% to their maximum amplitude, 100% (i_q=-21A)

For PMSG operation (PMSG with isotropic rotor), this new sensorless FOC solution has an excellent behavior, comparable to a sensor-based FOC, with the extra benefits that come from not having a sensor that can fail, get out of calibration, and is usually overpriced.

In comparison to other PLL solutions the SRF-PLL is the one that requires less computational effort, and therefore appropriated to real-time estimation. Experimental results also prove its robustness.

Based on this work with SRF-PLL, another new, more general, sensorless FOC is proposed. It is based on SRF-PLL, current measurements and two dq frames (one for flux and voltages, and the other for currents). With this new control methodology the current controller I_d reference can have any value different from zero.

This new, more general, sensorless FOC can be applied to control PMSGs with any kind of rotor topology and, regarding the same PMSG, can be used with different control strategies. Simulation results show the potential of this methodology. Additionally, this methodology has the potential to be applied not only to HEVs but also to wind energy systems and even to grid connected converters.

Regarding the modulation techniques and since SVM improves the modulation index in the linear zone by about 15% comparatively with SPWM, which leads to an improvement on the VSC dynamic response, it is decided to implement such modulation technique in PSIM simulator, to be used in the PSIM FOC simulations (now available in recent versions of PSIM).

Two new PSIM implementations of SVM technique are designed: conventional SVM and the third order odd harmonic injection PWM. The simulation results show equal performance, with the last one being adopted in simulation analyses because of its simplicity and faster simulations.

An experimental setup was designed whose control is based on Infineon's XMC4500 microcontroller. The C code that runs in the microcontroller is the same used in the simulation analysis.

The experimental results confirmed that:

- Sensor resistors placed on the VSC AC side terminals, in conjunction with the SRF-PLL, are an excellent solution, comparable to sensor-based FOC, to accurately estimate the electrical angle and speed for a wide range of the input variables, current and frequency, confirming the theoretical and simulation analysis;
- The new sensorless FOC dynamic response to steep changes in the current references does not affected the SRF-PLL operation. Again, the experimental results confirm the theoretical simulation analysis performed;
- After three hours of continuous operation including thermal analysis, no incidents were recorded. The system proves to be robust.

8.2 Future Work

The new sensorless PMSG control solutions proposed in this work should be tested in a real HEV, i.e. with an ICE directly coupled to the PMSG. Speed ranges above 1500rpm, e.g. up to 4500rpm, are expected as well as a higher power transfer, e.g. reaching the PMSG continuous power of 40kW.

For these higher speeds the DC bus would have a higher voltage, e.g. 600V or at least a different control strategy should be adopted in order to reduce the field and consequently the PMSG terminal voltage.

Regarding the new proposed sensorless FOC strategy which is based on SRF-PLL and two dq frames, and although the promising simulation results, it needs to be experimentally confirmed.

To apply the SRF-PLL technique to a PMSM operated as a motor is another research path. Since the sensorless FOC technique is based on the estimated electrical angle and speed, a minimum speed is needed to obtain minimal currents to get those estimations. Therefore, an initial motor startup strategy is required.

One solution may be the use of an open loop control routine that generates the required voltages in order to get the PMSM spinning (e.g. with a fixed torque and fixed acceleration rate). Based on these initial currents the SRF-PLL can estimate the electrical angle and speed and then, after a few shaft turns, the control switches to FOC.